Rutherford Appleton Laboratory

Proceedings of the First Joint Seminar of the
ISIS-InCr Collaboration in Crystallography
March 1993

Rutherford Appleton Laboratory
ISIS Facility - Crystallography Group

Russian Academy of Sciences
Institute of Crystallography

Collaboration in Crystallography

First Joint Seminar

The Cosener's House, Abingdon, UK
22-26 March 1993

A programme of scientific exchange and collaboration for mutual benefit between Crystallographers from Russia and the UK.

Edited by

C C Wilson & V I Simonov

RAL-94-031

Proceedings of the First Joint Seminar of the
ISIS-InCr Collaboration in Crystallography
March 1993

A programme of scientific exchange and collaboration for mutual benefit between Crystallographers from Russia and the UK.

The **Institute of Crystallography** in Moscow is one of the foremost establishments wholly devoted to crystallography and related sciences in the world. The work of the Institute ranges from sample preparation and characterisation to the measurement of physical properties and the study of structure in technological, physical, chemical and biological materials.

ISIS, the UK Spallation Neutron Source, is the world's most intense pulsed neutron source, providing neutron beams for the study of structure and dynamics in many areas of condensed matter science. The Crystallography group in the facility operates several novel instruments for structural studies with diverse research interests including the study of the structure of biological molecules, structural solid state chemistry and phase transitions.

Editors and Collaboration Chairs:

C C Wilson
ISIS Facility
Rutherford Appleton Laboratory
Chilton, Didcot, Oxon OX11 0QX
UK

V I Simonov
Institute of Crystallography
Leninsky Prospect 59
Moscow 117333
Russia

The Collaboration

During a visit of Dr C C Wilson, representing the Crystallography Group at ISIS, to the Institute of Crystallography of the (then) USSR Academy of Sciences on Friday 4th October 1991, in the course of an extensive discussion with Professor V I Simonov, Deputy Director of the Institute, the idea of initiating an exchange programme between ISIS and the InCr was tentatively but enthusiastically explored.

The Institute of Crystallography, now part of the Russian Academy of Sciences, is a huge establishment, encompassing four buildings on Leninsky Prospect in Central Moscow and employing some 1500 people, of whom no fewer than 350 are scientists involved in crystallographic research. As one might expect from such a sizeable organisation, the research programme of the Institute covers many aspects of crystallography, ranging from protein crystallography through organic/organometallic structures, fast ion conductors, phase transitions and high T_c materials, to crystal growth and characterisation techniques. The Institute has many facilities for all three aspects of crystallographic science: sample preparation and characterisation, construction of instrumentation and X-ray diffraction experiments.

ISIS, the world's most intense pulsed neutron source, is an establishment of the UK Science and Engineering Research Council. It is located at the Rutherford Appleton Laboratory, situated on the edge of the Berkshire Downs in rural Oxfordshire some 15 miles south of Oxford. The Laboratory employs some 1500 people, of whom over 200 work on the ISIS source, with some 50 neutron scattering scientists involved in condensed matter research using the 14 neutron and muon scattering instruments currently installed for experiments. The experimental programme encompasses all aspects of condensed matter science, ranging from biology through chemistry and physics to engineering and materials science. ISIS provides an often uniquely powerful source of neutrons for crystallography, allowing high resolution, high flux and convenient reciprocal space coverage using the time-sorted white beam produced by the source. The Crystallography Group operates the world's highest resolution neutron powder diffractometer, HRPD, a high flux, medium resolution powder diffractometer, POLARIS, which specialises in demanding sample conditions, and a Laue time-of-flight single crystal diffractometer, SXD, especially useful for reciprocal space surveying.

There are many fields in which a fruitful collaboration could be seen to have the potential to develop, since many of the interests of these two groups of crystallographers overlap. The most likely form of this Collaboration in Crystallography was perceived to be exchanges of personnel, with hospitality extended within the borders of the host country. Three scenarios were envisaged:

- 10-12 day seminars at each establishment, involving around a dozen scientists from each group. These presentations would encourage awareness of mutual interests and explore the options for collaborative work;
- Short term exchanges of around a month to encompass, say, one or two experiments (neutrons at ISIS, X-rays at the InCr) along with associated discussions;
- Long term exchanges of ½-1 year or so, once a particularly strong contact has been made.

An agreement covering this Exchange was signed in 1992 by Academician Vainshtein, Director of the Institute of Crystallography, and Dr Williams, Director of the Rutherford Appleton Laboratory, and the present Joint Seminar is the first formal fruition of this Collaboration in Crystallography.

Detailed Programme of Presentations

Monday 22 March
Seminal Lectures

11:45 - 12:45	**W I F David**	Crystallography at ISIS
14:30 - 15:30	**V I Simonov**	Crystal structure and its correlation with physical properties

Session I

16:00 - 16:30	**R I Smith**	The crystal structures of $Li_{4-3x}(Ga,Al)_xSiO_4$ and $Li_{3.7}Al_{0.1}GeO_4$ solid solutions
16:30 - 17:00	**N Bolotina**	Structural phase transitions and modulated state in the superionic $Na_4TiP_2O_9$

Tuesday 23 March
Session II

09:30 - 10:30	**N A Kiselev**	High resolution electron microscopy of epitaxial structures
10:30 - 11:00	**D A Keen**	Disorder in silver halides
11:30 - 12:00	**M A Estermann**	Determination of novel zeolite structures
12:00 - 12:30	**V N Molchanov**	Refinement of atomic models of Tl-phases of high temperature superconductors
12:30 - 13:00	**B P Sobolev**	New multicomponent materials based on metal fluorides and prospects for their practical applications (I)

Session III

14:30 - 15:00	**E Krivandina**	Preparation of single and polycrystalline multi-component materials using crystallisation from melts
15:00 - 15:30	**A R Armstrong**	Structural studies of alkali-metal loaded zeolites

Presentations (continued)

Tuesday 23 March
Session III (ctd)

16:00 - 16:30	**I Makarova**	Structure and phase transitions in ferroelectric Rb^+ and NH_4^+ selenates
16:30 - 17:00	**K S Knight**	Ionic conducting cerate perovskites
17:00 - 17:30	**M I Sirota**	Algorithm and techniques of refinement of crystal structures of twins

Wednesday 24 March
Session IV

09:30 - 10:00	**S Hull**	Neutron scattering studies of the fluorite structured fast-ion conductors
10:00 - 10:30	**B P Sobolev**	New multicomponent materials based on metal fluorides and prospects for their practical applications (II)
11:00 - 11:30	**R M Ibberson**	Organic structures from high resolution neutron powder diffraction
11:30 - 12:00	**C C Wilson**	Single crystal structure determination by time-of-flight Laue diffraction

Thursday 26 March

10:00 - 10:45	**M W Johnson**	Introduction to ISIS
15:00 - 16:00	**C C Wilson**	Summary of the First Joint Seminar
	C C Wilson/ V I Simonov	Specific collaborations
	V I Simonov	Second Joint Seminar

Contents of Proceedings

Summary of the First Joint Seminar

The First Joint Seminar was extremely successful. Both scientifically and socially, it is clear that our institutions have much in common. The scientific interests fit almost uncannily like lock and key - the wide ranging interests in phase transitions, diffuse scattering and advanced materials and their study by X-rays in Moscow and by neutrons in Oxfordshire illustrate the potential for our joint work. Valentin and I have a lot of work ahead of us to ensure the Collaboration bears fruit. It will not of course be easy - the ever changing political and economic situation in the states of the Former Soviet Union mean that our Collaboration must at least partially exist on external funding by bodies such as the EC and the Royal Society of Great Britain. We must work together to ensure funding can be obtained both for our joint projects and the Second Joint Seminar in Russia in 1994 or 1995.

As ever at scientific meetings, large and small, the social aspect of the contacts are extremely important. Our afternoon at the marvellous mediaeval White Hart pub in Fyfield, with its surroundings so evocative of 17th Century England, followed by a relaxing tour round Blenheim Palace in Woodstock, the home of the Duke of Marlborough and birthplace of Sir Winston Churchill, was appreciated by both UK and Russian delegates. The stroll in the extensive grounds afterwards probably provided as many ideas for collaboration and co-operation as did the formal sessions!

In my summary of the meeting, I attempted to identify areas in which we could profitably combine our knowledge and techniques, and these are summarised below. In many cases there are obvious contacts on each of the ISIS and InCr sides, and we expect communication between these to lead to future progress on our Collaboration.

1. Possible Joint proposals for ISIS neutron beam time

- High T_c materials, especially Tl materials. Specific emphasis on examination of O and Tl disorder. The requirement is for powders of mass greater than 1 g. The instruments to be used at ISIS will be HRPD and POLARIS. *V N Molchanov, W I F David*
- Non-stoichiometric fluorites. Single crystals to be studied on SXD. *V I Simonov, B P Sobolev, S Hull*
- Hydrogen atom ordering in ferroelectric materials. Again single crystal work, including phase transition monitoring. Requirement is for > 3 mm^3 single crystals *I P Makarova, C C Wilson, W I F David*

2. Possible samples for joint work

- Fluorites : $(Ca_{0.99}Y_{0.01})F_{2.01}$, $(Ca_{<0.75}Y_{>0.25})F_{>2.25}$ single crystals.
- Ordered yttrofluorite phases, e.g. tveitite (powder).
- Also, potentially for the future, $(Sr,Yb)F_{2+x}$ (Δr) and $(Sr,Tm)F_{2+x}$ (Δb) are possibly of interest. *B P Sobolev, S Hull*

Other oxides. All ideally neutron sized single crystals (>100 mm^3 if possible).

- $BaCe_{0.9}YO_{2.95}$, $BaCe_{0.9}NdO_{2.95}$ }
- Bi_2WO_6 }
- In_2O_3, Sn doped (^{113}In if possible) } *V I Simonov, S Knight*
- $Sn_3In_4O_{12}$ *V I Simonov, S Hull*
- C_{60} layers *N A Kiselev, W I F David*
- $LaNbO_4$ ferroelastic domains *I P Makarova, W I F David*
- Incommensurate oxides $Li_{1+x-y}Nb_{1-x-3y}Ti_{x+4y}O_3$ ($0.10<x<0.33$) *M I Sirota, R I Smith*

3. Software *M I Sirota, R I Smith, S Hull, C C Wilson*

- Incommensurate structures
- Twinned materials
- Diffuse scattering analysis, especially from non-stoichiometric fluorites.

C C Wilson

Atomic Structure and Its Correlation with Physical Properties of Crystals

V I Simonov
Institute of Crystallography, Russian Academy of Science, Moscow

Introduction

This year the 50th Anniversary of the foundation of the Institute of Crystallography, Russian Academy of Sciences, and its Laboratory of X-ray Structural Analysis will be marked. During that time, the For all those years the primary direction of research carried out in the Laboratory has been further development of X-ray diffraction techniques for structural studies of crystals and the establishment of correlations between the structure and physical properties of crystals. In recent years major attention has been focused on precise techniques for the refinement of crystal structures from X-ray diffraction data. Application of up-to-date equipment, along with novel techniques for the measurement and processing of integrated intensities, has led to a situation when errors in the observed structure amplitudes are mainly due to the quality of the samples under study. During data reduction ($I \rightarrow |F|$) and structural refinement, we take into account the geometry of the measured diffraction pattern, absorption in the sample, polarization, anomalous scattering, simultaneous reflections, thermal diffuse scattering and extinction. Among the structure parameters to be refined are atomic coordinates, qualitative characteristics of isomorphous replacements, varying occupancy of atomic sites, as well as the thermal motion parameters of the atoms, with account taken of anisotropy and also deviations from harmonic behaviour of the thermal motion. If the sample is of high quality,, deformation electron density maps can be constructed by the X-X' technique in order to reveal the character of chemical bonding in the crystal.

In our Laboratory we use various techniques for the study of twins, as well as commensurately and incommensurately modulated phases. Although a neutron source is not available at our Institute, several neutron diffraction studies of nonstoichiometric fluorite phases, selenites and other crystals have been carried out by scientists from our Laboratory. Important results of studies of atomic mechanisms of phase transitions in superionic crystals, ferroelectrics, high-temperature superconductors and other materials with properties, which are interesting for solid state physics and applied materials science have been obtained. Below we shall give some examples of structural studies carried out at the Laboratory of X-ray structural analysis of the Institute of Crystallography in Moscow.

Crystal structure of nonstoichiometric phases of $M^{2+}_{1-x}R^{3+}_{x}F^{1-}_{2+x}$

Single crystals of nonstoichiometric fluorite-type phases are attractive due to the fact that they are transparent within a wide range of the composition spectrum, as well as exhibiting significant F^--ion conductivity. In addition, they are promising for the possible fabrication of laser media based on these phases. For many years the structural model suggested by Willis [1] had been commonly recognized for these compounds, especially after the neutron diffraction study [2]. According to that fluorite-type model, additional F-atoms are statistically distributed over two crystallographically independent sites. As long ago as 1969, the compound $Ca_{0.6}Ce_{0.4}F_{2.4}$ was studied tt our Institute. In this phase, distribution of additional F-atoms over only one crystallographic site on the three-fold axes was found [3]. Later, for $Ba_{0.73}Pr_{0.27}F_{2.27}$, additional F-atoms were found to be located only at one site, this time on the two-fold axis [4]. The reason for the distribution of F-atoms over two sites reported in [2] can be seen well in Figure1. The additional F atoms are in fact located only on the two-fold axis, while a false maximum is located on the threefold axis. This maximum results from a combination of 'wings' of the three peaks from the atoms located on the two-fold axis. In all the compounds of this type studied by us [5], additional F atoms were distributed only over one of the two sites.

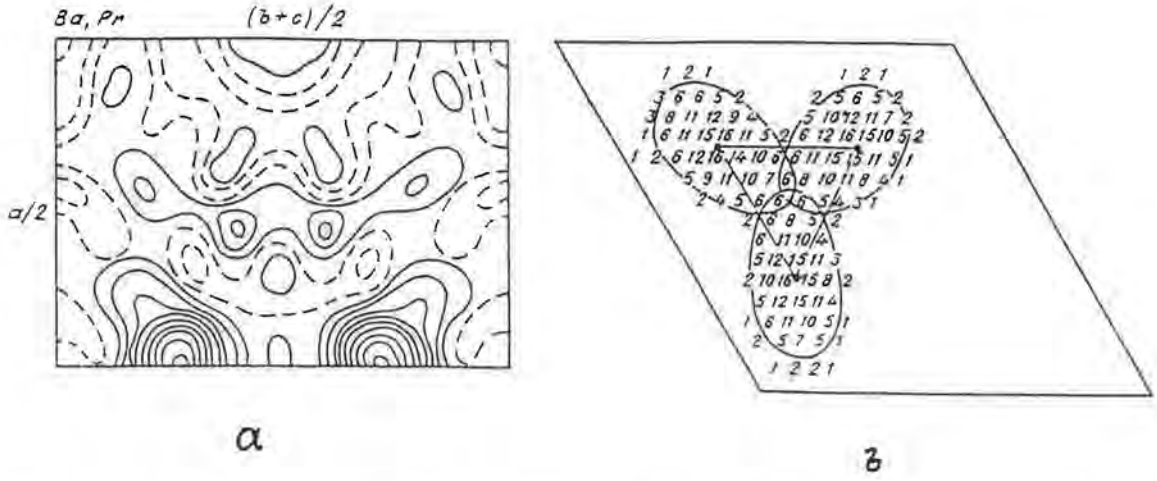

Figure 1 - Difference nuclear density distribution in $Ba_{0.73}Pr_{0.27}F_{2.27}$: (a) plane x-y=0, isolines are drawn every 0.1 fm A^{-3}; (b) the plane x+y+z=1.236. It is clear from this why a false density peak appeared on the threefold axis.

If we understand correlations between the chemical composition and crystal structure of $M^{2+}_{1-x}R^{3+}_xF_{2+x}$ compounds we can predict their properties. For instance, in the system BaF_2-LaF_3 one can calculate the composition of single crystals of the solid solution $Ba_{1-x}La_xF_{2+x}$ in which ionic conductivity will attain any desired value within the sigma range $10^{-10.7}$ to $10^{-4.3}$(ohm cm)$^{-1}$ or, alternatively, hardness H will reach any desired value from 80 to 250 kg mm^{-2}, etc.

Crystal structure and isomorphous replacements in sillenites

The unusual isomorphism typical of sillenites, allows one to control certain of their physical characteristics and leads to use of these crystals in piezotechnology, acousto- and optoelectronics and in holography. The commonly used chemical formula for sillenites is $Bi_{12}MO_{20}$, where M is a cation, or isomorphous mixture of cations, with effective valency rigorously equal to 4+ [6]. The results of structural studies of sellenites with M = Ge, Ti, (Fe,P), (Bi, Ga), (Bi,Fe), (Bi,Zn), (Bi,V) and the γ-phase of Bi_2O_3 carried out at the Institute of Crystallography, suggest another interpretation. In fact, there are sillenites whose stoichiometric composition differs from that mentioned above. In such cases the effective valency of the isomorphous mixture of cations M can deviate from 4+, either higher or lower. The number of oxygen atoms can also differ from 20.

The sillenite $Bi_{12}GeO_{20}$ has an ideal stoichiometric composition. The titanium selenite $Bi_{12}Ti_{0.90}O_{19.80}$, on the other hand, is characterized by reduced occupancies. The coordination sphere of the cation M in an ideal selenite comprises MO_4 tetrahedra. On thye other hand, if the site is partially populated by Bi atoms, the latter are trivalent (Bi^{3+}) and the umbrella-like group BiO_3 replaces the MO_4 tetrahedron. The fourth oxygen atom of this group is replaced by the $6s^2$ electron lone pair, denoted E, of the Bi^{3+} ion. The cubic symmetry of the crystal is retained, on average, owing to statistical re-orientations of the BiO_3E group. The chemical formulae of the sillenites under study, refined from the structural studies, are as follows:

$Bi_{12}(Fe_{0.35}P_{0.59}[\ ]_{0.06})O_{20}$;
$Bi_{12}(Bi_{0.50}Ga_{0.50})O_{19.50}$;
$Bi_{12}(Bi_{0.50}Fe_{0.50})O_{19.50}$;
$Bi_{12}(Bi_{0.67}Zn_{0.33})O_{19.33}$;
$Bi_{12}(Bi_{0.03}V_{0.89}[\ ]_{0.08})O_{20.27}$.

The mechanism of isomorphous replacements at the M site of various cations differ significantly in the various sillenites. A remarkable, from the point of view of crystal chemistry, isomorphous occupation of the M site by the cations Fe^{3+} and P^{5+}. Site sharing by these ions, whose ionic radii differ by a factor of almost 2, is effected by deformation of the main polyhedra of the BiO_5E structure and statistical alternation of large and small tetrahedra at the M site. If the valency of the cation M exceeds 4+, additional O atoms occupy the framework voids.

The various mechanisms of isomorphous replacement in sillenites provide an actual means for desirable changes of the chemical composition and hence the characteristics of those physical properties related to the composition. It seems very likely that in the near future sillenites will be used on a wide scale in various fields of technology.

Crystal structure and phase transitions in the solid electrolytes $Li_3Sc_2(PO_4)_3$ and $Li_3Fe_2(PO_4)_3$.

Crystalline materials with high ionic conductivity are attractive because of their diverse physical properties. Among such materials there are conductors with one-, two- and three-dimensional conductivity. The range of practical application of solid electrolytes are constantly broadening: gas sensors for determination of environment composition; capacitors with very high capacitance; secondary cells etc. Isostructural superionic crystalline materials of composition $Li_3Sc_2(PO_4)_3$ and $Li_3Fe_2(PO_4)_3$, which exhibit Li^+-ion conductivity, have been synthesized and studied at the Institute of Crystallography. They undergo two phase transitions, the temperatures of which can be altered by small quantities of isomorphous dopants. The basic structure is formed by a three-dimensional framework made up of Sc octahedra and P tetrahedra, in whose channels Li-atoms are located. The main structural transformation during the phase transitions is related to changes in Li atom distribution. There are three crystallographically independent Li-atom sites in the high temperature superionic phase. Only one of these is 100% Li occupied and the atoms on these sites are not mobile and are not engaged in the ionic transport. The occupancy of the other two sites is approximately 25%, and it is these ions that are responsible for electroconductivity. Figure 2 shows the Li ion distribution in all three phases, the low-temperature α- and β-phases and in the superionic γ-phase [7]. The specific features of the structures give a clear rationale for the remarkable anisotropy of ionic conductivity in these single crystals.

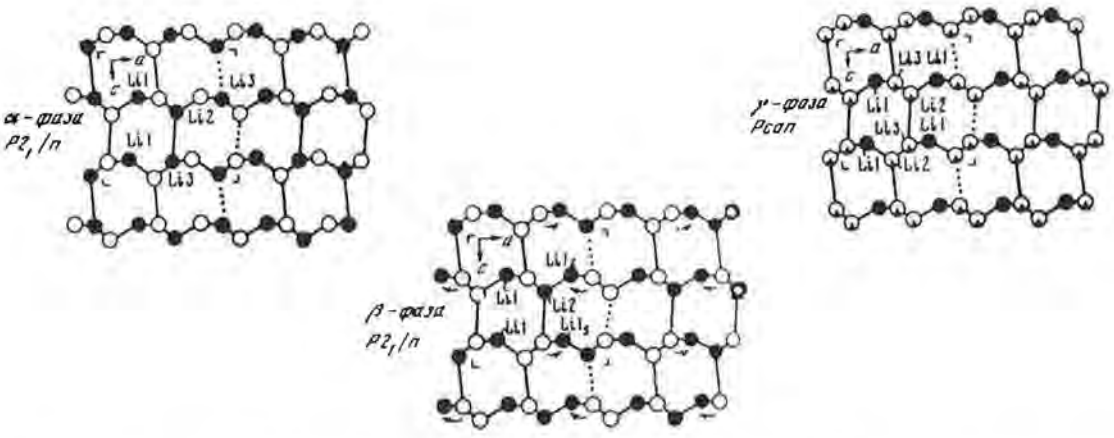

Figure 2 - Schematic distribution of Li ions in three phases of $Li_3Sc_2(PO_4)_3$: (●) - fully occupied sites, (⊙) - partially occupied sites in the superionic γ-phase, (o) - vacancies in the given phase, occupied in other phases.

Crystal structure and anharmonicity of atomic thermal motion in α-TeO_2 and $KMnF_3$ compounds.

Allowing for anharmonic thermal motion in crystals allows more accurate structural parameters to be obtained from diffraction data. In addition, it provides useful information which characterizes certain physical properties of the crystals under investigation. Let us consider, as a first example, the structure of single crystals of α-TeO_2, which possess unique acousto-optical features. In practice, a slow transverse acoustic wave which propagates in α-TeO_2 single crystals in the direction [110], polarized over [1 $\bar{1}$ 0], is used. This acoustic mode is characterized by a high absorption coefficient, some 290 db cm^{-1}, for frequency 1 GHz, exceeding by two orders of magnitude the attenuation of other acoustic waves in paratellurite. In the course of structural studies of this crystal its absolute configuration, described by space group $P4_32_12$, was established. Figure 3 shows the closest O atom coordination of the tellurium and a section of the anharmonic component of the probability density function of the Te atom in the course of its thermal motion. The character of this function unambiguously determines the unique acousto-optical properties of α-TeO_2 single crystals [8].

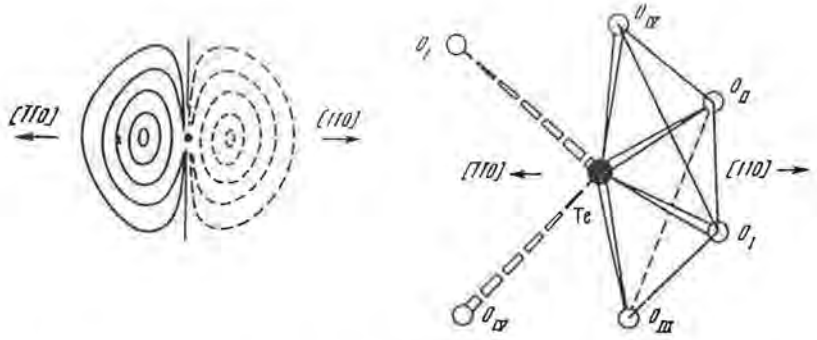

Figure 3 - Structure of α-TeO_2. Section of the anharmonic component of the probability density distribution of the Te atom location at a given point in the course of thermal motion. The closest oxygen coordination of Te atom in the structure.

As a second example illustrating the use of the information provided by studies of anharmonicity, we shall take a cubic perovskite-type structure of $KMnF_3$, which undergoes a transition to the tetragonal phase at T=185K. The mechanism of the phase transition is due to rotations of Mn octahedra about one of the four-fold symmetry axes. Precise structural studies of the cubic phase of $KMnF_3$ allowed us to reveal deviations of the fluorine atoms from harmonic thermal motion some 100° prior to the structural phase transition. The form of the probability density function for atomic shifts from the equilibrium positions allows one to predict, dozens of degrees prior to the phase transition, what atoms will be shifted, and in what directions they will shift, during the forthcoming phase transition [9].

Structural studies of HTSC single crystals.

Structural studies of various La-containing phases of the type $(La,Sr)_2CuO_{4-\delta}$, having different T_c, have shown that the superconducting transition temperatures are dependent not only on Sr content in the sample, but also on the nature of its distribution over the La sites. By using various crystal growing techniques and different thermal treatments, we have been able to obtain and study single crystals with an even Sr distribution over La sites $[(La_{0.97}Sr_{0.03})_2CuO_{4-\delta}]$, partial order in the Sr distribution $[(La_{0.94}Sr_{0.06})(La_{0.86}Sr_{0.14})CuO_{4-\delta}]$, and full order in the Sr distribution $[La(La_{0.76}Sr_{0.24})CuO_{3.92}]$. In the latter compound, the presence of Sr in certain double La layers gives rise to the loss of some oxygen in these layers and a consequent lowering of T_c. It is found that an even Sr atom distribution over the La sites is the best situation for superconductivity [10].

Studies of the crystal structure of Y-phases of $YBa_2Cu_3O_{7-\delta}$ with various oxygen contents showed that in single crystals with oxygen contents ranging from 6.0 to 6.5 atoms there co-exist regions with an ordered oxygen atom distribution, of tetragonal symmetry with the composition $YBa_2Cu_3O_6$, and regions of the orthorhombic phase II with composition $YBa_2Cu_3O_{6.5}$ and $T_c = 50$ K. In samples with oxygen content from 6.5 to 7.0 regions of two orthorhombic phases coexist: II $YBa_2Cu_3O_{6.5}$ and I $YBa_2Cu_3O_7$, the latter with $T_c = 90$ K. Those tetragonal superconducting phases described in the literature are always characterized by significant Cu atom deficiency or isomorphous replacement of some Cu atoms by Al, Ni, Zn or Co atoms. According to our data, such crystals are merohedral twins of orthorhombic phases, with the twins merely imitating the tetragonal symmetry. Vacancies, or other atoms replacing copper, are located at the twin junctures of such crystals. Twin partners are then rotated through 90°, which excludes the reflection splitting which is typical of more usual twins of Y-phases [11].

Studies of deformation electron density distribution in single crystals of high-temperature superconductors have recently been undertaken. The first subect of these studies is the Nd_2CuO_4 matrix, which acquires the features of an electronic superconductor when doped with Ce. Figure 4 shows sections of deformation electron density maps in $Nd_{1.890}CuO_{3.85}$. It is seen from these maps that the bonding character of the O_1 and O_2 atoms differ from one another. The first one has covalent bonds with Cu atoms, while the second one, bonded to neodymium, is in the ionic state. The maps exhibit the population of the $3d_{z^2}$ and $3d_{x^2-y^2}$ orbitals of the copper atoms and the departure of one electron from the 4f shell of Nd.

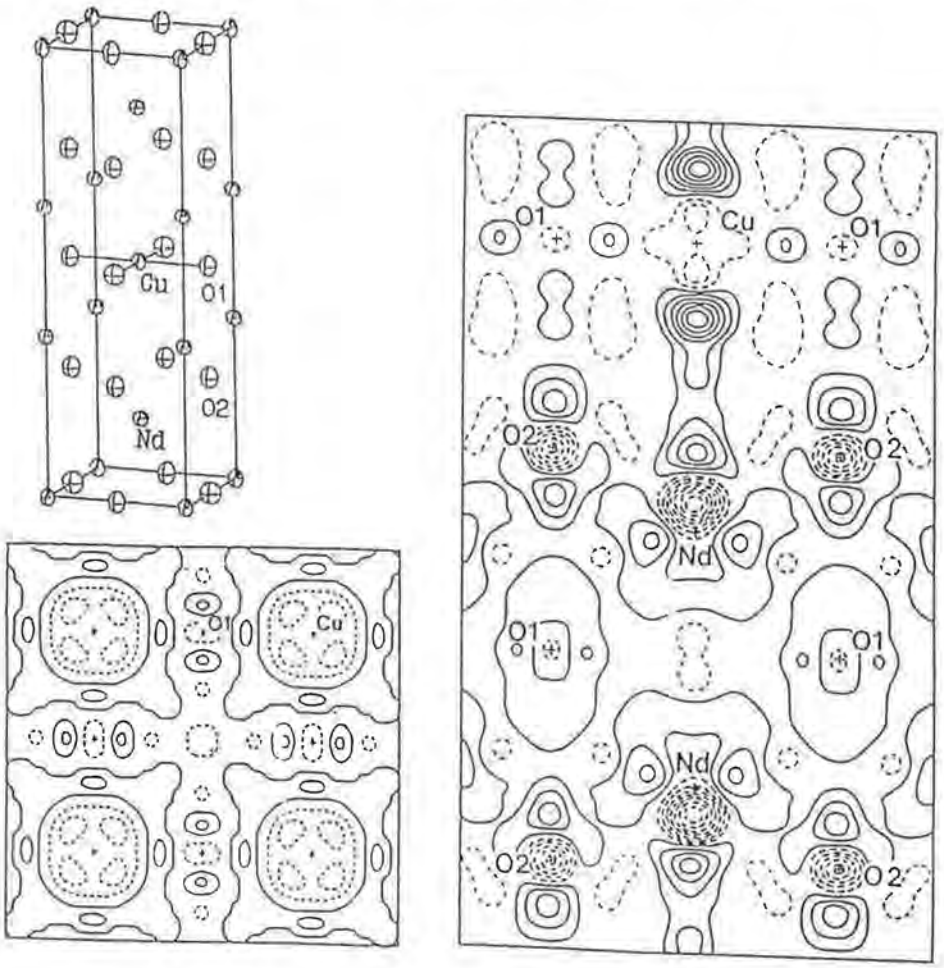

Figure 4 - Structure of $Nd_{1.890}CuO_{3.85}$. Sections of deformation electron density in planes parallel to (010) and (001).

These examples of precise structural studies clearly demonstrate the possibilities for finding a correlation between crystal structure and physical properties of crystals at the forefront of current scientific research. Further advances in this field can be made if, in the course of structural studies, X-ray and neutron diffraction techniques are combined.

References

[1] B T M Willis (1964) *J Phys* **25** 431-439.
[2] A K Cheetham, B E F Fender and M J Cooper (1971) *J Phys C: Solid State Phys* **4** 3107-3121.
[3] V B Aleksandrov and L S Garashina (1969) *DAN SSSR* **189** 307-310.
[4] V B Aleksandrov, L P Otroshchenko, L A Fykin, V A Sarin, V I Simonov and B P Sobolev (1984) *Kristallografiya* **29** 381-383.
[5] L A Muradyan, B A Maximov and V I Simonov (1987) *Koordinatsionnaya Khimiya* **12** 1398-1403.
[6] D C Craig and N S Stephenson (1975) *J Solid State Chem* **15** 1-8.
[7] A B Bykov, A P Chirkin, L N Demyanets, S N Doronin, E A Genkina, A K Ivanov-Shits, I P Kondratyuk, B A Maximov, O K Mel'nikov, L A Muradyan, V I Simonov and V A Timofeeva (1990) *Solid State Ionics* **38** 31-52.
[8] I P Kondratyuk, L A Muradyan, Yu V Pisarevskii and V I Simonov (1987) *Kristallografiya* **32** 609-617.
[9] A A Shevyrev, L A Muradyan, V E Zavodnik, K S Aleksandrov and V I Simonov (1980) *Kristallografiya* **25** 555-559.
[10] V I Simonov, L A Muradyan, R A Tamazyan, V V Osiko, V M Tatarintsev and K Gamayunov (1990) *Physica C* **169** 123-132.
[11] V I Simonov, L A Muradyan, V N Molchanov and E K Koviev (1988) *Kristallografiya* **33** 621-624.

The Structures Of Tl-Containing Superconducting Single Crystals

V N Molchanov
Institute of Crystallography, Russian Academy of Sciences, Moscow

Introduction

In this paper we report results of structure determinations carried out at the Laboratory of X-ray Structure Analysis of the Institute of Crystallography under the State Program of HTSC Investigations. In the past five years we have been working in collaboration with various groups of other Institutes of the Academy, such as Institute of Physics, Solid State Physics and the Institute of Chemical Physics. Due to these close contacts we have obtained high-quality single crystals for structure determinations. The main results of these investigations have been published elsewhere [1-4]. This communication reports X-ray diffraction studies of only Tl-containing superconducting materials and specific structural features of some thallium cuprates.

The diverse Tl-containing superconductors can be conditionally divided into two series of phases:

$TlBa_2Ca_{n-1}Cu_nO_{2n+3}$	(n = 1 - 5)	series I
$Tl_2Ba_2Ca_{n-1}Cu_nO_{2n+4}$	(n = 1 - 4)	series II

The 2223 phase of the second series is characterized by the highest superconducting transition temperature, 125K. The main difference between these two series is as follows: all the phases of the 1st series contain a single layer of Tl-octahedra, while the second series contains a double layer of such octahedra linked according to the rock-salt motif. The phases within each series differ in the number of Cu-O sheets located in the perovskite block of the structure.

Superconductivity in Tl-cuprates is believed to originate from the presence of holes in the CuO_2-planes, while the TlO-layers serve as reservoirs of charge carriers. In the case of strict stoichiometry the formal oxidation state of Cu in the 1st series varies from Cu^{3+} to $Cu^{2.2+}$ as n changes from 1 to 5. In the 2nd series all the copper atoms have formal oxidation state of exactly 2+. It is known, however, that a compound becomes a superconductor when some copper atoms are oxidized up to 3+, creating holes. This is why cationic vacancies and replacements of any kind, which are not of major importance for single-Tl-layer cuprates (except the 1st member with n=1), are vital for the whole family of cuprates with double-Tl-layers.

Various authors give different estimates regarding the presence of vacancies, isomorphous replacements and atomic shifts in the cationic and anionic sublattices of Tl-containing superconductors. The present study represents an attempt to determine the cation and oxygen distributions which may be dependent on growing technique and conditions.

Experimental

Preparation of HTSC samples suitable for X-ray structure analysis is a kind of art. Our colleagues from the Institute of Solid State Physics put their efforts into preparing samples with the highest possible T_c for the given phase under certain preparation conditions. As a result, we obtained samples of four different phases grown from solution in melt in oxygen flux under normal pressure; with T_c found from the temperature dependence of the magnetic moment (Table 1). Three phases were found to be superconductors; the lanthanum analogue of the 1212 phase did not undergo a superconducting phase transition. The samples selected for the experiment were thin plates except for those of the 2212 phase, for

which a thick plate was obtained, allowing us to prepare a rounded sample to make the absorption correction simpler.

Table 1

Composition and T_c for the crystals studied

Abbreviation	Crystal composition				T_c (K)
2201	$(Tl^{3+}_{0.93}Cu^{1+}_{0.07})_2Ba_2$			$Cu^{2.32+}O_6$	110
2212	$(Tl^{3+}_{0.92}Cu^{1+}_{0.08})_2Ba_2$		$Ca^{2+}_{0.88}Tl^{3+}_{0.12}$	$Cu_2^{2.09+}O_8$	110
Ca – 1212	Tl	Ba_2	$Ca^{2+}_{0.87}Tl^{3+}_{0.13}$	$Cu_2^{2.44+}O_7$	80
La – 1212	Tl	Ba_2	La^{3+}	$Cu_2^{2.00+}O_7$	–

Single crystal diffraction data were taken at room temperature on the ENRAF-NONIUS CAD4F diffractometer using AgK_α-radiation. All the samples were initially tested for absence of epitaxial phases, absence of twinning, absence of satellite reflections and reflections violating the space groups P4/mmm (1st series) or I4/mmm (2nd series). In our tests we mainly use two-dimensional angular scanning of the chosen areas of reciprocal space [2].

The data were collected in five octants of reciprocal space within a $\sin\theta/\lambda$ radius of 0.8 - 1.1 A^{-1} with background measurements optimized for weak reflections. Absorption correction was applied by numerical integration with an account of the crystal shape before averaging symmetry equivalent reflections (Table 2). The structural models were refined using a local PC-version of the PROMETHEUS program package [5].

Table 2

Summary of crystallographic information for 2201, 2212, Ca-1212 and La-1212 crystals

	2201	2212	Ca-1212	La-1212
Sample size (μm)	0.04-0.17	r=0.113	0.04-0.25	0.04-0.39
Space group	I4/mmm	I4/mmm	P4/mmm	P4/mmm
a (Å)	3.869(1)	3.852(3)	3.847(1)	3.944(1)
c (Å)	23.259(5)	29.290(6)	12.721(3)	12.607(3)
V ($Å^3$)	348.17(2)	434.60(2)	188.26(2)	196.10(2)
μm (cm^{-1})	333.9	279.2	206.5	220.1
Measured reflections	4268	2358	2509	4097
Independent reflections	429	239	284	674
$R(I)_{aver}$ (%)	2.0	6.5	3.6	5.9
R/R_w (%)	1.40/1.62	1.67/1.62	3.40/3.20	1.58/2.08

In the refinements we paid special attention to the strongly correlating parameters of the structural models, in particular, to occupancy coefficients, thermal parameters and slight shifts of the Tl and O atoms. In some cases we used step-by-step scanning of correlating parameters [6]. Besides the R-factor, we considered difference electron density maps as a criterion. The results of our studies are listed in Tables 3-7.

The R-factors (Table 2) provide evidence for a rather high reliability of the obtained parameters. None of the structures showed oxygen site deficiency. It is worthy of note that Tl atoms occupy Ca sites in the Ca-containing phases in similar amounts, with Cu atoms also occupying Tl sites at a similar level. This situation appears to reflect preparation conditions and explains the fact that different papers report different values for samples obtained at other Laboratories.

Table 3

Positional and thermal parameters for the atoms of Ca-1212 structure (for details see reference [3])

Atom	Occupancy	x	y	z	B_{eq}
Tl	1.0	0.0877(4)	0.0	0.0	1.76(4)
Ba	1.0	0.5	0.5	0.21550(5)	0.55(2)
Cu	1.0	0.0	0.0	0.3740(1)	0.44(2)
Ca/Tl	0.87(1)/0.13	0.5	0.5	0.5	0.47(4)
O1	1.0	0.5	0.0	0.3797(5)	0.7(1)
O2	1.0	0.0	0.0	0.1582(7)	1.1(1)
O3	1.0	0.5	0.5	0.0	2.6(3)

Table 4

Positional and thermal parameters for the atoms of La-1212 structure (for details see reference [12])

Atom	Occupancy	x	y	z	B_{eq}
Tl	1.0	0.0755(1)	0.0	0.0	1.46(4)
Ba	1.0	0.5	0.5	0.20654(2)	0.74(1)
Cu	1.0	0.0	0.0	0.35922(5)	0.68(1)
La	1.0	0.5	0.5	0.5	0.70(1)
O1	1.0	0.5	0.0	0.3733(2)	0.88(2)
O2	1.0	0.0	0.0	0.1648(4)	1.7(1)
O3	1.0	0.626(3)	0.5	0.0	2.0(2)

Table 5

Positional and thermal parameters for the atoms of 2201 structure (for details see ref [13])

Atom	Occupancy	x	y	z	B_{eq}
Tl	0.925(4)	0.520(2)	0.520(2)	0.2091(1)	1.09(6)
Cu'	0.075	0.5	0.5	0.196(4)	1.0(6)
Cu1	1.0	0.5	0.5	0.0	0.63(1)
Ba	1.0	0.0	0.0	0.08326(1)	0.745(6)
O1	1.0	0.0	0.5	0.0	0.85(4)
O2	1.0	0.5	0.5	0.1172(2)	1.09(5)
O3	0.925	0.551(5)	0.551(5)	0.2892(4)	2.3(4)
O3'	0.075	0.5	0.5	0.277(4)	1.2(4)

Table 6

Positional and thermal parameters for the atoms of 2212 structure (for details see ref [4])

Atom	Occupancy	x	y	z	B_{eq}
Tl	0.901(4)	0.5252(3)	0.5252(3)	0.21368(2)	1.00(2)
Cu'	0.099	0.5	0.5	0.20803(7)	1.01(4)
Cu1	1.0	0.5	0.5	0.05399(4)	0.47(2)
Ba	1.0	0.0	0.0	0.12156(2)	0.69(2)
Ca/Tl	0.883(4)/0.117	0.0	0.0	0.0	0.59(4)
O1	1.0	0.0	0.5	0.0524(1)	0.8(2)
O2	1.0	0.5	0.5	0.1451(3)	1.4(3)
O3	0.901	0.559(3)	0.559(3)	0.2817(5)	4.0(7)
O3'	0.099	0.5	0.5	0.2709(8)	1.2(5)

Table 7
Comparison of selected interatomic distances (Å)

Bond	La-1212	Ca-1212	2201	2212
Tl-O2	2.098(5)(x2)	2.040(9)(x2)	2.009(3)(x2)	2.010(7)(x2)
Tl-O3	2.297(6)(x2)	2.493(1)(x2)	2.445(1)(x2)	2.330(1)(x2)
Tl-O3	2.932(9)(x2)	2.968(1)(x2)	2.889(1)(x2)	2.850(1)(x2)
Cu-O1	1.980(2)(x4)	1.924(3)(x4)	1.934(3)(x4)	1.927(2)(x4)
Cu-O2	2.452(5)(x1)	2.745(9)(x1)	2.727(4)(x2)	2.675(7)(x1)
Cu'-O1	----	----	1.84(7) (x1)	1.84(6) (x1)
Cu'-O2	----	----	1.87(11)(x1)	2.84(9) (x1)
Cu'-O3	----	----	2.82(3) (x4)	2.79(3) (x4)
Ba-O1	2.882(2)(x4)	2.839(5)(x4)	2.737(1)(x4)	2.792(3)(x4)
Ba-O2	2.838(1)(x4)	2.816(2)(x4)	2.847(2)(x4)	2.811(2)(x4)
Ba-O3	2.651(2)(x1)	2.741(1)(x1)	2.980(2)(x1)	2.845(3)(x1)
Ca/La-O1	2.538(2)(x8)	2.458(4)(x8)	----	2.463(3)(x8)

In all our studies we observed disordering effects only in the Tl-O layers (Figures 1-2). Displacement of the oxygen atoms in double-Tl- layer phases has been reported by many authors. We have also, however, observed Tl-atom displacement from symmetry sites. This displacement is less pronounced than that of the O atoms but it occurs in the same *ab*-diagonal direction and is characteristic of both the 2212 and 2201 phases.

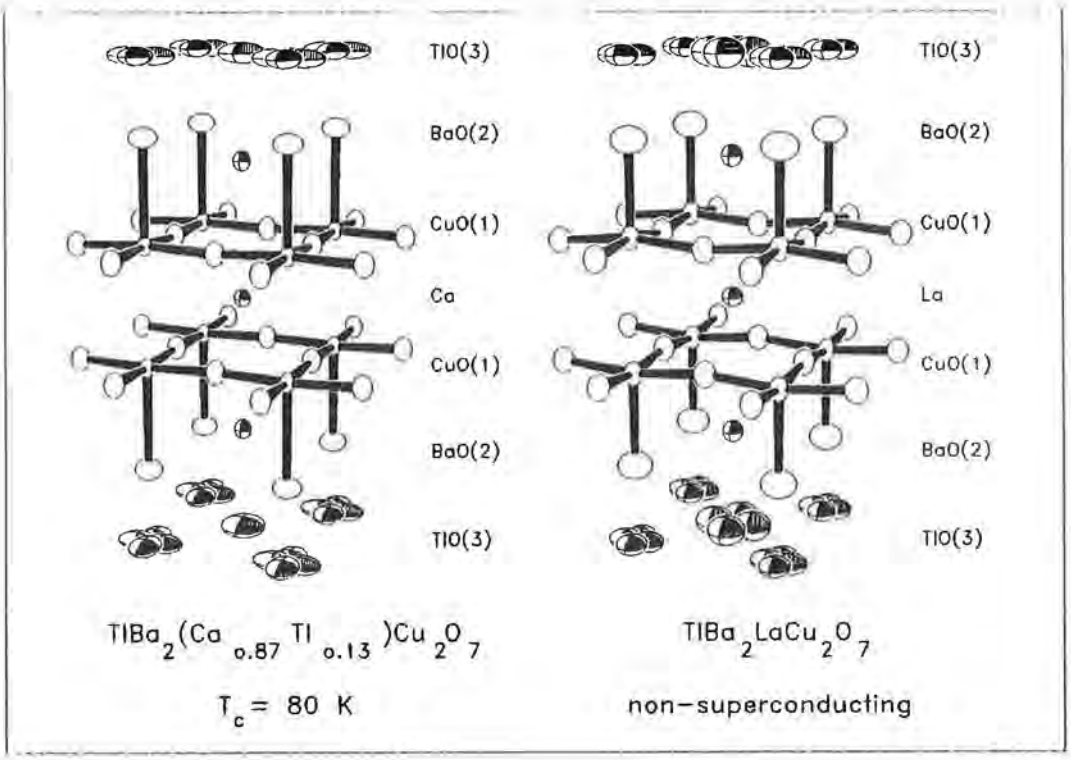

Figure 1 - Comparison of the fragments of Ca-1212 and La-1212 crystal structures. The thermal ellipsoids are drawn as 95% probability surfaces. Cu-O bonds are shown.

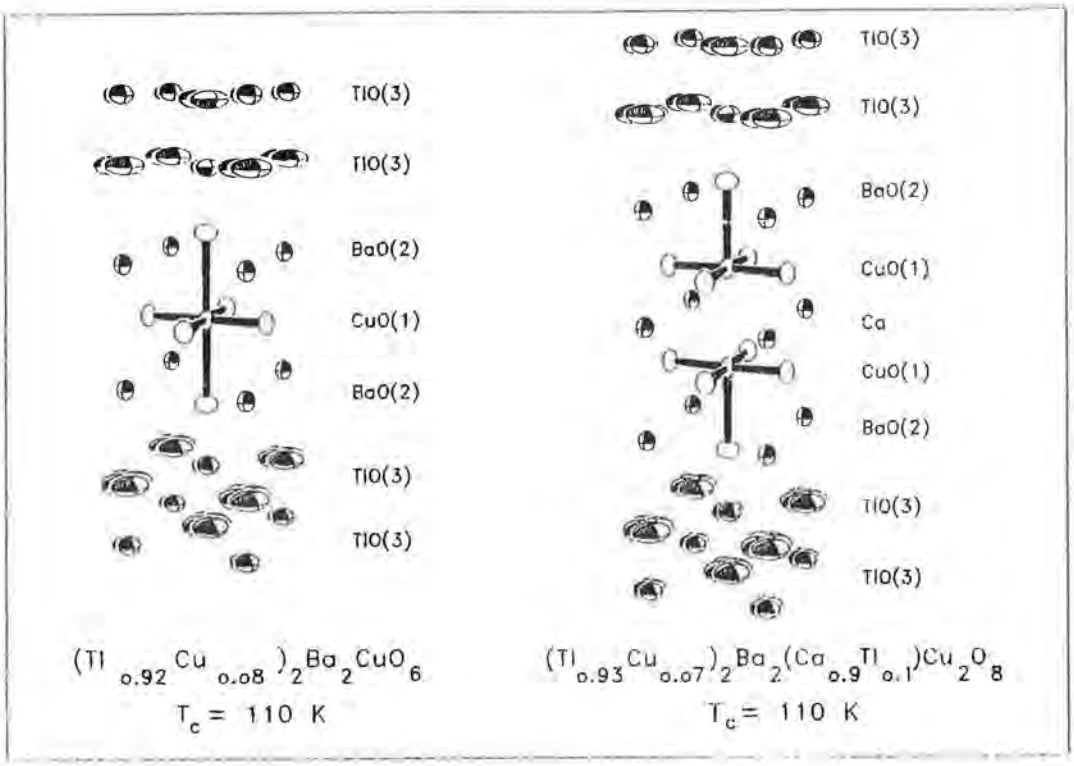

Figure 2 - Comparison of the fragments of 2201 and 2212 crystal structures. The thermal ellipsoids are drawn as 95% probability surfaces. Cu-O bonds are shown.

Single Tl-layer phases

In single-Tl-layer phases, Tl atom displacement is usually observed, a typical example being the 1212 phase containing Ca. But during substitution of Ca for La, oxygen atoms in the Tl-O layer are also shifted. When Ca^{2+} is replaced by La^{3+} in the 1212 structure, La atoms are located between CuO pyramids, setting them apart so that the Cu-Cu and O-O distances between pyramids become larger, while the Ba-Ba distances are decreased. If the O(3) atoms were in the same location, the Ba-O(3) distance would be too short, so a natural way to remove steric tensions in the Ba-O(3)-Ba fragment is to allow the O(3) atom to shift and disorder, making the Ba-O(3) distances equal to 2.651 Å.

Other changes in the 1212-structure are as follows: the *c*-axis is on the whole smaller when Ca is replaced by La, due to a significant shortening of the distance between Cu and the apical oxygen atom; copper atoms are displaced from the oxygen planes of the pyramid base; changes in the oxygen coordination of copper provide evidence for a variation in its electronic state from 2.44+ to 2+ in terms of formal oxidation state.

A similar disorder is observed in single-Tl-phase 1201, where both the O and Tl atoms are shifted from symmetry positions [7]. An example of this phase shows that the crystal can become a superconductor not only when Cu is oxidized from 2+ to 2.44+, as in the 1212 phase upon La^{3+} replacement by Ca^{2+},

$$TlBa_2La^{3+}(Cu^{2+})_2O_7 \rightarrow TlBa_2Ca^{2+}(Cu^{2.44+})_2O_7$$

but also by reduction of Cu from 3+ to 2.2+ in the 1201 phase upon partial replacement of Ba^{2+} by La^{3+}:

$$Tl(Ba^{2+})_2Cu^{3+}O_5 \rightarrow Tl(Ba_{0.6}La_{0.4})_2Cu^{2.20+}O_5$$

These two examples show that the effective oxidation state for Cu should be between 2+ and 3+ if this parameter is used as a criterion of the superconducting phase. Moreover, the optimum oxidation state leading to the maximum possible T_c for the given phase essentially depends on the structure of this phase.

Double Tl-layer phases

In double-Tl-layer phases the effective oxidation state is only 2.09-2.32$^+$, providing our model with partial Tl^{3+} replacement by Cu^{1+} is correct.

According to structural work the process of disorder involves only those Tl and O atoms that are located in the same layer, because the O atoms adjacent to these layers are fixed by large Ba atoms. The sum of ionic radii of Tl^{3+} and O^{2-} is 2.29 Å [8]; the doubled value is 4.58 Å. The length of the vertical 'axis' of the Tl-octahedra in 1212, 2212 and 2201 structures is only some 4.00 - 4.02 Å, while in the *ab*-plane it is 5.41 - 5.48 Å. It follows that if Tl and/or O were not shifted, the distances between Tl and the apical oxygen atoms would be too short, while those between Tl and the equatorial O atoms would be too long. In other words, an octahedra void due to other structural elements is inconvenient for Tl and so atomic disorder in the Tl- O layer can be regarded as an attempt to make a more suitable environment for Tl.

It has been shown [9] in a pair-distribution-function analysis of pulsed neutron scattering data that in the 2212 phase there is a correlation between shifted Tl atoms. In reference [10] a similar conclusion was made on the basis of electron diffraction data for the 2201 phase. Our experience of studies of nonstoichiometric phases also shows that when atoms statistically occupy their sites, such occupations are not independent [11]. As a rule, crystal chemistry regularities are observed locally; in this case correlated shifts of Tl and O atoms may lead to a lowering of the symmetry from tetragonal to orthorhombic. Because of the short range nature of this ordering, X-ray diffraction patterns retain the average tetragonal symmetry and do not show any incommensurate modulation as observed in Bi-containing materials, or twinning as observed in Y- and La-containing superconducting phases.

A Tl-2212 single crystal with T_c = 110 K was investigated before and after the transition to the superconducting state using X-ray diffraction. The data were collected on a HUBER-5042 four-circle diffractometer (MoK_α - radiation, graphite monochromator) supplied with a Displex-202 closed-type helium cryostat with two cooling cycles. The integrated intensities were measured on a spherical sample 0.226 mm in diameter at temperatures of 290, 160, 130, 90 and 60 K (Provisional results reported in reference [14]). The phase transition to a superconducting state was not accompanied by any change in symmetry (space group I4/mmm), or by the appearance of either satellite reflections or twinning.

Structural models were refined using full-matrix least squares. Anisotropic extinction parameters and anharmonic thermal motion parameters of heavy atoms were also tried, along with models with small shifts of thallium and oxygen atoms from the ideal symmetry positions. Final R-values did not exceed 2.8%.

Analysis of changes in cell dimensions and interatomic distances reveals a slight non-monotonic temperature dependence of some of these in the region of the phase transition. In this region, shortening of the Cu-O(planar) bonds are clearly identified while the Cu-O(apical) bond becomes slightly longer. These changes may be caused by increases in the local hole concentration around Cu during the superconducting phase transition.

References

[1] V I Simonov, L A Muradyan, R A Tamazyan, V V Osiko, V M Tatarintsev and K Gamayumov (1990) *Physica C* **169** 123.

[2] V N Molchanov, L A Muradyan and V I Simonov (1989) *JETP Lett* **49** 257.

[3] N N Kolesnikov, V E Korotkov, M P Kulakov, G A Lagvenov, V N Molchanov, L A Muradyan, V I Simonov, R A Tamazyan, R P Shibaeva and I F Shchegolev (1989) *JETP Lett* **50** 47.

[4] L A Muradyan, V N Molchanov, R A Tamazyan, V I Simonov, R P Shibaeva, V E Korotkov, N N Kolesnikov and M P Kulakov (1991) *Superconductivity: physics, chemistry, technology* **4** 277 (in Russian).

[5] U H Zucker, E Perenthaler, W F Kuhs, R Bachman and H Schulz (1983) *J Appl Cryst* **16** 358.

[6] T S Chernaya, L A Muradyan, A A Rusakov, A A Kaminskii and V I Simonov (1985) *Kristallografiya* **30** 72 (in Russian).

[7] M A Subramanian, G H Kwei, J B Parise, J A Goldstone and R B von Dreele (1990) *Physica C* **166** 19.

[8] R D Shannon and C T Prewitt (1969) *Acta Cryst* B**25** 925.

[9] W Dmowsky, B H Toby, T Egami, M A Subramanian, J Gopalakrishnan and A W Sleight (1988) *Phys Rev Lett* **61** 2608.

[10] M Verwerft (1990) *Appl Phys* A**51** 332.

[11] V I Simonov, L A Muradyan, V N Molchanov and E K Kov'ev (1988) *Sov Phys Crystallogr* **33** 366.

[12] R A Tamazyan, V N Molchanov, V I Simonov, N N Kolesnikov, M P Kulakov, V E Korotkov and R P Shibaeva (1992) *Kristallografiya* **37** 571 (in Russian).

[13] N N Kolesnikov, V E Korotkov, M P Kulakov, R P Shibaeva, V N Molchanov, R A Tamazyan and V I Simonov (1992) *Physica C* **195** 219.

[14] M K Blomberg, M Yu Merisalo, V N Molchanov, R A Tamazyan and V I Simonov (1992) *JETP Lett* **55** 550.

The Crystal Structures Of $Li_{4-3x}(Al,Ga)_xSiO_4$ And $Li_{3.7}Al_{0.1}GeO_4$ Solid Solutions.

R.I. Smith, The ISIS Facility, Rutherford Appleton Laboratory, Chilton, Didcot, Oxfordshire, OX11 0QX, U.K.

Abstract.

The crystal structures of several members of the series of lithium ion conducting solid solutions $Li_{4-3x}M_xXO_4$ (M=Al,Ga; X=Ge,Si), $0<x<0.5$, have been studied at temperatures up to 800°C by high resolution time of flight powder neutron diffraction. In the solid solution series $Li_{4-3x}Ga_xSiO_4$ a structural change at x~0.25 from Li_4SiO_4 solid solutions to a solid solution α whose structure is based on that of γ-$LiAlO_2$ is described. In γ-$Li_{3.7}Al_{0.1}GeO_4$, small changes in site occupancies are seen between the structures at room temperature and 800°C, along with an anomalous increase in the thermal expansion of the **a** and **c** unit cell parameters at ~650°C. These changes may account for the unusual temperature independent variation in conductivity observed above ~700°C in a previous study.

Introduction.

The Li_4SiO_4 structure can be regarded as the parent for a variety of lithium ion conductors formed by aliovalent substitution.[1] The introduction of additional Li^+ ions or Li^+ vacancies by suitable doping can greatly enhance the lithium ion conductivity in both these materials.

Li_4SiO_4 itself is a poor lithium ion conductor,[2-4] however in many studies the substitution of pentavalent ions for silicon with the concomitant creation of lithium ion vacancies has been shown to dramatically increase the lithium ion conductivity.[5-11] More recent work has shown that an increase in conductivity can also be produced in Li_4SiO_4 by substituting lithium for trivalent Al and Ga.[12-14] In the systems $Li_{4-3x}(Al,Ga)_xSiO_4$, $0\leq x\leq 0.5$ the lithium ion conductivity rises to a maximum at x~0.20-0.25 before dropping off almost to zero for x=0.5; the conductivities in the Al system generally being an order of magnitude higher than those in the Ga system. Powder X-ray diffraction data had revealed a possibly continuous phase transition in these materials at x~0.25, from Li_4SiO_4 solid solutions to α solid solutions based on the structure of the high temperature polymorph of the $Li_{2.5}(Al,Ga)_{0.5}SiO_4$ end members and in which Li, Al and Si cations are disordered over the Al sites of γ-$LiAlO_2$.[13,14]

Doping of Li_4GeO_4, whose structure is very similar to Li_4SiO_4, having only a minor difference in the lithium distribution, produces highly lithium ion conducting phases,[1] whose structures are based on that of γ-Li_3PO_4, of which LISICON, a range of interstitial solid solutions of formula $Li_{2+2x}Zn_{1-x}GeO_4$ ($0<x\leq0.87$), is a well known example.[15] Recently, a temperature independent variation in conductivity has been observed above ~700°C in γ-$Li_{4-3x}Al_xGeO_4$ solid solutions for low x and which has been attributed to the presence of a liquid like disorder of lithium ions in the structure.[16] The lithium ion conductivity of γ-Li_3PO_4 itself can be enhanced through suitable doping, with many studies reported.[1,17]

The results reported here describe structural studies recently carried out in the $Li_{4-3x}(Al,Ga)_xSiO_4$[18-22] and $Li_{4-3x}Al_xGeO_4$ systems.

Experimental.

Sample preparation was by solid state reaction from simple oxides and carbonates and has been described elsewhere.[12-14] Time of flight powder neutron diffraction data were collected on the HRPD diffractometer at ISIS, Rutherford Appleton Laboratory from $^7Li_{3.4}Ga_{0.2}SiO_4$, $^7Li_{3.00}Ga_{0.33}SiO_4$, $^7Li_{2.5}Al_{0.5}SiO_4$ and $^7Li_{3.7}Al_{0.1}GeO_4$ at room temperature and also from $^7Li_{3.7}Al_{0.1}GeO_4$ at temperatures between 100°C and 800°C. $Li_{2.5}Al_{0.5}SiO_4$ was studied in place of $Li_{2.5}Ga_{0.5}SiO_4$ since it could be readily obtained in the α form at room temperature. Structure refinement was carried out using the REFINE program of the Cambridge Crystallographic Subroutine Library (CCSL).[23]

Results And Discussion.

$Li_{3.4}Ga_{0.2}SiO_4$: This material is a monoclinic, disordered Li_4SiO_4 solid solution built from isolated SiO_4 tetrahedra which contain all the oxygen atoms in the structure, with lithium and gallium atoms located on partially occupied sites. All the gallium atoms are disordered over the partially occupied Li(1) site.

The structure can be described as containing two types of columns of polyhedra oriented perpendicular to the unique **b** axis, figure 1. The first type of column is composed of edge sharing SiO_4 and LiO_4 tetrahedra, the Li sites being only partially occupied, in which each pair of tetrahedra is rotated by 180° from the pair below it, giving rise to a 2_1 screw axis along the column axis. The second type of column has a more complex structure being composed of either pairs of face sharing $(Li,Ga)O_4$ tetrahedra or LiO_6 octahedra, again the cation sites being partially occupied.

These two types of columns are linked together in an ordered fashion to form the structural framework, giving rise to two types of symmetry independent channels in which the remaining lithium ions are located in partially occupied sites. One channel contains Li(4) atoms only while Li(3) and Li(5) atoms occupy the second channel.

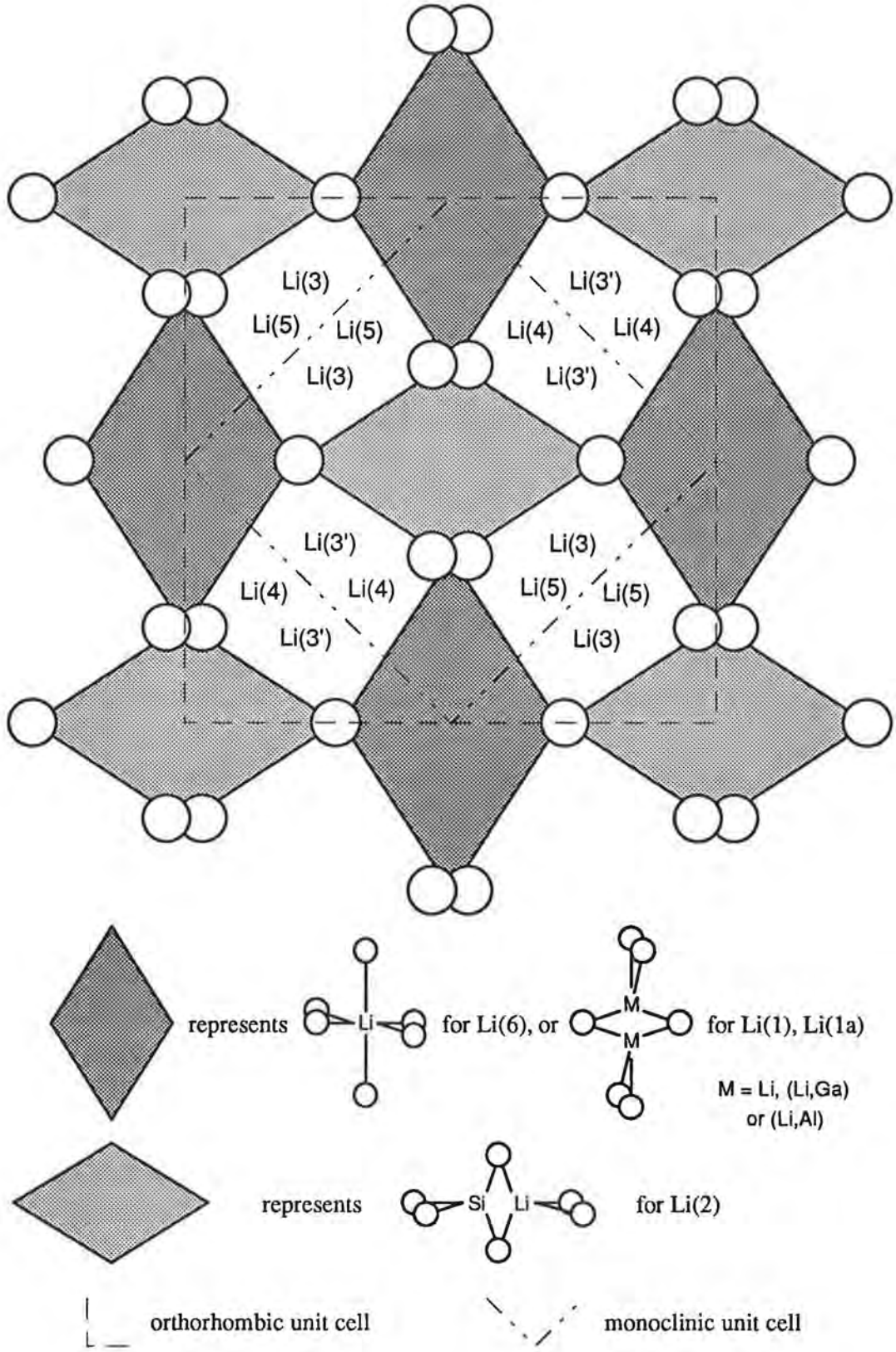

Figure 1. Schematic Diagram Of Structure Of $Li_{4-3x}(Al,Ga)_xSiO_4$ Solid Solutions.

The refined site occupancies show mutual exclusions, with several sets of face sharing sites that are too close together to be simultaneously occupied having total combined occupancies equal to, or very close to, unity; notably the Li/Ga(1) and Li(6) sites, Table 1. This means that the second type of column described above will have two variations: one kind is composed of pairs of $(Li,Ga)O_6$ tetrahedra only, the other being composed of LiO_6 octahedra only. These two variations must be spatially disordered as no evidence was found for the formation of an ordered superstructure, as has been seen in stoichiometric Li_4SiO_4.[24]

$Li_{3.00}Ga_{0.33}SiO_4$: This material was found to adopt a more complex structure than the originally assumed disordered tetragonal γ-$LiAlO_2$ structure. The diffraction profile showed many additional reflections not attributable to the tetragonal unit cell. Autoindexing indicated that $Li_{3.00}Ga_{0.33}SiO_4$ adopts a lower symmetry, orthorhombic structure in which the **c** axis of the orthorhombic cell is the **c** axis of the tetragonal cell but the **a** and **b** axes of the orthorhombic cell are the **ab** face diagonals of the tetragonal cell. The space group determined from the powder diffraction pattern is $C222_1$, and is a subgroup of the $P4_12_12$ space group of γ-$LiAlO_2$.[25]

In orthorhombic $Li_{3.00}Ga_{0.33}SiO_4$, the framework structure is similar to that of monoclinic $Li_{3.4}Ga_{0.2}SiO_4$, figure 1, with only minor changes in cation site occupancies. An essentially identical distribution of SiO_4 tetrahedra containing all the oxygen atoms in the structure is seen with similar columns of polyhedra formed and similar channels between them. Nevertheless, a subtle difference occurs in the lithium and gallium cation arrangement between the orthorhombic and monoclinic structures. In the orthorhombic structure, the Li(1) sites of monoclinic $Li_{3.4}Ga_{0.2}SiO_4$, which also contain all the gallium, are described by two sets of sites, Li(1) and Li(1a). However, in $Li_{3.00}Ga_{0.33}SiO_4$, the gallium is located on only half of these and shares only the Li(1a) site.

A more obvious difference between these two structures can be seen with the channel sites. In $Li_{3.00}Ga_{0.33}SiO_4$ all the channels in the structure are symmetry related and only one type of channel is seen. This channel contains similar cation sites to $Li_{3.4}Ga_{0.2}SiO_4$, however only one of these channel sites is occupied, Li(3) (labelled Li(3) and Li(3') in figure 1).

The oxygen anion arrangement in the α structure is closely related to the Li_4SiO_4 solid solutions structure. In $Li_{3.4}Ga_{0.2}SiO_4$ the oxygen atoms of the shared LiO_4,SiO_4 edge are described by two atoms, O(2) and O(3), whereas in $Li_{3.00}Ga_{0.33}SiO_4$ they are described only by the one atom, O(2). The loss of a mirror plane perpendicular to the column axis in the orthorhombic structure means that the O(1) atoms no longer superpose on projection along the column axis, as in the monoclinic structure, but have their centres separated by ~0.02Å.

As with the monoclinic structure, a similar mutual exclusion of face sharing sites is seen, Table 1, such that a similar formation of columns composed of either pairs of LiO_4

tetrahedra only or LiO_6 octahedra only must occur. Again, no evidence was found to indicate spacial ordering of these columns.

	Li_4SiO_4 (s.s.)				α (s.s.)	
site	x=0.0 [30,31]		x=0.20	site	x=0.33	x=0.50
4f O(1)	1.00	1.00	1.00	8c O(1)	1.00	1.00
2e O(2)	1.00	1.00	1.00	8c O(2)	1.00	1.00
2e O(3)	1.00	1.00	1.00			
framework sites						
2e Si	1.00	1.00	1.00	4a Si	1.00	1.00
4f Ga/Al	-	-	0.10	4b Ga	0.33	0.50
Li(1)	2/3	0.57	0.66	Li(1a)	0.55	0.50
				4b Li(1)	0.84	1.00
2e Li(2)	1/2	0.53	0.47	4b Li(2)	0.68	1.00
2e Li(6)	1/3	0.48	0.26	4b Li(6)	0.11	0.00
channel sites						
2e Li(3)	1/2	0.41	0.39	8c Li(3)	0.32	0.00
4f Li(4)	1/3	0.47	0.25	-		
4f Li(5)	1/3	0.25	0.16	-		

Table 1. Comparison Of Sites And Occupancies In $Li_{4-3x}(Al,Ga)_xSiO_4$ Solid Solutions.

$Li_{2.5}Al_{0.5}SiO_4$: This material was found not to be tetragonal, as had been originally reported, [13] but also adopts the orthorhombic $C222_1$ space group. At this composition, as expected, all the 'framework' cation sites were found to be fully occupied, with the 'channel' sites all empty, Table 1. The columns are composed only of pairs of edge sharing tetrahedra, with no evidence found for columns containing LiO_6 octahedra. Again, the substituting trivalent atom, in this case aluminium, shares only the tetrahedral Li(1a) site.

The lithium sites of γ-$LiAlO_2$ are seen to contain lithium only in $Li_{2.5}Al_{0.5}SiO_4$ while the Al sites of γ-$LiAlO_2$ are split into two sets of sites, one containing silicon only, the other containing a disordered mixture of lithium and aluminium. The lowering of symmetry from tetragonal to orthorhombic is caused by this ordering of silicon and aluminium and lithium onto the aluminium sites of γ-$LiAlO_2$. The oxygen array is seen to have much similarity to that of $Li_{3.00}Ga_{0.33}SiO_4$. Again, the centres of the O(1) atoms on projection down the column axis are separated, in this case by ~0.1Å.

It is assumed that the high temperature α form of $Li_{2.5}Ga_{0.5}SiO_4$ is isostructural with α-$Li_{2.5}Al_{0.5}SiO_4$, which is also similar to the structure of γ-Li_2BeSiO_4.[26] Both have the same $C222_1$ space group, however the equivalent of the disordered (Li+Al,Ga) site in the α phases contains beryllium only in γ-Li_2BeSiO_4.

It is seen that on increasing x in $Li_{4-3x}(Al,Ga)_xSiO_4$ solid solutions, the net effect is to cause the occupancies of the framework sites to increase, while the channel site occupancies decrease at a greater rate. At the x=0.5 composition, all the framework sites are fully occupied, the channel sites are empty and the structure becomes one in which all species, both cations and anions, are tetrahedrally coordinated. At the phase transition a subtle change in occupied sites occurs involving the location of the substituting gallium/aluminium and the type of channel sites occupied, Table 1.

$Li_{3.7}Al_{0.1}GeO_4$: The crystal structure of Li_4GeO_4[29] is very similar to that of Li_4SiO_4.[30,31] However, $Li_{3.7}Al_{0.1}GeO_4$ differs in structure from the silicates described above in that its structure is related to that of γ-Li_3PO_4.[32] Although in γ-Li_3PO_4 similar columns built from edge sharing LiO_4 and PO_4 tetrahedra are formed, in $Li_{3.7}Al_{0.1}GeO_4$ (and also in Li_4GeO_4 and lisicon) this lithium site is now unoccupied, possibly due to the larger size of germanium. The GeO_4 tetrahedra, however, still contain all the oxygen atoms in the structure, figure 2.

By analogy with lisicon and related structures, it was assumed that the aluminium shared the partially occupied tetrahedral Li(1) site, this assumption appearing to be confirmed during refinement. The structure does, however, have similar features to the silicates containing an interconnected network of partially occupied lithium sites, and mutual exclusions between face sharing sites are seen.

Refinement of site occupancies located ~90% of the expected lithium content, in good agreement considering the disordered nature of this material, and showed that the Li/Al(1) site has a total occupancy of ~0.90, with an occupancy of ~0.10 on the face sharing Li(4) site. Similarly, the combined occupancies of the Li(2) and Li(5) sites are also ~1.0. Similar mutual exclusions have been observed previously in the structures of $Li_{3.4}Si_{0.7}S_{0.3}O_4$ (also a γ phase) and the lisicon $Li_{3.5}Zn_{0.5}GeO_4$ and, along with site occupancies of certain adjacent Li sites, have been interpreted as being indicative of defect clustering.[27,28]

At 800°C, there appears to be very little change in structure apart from minor changes in site occupancies. Again, almost 90% of the expected lithium content could be located during refinement, which would suggest that if there is a liquid like distribution of lithium ions, only a small proportion of the total are involved. At 800°C, the Li(3) site had to be located on the 4c) special position with y=¼, however this was solely to permit the stable

refinement of positional parameters, site occupancy and temperature factor, and may in fact be indicative of some form of anharmonic thermal motion. Further work is required here.

On heating up to 800°C , an anomalous change in the slope of the **a** and **c** cell parameters versus temperature can be seen at 650°C, figure 3. This in part may be responsible for the observed region of temperature independent lithium ion conductivity, or may be caused by a change in lithium ion distribution.

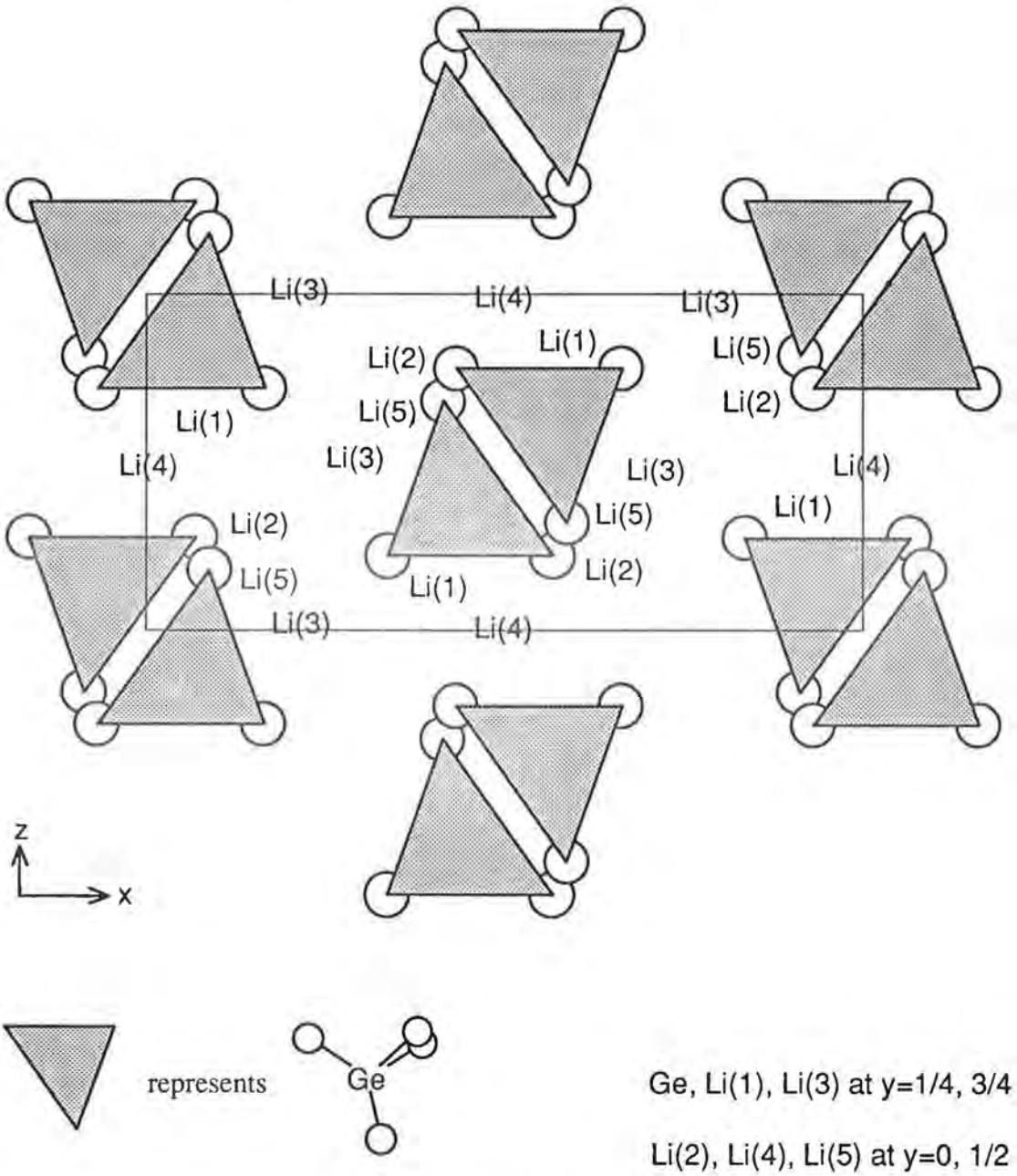

Ge, Li(1), Li(3) at y=1/4, 3/4

Li(2), Li(4), Li(5) at y=0, 1/2

Figure 2. Schematic Diagram Of γ-$Li_{3.7}Al_{0.1}GeO_4$ Structure.

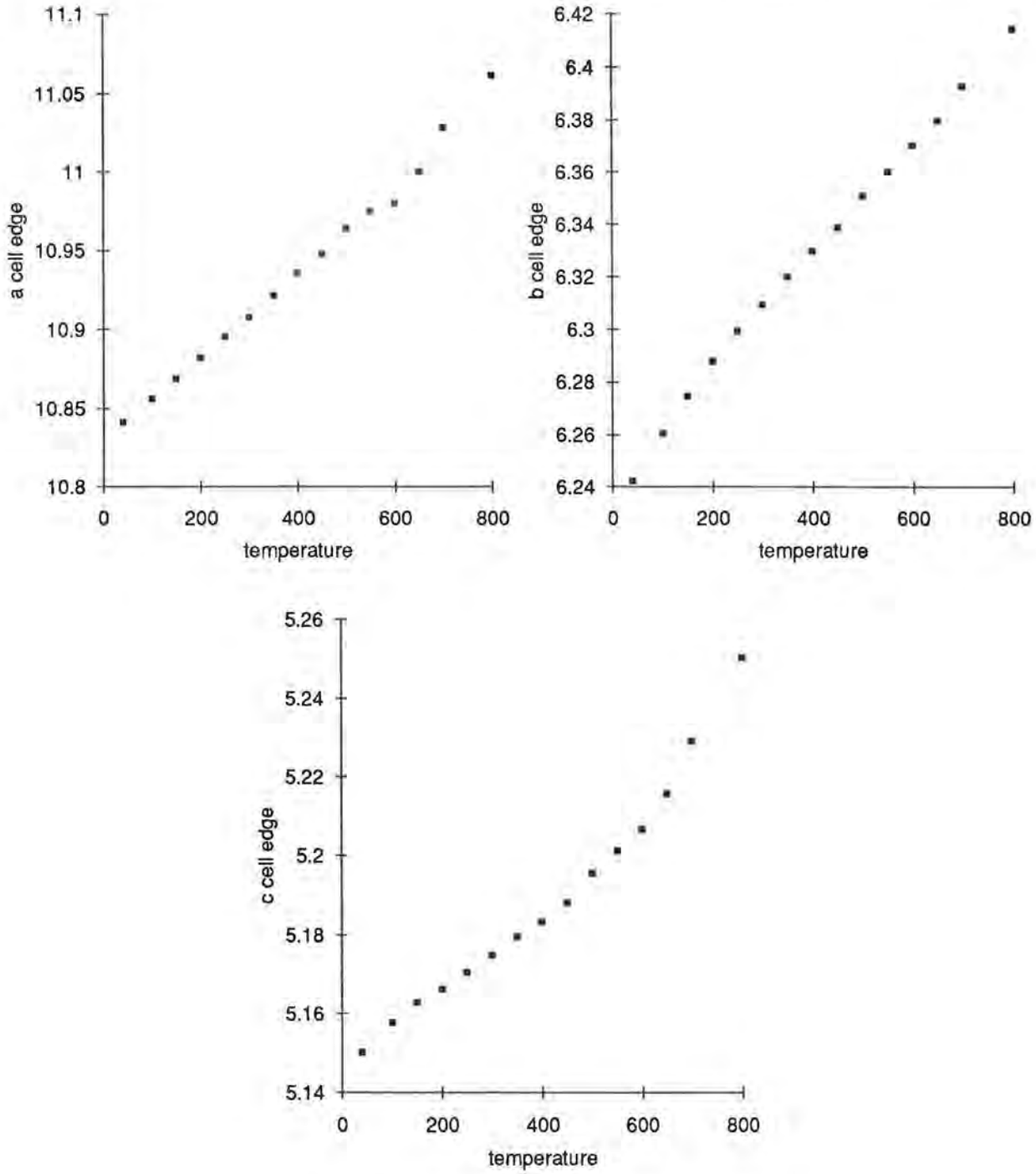

Figure 3. Variation with temperature of $Li_{3.7}Al_{0.1}GeO_4$ cell parameters. Unit cell edges in Ångstroms, temperature in °C.

Conclusions.

The crystal structures of $Li_{4-3x}(Al,Ga)_xSiO_4$ solid solutions have been determined and relationships between the phases described. Although the Li_4SiO_4 to α phase change appeared to be continuous in previous phase diagram studies, the present structural studies

reveal there must be discontinuities associated with certain lithium and gallium/aluminium site occupancies at the phase transition.

In $Li_{3.7}Al_{0.1}GeO_4$ very little structural change is seen to accompany the transition to the phase showing a liquid like conductivity of lithium ions. Only to a small proportion of the total lithium content of the structure is likely to be involved, as has been suggested in other studies.[16] An anomalous increase in thermal expansion of certain cell parameters is also observed close to the transition to this liquid like behaviour.

In both systems, examination of refined site occupancies shows the presence of mutual exclusions between face sharing cation sites and may be indicative of the formation of defect clusters.

Acknowledgement.

This work was performed in collaboration with J.M.S. Skakle and A.R. West, Department Of Chemistry, University Of Aberdeen, Meston Walk, Old Aberdeen, AB9 2UE, U.K.

References.

(1) J.T.S. Irvine and A.R. West, in "High Conductivity Ionic Conductors, Recent Trends And Applications", (ed. T. Takahashi), World Scientific, Singapore (1989).
(2) A.R. West, J. Appl. Electrochem., **3**, 327 (1973).
(3) W. Gratzer, H. Bittner, H. Nowotny and K. Siefert, Z. Kristallogr., **133**, 260 (1971).
(4) I.M. Hodge, M.D. Ingram and A.R. West, J. Amer. Ceram. Soc., **59**, 360 (1976).
(5) Y.-W. Hu, I.D. Raistrick and R.A. Huggins, Mater. Res. Bull., **11**, 1227 (1976).
(6) Y.-W. Hu, I.D. Raistrick and R.A. Huggins, J. Electrochem. Soc., **124**, 1240 (1977).
(7) R.A. Huggins, Electrochim. Acta, **22**, 773 (1977).
(8) R.D. Shannon, B.E. Taylor, A.D. English and T. Berzins, Electrochim. Acta, **22**, 783 (1977).
(9) A. Khorassani and A.R. West, Solid State Ionics, **7**, 1 (1982).
(10) A. Khorassani and A.R. West, J. Solid State Chem., **53**, 369 (1984).
(11) A. Khorassani, G. Izquierdo and A.R. West, Mater. Res. Bull., **16**, 1561 (1981).
(12) P. Quintana, F. Velasco and A.R. West, Solid State Ionics, **34**, 149 (1989).
(13) A. Garcia, G. Torres-Treviño and A.R. West, Solid State Ionics, **40-41**, 13 (1990).
(14) P. Quintana and A.R. West, J. Solid State Chem., **81**, 257 (1989).
(15) H.Y.-P. Hong, Mater. Res. Bull., **13**, 117 (1978).
(16) C.K. Lee and A.R. West, J. Mater. Chem., **1**, 149 (1991).
(17) A.R. Rodger, J. Kuwano and A.R. West, Solid State Ionics, **15**, 185 (1985).
(18) R.I. Smith and A.R.West, J. Solid State Chem., **88**, 564 (1990).
(19) R.I. Smith and A.R. West, J. Mater. Chem., **1**, 91 (1991).
(20) R.I. Smith and A.R. West, J. Solid State Chem., **93**, 436 (1991).

(21) R.I. Smith, P. Quintana and A.R.West, ISSI Lett., **1**, 7 (1990).

(22) R.I. Smith and A.R. West, in Mater. Res. Soc. Symp. Proc., Solid State Ionics II, (ed G.-H. Nazri, D.C. Shriver, R.A. Huggins and M. Bolkanski), **210**, 593 (1991).

(23) a) W.I.F. David, D.E. Akporiaye, R.M. Ibberson and C.C. Wilson, Report RAL-88-103, Rutherford Appleton Labortory (1988). b) P.J. Brown and J.C. Matthewman, Report RAL-87-010, Rutherford Appleton Laboratory (1987).

(24) D. Tranqui, R.D. Shannon, H.-Y. Chen, J. Iijima and W.H. Baur, Acta Crystallogr., Sect. B **35**, 2479 (1979).

(25) M. Marezio, Acta Crystallogr., **19**, 396 (1965).

(26) R.A. Howie and A.R. West, Acta Crystallogr., Sect. B **30**, 2434 (1974).

(27) A.N. Fitch, B.E.F. Fender and J. Talbot, J. Solid State Chem., **55**, 14 (1984).

(28) I. Abrahams, P.G. Bruce, W.I.F. David and A.R. West, Acta Crystallogr., Sect. B **45**, 457 (1989).

(29) H. Völlenkle and A. Wittmann, Z. Kristallogr., **128**, 66 (1969).

(30) H. Völlenkle, A. Wittmann and H. Nowotny, Monatsh. Chem., **99**, 1360 (1968).

(31) W.H. Baur and T. Ohta, J. Solid State Chem., **44**, 50 (1982).

(32) J. Zemann, Acta Crystallogr., **13**, 863 (1960).

Structure and Phase Transitions in Ferroelectric Rb^+ and NH_4^+ Selenates

I P Makarova
Institute of Crystallography, Russian Academy of Sciences, Moscow

Introduction

Modern levels of diffraction structural analysis allow the determination of not only geometric parameters of a crystal structure but also the fine atomic structure. Analysis of atomic displacement parameters, anomalous scattering, extinction parameters, twinning of crystal specimens and the distribution of the electron density provides information about details of the structure and about the physical properties of crystals. Precise structural studies require, however, an individual approach to each sample taking into account specific physical factors for the specimen under investigation.

The object of our studies are crystals with hydrogen bonds. All the crystals studied exhibit structural phase transitions which are accompanied by changes in hydrogen bonding. Neutron and X-ray diffraction data on single crystals have been used to study the structural changes during the phase transitions.

Similar sequences of phase transitions have been found in $RbHSeO_4$ and NH_4HSeO_4 crystals. Replacement of the Rb atom by the $[NH_4]$ group lowers the ferroelectric phase transition temperature by 120 K (from 370 to 250 K) [1,2]. To investigate the structural reconstruction during the ferroelectric phase transition and the changes in hydrogen bonding we have carried out a neutron diffraction study of $RbHSeO_4$ in the paraelectric phase at 383 K and in the ferroelectric phase at 293 K, and also for NH_4HSeO_4 in the paraelectric phase at 293 and 400 K [3-5].

Structures and hydrogen bonding

$RbHSeO_4$ and NH_4HSeO_4

The experimental data were collected from spherical specimens of $RbHSeO_4$ and NH_4HSeO_4 crystals of diameter 0.7 and 0.6 cm, respectively, on a Syntex P1 diffractometer at the VVR-C reactor (λ = 1.1674 Å) (Table 1). All structural computations, including structure refinement, were carried out using the PROMETHEUS program system [6]. Diffraction intensities were corrected for L factor (Lp factor in cases of X-ray data) and absorption. Extinction was taken into account in the Becker-Coppens isotropic approximation [7].

Table 1
Crystal data

	$RbHSeO_4$		NH_4HSeO_4	
	383 K	**293 K**	**400 K**	**293 K**
Space group	B2	B1	B2	B2
a (Å)	19.962(9)	19.852(8)	19.863(13)	19.754(8)
b (Å)	4.634(2)	4.622(1)	4.620(3)	4.607(1)
c (Å)	7.611(3)	7.575(3)	7.593(7)	7.550(2)
α (°)	90	90.64(3)	90	90
β (°)	90	90.04(3)	90	90
γ (°)	102.76(3)	102.75(3)	102.59(5)	102.59(3)
Z	6	6	6	6
Max $\sin\theta/\lambda$ ($Å^{-1}$)	0.79	0.79	0.79	0.79
Unique reflns	1069	2317	532	744
R_w	0.053	0.053	0.055	0.051
R	0.039	0.044	0.054	0.047

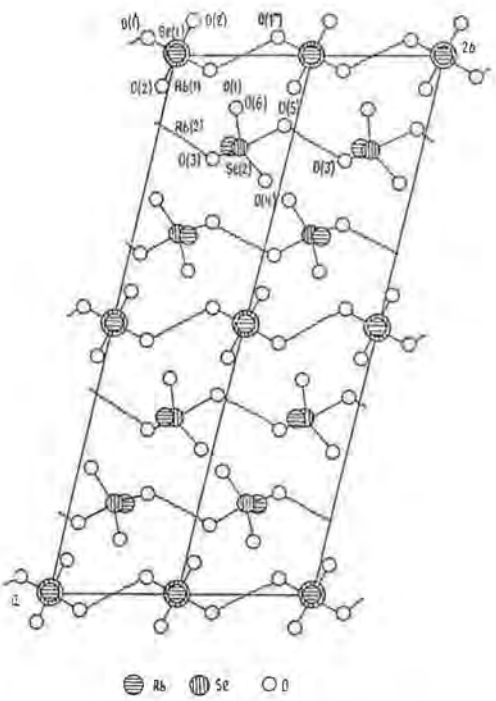

Figure 1 - The structure of $RbHSeO_4$ in the paraelectric phase projected along the two-fold axis (z). The hydrogen bonds are shown as wavy lines.

The H-bond network in $RbHSeO_4$ and NH_4HSeO_4 is 'one-dimensional' (Figure 1). The structures are based on $[SeO_4]$ tetrahedra, linked by hydrogen bonds so as to form chains extending along the y axis. As for the paraelectric phase, the asymmetric unit contains two symmetrically nonequivalent groups: $[Se(1)O_4]$, lying on the twofold axis, and $[Se(2)O_4]$ in a general position. The former are joined by hydrogen bonds of the a-type, the latter by b-type bonds. In the ferroelectric phase there are three symmetrically nonequivalent $[SeO_4]$ groups, because the disappearance of the twofold axis leads to non-equivalence of two $[Se(2)O_4]$ tetrahedra, denoted below as $[Se(2)O_4]$ and $[Se(22)O_4]$. Here and below, the indices I and II denote the positions of atoms which were symmetrically equivalent with respect to the twofold axis in the paraelectric phase.

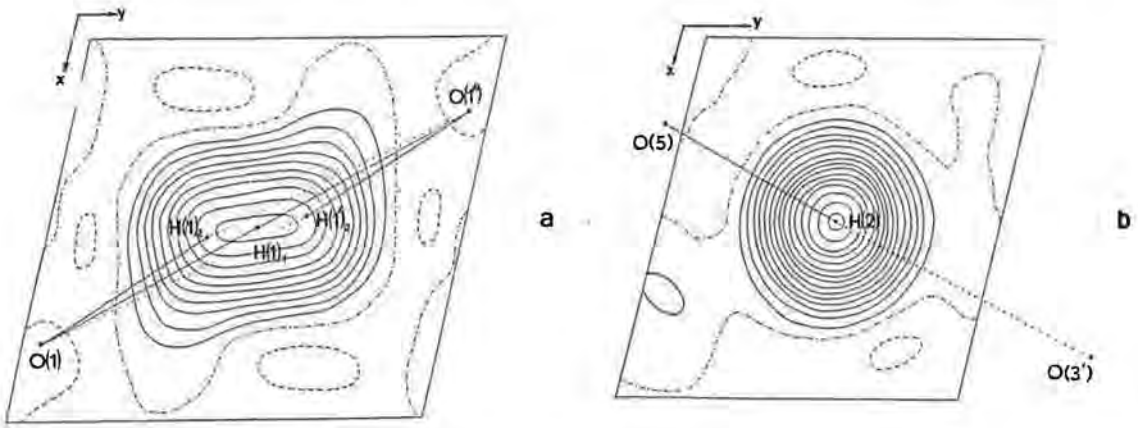

Figure 2 - The H-atom distribution of (a) the α bond and (b) the β bond at 383 K in $RbHSeO_4$ in the xy plane. Contours at 0.5 FmÅ^{-3}. Solid contours - negative density (hydrogen has negative neutron scattering length), dashed contours - positive density, dotted-and-dashed contours - zero density.

Figure 2 shows the nuclear density map in planes of a-type (a) and b-type (b) hydrogen bonds for $RbHSeO_4$ in the paraelectric phase (the nuclear density maps for NH_4HSeO_4 are similar). The H distributions of the a- and b-bonds differ significantly. The hydrogen b-bond O(5)-H(2)...O(3') has a typical asymmetrical geometry with a compact H(2) peak. On the other hand, the H(1) peak is extended along the a-bond O(1)-O(1") and the highest value of the nuclear density is about 1.5 times less than the corresponding value for the H(2) atom. We have carried out the refinement of two structural models of the H(1)-atom distribution: static disorder with a 50% occupation of two H(1) sites (the $H(1)_2$ and $H(1')_2$ sites in Figure 2), which provides an asymmetrical geometry of the bonds O(1)-$H(1)_2$...O(1") and O(1)...$H(1')_2$-O(1"); the arrangement of the H(1) atom on the twofold axis with possible anharmonicity (the Gram-Charlier expansion was applied). The anharmonic parameters obtained yielded the effective one-particle potential for the H(1) atom with two minima corresponding to the $H(1)_2$ and $H(1')_2$ sites of the two-site harmonic model. For the compounds under investigation, therefore, the anharmonic model of the H(1) distribution, with the averaged H(1)-atom site lying on the twofold axis and the probability of the atom location, as the atom undergoes thermal vibrations, being higher in the regions of the two minima of the potential, led to the same geometry as the two-site harmonic model. The difference between these models lies in the time the H(1) atom spends at various points in space during the course of its motion. Refinement of these structural models for the H(1) distribution (the two-site harmonic model and the anharmonic model) led to equal R factors for each case. Therefore, we came across a situation in which using diffraction methods it is impossible to determine a preference for one of the models purely from the value of the R factor. While the limited diffraction data do not provide a direct answer, however, analysis of the geometry of the a- and b-bonds and the thermal motion ellipsoids favour the model of anharmonic motion of the H(1) atom in the a-bond.

In the ferroelectric phase the geometry of the hydrogen b-bonds turned out to remain the same, while the H(1) distribution displays a change in the a-bond: it becomes asymmetrical and equivalent in geometry to the b-bond (Figure 3). Some asphericity of the peak corresponding to the H(1) atom is explained by the presence of second orientation domains in the sample, so structural parameters in the ferroelectric phase have been refined with allowance for twinning.

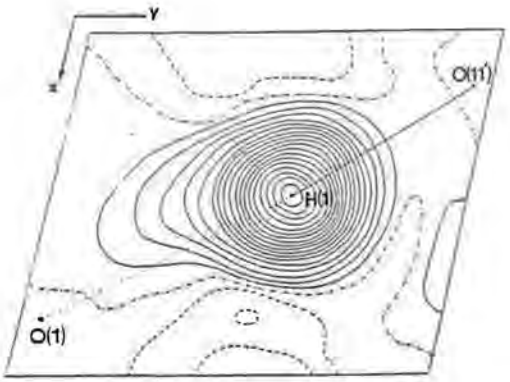

Figure 3 - The H-atom distribution of the α bond in $RbHSeO_4$ in the ferroelectric phase in the xy plane. Notation as in Figure 2.

The differences in Se-O distances in the tetrahedra are due to structural features (Table 2). In the $[Se(2)O_4]$ group the distances between the Se(2) and O(3), O(5) atoms engaged in b-bonds exceed those between the Se(2) and O(4), O(6) atoms. In addition, the Se(2)-O(3) and Se(2)-O(5) distances differ considerably and this difference is correlated with the functions of the O atoms in the hydrogen b-bonds: O(3) - acceptor, O(5) - donor.

Table 2

Main interatomic distances (Å) and angles ( ) in $RbHSeO_4$ and NH_4HSeO_4 crystals. Parameters of the a bond are given for the two-site model. Two values in the column for the B1 phase of $RbHSeO_4$ correspond to distances which are equivalent in the B2 phase.

	$RbHSeO_4$		NH_4HSeO_4	
	383 K	**293 K**	**400 K**	**293 K**
O(1)-O(1")	2.530(5)	2.524(3)	2.48(2)	2.53(1)
O(1)-H(1)	1.02(1)	1.030(4)	1.04(6)	1.03(1)
O(1")...H(1)	1.52(1)	1.498(4)	1.46(5)	1.51(1)
O(1)-H(1)-O(1")	171(1)	173.4(4)	170(3)	172(2)
H(1)-H(1')	0.53(2)	-	0.46(6)	0.49(2)
O(3')-O(5)	2.578(4)	2.575(3)/2.577(3)	2.57(1)	2.565(6)
O(5)-H(2)	1.010(5)	1.018(5)/1.019(5)	1.00(1)	1.011(9)
O(3')...H(2)	1.570(5)	1.558(5)/1.561(5)	1.57(1)	1.556(9)
O(3')-H(2)-O(5)	175.3(5)	175.9(5)/175.2(5)	177(1)	176(1)
Se(1)-O(1),O(1')	1.671(3)	1.632(3)/1.715(2)	1.677(7)	1.670(5)
Se(1)-O(2),O(2')	1.607(3)	1.611(2)/1.613(2)	1.608(8)	1.607(5)
Se(2)-O(3)	1.632(3)	1.633(3)/1.631(3)	1.623(8)	1.636(5)
Se(2)-O(4)	1.603(3)	1.608(3)/1.606(3)	1.603(8)	1.606(5)
Se(2)-O(5)	1.716(3)	1.716(3)/1.715(3)	1.712(8)	1.709(5)
Se(2)-O(6)	1.611(3)	1.614(3)/1.612(3)	1.599(8)	1.616(6)

In the paraelectric phase the distances between the Se(1) and O(1), O(1') atoms involved in a-bonds in the $[Se(1)O_4]$ group on the twofold axis also exceed those between the Se(1) and the O(2) atoms which are not H-bonded. These distances are equal to the averaged Se(2)-O(3) and Se(2)-O(5) distances, which is to be expected because the O(1) atoms perform the functions of donor or acceptor with a probability of ½.

The principal changes during the ferroelectric phase transition are due to the H(1)-atom ordering and appropriate transformations of the $[Se(1)O_4]$ tetrahedra. In these tetrahedra the distances between the Se(1) atom and the O(2), O(22) atoms, which are not H-bonded, change by an insignificant amount and remain the shortest. Ordering of the H(1) atom causes the distances between the Se(1) and those O atoms involved in hydrogen bonding to be no longer equivalent: the Se(1)-O(1) distance is reduced by 0.039 Å, while the Se(1)-O(11) distance is increased by 0.044 Å. The ordering of the H(1) atoms and transformation of $[Se(1)O_4]$ tetrahedra means that all $[Se(1)O_4]$, $[Se(2)O_4]$ and $[Se(22)O_4]$ tetrahedra show similar distortions in the ferroelectric phase.

The presence of hydrogen bonds with ordered H atoms leads to a regular difference between the lengths of Se-O bonds and this difference, which is correlated with the functions of the O atoms, is about 0.083 Å. From this viewpoint let us consider the two-site model for the H(1) distribution on the a-bond. The two-site model with a static spatial disorder means that in each unit cell an equilibrium position of the H(1) atom corresponds to one of the two possible sites $H(1)_2$ or $H(1')_2$. The O(1) atoms therefore play different roles (donor or acceptor) in different unit cells, manifest in differences in the Se(1)-O bond length as described above for the ferroelectric phase and comparable to the Se(2)-O distances which should be regarded as standard at the temperature of the investigation. The positional parameters of the O(1) atom in the averaged unit cell of the paraelectric phase would naturally correspond to a mean Se(1)-O(1) distance, while O(1)-atom disorder over the sites corresponding to the donor or acceptor functions would affect the parameters of the thermal motion of this atom. Analysis of the thermal parameters of the O(1) atom within the accuracy of our experiment and calculations does not reveal such an effect.

With due regard for the above, the positional and thermal parameters of the H(1) atom obtained in the refinement of the two-site model can be regarded as an estimation of the H(1)-atom parameters when it is located at one of the two potential minima, assuming that

$$\langle u_1^2 \rangle \equiv \langle u_2^2 \rangle + (\delta/2)^2,$$

where $\langle u_1^2 \rangle$ is the mean-square amplitude obtained for the single-site model, $\langle u_2^2 \rangle$ - for the two-site model and δ is the separation between the $H(1)_2$ and $H(1')_2$ sites in the two-site model. If the two-site model is used one should bear in mind the correlation between positional parameters, which define the separation δ, and thermal parameters of the atoms. When there is a strong correlation between the refined parameters, the appropriate section of the minimized function exhibits a plateau of practically the same values of the function instead of an abrupt minimum, i.e. the function is insensitive to variations of the refined parameters, and the estimated standard deviations no longer provide a means of assessing errors. Instead, analysis of the dependence of the type $R_w = f(x_i, x_k)$, where x_i and x_k, are correlating parameters, is required in the vicinity of the minimum of the minimized function. Figure 4 shows the dependencies $R_w = f(\delta/2)$ obtained for $RbHSeO_4$ and NH_4HSeO_4. Curves 1,2 and 3 were plotted for a discrete fixed set of values of the $\delta/2$ parameter during full refinement of the other parameters of the two-site model. The appropriate equivalent isotropic thermal parameters (B_{eq}) for the H(1) atom are also presented. For comparison, curves 4 were plotted from results of a similar refinement of the ferroelectric phase of $RbHSeO_4$. The R_w dependence for the ferroelectric phase exhibits a sharp minimum corresponding to one H(1) site. On the other hand, the minima of the R_w function of the two-site model refinement of paraelectric phase are hardly discernible. In this case, step-by-step scanning of the δ parameter is a unique means of estimating the true value of δ.

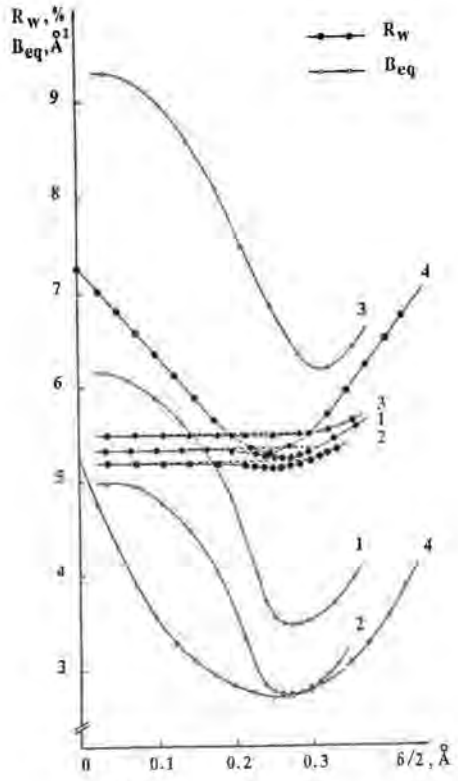

Figure 4 - The δ/2 dependence of the R_w factor and the Beq parameter for RbHSeO4 at 383 K (1), for NH4HSeO4 at 293 K (2), for NH4HSeO4 at 400 K (3) and for the ferroelectric phase of RbHSeO4 at 293 K (4).

$Rb_3H(SeO_4)_2$

In comparison with the compounds mentioned above, $Rb_3H(SeO_4)_2$ exhibits restructuring of the system of hydrogen bonds during the ferroelastic phase transition at T_c = 449 K [8]. In the high-temperature phase the proton sublattice is disordered. As a result, the protons can execute jumps with low activation energy, and this is manifest in the high proton conductivity ($\approx 10^{-2}\Omega^{-1}cm^{-1}$) in this phase.

To investigate the structural change, we have collected experimental X-ray diffraction data from an $Rb_3H(SeO_4)_2$ crystal at T=293 K and 473 K, below and above the ferroelastic phase transition. Data collection parameters: CAD-4F diffractometer; Mo Kα-radiation; at 293 K space group A2/a, a=10.475(1), b=6.090(1), c=15.418(3) Å, b=102.91(1) , Z = 4, 1008 unique reflections, $\sin\theta/\lambda < 0.90$ Å^{-1}, R_w = 2.9%, R = 3.7%; at 473 K space group R3m, a=6.118(1), c=22.629(7) Å, Z=3, 182 unique reflections, $\sin\theta/\lambda < 0.79$ Å^{-1}, R_w = 1.7%, R = 2.7% [8,9]. In the ferroelastic phase the crystals of $Rb_3H(SeO_4)_2$ display a domain structure in polarized light which vanishes above T_c. For the structural studies we have cut a monodomain specimen and then formed it into a sphere of diameter 0.014 cm.

In the ferroelastic phase the [SeO_4] tetrahedra are linked in pairs by hydrogen bonds O(2)...H...O(2') equal to 2.514(7) Å (Figure 5). The atom O(2), which is involved in the hydrogen bond, is furthest from the Se atom. In the high-temperature phase this atom is found to occupy a disordered position. Figure 6 shows the difference probability density function (PDF) of the O(2) atom, which displays the deviations from a purely harmonic PDF. The three positive peaks of the PDF, related by the threefold axis, show the directions of the most probable displacements of the O(2) atom. In the superionic phase the atoms O(2) are shifted from their equilibrium positions to positions between which hydrogen bonds can be established (O(2)...O(2') 2.67(2) Å). As a result, the system of hydrogen bonds joining the O(2) atoms in pairs in the low-temperature phase transforms to a network of such statistical hydrogen bonds (Figure 7), i.e., a system of symmetrically equivalent positions which can be occupied by protons (involved in bonds) is formed. So the feature of the ferroelastic phase transition in $Rb_3H(SeO_4)_2$, distinguishing it from the known structural phase transitions in crystals with hydrogen bonds, is that it is accompanied by structural change (disordering) of the system of hydrogen bonds.

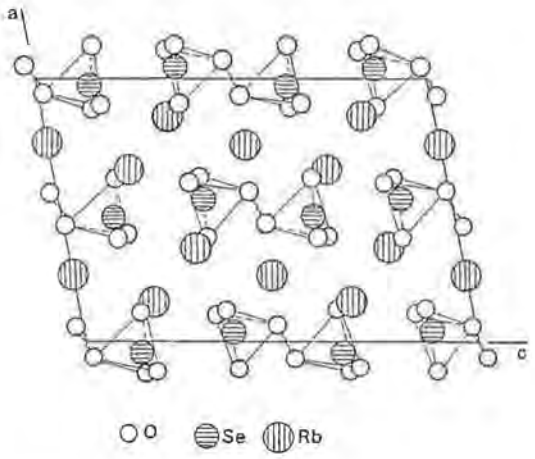

Figure 5 - xz projection of the $Rb_3H(SeO_4)_2$ structure in the ferroelastic phase at 293 K.

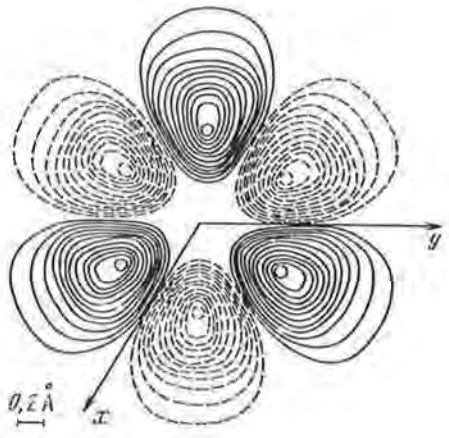

Figure 6 - The xy section of the difference PDF of the O(2) atom in the high-temperature phase at 473 K.

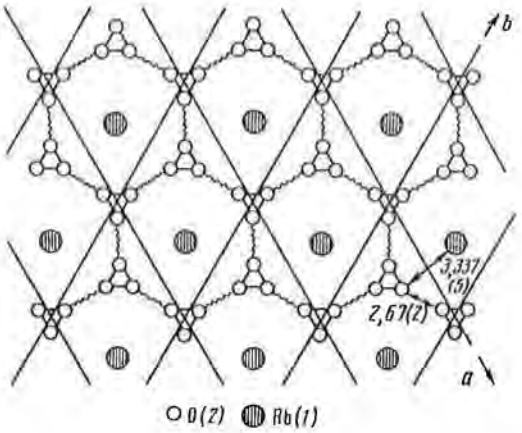

Figure 7 - xy projection of the $Rb_3H(SeO_4)_2$ structure at 473 K. Only the O(2) and Rb(1) atoms are shown (i.e., the atoms lying near a level z = 0.33). Triangles mark the O(2) positions.

$(NH_4)_2Se_2O_5$

In the $(NH_4)_2Se_2O_5$ system N-H...O hydrogen bonds linking ammonium groups with pyroselenite ions form a three-dimensional framework in the structure. During the phase transition at 312 K in these crystals [10] the system of hydrogen bonds changes while the space group ($P2_12_12_1$) is preserved.

Neutron diffraction studies of $(NH_4)_2Se_2O_5$ crystals have been carried out in the low-temperature (293 K) and high-temperature (333 K) phases [11]. Data collection parameters: spherical sample diameter = 0.6 cm; Syntex P1 diffractometer; VVR-C reactor; λ = 1.1674 Å; at 293 K, a=7.481(4), b=13.429(8), c=6.991(3) Å, Z = 4, 1303 unique reflections, $\sin\theta/\lambda < 0.79$ Å^{-1}, R_w = 4.0%, R = 4.0%; at 333 K, a=7.546(6), b=13.115(9), c=7.137(5) Å, Z = 4, 859 unique reflections, $\sin\theta/\lambda < 0.79$ Å^{-1}, R_w = 4.4%, R = 4.7%. The asymmetric unit contains a $[Se_2O_5]$ pyroselenite group and two symmetry non-equivalent $[N(1)H_4]$ and $[N(2)H_4]$ ammonium groups. The pyroselenite ion $[Se_2O_5]$ contains two pyramidal $[SeO_3]$ groups with O(3) as the bridging atom. Each $[NH_4]$ group is linked by four hydrogen bonds with four $[Se_2O_5]$ ions. Each O atom, except the bridging O(3) atom, which is not H-bonded, is an acceptor in two such hydrogen bonds with the N(1) and N(2) atoms as donors.

The space group is not changed during the phase transition, but the structural transformations are significant. For example, the O(1) displacement exceeds 0.8 Å. The interatomic distances in the $[NH_4]$ and $[SeO_3]$ groups are changed less, but these groups are rotated to a great degree relative to one another. As a result of these rotations, considerable changes are observed in the hydrogen bonding. In the high-temperature phase the N(1)-O(1) distance is increased from 2.891(4) Å to 3.312(5) Å, while the N(1)-O(2) distance is reduced from 4.063(5) Å to 2.956(5) Å. The N(1)-H(14)...O(1) hydrogen bond breaks and a new N(1)-H(14)...O(2) bond is formed. The switching of the hydrogen bond from the O(1) atom to the O(2) atom changes the Se(1)-O distances in the $[Se(1)O_3]$ group: the Se(1)-O(1) distance is reduced by 0.016 Å, while the Se(1)-O(2) distance is increased by 0.017 Å.

Changes in the hydrogen bonding cause symmetrization of the $[N(1)H_4]$-group environment (Figure 8, 9), although the space group is retained. Chains formed of $[N(1)H_4]$ groups along the c-axis can be singled out in the structure. In the high-temperature phase N(1)-H(14)...O(2) bonds form a pseudoplane in these chains, and the N(1)-H(11)...O(5) and N(1)-H(12)...O(4) bonds are pseudosymmetric with respect to this plane.

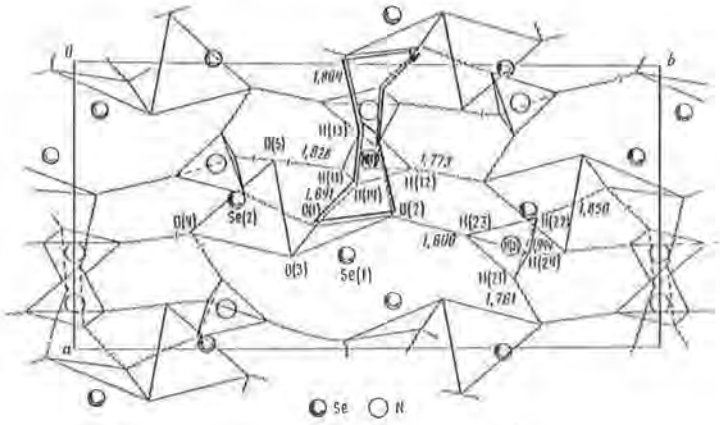

Figure 8 - xy projection of $(NH_4)_2Se_2O_5$ structure at 293 K. $[NH_4]$ tetrahedra are shown as well as oxygen bases of $[SeO_3]$ groups. Hydrogen bonds are shown by wavy lines.

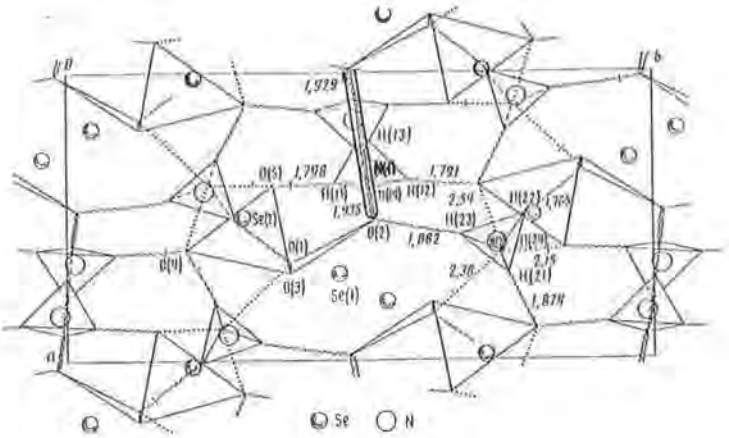

Figure 9 - xy projection of $(NH_4)_2Se_2O_5$ structure at 333 K. Notation as in Figure 8. The weakest hydrogen bonds are denoted by dotted lines.

In comparison with the values at 293 K, the thermal parameters of all the atoms are increased in the high-temperature phase, except for those of the O(2) atom. The reducing of the parameter B_{eq} of the O(2) atom from 2.94(7) to 2.50(6) Å^2, while the temperature is increasing, is due to the involvement this atom in one more hydrogen bond. Changes of the displacement parameters of atoms during the phase transition are therefore connected with structural features.

References

[1] R Poprawski, J Mroz, Z Czapla and L Sobczyk (1979) *Acta Phys Pol* A**55**, 641-646.

[2] Z Czapla, T Lis and L Sobczyk (1979) *Phys status solidi* A**51**, 609-612.

[3] I P Makarova, E E Rider, V A Sarin,, I P Aleksandrova and V I Simonov (1989) *Kristallografiya* **34**, 853-861.

[4] I P Makarova, L A Muradyan, E E Rider et al (1990) *Kristallografiya* **35**, 647-657.

[5] I P Makarova. (1993) *Acta Cryst* B**49**. in press.

[6] U H Zucker, E Perenthaler, W F Kuhs, R Bachmann and H Schulz (1983) *J Appl Cryst* **16**, 358.

[7] P J Becker and P Coppens (1974) *Acta Cryst* A**30**, 129-147.

[8] A I Baranov, I P Makarova, L A Muradyan et al (1987) *Kristallografiya* **32**, 682-694.

[9] I P Makarova, I A Verin and N M Shchagina (1986) *Kristallografiya* **31** 178-180.

[10] O I Nasluzova, I S Vinogradova, L L Zhidkov and A G Lundin (1988) *Kristallografiya* **33** 1174.

[11] I P Makarova, L A Muradyan, I S Vinogradova and V I Simonov (1990) *Ferroelectrics* **107** 275-280.

Ionic Conducting Cerate Perovskites

K S Knight

1. INTRODUCTION

Solid oxide fuel cells as currently envisaged require high operating temperatures, in the region of 900 to 1200°C, to overcome both the limitations in ionic conductivity in solid electrolytes and of kinetics in electrode materials. These temperatures both add to materials costs and reduce thermodynamic efficiency [1], however moderate temperatures in the range 600 to 800°C are more managable from a materials perspective and provide for the generation of high-quality waste heat. Unfortunately most protonic conductors in which the proton is transported via H_3O^+ are inherently unstable at these temperatures and hence a new class of compounds must be sought [2]. The perovskite solid solutions, pioneered by Iwahara and co-workers, have been found to withstand the rigorous thermal, oxidising and reducing conditions encountered in solid oxide fuel cells [3-6].The most widely studied materials, which exhibit these properties, are the solid solutions of $SrCeO_3$ and $BaCeO_3$, and in particular, $SrCe_{0.95}Yb_{0.05}O_{2.975}$, $BaCe_{0.9}Y_{0.1}O_{2.95}$ and $BaCe_{0.9}Gd_{0.1}O_{2.95}$ [3-9]. The conductivity of these compounds at 600°C approaches that of state-of-the-art ceria-gadolinia and exceeds that of commercially available zirconia-yttria, however by 800°C the fluorite structured materials surpass the perovskites, Table 1 [7 and references therein]. As a comparison, the conductivity of strong (liquid) electrolytes are of the order of 1 to 1000mScm^{-1}.

Table 1

Compound	conductivity at 600°C/mScm^{-1}	conductivity at 800°C/mScm^{-1}
CeO_2:Gd (x=0.2)	19	93
$BaCeO_3$:Gd (x=0.1)	11	16
$BaCeO_3$:Nd (x=0.1)	8	18
$BaCeO_3$:Y (x=0.1)	6	13
ZrO_2:Y (x=0.18)	5	20
$SrCeO_3$:Yb (x=0.05)	2	5

2. CONDUCTIVITY MEASUREMENTS

One of the remarkable properties of these compounds is that although their chemical formulae do not include hydrogen, they have a well documented protonic conductivity. This protonic conductivity arises due to interaction with water vapour from the atmosphere on cooling from the preparation temperature. Free protons could be generated from hydrogen-rich and hydrogen poor atmospheres by the oxidation of hydrogen in the former and the oxidation of water in the latter. However both reactions yield as many free electrons as protons, and hence n-type electronic conduction should always coexist with protonic conductivity. Moreover, as carrier mobility is inversely proportional to effective mass, the transport number for protons should be small. In practice neither effect is observed.

The doping of trivalent rare earth ions for cerium introduces oxygen ion vacancies ($ACe_{1-x}REE_xO_{3-x/2}$, A: Ba or Sr) which removes the constraint of generating a free electron per proton via dissolution of water in the lattice.

$$\tfrac{1}{2}H_2O(g) + \tfrac{1}{2}V_O^{\bullet\bullet} \rightarrow H_i^{\bullet} + \tfrac{1}{2}O_O$$

Where oxygen is also present, the dissolution of oxygen to produce holes competes for the available oxide ion vacancies.

$$\tfrac{1}{4}O_2(g) + \tfrac{1}{2}V_O^{\bullet\bullet} \rightarrow \tfrac{1}{2}O_O + h^{\bullet}$$

From the equilibrium equations for these reactions, it is apparent that the protonic conductivity depends on the water partial pressure whilst the p-type conductivity is dependent on the oxygen partial pressure. The occurrence of p-type conductivity, with only rare observations of n-type conductivity in these materials, coupled with thermogravimetric analysis confirming the dissolution of water, gives strong evidence for the occurrence of these reactions. However, although these reactions successfully describe the generation of protons and holes in the perovskites, the reason why these chemical equilibria are favourable has not yet been satisfactorily explained. Indeed recent results reported at the 1993 Pisa meeting on solid state ionics and mineralogy have suggested that these mechanisms may be too simple and that a crossover between protonic to oxide ion conduction may be dopant type and concentration dependent.

Norby [11] has pointed out that the proton can not really occupy an interstitial site because of its small size but probably attaches itself to an oxide ion, thus forming a

hydoxyl ion $OH_O^{\bullet}$. Note that the protons entering the lattice as either interstitials or hydroxyls substituing for oxide ions have the same effective charge of +1. For ionic conductivity it is usual to relate the conductivity to the self diffusion coefficient through the Nenst-Einstein equation. For an activated jump the conductivity is given by

$$\sigma T = (Nq^2\lambda^2\nu_0/6K_B)\exp(-E_a/RT)$$

where N is the carrier number density, λ is the distance between neighbouring sites, and ν_0 is the attempt frequency.

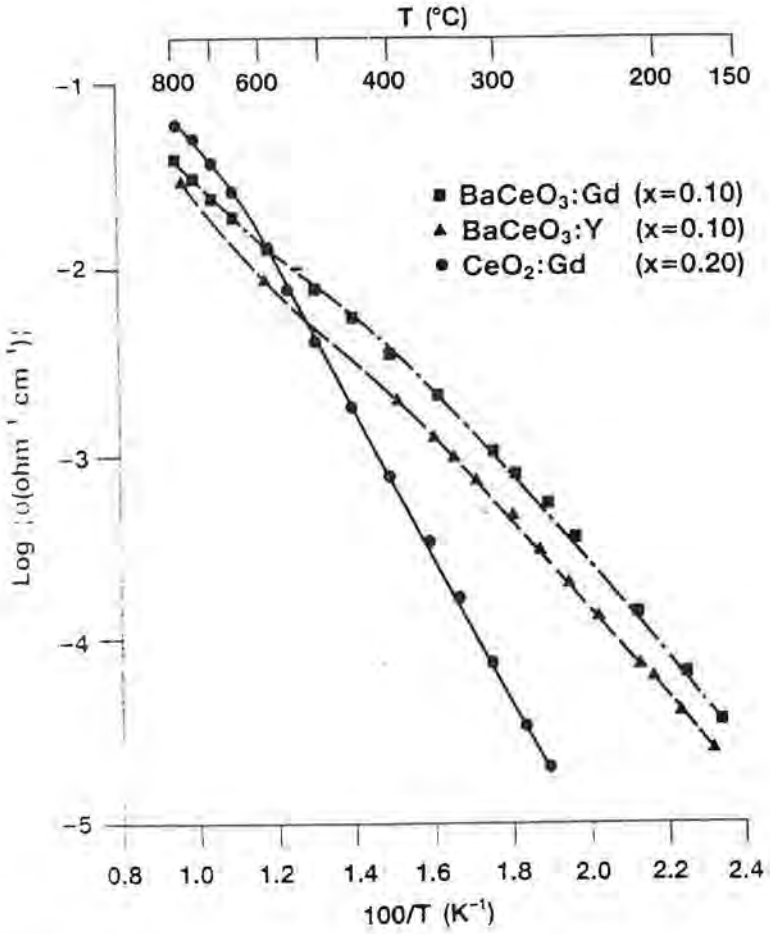

Fig. 1 Arrhenius plot of the total bulk conductivity, in air, of $BaCeO_3$:Gd, $BaCeO_3$:Y and CeO_2:Gd in the temperature range 150 to 800°C.
Data from reference 7.

Table 2 shows activation energies and the natural logarithm of the pre exponential for $BaCeO_3$:Gd in air, in the temperature range 150 to 300°C, for a variety of doping levels.

Table 2

$BaCe_{1-x}Gd_xO_{3-x/2}$	Ea/eV	ln(A/Scm-1)
x=0.05	0.46	8.2
x=0.10	0.52	10.1
x=0.15	0.56	10.7
x=0.20*	0.56	10.8
x=0.30*	0.55	9.6

* two phase material, $BaCeO_3$:Gd and $BaGd_2O_4$.

Recent calculations of the attempt frequency using the Arrhenius pre-exponent from conductivity measurements of both $BaCe_{0.9}Gd_{0.1}O_{2.95}$ and $BaCe_{0.95}Y_{0.05}O_{2.975}$ have shown that it is in the range of frequencies consistent with vibrations of metal-co-ordinated hydroxyl groups [12]. In addition, conductivity measurements on $SrZr_{0.94}Y_{0.06}O_{2.97}$ [13], $SrCe_{0.95}Yb_{0.05}O_{2.975}$ [14] and $BaCe_{0.9}M_{0.1}O_{2.95}$ (M=Y, Gd) [12] have shown that a strong isotope effect exists for the pre-exponential factor for H_2O and D_2O stabilised materials. The observation of this effect proves that proton hopping is the dominant transport mechanism in these perovskites at low to moderate temperatures. and not the vehicular transport via a hydronium ion.

The conductivity of some of these compounds has been shown to be more subtle than the simple production of protons via dissolution of water in the lattice. In a H_2/O_2 fuel cell, protonic conduction causes water evolution at the cathode whilst oxide ion conduction produces water at the anode and hence exhaust gas analysis is a valuable analytical tool to investigate the transport properties of these materials. Using this method there is good evidence that in $BaCe_{0.9}M_{0.1}O_{2.95}$ (M=Gd, Nd) that there is a cross-over from protonic to oxide ion conduction at temperatures between 600 to 1000°C. Bonanos has shown for the Gd-doped compound that there is a monotonic increase in oxide ion conductivity with temperature from 600°C and that the protonic component has a maxima at approximately 800°C [15], Figure 2.

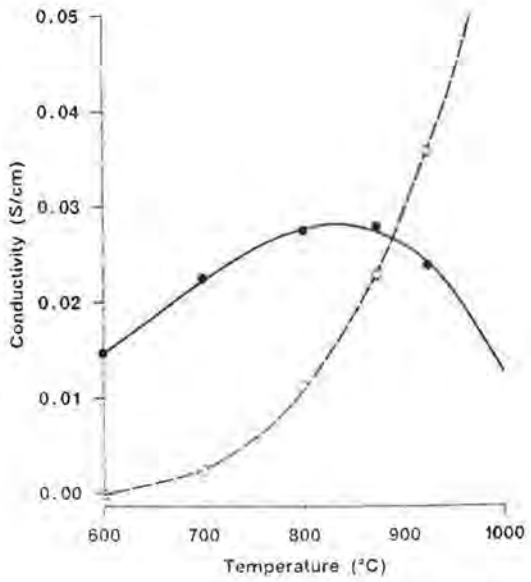

Fig. 2. Ionic conductivity of BaCe0.9Gd0.1O2.95, apportioned into protonic (•) and oxide ion components (◦).

This observation has lead to a detailed study of the conductivity of $BaCe_{0.9}Gd_{0.1}O_{2.95}$ as a function of temperature, using impedance spectroscopy at low temperatures, and an AC Van der Pauw technique at high temperatures, where the resistivity is low. The results are shown in Fig. 3 where there is some evidence for three linear regions with slightly differing gradients (asterisks indicating the three separate regions).The importance of these three separate regions will be commented on in the discussion section of this paper.

In conclusion, the lightly doped alkaline earth cerate perovskites exhibit protonic, p-type electronic and oxide ion conductivity resulting from reaction of water vapour with, and the presence of oxygen vancancies. The conductivity exhibits crossover from protonic to oxide ion, depending on temperature and doping level and possibly dopant type. The observation of a strong isotope effect in the activation energy shows the transport mechanism in these materials is due to proton hopping, and the attempt frequency calculated suggests that the proton ia associated with oxygen as a hydroxyl group.

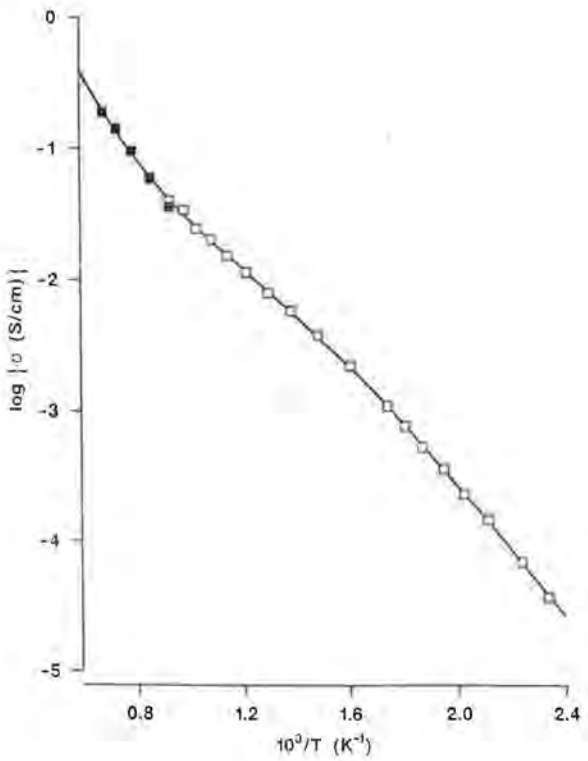

Fig. 3. Temperature dependence of the conductivity of $BaCe_{0.9}Gd_{0.1}O_{2.95}$, in air using impedance spectroscopy (unfilled symbols) and A.C. Van der Pauw (filled symbols).

3. CRYSTALLOGRAPHY

Although the conductivity of these compounds has been the subject of careful study, the crystallography of both $BaCeO_3$ and $SrCeO_3$ has been fraught with contradiction for many years. $BaCeO_3$ has been variously described as cubic [16-21] or tetragonal [21, 22] despite the definitive study of Mastromonaco *et al* [23] and the structure solution by Jacobson *et al.* [24]. In the most recent determination by Longo *et al.*, the crystal system was found to be tetragonal. In a neutron powder diffraction study of $BaCe_{0.9}M_{0.1}O_{2.95}$ (M=Y, Gd) [25] we have re-confirmed the crystal system determined by Mastromonaco *et al.* [23] and also that the structure of the undoped phase is retained on doping. $BaCe_{0.9}Y_{0.1}O_{2.95}$ is orthorhombic, space group *Pmcn*, with lattice constants a = 8.773(3)Å, b = 6.222(1)Å, c =6.244(1)Å and Z = 4. Rietveld refinement of POLARIS data converged at $\chi 2 = 1.41$ for an isotropic model, the final fit to the data is shown in Fig. 4. One somewhat surprising result from the refinement

was the localisation of the oxygen vacancy to only one of the two different oxygen sites, O2. The crystal structure is shown in Fig. 5. The crystal structure of the Gd doped sample was refined from neutron data, even though Gd has an extreme absorption cross section, after it was found that a refinement of synchrotron data gave chemically unreasonable oxygen coordinates due to the strong atomic number dependence of X-ray scattering. Recently we have re-determined the crystal structure of the undoped compound and investigated the effects of lightly doping with Pr [26].

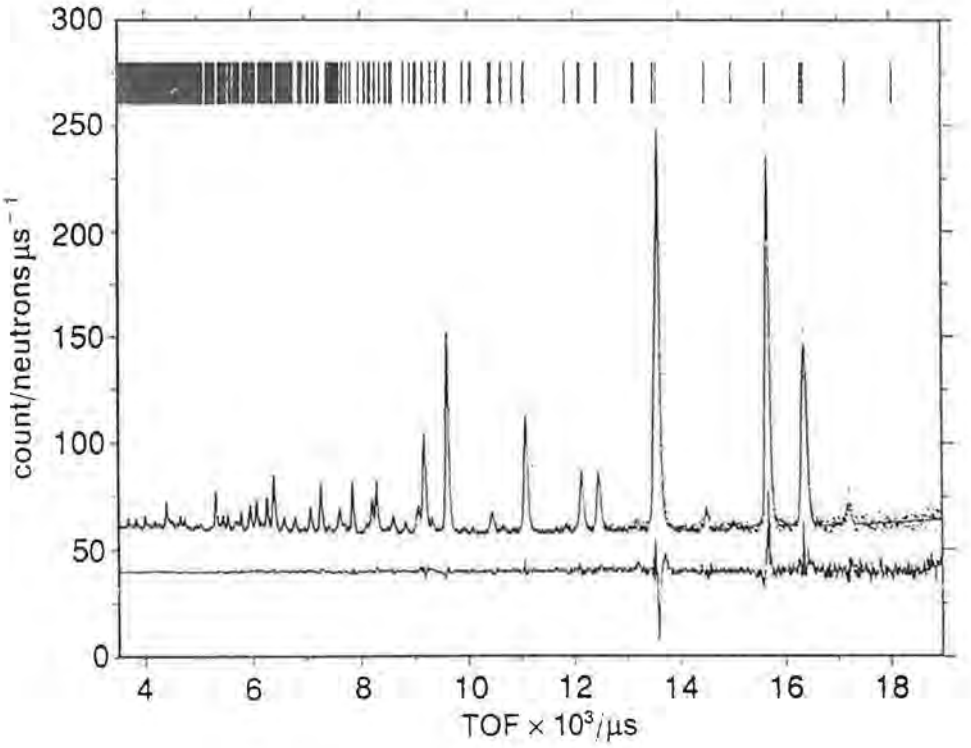

Fig. 4. Observed (dots), calculated (line) and difference plot for the POLARIS data for $BaCe_{0.9}Y_{0.1}O_{2.95}$. Data offset by 50 neutrons μs^{-1}.

The crystal system of $SrCeO_3$ has also been in dispute, having been reported as cubic [20,21], tetragonal [17,21], orthorhombic [18,23,27,28] and monoclinic [29,30]. The most recent determination, by Longo *et al.* found it to be orthorhombic with lattice constants a = 5.997Å, b = 12.308Å, c = 8.615.Å. Currently there is no published structure for the compound and hence a re-evaluation of the published data was carried out, prior to an attempt to solve the crystal structure from powder data (an attempt to refine the data from the Ba conmpound coordinates was unsuccessful).

High-resolution synchrotron and neutron powder data were collected using station 9.1 on the SRS and HRPD on ISIS. Assessment of the diffraction data showed the crystal system to be orthorhombic with lattice constants in agreement with the indexed data of Mastromonaco *et al.* [23] and hence the unit cell of Longo *et al.* can be rejected. Model independent fitting the HRPD data with the lattice constants of Mastromonaco *et al.* as starting values and using space group *Pmmm* allowed the systematic absences to be evaluated and the space group to be determined as *Pmcn*.

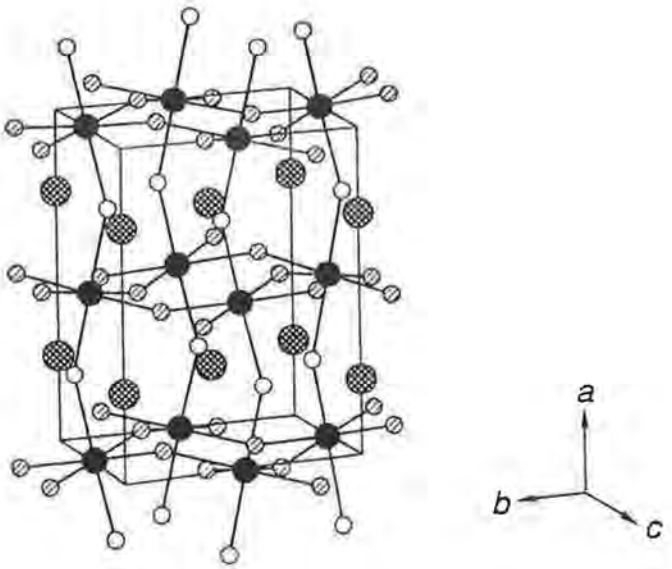

Fig. 5. Crystal structure of $BaCe_{0.9}Y_{0.1}O_{2.95}$, unfilled symbol O1, hatched O2, black Ce, cross-hatched Ba.

Glazer has shown, that providing the octahedral tilt angles around the psuedocubic axes are small, then the order of application of the tilts to an undistorted ideal perovskite structure is a second order effect [31]. In addition he showed that the psuedocubic lattice constants may be related to the anion-anion distance (through the centre of the octahedron) via the octahedron tilt angles, as below

$$a_p = \xi \cos\beta \cos\gamma$$
$$b_p = \xi \cos\alpha \cos\gamma$$
$$c_p = \xi \cos\alpha \cos\beta$$

where ξ is the anion-anion distance. Using the anion-anion distance determined from the crystal structure refinements of the Ba analogues, values of the tilt angles were determined. The eight possible sign permutations for the rotations fall into two sets of four (which represent different origin tilt combinations). Trial coordinates were found for the two potential structural models and each was refined using the Rietveld method from POLARIS data. Only one model satisfactorily refined, converging to $\chi 2 = 1.7$. Using this structural model, the more important Yb doped system was investigated which showed the same oxygen vacancy character as the Ba compound [26]. The lattice constants of $SrCe_{0.95}Yb_{0.05}O_{2.975}$ are a = 8.5833(1)Å, b = 6.0061(1)Å, c = 6.1445(1)Å. The coordinates of $BaCe_{0.9}Y_{0.1}O_{2.95}$ and $SrCe_{0.95}Yb_{0.05}O_{2.975}$ are given in Table 3.

Table 3

Atom	x/a	y/b	z/c	Biso/Å^2	Site Occupancy
Ba	0.2500	0.9968(7)	0.0147(5)	0.97(3)	1.0
Ce/Y	0.000	0.000	0.0000	0.33(2)	1.0
O1	0.2500	0.0732(4)	0.4861(6)	0.94(4)	1.0
O2	0.0401(2)	0.7303(3)	0.2726(3)	1.22(4)	0.975
Sr	0.2500	0.0124(2)	0.9554(1)	0.77(2)	1.0
Ce/Yb	0.0000	0.0000	0.0000	0.36(2)	1.0
O1	0.2500	0.8945(2)	0.5432(4)	0.63(2)	1.0
O2	0.9439(1)	0.7005(2)	0.2992(2)	0.77(1)	0.9875

4. DISCUSSION

Neutron powder diffraction has shown that the potentially commercially useful ionic conducting perovskites $BaCeO_3$ and $SrCeO_3$, doped with trivalent rare earths, are isostructural and have an intrinsic anion vacancy on only one of the two oxygen sites. Although we have carried out a limited study of dopants and doping levels the results so far suggest that any rare earth dopant may be accomodated in the octahedral site providing the doping level is less than 15mol %. Using X-ray powder diffraction, we have found that for Gd doping above this value there is a rapid degradation of the crystalline quality of the material with excessive line broadening and the appearance of a second phase.

Clearly it is important to find out whether this disorder is retained at temperatures where fuel cells and sensors operate and whether it plays any rôle in the conduction process. Scherban *et al.*[31] have recently shown using high-temperature Raman spectroscopy that there are changes in the modes associated with the CeO_6 octahedra. In particular, they show evidence for mode softening and claim an orthorhombic to tetragonal transition between 200 to 400°C, and predict a transition to an ideal perovskite at approximately 800°C. This upper temperature corresponds to the higher temperature change in the Arrhenius plot of Fig. 3 and the lower temperature is not inconsistent with the lower temperature change in gradient in the same figure. We have recently collected data from 100 to 1000°C in 25°C steps on $BaCe_{0.9}Y_{0.1}O_{2.95}$ using the POLARIS diffractometer. Data analysis has not started yet, however there is clear evidence for weak reflections disapearing at around 225°C and by 825°C the compound may be indexed as cubic. Preliminary assessment of this data suggests that the situation may not be as simple as Scherban *et al.* have implied and that residual tilting may remain and the Bravais lattice may be centred. A similar set of data collected on $SrCe_{0.95}Yb_{0.05}O_{2.975}$ shows little variation with temperature and hence any structural phase transitions that may have occurred may require higher resolution data to aid interpretation.

There clearly remains a significant amount of work to be carried out on these materials before the structural characterisation matches the electrical measurements, in particular high-temperature experiments under a variety of ambients may shed light on the nature of the conductivity crossover.

5. Acknowledgements

It is with great pleasure I acknowledge my former colleague and collaborator , Nicky Bonanos, for introducing me to these materials and for discussions on his electrical measurements. Steve Hull and Ron Smith (RAL) are thanked for help with the data collections on POLARIS.

6. REFERENCES

1. F.J.R. Rohr, in: Solid Electrolytes, eds. P. Hagenmuller and W. Van Gool (Academic Press, New York, 1978).

2. F.W. Poulsen, Protonic Conduction in Solids, in: High Conductivity Solid Ionic Conductors, ed. T. Takahashi (World Scientific, Singapore, 1988).

3.H. Iwahara, T. Esaka, H. Uchida and N. Maeda, Solid State Ionics **3/4**, (1981), 359.

4. H. Uchida, N. Maeda and H. Iwahara, Solid State Ionics 11, (1983) 117.

5. H. Iwahara, Solid State Ionics **28-30**, (1988) 573.

6. H. Iwahara, H. Uchida, K. Ono and K. Ogaki, J. Electrochem. Soc. **137**, (1990) 462.

7.N. Bonanos, B. Ellis, K.S. Knight and M.N. Mahmood, Solid State Ionics **35**, (1989) 179.

8. N. Bonanos, B. Ellis and M.N. Mahmood, Solid State Ionics **28-30**, (1988) 579.

9. N. Bonanos, B. Ellis and M.N. Mahmood, Solid State Ionics **44**, (1991) 305.

10.R.C.T. Slade and N. Singh, Solid State Ionics **46**, (1991) 111.

11. T. Norby, Solid State Ionics **40-41**, (1990) 849.

12. R.C.T. Slade and N. Singh, J. Mater. Chem. 1, (1991) 441.

13. H.H. Huang, M. Ishigame and S. Shin, Solid State Ionics **47**, (1991) 251.

14. T. Scherban and A.S. Nowick, Solid state Ionics **35**, (1989) 189.

15. N. Bonanos, Solid State Ionics **53-56**, (1992) 967.

16. A. Hoffman, Z. Physik. Chem. **B28**, (1935) 65.

17. E.K. Keler, N.A. Godina and A.N. Kalinina, Zh. Neorg. Khim. **1**, (1956) 2556.

18. A.J. Smith and A.J.E. Welch, Acta Crystallographica **13**, (1960) 653.

19. E.A. Wood, Acta Crystallographica **4**, (1951) 353.

20. J.P. Guha and D. Kolar, J. Mat. Sci. **6**, (1971) 1174.

21. M. Preda and R. Dinescu, Rev. Roum. Chim. **21**, (1976) 1023.

22. V. Longo, F. Ricciardiello and D. Minichelli, J. Mat. Sci **16**, (1981) 3503.

23. M.D. Mastromonaco, I. Barbariol and A. Cocco, Ann. Chim (Rome) **59**, (1969) 465.

24. A.J. Jacobson, B.C. Tofield and B.E.F. Fender, Acta Crystallographica **B28**, (1972) 956.

25. K.S. Knight, M. Soar and N. Bonanos, J. Mater. Chem **2**, (1992) 709.

26. K.S. Knight and N. Bonanos, Submitted to Mat. Res. Bull.

27. R.S. Roth, J. Res. Nat. Bur. Stand. **58**, (1957) 75.

28. A.E. Solov'eva, A.M. Gavrish and E.I. Zoz, Izv. Akad. Nauk SSSR, Neorg. Mater. **10**, (1974) 469.

29. I. Naray-Szabo, Naturwiss **31**, (1943) 466.

30. M. Yoshimura, T. Nakamura and T. Sata, Chem. Lett., (1973) 923.

31. T. Scherban, R. Villeneuve, L. Abello and G. Lucazeau, Solid State Communications **84**, (1992) 341.

Structural phase transitions and modulated state in the superionic $Na_4TiP_2O_9$

N.Bolotina
Institute of Crystallography, Russian Academy of Sciences, Moscow

Introduction

$Na_4Ti[PO_4]_2O$ (NTP) crystals are superionic conductors with Na^+ ion conductivity. Electrophysical studies of these crystals [1] have shown that a superionic phase transition occurs in the temperature range 520 - 540 K. In this case the ionic conductivity σ is increased by more than one order of magnitude, reaching $2\text{-}3 \times 10^{-2}\ \Omega^{-1}cm^{-1}$, while E_a, the activation energy of electroconductivity, is decreased from 0.80 eV to 0.31 eV. This phase transition may be attributed to significant changes of crystal structure, which give rise to the formation of conductivity channels for the Na^+ ions. Our study was aimed at the elucidation of structural mechanisms to explain the variations in ionic conductivity parameters

The first stage studied the temperature dependence of the unit cell parameters of NTP crystals. We found that close to T = 523 K the behaviour of the unit cell parameters is no longer monotonic. In addition, the temperature dependencies of the parameters exhibited two more anomalies at higher temperatures, 633 K and 723 K. The drastic variations in unit cell parameters at T = 523 K suggest a first order phase transition at this point. This phase transition is usually accompanied by cracking of the sample and after two or three heating and cooling cycles through this temperature, the sample is fractured. At the two other phase transitions, tha changes in unit cell parameters are smoother and not so significant. It is likely that these phase transitions are second order.

Thus, we have established three phase transitions in NTP crystals using X-ray diffraction techniques. Accordingly, X-ray structural studies of four crystal phases at temperatures 743 K [2], 663 K [3], 573 K [4] and 293 K [5] have been carried out. The results show that the phase with the highest symmetry, which is stable above 723 K, is the structural prototype for other structural modifications studied by us. Upon lowering the temperature, the basic high temperature cell undergoes distortions which can be described by modulation waves.

Structure of $Na_4Ti[PO_4]_2O$: structural mechanism of phase transitions and changes in the reciprocal lattice

The basis of the crystal structures of all the temperature modifications of NTP crystals studied by us are infinite columns of $\{Ti_2[PO_4]_4O_2\}_\infty$ along the c axis, made up of $[TiO_6]$ octahedra and $[PO_4]$ tetrahedra. The voids between the columns are filled by Na atoms (Figure 1). Some Na atoms fully occupy their sites and provide for linking of linear radicals which form a three-dimensional framework. Other Na atoms occupy their sites statistically and mainly serve for compensation of framework charges. It is these latter atoms that account for the ionic transport in superionic modifications of NTP crystals.

Among all the structure modifications of NTP crystals studied by us the high temperature paraphase [2] has the highest symmetry. Its unit cell is orthorhombic, space group Bmcm, with a = 15.752(1), b = 7.524(1), c = 7.095(1) Å at T = 743 K . The radical columns are located periodically along the c axis, the period being two Ti octahedra. The neighbouring radical columns, along the b axis, are translationally identical, while the neighbouring columns along the a axis are translationally identical, with ½ lattice period shift along c. Figure 2a shows schematically the location of reciprocal lattice points of the high temperature phase.

At 723 K there is a phase transition to an incommensurately modulated phase. The basic orthorhombic unit cell parameters are a = 15.711(3), b = 7.516(1), c = 7.090(1) Å, with a modulation wave vector $q = a^* + \frac{1}{2}b^* + \gamma c^*$ ($\gamma = 0.2$). It should be noted that the choice of the wave vector in this case is nonstandard. In the nomenclature of Ref [7], the symmetry of the

modulated phase is described by a four-dimensional space group B(Bmcm:11-1) with the same basic unit cell and wave vector $q' = ½b^* + (1-\gamma)c^*$. We consider this choice improper, however, as first, the wave vector is beyond the Brillouin zone, while secondly, for calculations related to the refinement of modulation structure parameters, a wave vector with a non-zero rational component $½b^*$ is the most unsuitable.

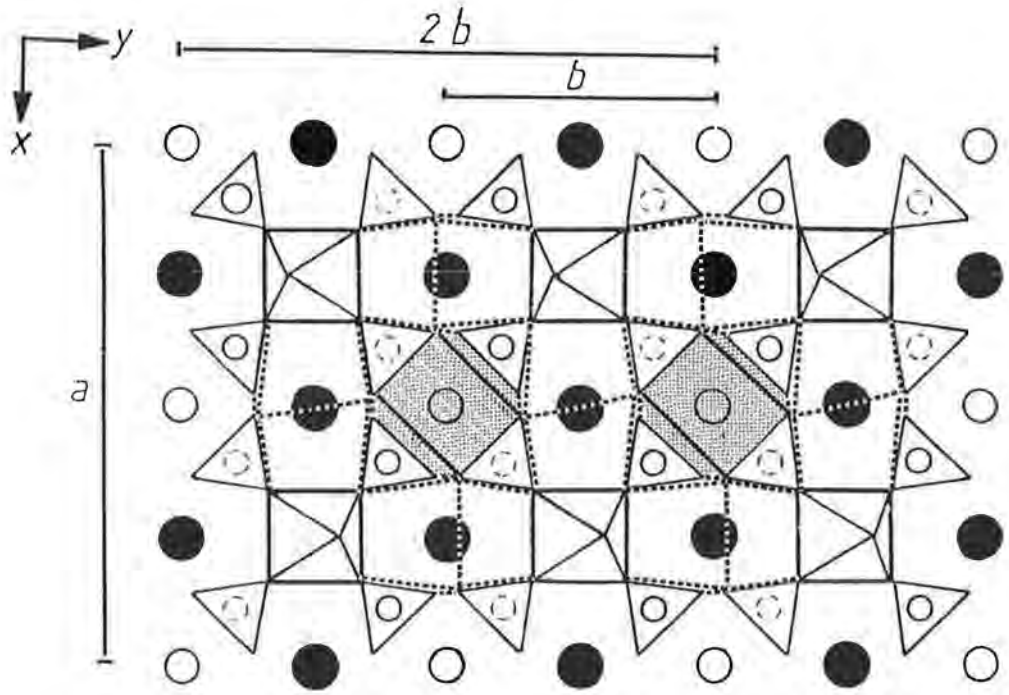

Figure1 - The structure of the high temperature orthorhombic paraphase projected onto (001). Inside the octahedra there are Ti atoms, inside the tetrahedra there are P atoms. The dark circles are Na atoms fully occupying their positions. The open circles are Na atoms statistically occupying them. The solid-line small circles are Na atoms located above P-octahedra, the dashed-line circles are Na atoms located under them. The possible channels of conductivity in the c-direction are dotted.

Consequently, the NTP structure was refined at 663 K [3] in the nonconventional four dimensional space group I(bam:11-1) with additional translations (0,½,0,½) and (½,0,½,½), and inthis case the wave vector $q'' = \gamma c$. The parameters of the basic orthorhombic unit cell are as follows: $a'' = a = 15.711(3)$, $b'' = 2b = 15.032(2)$, $c'' = c = 7.090(1)$ Å. Analysis of the results of refinement of the modulation parameters showed that during this phase transition mainly modulations of atomic displacements occur. These displacements are due to small rotations of the basic columns of the structure about the c axis. The column is rotated not as a rigid construction, but with the rotation angle modulated over the wave vector q''. The modulation wave length $\lambda = 5c$ is determined by the parameter $\gamma = 0.2$. The fact that the wave vector q contains a rational component $½b^*$ indicates that the columns which are neighbouring in the b-direction are modulated in anti-phase. Figure 2b presents schematically the satellite reflections typical of this modulated phase. The end of the wave vector q is positioned on the edge of the Brillouin zone, formed by the intersection planes perpendicular to a^* and b^* axes. In our case γ is a rational number and does not exhibit any temperature dependence. However, it is possible that one might observe incommensurate modulation with more accurate measurements. This possibility is based on the comparison of the phase with its closest structural analog $Na_{4.5}Fe[PO_4]_2(O,F)$ at T = 623 K, which was studied previously by us [6]. For the latter phase, the parameter $\gamma \cong 0.267$ and does exhibit a weak temperature dependence.

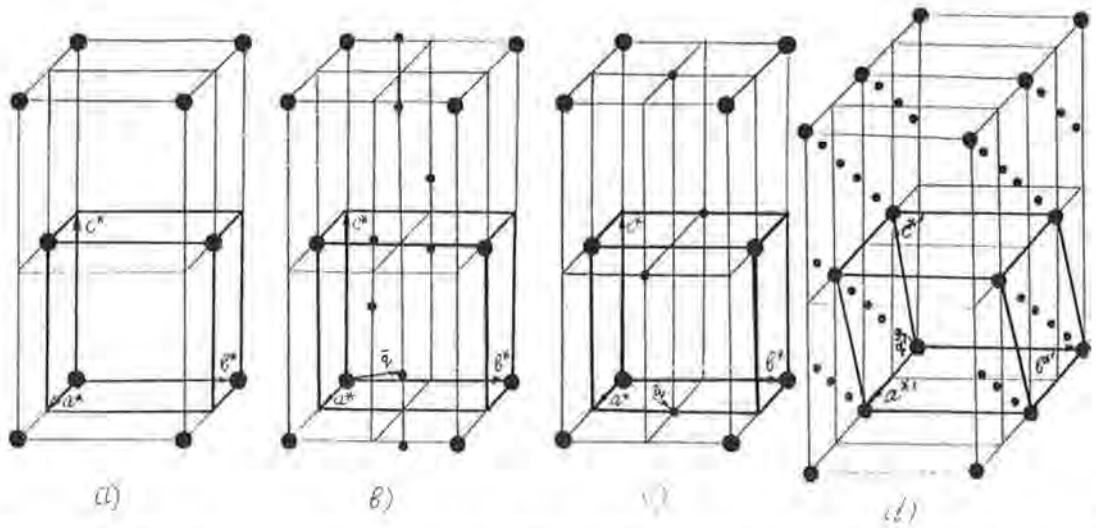

Figure 2 - The changes in the reciprocal lattice under the phase transitions. (a) paraphase, T = 743 K, (b) incommensurate phase, T = 663 K, (c) commensurate phase I, T = 573 K, (d) commensurate phase II, T = 293 K. The large circles are main reflections, the small circles are satellite ones.

For the phase transition at T =633 K the parameter γ becomes zero, and the wave vector is $q = a^* + \frac{1}{2}b^*$ (Figure 2c). The end of the wave vector is shifted to the middle of the edge of the Brillouin zone, i.e., a phase transition to a commensurately modulated phase occurs. In the nomenclature of Ref [7], the symmetry of this phase can be described either by the four-dimensional space group L(Bmcm:1-11) and the wave vector $q = a^* + \frac{1}{2}b^*$ or by the space group N(Bmcm:1-11) and the wave vector $q' = c^* + \frac{1}{2}b^*$. The basic orthorhombic unit cell parameters for this phase are a = 15.647(8), b = 7.445(4), c = 7.081(5) Å at T = 573 K. The columns are no longer modulated along the c axis, but those which are neighbouring in the b-direction are still rotated in opposite directions through a small angle about the c axis. The structure of this phase was refined in the conventional space group Ibam with unit cell parameters a' = a = 15.647(8), b' = 2b = 14.989(8), c' = c = 7.081(5) Å.

The phase transition at T = 523 K is accompanied not only by more significant structural distortions, but also by drastic variations of the parameters which characterize the ionic conductivity of the crystal. In fact, the crystal ceases to be an ionic conductor. In nonstandard representation the symmetry of the basic lattice is described by a pseudo - orthorhombic B-centered cell with lattice parameters a = 15.548(1), b = 7.541(1), c = 7.049(1) Å, β = 92.21(2)°. In reciprocal space, the satellite reflections of the previous modulated phase vanish, while new satellite reflections with the wave vector $q = \gamma(3a^* + c^*)$, γ = 0.2, arise (Figure 2d). It should be noted that the value γ is the same as for the phase at 663 K and it is not yet clear whether this is accidental or not. If in the previously considered cases of phase transitions the end of the wave vector was located on the edge of the Brillouin zone, now it is moved inside the zone. We refined the structure of the monoclinic commensurately modulated phase at T = 293 K in the basic primitive unit cell a' = (a - c)/2, b' = b, c' = c with the following parameters: a' = 8.631(1), b' = 7.541(1), c' = 7.049(1) Å, β' = 116.10(2)° in the standard four-dimensional space group P(P2/c:-1s) with the wave vector $q' = \gamma(a'^* + c'^*)$, γ = 0.2. Spontaneous deformation of the structure during this phase transition is also caused by rotations of the $\{Ti_2[PO_4]_4O_2\}_\infty$ radicals. As the wave vector does not now contain a component with vector b, the columns which are neighbouring in the b-direction again become translationally identical, similar to the high temperature paraphase, and are rotated through an angle of about 2° about the b-axis, giving rise to monoclinic distortions.

In all the structural modifications considered above, the main role in the structure modulation was played by modulations of atomic shifts, although the modulations of Na site occupancies were also taken into account during refinement of the structure. In all the modulated phases, except the monoclinic one, occupancy modulations were relatively insignificant. We suppose that the influence on the structural phase transitions in these phases, of those Na atoms which partially occupy their sites, is insignificant. The modulation of Na site occupancies provides evidence that it is these atoms that are the charge carriers in a superionic conductor. The monoclinic phase is characterized by totally different features. The amplitudes of site occupancy modulations are so large at the statistically populated Na_3 and Na_4 sites that the atomic sites are, in fact, either non-occupied or fully occupied. In the superstructural cell with parameters 5a' = 43.155, b' = 7.541, 5c' = 35.245 Å, $\beta' = 116.10°$, with five types of different subcells, Na_3 atoms occupy four out of five subcells, with Na_4 atoms occupying only two out of five. In this case the closest oxygen coordination of Na_4 contains not six (as in conducting phases), but only four O atoms, the Na - O distances being 2.30(3) - 2.50(3) Å. The sizes of the conductivity windows are reduced to a large extent, resulting in blocking of the main conductivity channels in the monoclinic phase of NTP crystals. We consider this result as one of the main results of this study. The reason for the changes in the ionic conductivity parameters is steric hindrances for ionic transport (hindrances which are absent in orthorhombic phases). Our structure investigations of these phase transitions have therefore allowed an understanding of the correlation between crystal structures and high ionic conductivity in these materials. The scheme of phase transitions in $Na_4Ti[PO_4]_2O$ crystals is shown in Table 1.

Table 1

Structural phase transitions in $Na_4Ti[PO_4]_2O$

Paraphase (high - temperature phase) Space group Bmcm The lattice parameters at 743 K are: a = 15.752(1); b = 7.524(1); c = 7.094(1) Å; Z = 4
The first phase transition at 723 K
Incommensurately modulated phase Super space group B(Bmcm:11-1) The lattice parameters of the basic structure at 663 K are: a = 15.711(3); b = 7.516(1); c = 7.090(1) Å; Z = 4 $q = 0.5b^* + (1-\gamma)c^*$, $\gamma = 0.2$
The second phase transition at 633 K
Commensurately modulated phase I Super space group N(Bmcm:1-11) The lattice parameters of the basic structure at 573 K are: a = 15.647(8); b = 7.445(4); c = 7.081(5) Å; Z = 4 $q = c^* + 0.5b^*$
The third phase transition at 523 K
Commensurately modulated phase II Super space group P(P2/c:-1s) The lattice parameters of the basic structure at 293 K are: a = 8.631(1); b = 7.541(1), c = 7.049(1); b = 116.10 Å; Z = 2 $q = 0.2a^* + 0.2c^*$

Microtwinning of the monoclinic phase

The transformation of the orthorhombic lattice to a monoclinic one during the phase transition is accompanied by pseudomerohedry over the vanished elements of the orthorhombic symmetry. In Figure 3 the character of twinning in reciprocal space is presented schematically. The twinning plane can be characterized either by 0kl indices in a pseudo orthorhombic reciprocal basis, or by h,k,2h indices in the monoclinic basis. Monoclinic twin lattices are related by the relationship $a_{(2)} = a_{(1)} + c_{(1)}$, $b_{(2)} = b_{(1)}$, $c_{(2)} = c_{(1)}$. As one can see from Figure 3, reflections from two twin partners ideally overlap only in the twinning plane. All the other twin reflections prove to be split. The angle δ between the directions $a_{(1)}$ and $a_{(2)}$ in reciprocal space is 4.42°. Each main reflection is surrounded by one to four satellite reflections, which are also split. We have worked out a special technique for measurements of integrated intensities of both components of such split reflections on a four-circle diffractometer. Each reflection **H**, prior to the measurements, was conventionally put into a reflecting position in the equatorial plane of the diffractometer. Then the diffraction node was rotated through an angle ψ about the vector **H**, so as to bring the vector **H'** (corresponding to the second component of the split reflection) also into the equatorial plane of the diffractometer. In this orientation the diffraction nodes **H** and **H'** are maximally split in terms of the diffractometer angle ω and are thus in optimum positions for separate measurements. We therefore managed to divide and measure, using either ω or $\omega/2\theta$ scans, the integrated intensities of almost all reflections (except, of course, those in the twinning plane).

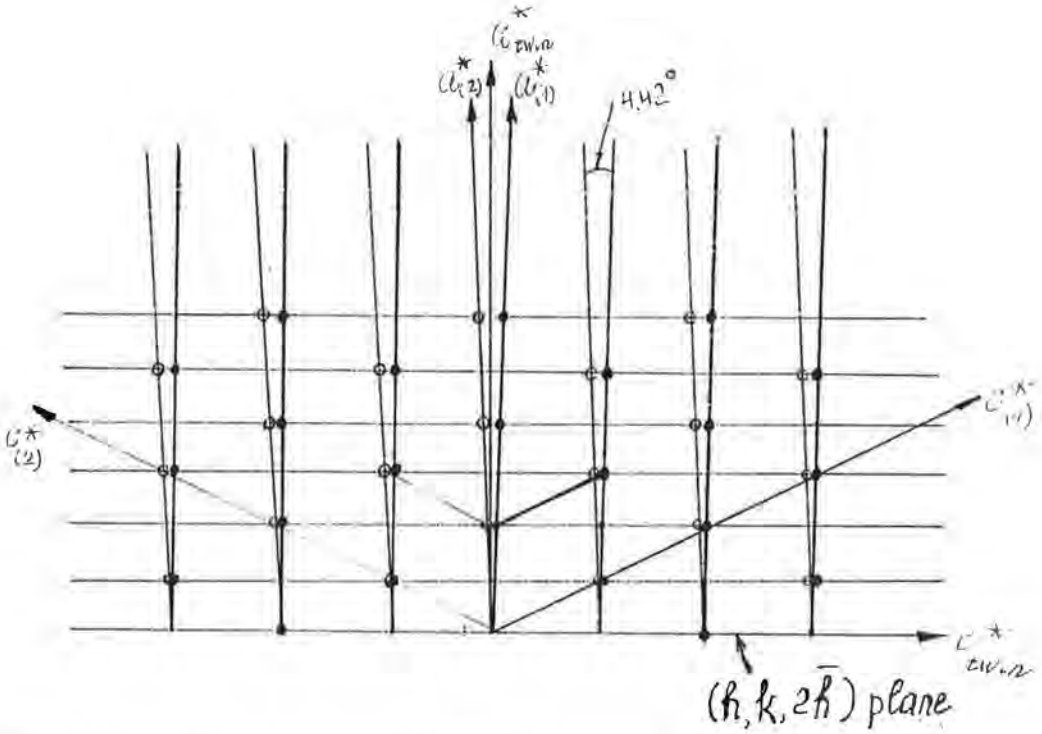

Figure 3 - Schematic of the diffraction pattern of the twinning of the monoclinic phase.

It should be pointed out that the full study reported here, including structure refinement of the modulated phases, especially the modulated microtwinned monoclinic phase, was completed only because special techniques and programs were used. To refine the structure of the modulated phases we used the JANA program system [8] developed by Dr V Petricek (Institute of Physics, Prague, Czech Republic), which provides a wide range of computational and service possibilities for refinement of commensurately and incommensurately modulated structures of single crystals, as well as composite and twinned structures.

References

[1] A K Ivanov-Shitz and S E Sigaryev (1990) *Solid State Ionics* **40/41** 76-78.
[2] N E Klokova, B A Maximov and R A Tamazyan (1993) *Kristallografiya*, submitted.
[3] N B Bolotina, B A Maximov, R A Tamazyan and N E Klokova (1993) *Kristallografiya*, submitted.
[4] B A Maximov, N E Klokova, I A Verin and V A Timofeeva (1990) *Kristallografiya* **35** 847-851.
[5] B A Maximov, N Bolotina, V Simonov and H Schulz (1992) ECM-XIV, Netherlands, Abstracts S360.
[6] B A Maximov, R A Tamazyan, N E Klokova, V Petricek, A N Popov and V I Simonov (1992) *Kristallografiya* **37** 1152-1163.
[7] P M de Woolf, T Janssen and A Janner (1981) *Acta Cryst* A**37** 625-636.
[8] V Petricek, P Coppens and P Becker (1985) *Acta Cryst* A**41** 478-483.

Determination of novel zeolite structures

By Michael A. Estermann

ISIS Science Division, Rutherford Appleton Laboratory, Chilton, Didcot, Oxfordshire OX11 0QX, UK.

Introduction

Novel zeolites and molecular sieves frequently challenge the traditional way of solving a crystal structure from X-ray or neutron diffraction data. Many of these materials are only available as polycrystalline powders and not as single crystals. In the absence of conventional single-crystal diffraction data, most of their structures were previously solved by informed model building, *i.e.* by the combination of chemical, geometric, symmetry and unit-cell information from powder diffraction.

Recent structure solutions [1, 2, 3] have now shown the feasibility of *ab initio* structure solution of new zeolite frameworks using integrated intensities extracted from powder data as input for traditional single-crystal techniques, such as Patterson or direct methods. The possibilities and limitations of this approach will be illustrated with powder data of various molecular sieves. However, uncritical application of single-crystal software packages, such as MULTAN [4], XTAL [5] or SHELX [6], to extracted powder intensities, is not without pitfalls.

Extracting integrated intensities from the powder pattern

The key problem in applying single-crystal software to powder data arises from the fact that a powder diffraction pattern is a one-dimensional projection (on 2θ) of the three-dimensional reciprocal lattice. Thus, reflections with similar 2θ values overlap in the powder pattern. Based on the original idea of Pawley [7], a number of programs have been written to extract reflections intensities in the absence of a structural model [8] and, in general, they cope well with partially overlapping reflections. For severely or exactly overlapping reflections, the extraction process can only reliably provide the sum of the intensities $S = m_{h_1} | F_{h_1} |^2_{pow} + ... + m_{h_n} | F_{h_n} |^2_{pow}$ and not the individual contributions $| F_{h_i} |^2_{pow}$, where m_h is the number of Laue-group equivalent reflections for index h. The intensity ratio (|E| values) of these reflections is usually set to one (equipartition).

Unravelling the intensities of severely overlapping reflections

Various methods have been developed to tackle the problem of overlapping intensities. Algebraic and probabilistic relations between structure-factor magnitudes can be used to improve the estimation of overlapping reflections. A different approach, involving an improved Patterson function obtained from density modification or maximum-entropy methods [9] allows the intensities of overlapping reflections to be retrieved by a Fourier back transformation (for details and a list of references see [10]).

This discussion will concentrate on the *Fast Iterative Patterson Squaring (FIPS)* method [10]. It involves an iterative procedure in which 1) a Patterson function is calculated using equipartitioned data, 2) each point in the map is squared, 3) the new map is back transformed to obtain new Fourier coefficients, and 4) these coefficients are then extrapolated to give a new set of $|F_{\mathbf{h}}|^{2\ overlap}$ and a new intensity distribution for the overlapping reflections (non-overlapping ones remain unaffected). The cycle is repeated until the intensity statistics of the overlapping reflections approximate those of the non-overlapping ones.

Using conventional single-crystal software with powder data: the pitfalls

The following discussion about structure solution using single-crystal software will be illustrated with powder data of the structures MCS-1 [2], SAPO-40 (a 12-ring silicoaluminophosphate) [3] and Cloverite (a gallophosphate with 20-ring pore openings) [11], see Table 1 and Fig. 1, 2 and 3.

Table 1. Type material, unit cell content, space group, resolution of data, number of reflections.

Type material	MCS-1	SAPO-40	Cloverite
Framework	$Al_{24}P_{24}O_{96}$	$[(Si,Al,P)_{32}O_{64}]$	$[Ga_{96}P_{96}O_{372}(OH)_{24}]$
Template	none	2 TPAOH	24 RF
Space group	Pbcn	Pmmn	$Pm\bar{3}m$
a (Å)	9.67	21.94	25.8
b (Å)	18.04	13.69	-
c (Å)	13.93	7.12	-
Volume ($Å^3$)	2430	2139	17,174
Resolution (Å)	1.2	1.3	1.5
Reflections	713	524	617
overlapping	68	340	552

TPAOH = tetrapropylammoniumhydroxide, RF = quinuclidiniumfluoride

(a) Estimating negative temperature factors with the Wilson method

The Wilson method [12] for the calculation of normalised intensities (|E| values) can be applied without modification to powder data. The least-squares fit estimating the overall scale k and overall temperature factor B does not depend on the decomposition of overlapping intensities. However, different implementations of the Wilson method can result in considerable differences in the estimated values for scale and temperature factor.

An example is given with the powder data of the clathrasil Sigma-2 [1]. Negative B factors were estimated with program MITHRIL [12] B = -2.52 $Å^2$, SIRPOW.91 [13] B =- 1.0 $Å^2$, whereas a positive value was obtained with the program XTAL2.6 [5] B = 3.63 $Å^2$.

The negative temperature factors are due to the limited resolution of the powder data (1.3 Å), the pronounced Debye [14] scattering curve for zeolites and the use of a straight forward least squares fit. The positive value was obtained by the use of the inflexion-point least-squares method [15]. This method is based on the close similarity of Debye scattering curves for structures containing the same structural components.

(b) Misinterpretation of intensity statistics

Intensity statistics of severely overlapping powder data suffer from an artefact caused by equipartitioning. It effectively averages the |E| values for overlapping reflections; the number of medium-sized |E| values increases while the number of small and large |E| values decreases. As a consequence, the intensity statistics of a centrosymmetric structure become misleadingly indicative of a non-centrosymmetric structure (Fig. 4). However, the intensity statistics can still be used for the discrimination between centrosymmetric and non-centrosymmetric structures when based on the non-overlapping reflections only. In the structure solution of SAPO-40 this was used to discriminate the correct centrosymmetric space group (Pmmn) from two other possible non-centrosymmetric candidates ($P2_12_12$ and $Pmn2_1$).

(c) Underestimating strong triplets and quartets in direct methods

The triplet products $\kappa \propto |E_hE_kE_{-h-k}|$ are essential to the success of direct methods, and large κ values are particularly important for the phasing process [16]. Only reflections with |E| values greater than 1.0 and triplet products with κ values greater than 1.1 are normally included at the phasing stage. Since equipartitioning effectively averages the |E| values for overlapping reflections, high |E|, and hence high κ, values are often obscured. The correlation between the triplet products obtained from the perfectly partitioned data set (PP) (with the intensity distribution for overlapping reflections calculated *a posteriori* from the solved structure) and those obtained from the equipartitioned (EQ) and the FIPS data have been examined, and the results are compared in Fig. 5. The better correlation between the κ(PP) and the κ(FIPS) and the increase in the number of triplets satisfying the minimum |E| and κ criteria, reflects the improvement attained by the use of the FIPS method. The large κ values, in particular, become more reliable, and thus the chances of a successful run with direct methods are improved.

This fact was recently illustrated by the attempted structure determinations of MCS-1, SAPO-40 and Cloverite, whose framework structures could not be solved from the conventionally treated (equipartitioned) powder data. It was only after using the *Fast Iterative Patterson Squaring* for unravelling the intensities of overlapping reflections that the structure solutions of MCS-1 and SAPO-40 became possible. Cloverite resisted all attempts. Fortunately, the continuing synthesis effort produced

single crystals large enough for conventional crystal-structure analysis. For comparison, there were 617 reflections (552 overlapping, d≥1.5 Å) from powder data; 2,776 unique reflections (d≥1.0 Å) from single crystal data.

(d) Failure to recognise a partial model

Emaps are calculated using the best phase sets produced by direct methods and the extracted powder intensities. An automated search for connected fragments using the strongest peaks from the Emap is included in most software packages for structure solution. The values of expected bond lengths and angles are set by default set for organic compounds, and have to be adjusted to zeolite structures: bond lengths to 1.6 Å (T-O bond) and bond angles ranging from 109° (O-T-O angles) up to 150° (T-O-T angles). The symbol T stands for a tetrahedral atom (Si, Al, P, Ga, Be, etc.). However, the complete structure can be found in this way only in exceptional cases. Normally, the correct positions are difficult to identify because there are either none or too many connected positions. This is due to the fact that (a) correct atomic positions present in the Emap are not necessarily amongst the strongest peaks and (b) many oxygen positions of the framework are simply not present.

Alternatively, the typical distance of about 3 Å between any two T-atoms allows the search to be restricted to four-connected T-positions only; missing oxygen positions do not interrupt the connectivity. All subsets of n peaks selected from the peak list are tested as possible solutions, where n is the number of expected T-atoms in the asymmetric unit. A subset is only accepted if all peaks have four first neighbours in a distances of approximately 3 Å. Once the T-atom positions are found any oxygen positions present in the Emap are easy to identify.

Testing a model

Whether or not a model of a tetrahedral framework is geometrically consistent with the measured unit-cell dimensions and the observed symmetry can be evaluated with a distance-least-squares (DLS) refinement [17]. The atomic co-ordinates of the tetrahedral atoms (T-atoms) and the bridging oxygen atoms are refined with a least-squares procedure to give the T-O distances and O-T-O and T-O-T angles typical for the particular framework composition (*e.g.* silicate, aluminosilicate, aluminophosphate, gallophosphate). A residual function

$$R_{DLS} = \sum_j w_j \left(D_j^{pres} - D_j^{calc} \right)^2$$

is minimised where $D_j^{prescribed}$ is the prescribed distance between two atoms (defined by the framework composition), D_j^{calc} the calculated distance (from the model) and w_j the weight for that distance (usually the reciprocal of the estimated standard deviation for the prescribed distance). Models which cannot be optimised by DLS refinement are unlikely to be correct.

Alternation of Al and Si or Al and P atoms in the tetrahedral positions of the framework must be taken into account. The symmetry of the average structure is reduced and the cell has to be adjusted accordingly. A DLS optimisation provides the desymmetrised starting co-ordinates for a subsequent Rietveld refinement (Fig. 3).

Have we got a new structure type for you ?

After DLS optimisation, feasible models are identified by comparison with known structure types from the *Atlas of Zeolite Structure Types* [18], the *ICSD* database [19], or a database of hypothetical zeolite structures [20]. However, unit-cell size and observed symmetry are not ideal search criteria because they change with the framework composition and the presence of non-framework species, such as cations or water, in the channels. An example is given for the aluminophosphates $AlPO_4$-EN3 [21] and MCS-1 which have different symmetries but the same framework topology (connectivity of tetrahedral atoms). The structure of $AlPO_4$-EN3 was solved from single crystal data with direct methods whereas MCS-1 was later solved independently from powder data with the *FIPS / direct methods* approach. In Table 2, the symmetry of the $AlPO_4$-EN3 and the MCS-1 structure are compared with the highest possible symmetry of the framework (The symbol T is used when Al and P atoms are not distinguished).

Table 2. Isotopic frameworks.

	$AlPO_4$-EN3	MCS-1		Topology
		solution	refinement	
Space group	$P2_12_12_1$	Pbcn	$Pca2_1$	Cmca
General positions	4	8	4	16
Asymmetric unit	$Al_6P_6O_{24}$	T_6O_{12}	$Al_6P_6O_{24}$	T_3
Non-framework species	ethylene-diamine	none	none	none

They were identified as the same structure type, already known as hypothetical type (Net 570, label *fsy*) [20], by the use of co-ordination sequences [22, 23]. In a typical zeolite framework each T-atom is connected to N_1 4 neighbouring T-atoms through oxygen bridges. These neighbouring T-atoms are then linked in the same manner to N_2 T-atoms in the next shell. The latter are connected with N_3 T-atoms etc. In this way a co-ordination sequence can de determined for each T-atom of the 4-connected net of T-atoms. Interrupted tetrahedral frameworks such as Cloverite excepted, it follows that $N_1 \leq 4$, $N_2 \leq 12, N_3 \leq 36, ..., N_k \leq 4 \cdot 3^{k-1}$. Isotopic frameworks have the same co-ordination sequence. The co-ordination sequence for the above framework is given by Table 3.

Table 3. The co-ordination sequence for the isotopic frameworks $AlPO_4$-EN3 and MCS-1

	N_1	N_2	N_3	N_4	N_5	N_6	N_8	N_9	N_{10}	N_{11}
T1	4	11	24	41	60	86	123	162	199	248
T2	4	11	22	39	64	90	119	155	201	250
T3	4	11	22	38	63	90	116	155	204	250

Conclusions

The discussed pitfalls in the course of a structure solution can be easily avoided. The degree to which reflections overlap, the resolution of the data (min d-spacing) and the complexity of the structure involved are the prime factors controlling whether or not a structure can be solved from powder data using conventional crystallographic techniques. The resolution of the data is probably the most crucial factor since direct methods work best with data of atomic resolution [6].

References

[1] McCusker, L. B. (1988). *J. Appl. Cryst.* **21**, 305-310.

[2] Simmen, A. (1992). PhD thesis. ETH, Zürich, Switzerland.

[3] Estermann, M. A.; McCusker, L. B. & Baerlocher, Ch. (1992). *J. Appl. Cryst.* **25**, 539-543.

[4] Main, P.; Fiske, S. J.; Hull, S. E.; Lessinger, L., Germain, G.: Declercq, J.-P. & Woolfson, M. M. (1980). MULTAN80. A system of computer programs for the Automatic Solution of Crystal Structures from X-ray Diffraction Data. Univs. of York, England & Louvain, Belgium.

[5] Hall, S. R. & Stewart, J. M. (1989). Editors. *XTAL2.6 User's Manual*. Universities of Western Australia, Australia, and Maryland, USA.

[6] Sheldrick, G. M. (1990). *Acta Cryst.* **A46**, 467-473.

[7] Pawley, G. S. (1981). *J. Appl. Cryst.* **14**, 357-361.

[8] David, W. I. F. (1993). CCSL program for the extraction of integrated intensities from powder data, ISIS Science Division, Rutherford Appleton Laboratory, England.

[9] David, W. I. F. (1990). *Nature (London)*. **346**, 731-734.

[10] Estermann, M. A. & Gramlich, V. (1993). *J. Appl. Cryst.* in press.

[11] Estermann, M., McCusker, L. B., Baerlocher, CH., Merrouche, A. & Kessler, H. (1991). *Nature (London)* **352**, 320-323.

[12] Gilmore, C. J.; Henderson, K. & Bricogne, G. (1991). *Acta Cryst.* **A47**, 830-841.

[12] Wilson, A. J. C. (1942). *Nature (London)*. **150**, 151-152.

[13] Cascarano, G.; Favia, L. & Giacovazzo, C. (1992). *J. Appl. Cryst.* **25**, 310-317.

[14] Debye, P. (1915). *Ann. Phys. (Leipzig)*. **46**, 809-823.

[15] Hall, S. R. & Subramanian, V. & (1982). *Acta Cryst.* **A38**, 590-598.

[16] Cochran, W. (1955). *Acta Cryst.* **8,** 473-478.

[17] Meier, W. M. & Villiger, H. (1969). *Z. Kristallogr.* **129**. 411-423.

[18] Meier, W. M. & Olson, D. H. (1992). Atlas of Zeolite Structure Types. *Zeolites*, **12**, 449-654.

[19] ICSD (1986). *Inorganic Crystal Structure Database*, Bergerhoff, Anorganisch-Chemisches Institut der Universitat Bonn, Germany.

[20] Smith, J. V. (1989). *Proc. of the 8th IZC, Amsterdam.* Jacobs, P. A., van Santen, R. A.: Zeolites: Facts, Figures, Future (Studies in surface science and catalysis Vol. 49) 29-47. Elsevier Science Publishers B. V., Amsterdam.

[21] Parise, J. B. (1984). *25. Proc. Int. Symp. Portoroz.* Drzaj, B. Hocevar, S. Pejovnik, S.: Zeolites. Synthesis, Structure, Technology and Application (Studies in surface science and catalysis Vol. 24) 271-278. Elsevier Science Publishers B. V., Amsterdam.

[22] Brunner, G. O. & Laves, F. (1971). *Wiss. Z. Techn. Univers. Dresden* **20**, 387 H.2.

[23] Meier, W. M. & Moeck, H. J. (1979). *J. Solid State Chem.* **29**, 41.

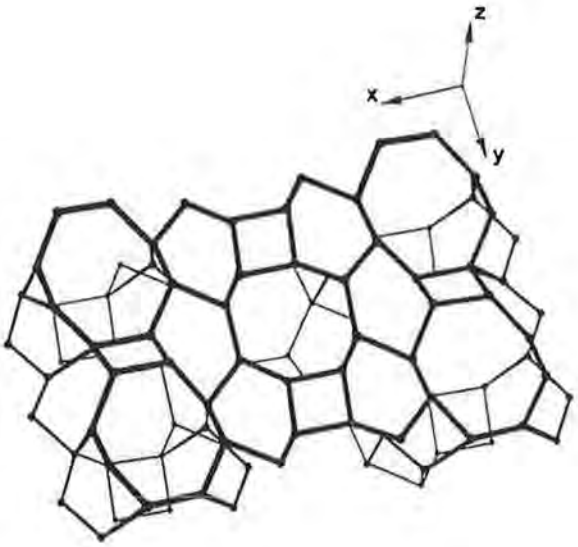

Fig. 1. The framework topology (Cmca) of the aluminophosphate MCS-1. The nodes represent tetrahedral atoms (either Al or P). O atoms have been left out for clarity.

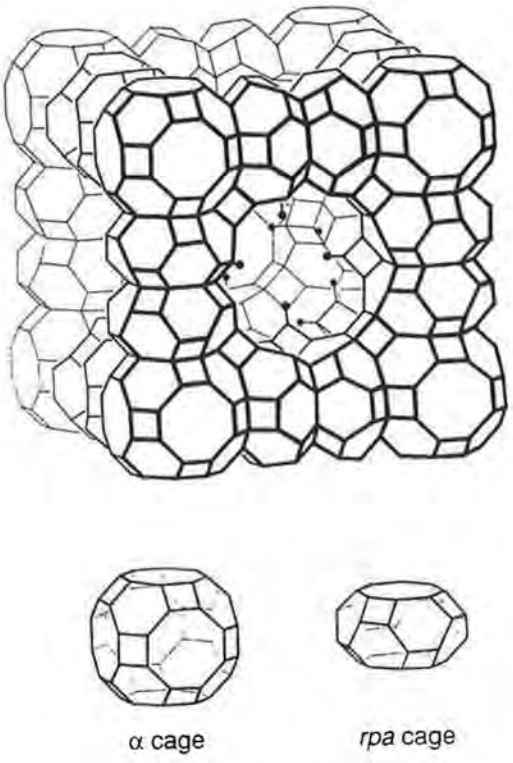

Fig. 2. The framework topology ($Pm\bar{3}m$) of the gallophosphate Cloverite showing the cubic arrangement of α– and *rpa*-cages. The nodes represent tetrahedral atoms (either Ga or P), the filled circles, terminal hydroxyls.

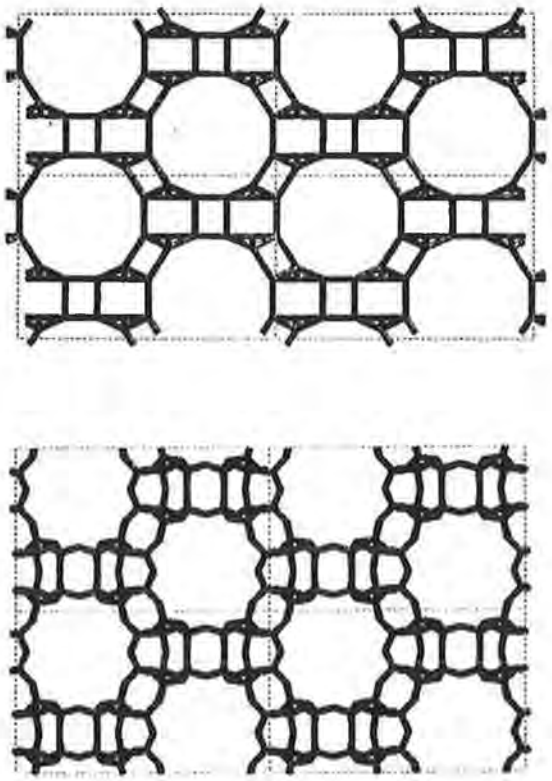

Fig. 3. SAPO-40 structure: topology (Pmmn), T-atoms only (top); DLS optimised framework (P112/n, c-axis doubled) with alternating Al and P atoms (bottom).

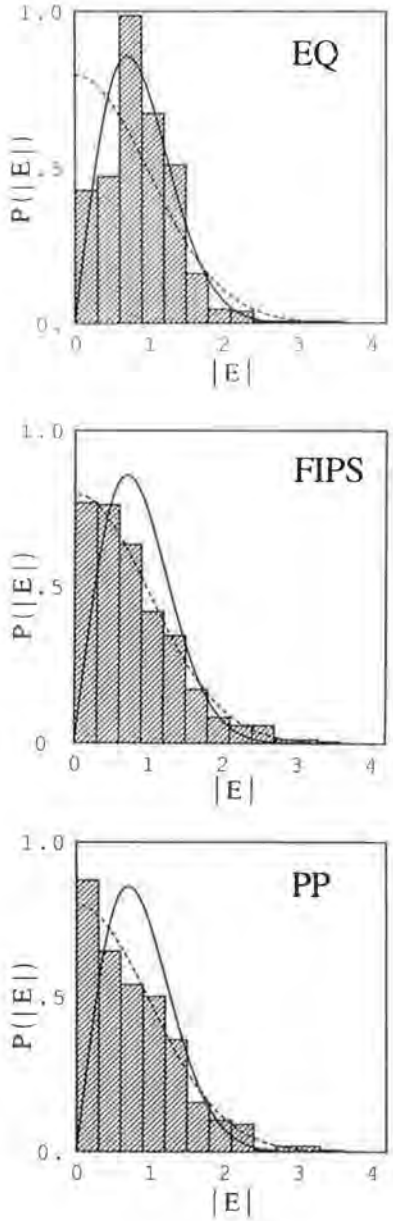

Fig. 4. Comparison of the ideal acentric (solid line) and ideal centric (dashed line) probability distribution function P(|E|) with that calculated from the three SAPO-40 data sets (histogram): equipartitioned (EQ), FIPS-improved (FIPS), and perfectly partitioned (PP) data.

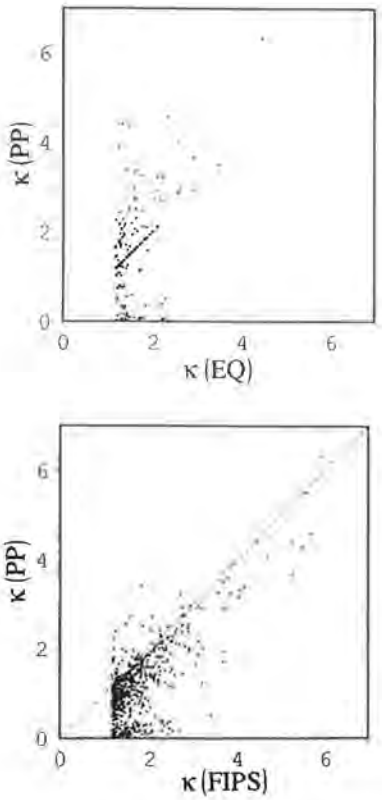

Fig. 5. The correlation of the triplet products $\kappa \propto |E_h E_k E_{-h-k}|$ obtained from perfectly partitioned data (PP) and those obtained from equipartitioned (EQ) and FIPS-improved (FIPS) data. If all three reflections contributing to a triplet product are non-overlapping, the values fall on the dashed diagonal line. Generating reflections have $|E| > 1.0$ and selected triplets have $\kappa > 1.1$.

Structural Studies of the Inclusion Compounds of Alkali Metals in Zeolites

A.R. Armstrong
ISIS Science Division, Rutherford Appleton Laboratory,
Chilton, Didcot, Oxon., OX11 0QX.

Abstract

As a result of their regular intracrystalline cavities zeolites have long been valued as molecular sieves and catalysts. More recently there have been investigations into the possibility of using these minerals and their synthetic analogues as host materials for the creation of new solid state compounds.[1] Among the oldest examples of such materials are the inclusion compounds of the alkali metals in zeolites.[2-17] The structures of these materials are largely unknown. Here we describe the preparation and structural characterisation of two widely differing inclusion compounds: a lightly potassium loaded sample of potassium zeolite L and a sample of potassium zeolite A that is saturated with potassium metal. In the former case the added potassium fills the partially occupied K(4) site, demonstrating that ionization occurs on alkali inclusion. In saturated zeolite A a zeolite-directed potassium superlattice is observed in which the ionic separation is similar to that in the bulk metal. This superlattice can be viewed as a highly dispersed or 'foamed' metal, but with fewer than 5 potassium valence electrons for every 17 cations. Spontaneous segregation into electron-rich and purely cationic regions suggests that this metal 'foam' may be close to a metal-insulator transition.

Introduction

The possibility of engineering filamentary networks and cluster arrays at the molecular level in the channels and cavities of porous aluminosilicates was first mooted by Barrer.[1] The inclusion compounds of the alkali metals in zeolites represent just such a class of compounds. The electronic and magnetic properties of these compounds have been extensively studied by electron spin resonance (ESR) spectroscopy and in a few cases solid state nuclear magnetic resonance (NMR). In its early stages the reaction often results in the formation of unusual ionic 'clusters' such as K_4^{3+}, Na_4^{3+}, K_3^{2+} and Na_6^{5+}. Such clusters have only been observed in zeolites containing the sodalite cage structural unit. The nature of the cluster is primarily dependent on the zeolite host; the formation of Na_4^{3+} may be written as follows:

$$M^0 + 4Na^+ \rightarrow M^+ + Na_4^{3+}$$

where M = Na, K, Rb, Cs. Thus the guest atom loses its valence electron to the four cations already present in the zeolite which form the cluster. Whilst these entities are conventionally referred to as clusters the ions that make up the cluster are bonded to the framework rather than to each other and should be regarded as electron traps. As more metal enters the zeolite structure, the ESR spectra of these compounds all exhibit a symmetric singlet resonance. This has commonly been attributed to the presence of metal particles within the zeolite pores. However latest results indicate that the guest atoms give up their valence electrons and occupy framework coordination sites. These electrons then interact loosely with both host and newly created guest ions. Although much is known about the electronic and magnetic properties of these materials, the actual effects on the zeolite crystal structure of reaction with alkali vapour are unknown. The studies reported here are the first to address this problem.

A metal is conventionally thought of in terms of a regular ionic array and a 'gas' of free electrons. The dehydrated zeolites can be viewed as a close approximation to the former. Reaction with alkali vapour has the simultaneous effects of increasing the number of cations in the zeolite and also introducing valence electrons. Thus these materials may contribute to the understanding of the metal to non-metal transition and provide an insight into the nature of the metallic state.

Experimental

The deep blue solid K_1/K_9-L was prepared through the reaction, in a sealed evacuated quartz tube, of dehydrated potassium zeolite LTL (K_9-L) with an amount of potassium vapour equivalent to 1 potassium atoms per unit cell, at temperatures between 200 and 250°C.[3,15] The greenish-brown solid K_5/K_{12}-A was prepared in a similar fashion. In this case a small amount of unreacted potassium formed a mirror on the surface of the tube indicating that the product was saturated with metal. Although unlike the parent alkali metals the compounds do not react dangerously with oxygen or water they are still extremely sensitive to air, decomposing rapidly on exposure. This necessitates the performing of diffraction experiments under inert conditions. Neutron powder diffraction data were collected at room temperature on the POLARIS diffractometer at ISIS with the samples kept in their sealed quartz reaction vessels. In order to eliminate the amorphous silica background, data were also collected from an empty sample tube. These data were then smoothed, appropriately scaled, and subtracted from the zeolite diffraction patterns to produce an essentially flat background. To ensure a consistent sample geometry the bulk of the quartz tube was shielded with cadmium foil.

Rietveld refinement of the structures used the least squares program TF14LS based on the Cambridge Crystallographic Subroutine Library.[18,19] Scattering lengths for K,

Si, Al and O were taken to be 0.367, 0.41534, 0.3449, and 0.5803 (all $x10^{-12}$ cm) respectively. The structure of K_1/K_9-L was refined assuming the space group *P6/mmm* as reported in previous studies by Barrer and Villiger[20] and Newsam.[21,22] The starting model for each refinement was that of Newsam,[21] with initially the only potassium sites considered being K(2), K(3) and K(4) (also referred to as B, C, and D), which are those which were reported to contain the bulk of the potassium ions. The positions of the framework atoms were refined before introduction of the potassium sites. Although different site preferences for silicon and aluminium have been reported, in view of the similarity in scattering lengths, the Si to Al ratio was fixed at the theoretical value of 3.0 for both sites throughout the analyses. The starting model for the structure refinement for K_5/K_{12}-A used the primitive cubic space group $Pm\bar{3}m$, and included framework atoms and the principal potassium sites K(1) at (0.23, 0.23, 0.23) and K(2) at (0, x, x) ($x \sim 0.5$).[23,24] Difference Fourier methods were used to locate further potassium sites.

Results and Discussion

The refinement of dehydrated, unloaded potassium zeolite L converged to give the final parameters shown in **table 1**. All the potassium ions were located in the sites K(2) (in the centre of the cancrinite cage), K(3) (between cancrinite cages) and K(4) (in 8-ring windows on to the main channel), as shown in **fig. 1**. No evidence was found for potassium occupation of the sites K(1) (in hexagonal prisms) or K(5) (in the intercage region) and the total refined potassium content of 9.3(4) is in excellent agreement with the theoretical value of 9.0. Addition of a single extra potassium atom per unit cell resulted in only minor structural changes. The only significant structural change was an increase in the fractional occupancy of the K(4) site (6j) from 0.72(7) to 0.93(6). Once again there was no evidence for potassium occupation of the 2c and 3f sites. This produced a total refined potassium content of 10.5(3), again in good agreement with the theoretical value and showing a significant increase over the value obtained for the dehydrated zeolite. A shift in the K(4) site away from O(4) and O(6) was observed. The observation that the added potassium atoms occupy ionic sites implies that ionisation is occurring with donation of an electron to the framework. The profile fit to the data for both dehydrated K_9-L and K_1/K_9-L is shown in **fig. 2**.

The refinement of K_5/K_{12}-A in space group $Pm\bar{3}m$ gave a satisfactory fit to the data. Difference Fourier methods indicated the presence of additional potassium sites in the sodalite cage at around (0.13, 0.13, 0.13) (K(3)), and in the α-cage at approximately (0.25, 0.25, 0.5) (K(4)). All four potassium sites are known in dehydrated K_{12}-A,[23,24] and thus may be regarded as primarily ionic in character. Hence no distinction can be drawn between potassium originally present in the zeolite and that absorbed from the vapour phase. The profile

Table 1. Structural Parameters for Zeolite L in space group *P6/mmm*

a) Dehydrated K_9 zeolite L a = 18.483(1)Å c = 7.4938(4)Å

Atom	Wyckoff symbol	*x/a*	*y/b*	*z/c*	B_{iso}(Å^2)	Site occupancy
Si1/Al(1)	12q	0.0921(6)	0.3546(6)	0.5000	2.0(2)	0.75/0.25
Si2/Al(2)	24r	0.1666(5)	0.4990(4)	0.2110(7)	0.9(1)	0.75/0.25
O(1)	6k	0.0000	0.2749(5)	0.5000	1.2(1)	
O(2)	6m	0.1657(3)	0.3313(6)	0.5000	2.3(2)	
O(3)	12o	0.2653(2)	0.5307(4)	0.2576(9)	1.7(1)	
O(4)	24r	0.1004(4)	0.4143(4)	0.3225(6)	2.4(1)	
O(5)	12o	0.4261(2)	0.8521(5)	0.2720(9)	2.4(2)	
O(6)	12p	0.1457(4)	0.4779(4)	0.0000	1.7(1)	
K(2)	2d	0.3333	0.6667	0.5000	2.0(5)	
K(3)	3g	0.0000	0.5000	0.5000	3.5(6)	
K(4)	6j	0.0000	0.3156(14)	0.0000	2.5(7)	0.72(7)

R_{wP} = 2.9%; R_E = 2.8%; R_I = 7.0%.

b) K_I/K_9-L a = 18.4503(5)Å c= 7.4852(2)Å

Atom	Wyckoff symbol	*x/a*	*y/b*	*z/c*	B_{iso}(Å^2)	Site occupancy
Si1/Al(1)	12q	0.0911(4)	0.3553(5)	0.5000	1.5(1)	0.75/0.25
Si2/Al(2)	24r	0.1673(3)	0.4999(3)	0.2113(5)	0.5(1)	0.75/0.25
O(1)	6k	0.0000	0.2739(4)	0.5000	0.9(1)	
O(2)	6m	0.1651(2)	0.3303(4)	0.5000	1.8(1)	
O(3)	12o	0.2652(1)	0.5303(3)	0.2569(7)	1.8(1)	
O(4)	24r	0.1011(2)	0.4148(3)	0.3191(4)	1.9(1)	
O(5)	12o	0.4267(2)	0.8534(4)	0.2728(7)	2.2(1)	
O(6)	12p	0.1457(3)	0.4777(3)	0.0000	1.5(1)	
K(2)	2d	0.3333	0.6667	0.5000	0.9(3)	
K(3)	3g	0.0000	0.5000	0.5000	3.3(4)	
K(4)	6j	0.0000	0.3138(11)	0.0000	5.6(8)	0.92(6)

R_{wP} = 4.6%; R_E = 3.0%; R_I = 6.1%.

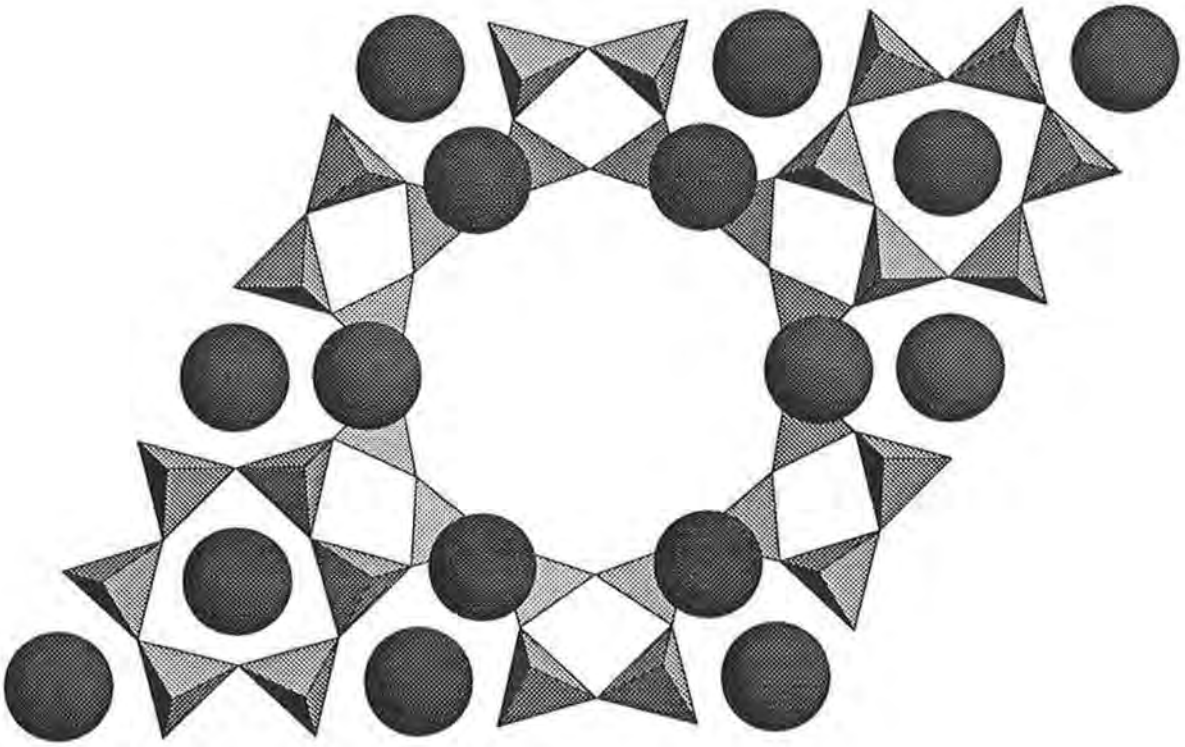

Figure 1. Structure of zeolite L.

Figure 2.

a) Profile fit for dehydrated Zeolite L

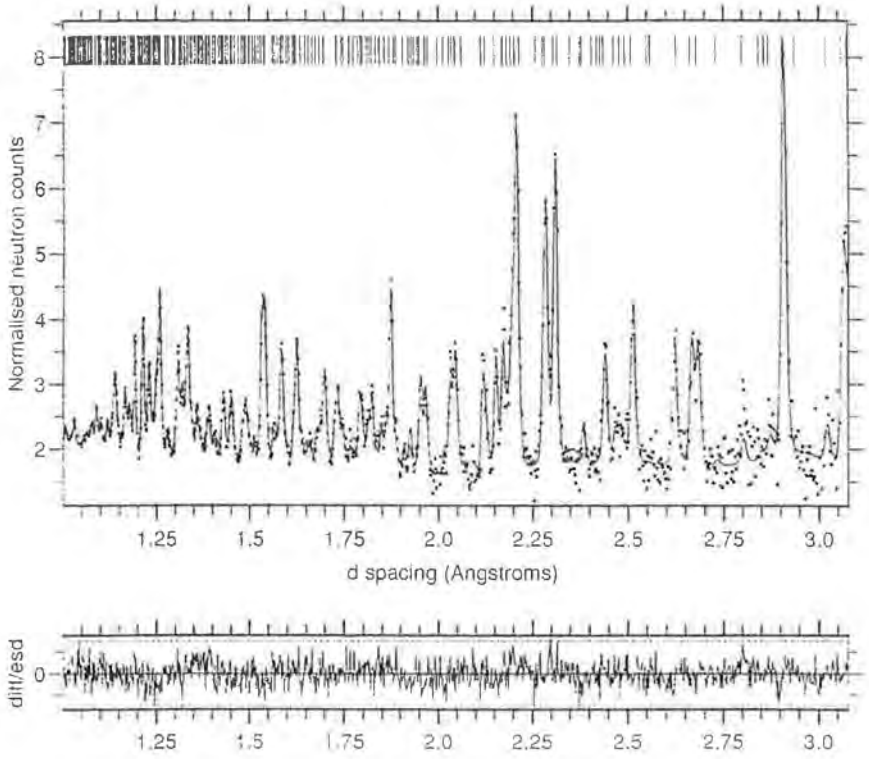

b) Profile fit for K_1/K_9-L

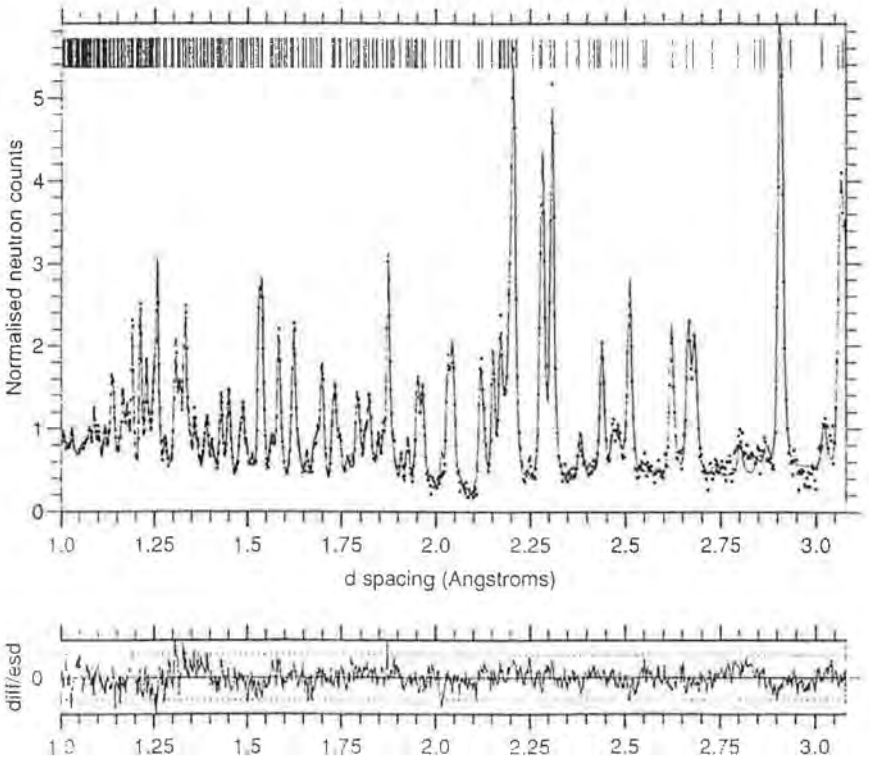

fit clearly contains a significant number of supercell reflections (shown in **fig. 3a**). The standard supercell in zeolite A involves Si and Al ordering (space group $Fm\bar{3}c$);[25] whilst this model gave an improved refinement the prominent supercell reflections were not fitted. The refined occupancies of sites K(1), K(3) and K(4) were all close to 0.5. An impossibly short K(1)-K(3) separation of 2.1Å across the 6-rings of the sodalite cage prevents occupation of adjacent sites and this topological constraint leads to cation ordering. The most energetically favourable arrangement is a tetrahedron of K(3) ions with faces capped by a further tetrahedron of K(1) as illustrated in **fig. 4a**. On average each α-cage contains 4 K(1) and 6 K(4), which would require short K(1)-K(4) interactions of 3.3Å. Further ordering with alternate α cages containing either 8 K(1) or 12 K(4), was accommodated in space group $Fm\bar{3}m$ (assuming Si/Al disorder) and gave a significantly improved refinement, successfully fitting all superlattice reflections as shown in **fig. 3b**. Final crystallographic data are shown in **table 2**.

The observation that included potassium in K_5/K_{12}-A is found in ionic sites is consistent previous electron spin resonance (ESR) results which reveal the spontaneous ionization of alkali metal atoms on entering potassium zeolites.[3,8] The cations of dehydrated K_{12}-A represent a more or less regular array into which precise numbers of electrons may be injected through reaction with controlled amounts of potassium vapour.[15] In zeolites X, Y and A excess electrons are often trapped as K_3^{2+} or K_4^{3+} paramagnetic centres in the sodalite cages.[3,8] In K_5/K_{12}-A the single-line ESR spectrum (g = 1.9978, ΔH_{pp} = 21.6 G) testifies to a high degree of delocalization of the excess electrons over large areas of the potassium lattice. However it is important to stress that only five valence electrons per seventeen potassium ions leads to a net charge in excess of +0.7 per cation.

However, the distribution of potassium in K_5/K_{12}-A is inhomogeneous: the α-cages containing 8 K(1) retaining the structure of the parent zeolite, whilst those containing 12 K(4) are much more densely packed (**fig. 4b**). Both the ESR g-value and the potassium-potassium nearest neighbour distances in the denser region of the structure are comparable to those observed in the bulk metal.[26,27] These potassium-potassium distances fall in the range 4.238(3) to 4.884(3) Å compared with a value of 4.54 Å for potassium metal.[27] Bond valence sums (BVS) for potassium have been calculated using the method of Brown.[28,29] Whilst these should be treated with some caution,[28] K(1) and K(3) are directly comparable since both coordinate to the 6-rings of the sodalite cage. Interestingly, whereas K(1) (BVS = 1.00) behaves as K^+ the value for the tetrahedron of K(3) (0.78) is close to that expected for K_4^{3+} (0.75). This represents the first crystallographic observation of K_4^{3+} albeit at such a high concentration that it can no longer be detected using ESR. Although the low value for K(4) (0.50) in part reflects its lower coordination number, these ions appear electron-rich compared with K(1). Apparently both electronic and structural segregation has occurred in K_5/K_{12}-A, with half the α-cages remaining as pristine pockets of dehydrated zeolite with the excess

Figure 3. Observed and calculated diffraction profiles for K_5/K_{12}-A.

a) Profile fit in space group $Pm\bar{3}m$. The presence of several prominent superlattice reflections which are not fitted in this model should be noted.

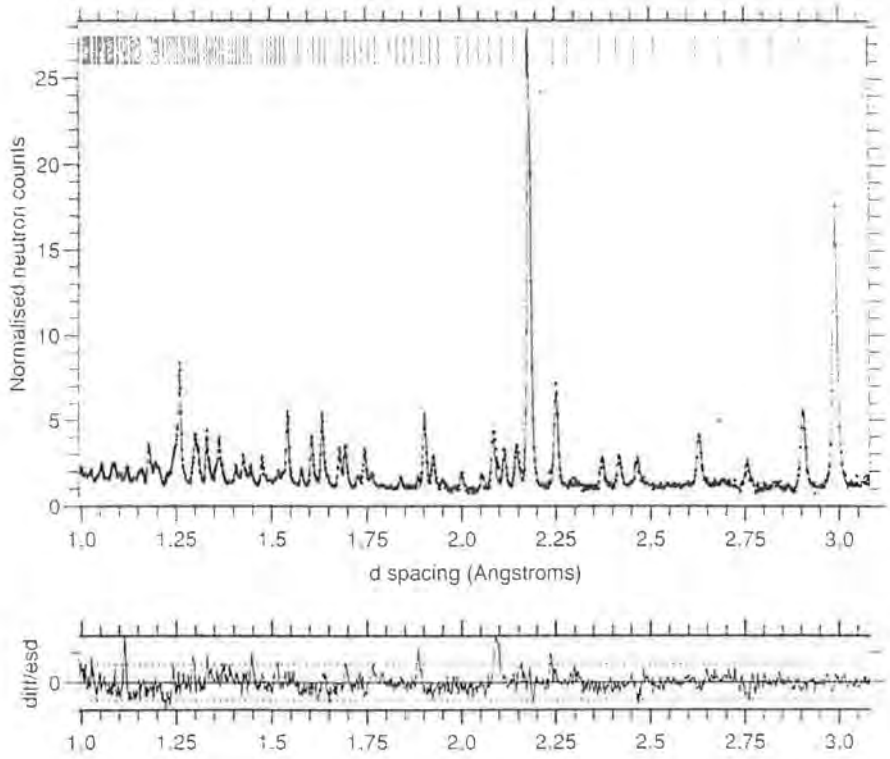

b) Profile fit in space group $Fm\bar{3}m$. The superlattice reflections are now very well fitted.

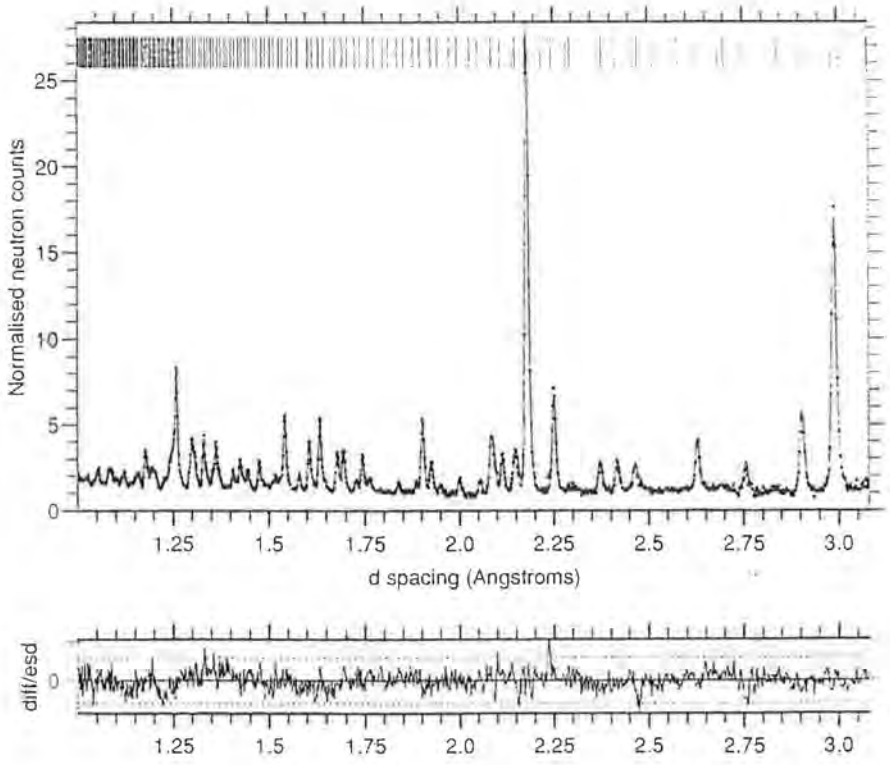

Figure 4. Structure of K_5/K_{12}-A.

a) The sodalite cage in K_5/K_{12}-A showing a tetrahedron of K(3) ions inside the cage (dark circles) with faces capped by a tetrahedron of K(1) ions outside the cage (pale circles).

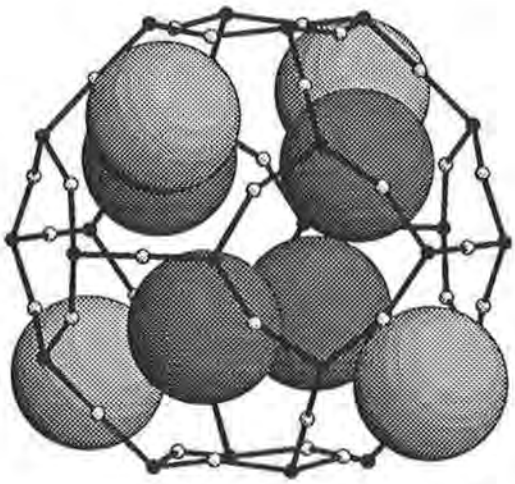

b) Fragment of the structure showing neighbouring α-cages and a sodalite cage. The much less open structure of the left hand cage containing K(4) is readily apparent.

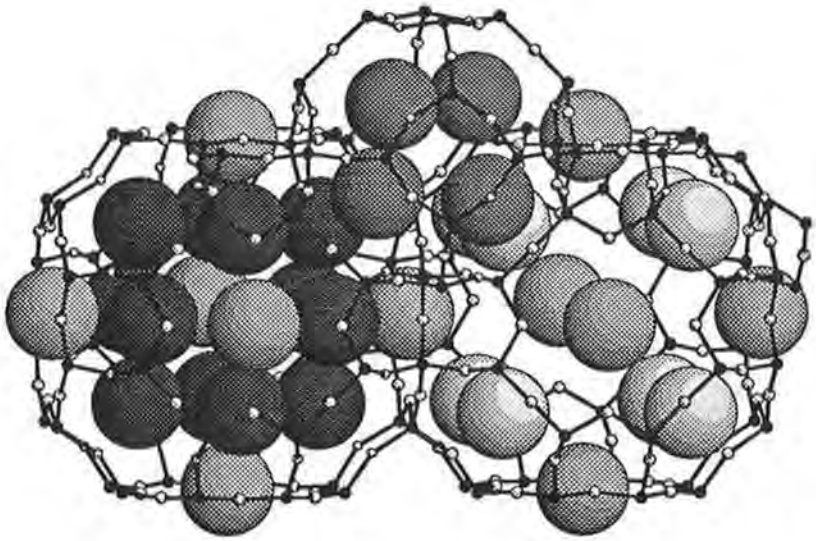

electrons confined to a cationic network located in the sodalite cages and the more densely occupied α-cages.

Table 2. Final crystallographic data for K_5/K_{12}- A.

Cubic: space group $Fm\bar{3}m$ (no. 225) $a = 24.6324(2)$ Å.

Atom	Wyckoff symbol	*x/a*	*y/b*	*z/c*	Site occupancy
Si/ Al	192l	0.75	0.8430(2)	0.9389(1)	0.5/0.5
O(1)	96j	0.0	0.8731(2)	0.7450(2)	1
O(2)	96k	0.8915(1)	0.8915(1)	0.7539(3)	1
O(3)	96k	0.8053(2)	0.8053(2)	0.9327(2)	1
O(4)	96k	0.3070(2)	0.3070(2)	0.4280(3)	1
K(1)	32f	0.8676(4)	0.8676(4)	0.8676(4)	1
K(2)	96k	0.0069(10)	0.0069(10)	0.75	0.140(10)
K(3)	32f	0.3177(3)	0.3177(3)	0.3177(3)	1
K(4)	48i	0.5	0.3727(3)	0.3727(3)	1

$R_{wP} = 2.9\%$; $R_E = 2.3\%$; $R_I = 6.2\%$.

b) Temperature factors

Atom	B_{11} (Å^2)	B_{22} (Å^2)	B_{33} (Å^2)	B_{23} (Å^2)	B_{13} (Å^2)	B_{12} (Å^2)	B_{iso} (Å^2)
Si/Al	0.4(1)	0.7(1)	0.6(1)	0.1(1)	0.1(2)	–0.1(2)	
O(1)	1.8(2)	1.0(1)	1.5(2)	0.9(2)			
O(2)	0.8(1)	0.8(1)	1.5(2)	–0.5(1)	–0.5(1)	1.0(1)	
O(3)	2.3(2)	2.3(2)	1.1(2)	–0.3(1)	–0.3(1)	–0.1(3)	
O(4)	1.3(1)	1.3(1)	1.8(2)	0.4(1)	0.4(1)	0.1(2)	
K(1)	2.1(3)	2.1(3)	2.1(3)	0.5(3)	0.5(3)	0.5(3)	
K(2)							0.0(7)
K(3)	2.0(2)	2.0(2)	2.0(2)	1.4(3)	1.4(3)	1.4(3)	
K(4)	2.3(6)	2.6(4)	2.6(4)	–0.4(4)			

As structural instability and phase separation are frequent harbingers of an incipient insulator–metal transition,[30] the potassium ordering observed in K_5/K_{12}-A may be electronically as well as structurally driven. Electron spin resonance,[15] nuclear magnetic

resonance,[17] and preliminary magnetic susceptibility measurements already demonstrate the importance of antiferromagnetic ordering, with few (<1%) unpaired electron spins contributing to the observed paramagnetism.

Acknowledgements

This work was done in collaboration with Dr. P.A. Anderson (Cambridge) and Professor P.P. Edwards (Birmingham). We would like to thank the SERC for provision of neutron beam facilities. The structure diagrams were drawn using ATOMS by Shape Software.

References

1) R.M. Barrer, *Hydrothermal Chemistry of Zeolites* (Academic Press, London, 1982).
2) J.A. Rabo, C.L. Angell, P.H. Kasai, and V. Schomaker, *Discuss. Faraday Soc.*, **41**, 328-349 (1966).
3) M.R. Harrison, P.P. Edwards, J. Klinowski, D.C. Johnson, and C.J. Page, *J. Solid State Chem.*, **54**, 330-341 (1984).
4) U. Westphal and G. Geismar, *Z. anorg. allg. Chem.*, **508**, 165-175 (1984).
5) L.R.M. Martens, P.J. Grobet, and P.A. Jacobs, *Nature*, **315**, 568-570 (1985).
6) K.W. Blazey, K.A. Müller, F. Blatter, and E. Schumacher, *Europhys. Lett.*, **4**, 857-861 (1987).
7) Y. Katayama, K. Maruyama, and H. Endo, *J. non-cryst Solids*, **117**, 485-488 (1990).
8) P.A. Anderson, R.J. Singer, and P.P. Edwards, *J. chem. Soc. Chem. Commun.*, **1991**, 914-915.
9) P.A. Anderson and P.P. Edwards, *J. chem. Soc. Chem. Commun.*, **1991**, 915-917.
10) B. Xu and L. Kevan, *J. chem. Soc. Faraday Trans.*,. **87**, 2843–2847 (1991).
11) P.A. Anderson, D. Barr, and P.P. Edwards, *Angew. Chem.* **103**, 1511–1512 (1991); *Angew. Chem. Int. Ed. Engl.* **30**, 1501–1502 (1991).
12) F. Blatter, K.W. Blazey, and A.M. Portis, *Phys. Rev. B*, **44**, 2800-2802 (1991).
13) B. Xu and L. Kevan, *J. chem. Soc. Faraday Trans.*, **88**, 1695-1699 (1992).
14) Y. Nozue, T. Kodaira, and T. Goto, *Phys. Rev. Lett.*, **68**, 3789-3791, (1992).
15) P.A. Anderson and P.P. Edwards, *J. Am. chem. Soc.*, **114**, 10608-10618 (1992).
16) T. Sun, K. Seff, N.H. Heo, and V.P. Petranovskii, *Science*, **259**, 495-497, (1993).
17) G. Schäfer, W.W. Warren, P.A. Anderson, and P.P. Edwards, *J. non-cryst Solids*, (in the press).
18) J.C. Matthewman, P. Thompson, and P.J. Brown, *J. Appl. Crystallogr.*, **15**, 167 (1982).
19) P.J. Brown and J.C. Matthewman, Rutherford Appleton Laboratory Report, RAL-87-010 (1987).

20) R.M. Barrer, and H. Villiger, *Z. Kristallogr., Kristallgeom., Kristallphys., Kristallchem.*, **128**, 352 (1969).

21) J.M. Newsam, *J. Phys. Chem.*, **93**, 7689 (1989).

22) J.M. Newsam, *Mat. Res. Bull.*, **21**, 661 (1986).

23) P.C.W. Leung, K.B. Kunz, K. Seff, and I.E. Maxwell, *J. Phys. Chem.*, **79**, 2157-2162 (1975).

24) J.J. Pluth and J.V. Smith, *J. Phys. Chem.*, **83**, 741-749 (1979).

25) V. Gramlich and W.M. Meier, *Z. Kristallogr.*, **133**, 134-149 (1971).

26) R.C. McMillan, *J. Phys. Chem. Solids*, **25**, 773-775 (1964).

27) N.N. Greenwood and A. Earnshaw, *Chemistry of the Elements* , (Pergamon Press, Oxford, 1984).

28) I.D. Brown, *Chem. Soc. Rev.*, **7**, 359-376 (1978).

29) I.D. Brown and D. Altermatt, *Acta Cryst. B*, **41**, 244-247 (1985).

30) P.P Edwards and M.J. Sienko, *Int. Rev. Phys. Chem.*, **3**, 83-137 (1983).

Electron Microscopy of Epitaxial Structures

N A Kiselev

Institute of Crystallography, Russian Academy of Sciences, 59 Leninsky pr., Moscow 117333, Russia.

ABSTRACT: This paper describes recent applications of SEM and HREM to the studies of epitaxial structures, carried out at the Institute of Crystallography, Russian Academy of Sciences: semiconductor epitaxial layers and interfaces, high-Tc superconductor epitaxial layers on different substrates, edge-type Josephson junctions with PrBaCuO barrier layers, nanometric tips, prepared from epitaxially grown silicon whiskers using the one-stage and the two-stage techniques.

1. INTRODUCTION

The effect of epitaxy, when oriented over-growth of one crystal on another occurs, is widely used in modern technology. HREM of epitaxial layers and interfaces is closely related to the development of semiconducting and superconducting material technology. The silicon tips are used for field-emission studies as well as a new tool for nanostructural physics and technology. SEM and HREM are playing an important part in this development.

2. EPITAXIAL LAYERS AND INTERFACES

The following epitaxial structures are being investigated at the Institute of Crystallography in collaboration with the Institute of Semiconductor Physics (Novosibirsk) and the Physical Technological Institute (Moscow) of the RAS: InAs/(001)GaAs (Karasev et al 1991), CaF_2/(001)Si (A Kiselev et al 1993), $TiSi_2$/(111)Si and (100)Si (Vasiliev et al 1991) and some others. Studies were carried out on a Philips EM 430 ST at 200 kV and 300 kV. Cross-sectional and plan-view specimens were used. The cross-sectional specimens were prepared by cutting out two bars and glueing them together "face-to-face". After mechanical treatment, grinding and polishing to about 30μm thickness the specimens were ion thinned by Ar^+ ions with 3-5 keV energy at 8-10° angles relative to the specimen surface until holes began to appear in them. A wedge shaped part of the specimens near the hole (thickness 3-20 nm) "transparent" for electrons was investigated.

InAs/(001)GaAs is an example of an interface with similar structure and large lattice mismatch (7%). Two types of MBE grown InAs/(001)GaAs specimens were investigated: strained layer superlattices (SLS) and specimens with varying InAs layer thickness (0.6-0.9 nm for the first layer; 1.2 nm for the second and the third one; 1.8 nm for the fourth and the fifth layers and 10 nm for the sixth one).

Cross-sectional (110) images of SLS and the first InAs layer of the heterosystem show that the interface is coherent, i.e. does not contain MDs. Thus, pseudomorphic layers are observed. The lattice mismatch is compensated by distortions of the layers lattice: it is extended in the growth direction and compressed in the (001) plane, resulting in a relative rotation of the InAs and GaAs ({111} plane by a kink angle $\psi_k\{111\}=3°$.

There are two ways to minimize the system energy, the strain energy included. The first is the elastic strain relaxation with creation of MDs, keeping the surface energy constant.

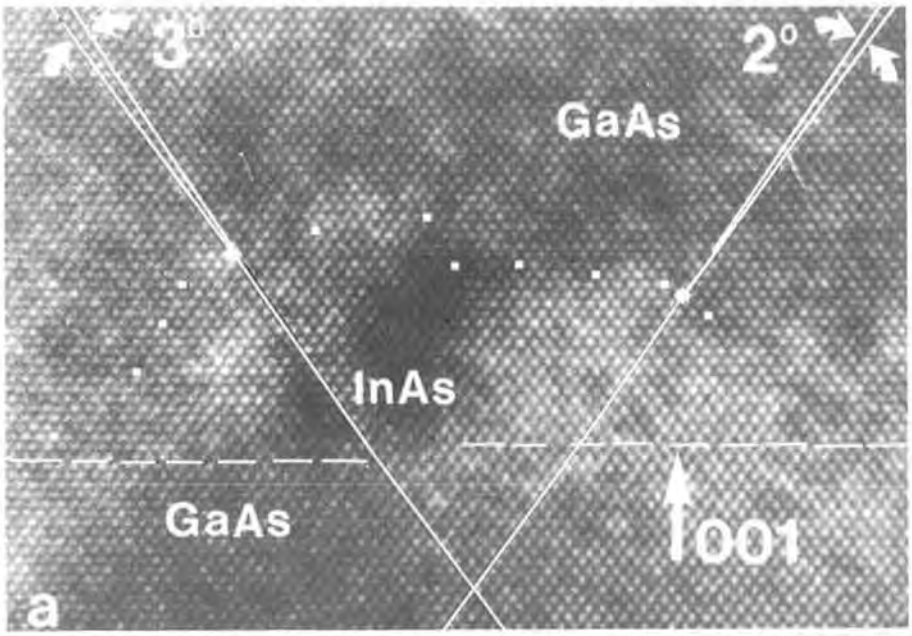

Fig. 1 Cross sectional (110) HREM images (300 kV) of an InAs/(001) GaAs interface. In island (a) the lattice mismatch is compensated by InAs lattice distortion, in (b) MD halfplanes are arrowed.

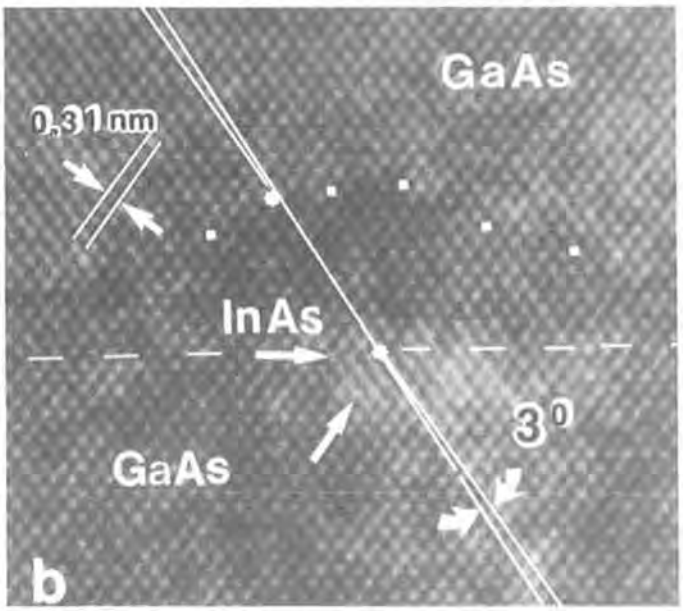

Fig. 2 Cross sectional (110) digitally filtered image of $TiSi_2$/Si(111) interface. Extra planes in $TiSi_2$ and distorted layer are arrowed.

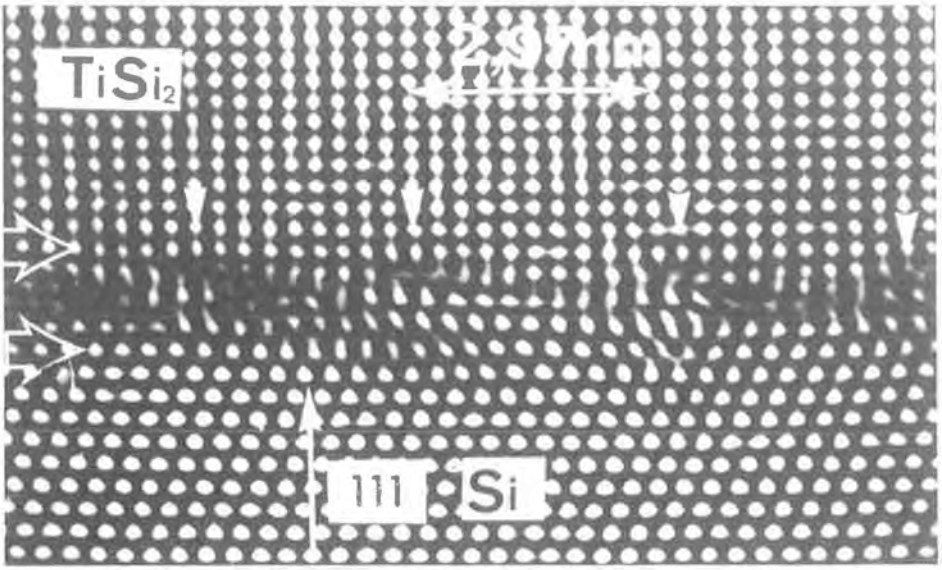

The second is collapse of the film into islands in order to minimise the surface energy. These two mechanisms may operate simultaneously.

At h>0.9 nm (second layer) the heteroepitaxial strain is relaxed by MDs generation and the initially continuous layer is transformed into an island one. Small islands are visible at the interface. One of the islands (Fig. 1a) is free from dislocations. The lattice mismatch is compensated by very small distortion of the island lattice. On the other island (Fig. 1b) extra half-planes in the (1$\bar{1}$1) and (001) families are arrowed. Most probably this is a 60° dislocation with the Burgers vector bo=1/2 a[110]. In the left part of the island {111} atomic plane kink is observed. So in this island the InAs/GaAs lattice mismatch is accommodated partly by lattice deformations and partly by single dislocation. The fifth layer of the specimen demonstrates an increase of the island dimensions as well as the number of 60° dislocations on the upper and lower interfaces.

At h=10 nm (sixth layer) the islands coalesce, the layer is continuous and contains a quasi-periodic MD network at the interface. Two dislocation types are observed: Lomer dislocations and two closely situated 60° dislocations. The presence of two dislocation types gives evidence that Lomer dislocations in the InAs/GaAs system are formed as the result of two 60° dislocation interaction.

Titanium disilicide films are used in electron device technology. The $TiSi_2$ film has an orthorhombic lattice and may give large mismatch with the Si substrate. $TiSi_2$/Si is a reactive solid/solid interface. The $TiSi_2$/Si system was investigated by HREM (see for example, Catana et al 1990). It was shown that (101) $TiSi_2$ is a preferential plane for epitaxial growth on Si (111).

Vasiliev et al (1991) used electron-beam evaporation from Ti and Si targets onto a heated substrate. Polycrystalline film was obtained with the following epitaxial relations (202)$TiSi_2$//(111)Si, [010]$TiSi_2$//[110]Si, which are the same as described by Catana et al (1990). In cross-sectional micrographs of $TiSi_2$/Si(111) contrast variations with a mean spacing of 2.8-3 nm caused by elastic strain were observed along the interface.

Superposition of "surface lattices" of (111)Si and (101)$TiSi_2$ ([010]$TiSi_2$//[110]Si) shows that in (110) cross-sections the mismatch along the interface is 11.9%. In cross-sectional micrographs (Fig. 2) it is possible to observe regions, where a few (202)-$TiSi_2$ and (111)Si planes fit rather well. These regions are separated by 9 or 10 (202)$TiSi_2$ planes and by wedge-shaped defects formed by extra planes in $TiSi_2$. Near the wedge-shaped defects the lattice in $TiSi_2$ is distorted. This distortion most probably is the nature of periodic strain observed along the interface. Sometimes inclined lattice planes are visible. All this gives evidence that the misfit compensation at this interface is complex.

3. MICROSTRUCTURE OF EDGE-TYPE JOSEPHSON JUNCTIONS (EJJ)

In collaboration with the Institute of Applied Physics, RAS YBCO films, obtained by laser ablation on different substrates were investigated (Vasiliev et al 1990). It was shown that films on $SrTiO_3$ (100) are single crystals. For such films, the c-axis is oriented normal to the interface and the critical current density (Jc) reaches 7.5×10^6 A/cm^2.

The lattice mismatch for YBa2Cu3O7-x (orthorhombic phase)/SrTiO3 at room temperature in different directions is: fa=2.07%; fb=0.33% and fc/3=0.07%. The system could be related to materials with different structure and small mismatch. At the deposition temperature fc/3>fab. This is one of the possible explanations, why the c-axis is oriented normal to the interface.

An EJJ with PrBa2Cu3O7-x barrier layer is schematically shown in Fig. 3a (Lebedev et al 1992): Y1 is the YBCO superconducting layer, PI is the PrBa2Cu3O7-x insulating layer, PB is the PrBa2Cu3O7-x barrier layer and Y2 is the YBCO superconducting layer. All layers were obtained by laser ablation on a SrTiO3 substrate. So the EJJ is a multilayered system of epitaxially grown superconducting and non-superconducting, i.e. insulating, films, properties of which are strongly dependent on stoichiometry, deposition conditions and state of the underlying film.

The structure was formed in two stages. In the first stage Y1 and PI layers were deposited in one vacuum cycle. Either a PrBa2Cu3O7-x or a non-superconducting YBa2Cu3O7-x layer, deposited at 500°C temperature served as an insulator. The edges were formed by ion sputtering (Ar^+, 2 KeV) using a photoresist mask. After removal of the

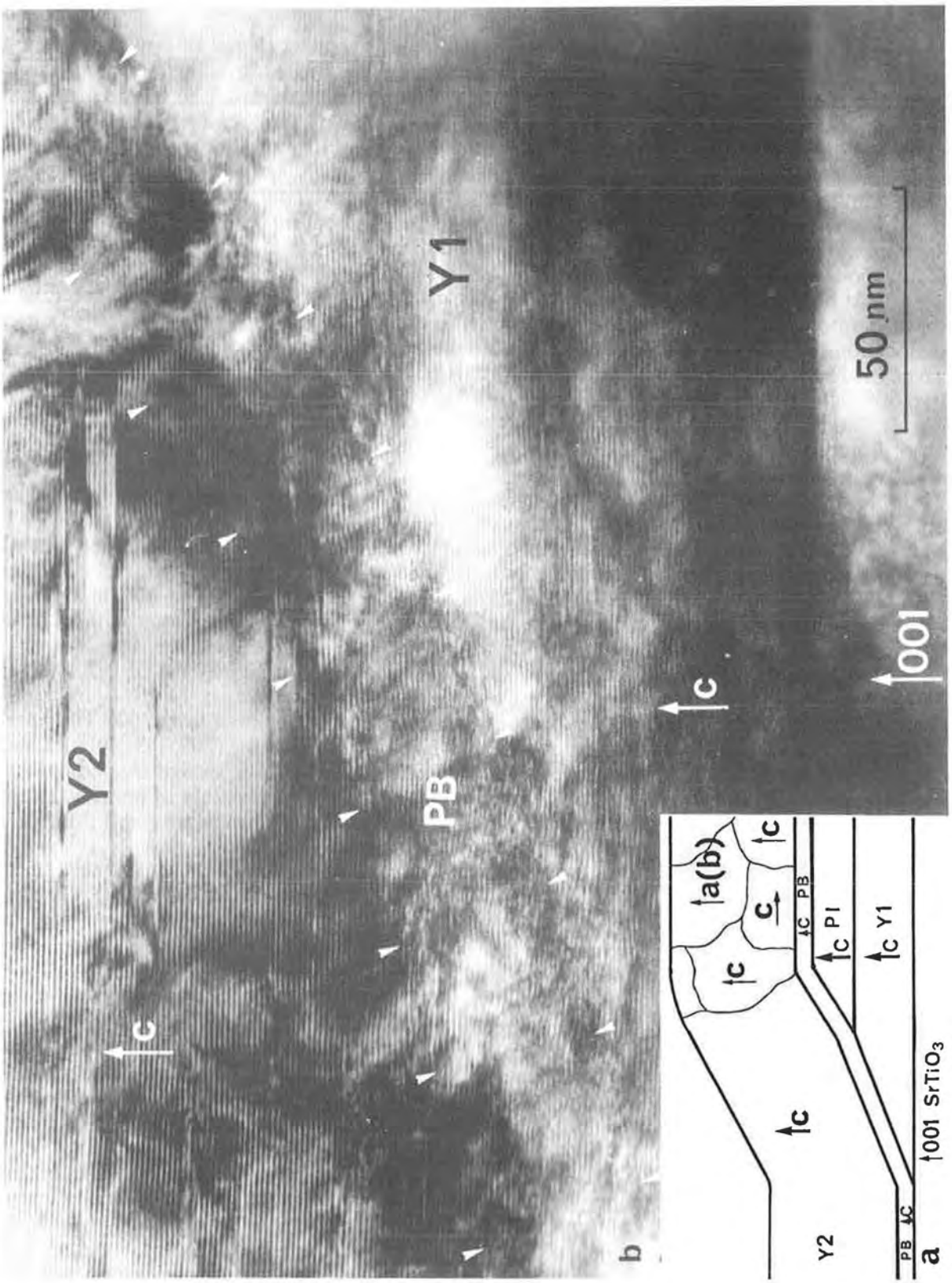

Fig. 3 Scheme of Edge-type Josephson junction (a) and cross sectional image (200 kV) (b). Y1 and Y2 - superconducting layers; P1 - insulating layer; PB - barrier layer.

photoresist the specimens were ultraviolet treated for restoring the edge surface properties. After that, the 20-25 nm thick barrier layer and the Y2 were deposited. EJJ demonstrates Josephson conductivity at Tc=77K, giving Jc-10^4 A/cm^2 at characteristic voltage Uc~50μV.

Cross-sectional low magnification image of the EJJ is shown in Fig. 3b. Y1, PI and PB films are single crystalline with the c-axis normal to the substrate surface. In the right hand side region the terminating Y2 layer is polycrystalline (the grain c-axis may be normal or parallel to the interface). The reason for this may be an insufficiently flat PB surface or its contamination after the lithography process. The PB/Y1 interface in the region of the edge contact is inclined by 20-35° to the substrate. The PB layer thickness in this region is 20-25 nm. Lattice resolution images reveal epitaxial growth of both the PB and Y2 films. On the Y1/PB interface the APBs-like boundaries are observed. The Y2 film in the edge contact region is characterised by a high APB concentration and by CuO double layers.

It could be mentioned that another way to make EJJ is to use artificial grain boundary (GB). Dimos et al (1990) fabricated artificial GB weak links by depositing YBCO epitaxial films on $SrTiO_3$ bicrystal substrates. The GB between the two crystals of different orientations was inherited by the overgrown film and a weak link was formed. Ivanov et al (1991) showed that the weak link properties, such as Jc and normal state resistance (Rn) depend on the misorientation angle (θ) between the two halves of the bicrystal Y-ZrO_2 substrate. Bicrystals of Y-ZrO_2 were made at the Institute of Crystallography by means of solid phase intergrowth (Stepantsov, 1984). Single crystals were cut and polished to obtain flat surfaces with desired orientations accurate to 10'. A pair of single crystals aligned along the oriented surfaces was annealed well below the melting point under pressure applied normal to the conjugated surfaces in high vacuum. The 5 x 5 x 0.5 mm bicrystals were used as the (001) substrate and the c-orineted films were grown by laser deposition. It was shown that good magnetic field response above 77K could be achieved for SQUIDS fabricated on bicrystals with certain misorientation angle (θ) between two halves of the bicrystal. The best results were obtained for a SQUID on a substrate with θ=32°. The observed Jc(θ) dependence shows that the transport properties of the weak links could be related to the intrinsic characteristics of the artificial nonsymmetric grain boundaries (Ivanov et al 1991).

4. NANOMETRIC Si TIPS

The most important part of the Scanning Tunnelling Microscope (STM) and all Scanning Probe Devices (SPDs) is an ultra sharp tip. For SPDs not only the very end, but also the general shape of the tip is very important. Thus, for profilometry a specially shaped tip with relatively thick body (necessary for higher vibration stability) and a very thin end with a small curvature radius is extremely desirable. Sharp silicon microtips have potential application as field emitters and as electrical or mechanical microsensors.

The whiskers were prepared by the vapor-liquid-solid (VLS) technique (Wagner and Ellis 1964). Small islands of gold were deposited onto a (111) Si wafer as a substrate. According to the phase diagram of these two elements, they can form a low-melting point (about 360°C) eutectic. At the temperature of 800-900°C, a droplet of the Si-Au alloy is formed on the substrate. In the presence of a gaseous mixture $SiCl_4 + 2H_2 \rightarrow Si + 4HCl$ above the substrate silicon is absorbed by the droplet, the Si-Au solution becomes supersaturated in respect to Si, and the excess Si is deposited on the solid-liquid interface (Fig. 4a). As a result, the liquid droplet is pushed out from the original substrate, remaining on the tip of the growing crystal (Fig. 4b). Gold droplets may be obtained by heating gold films evaporated onto the substrate, by deposition through a mask, or with the help of photolitigraphy.

Whiskers were treated in a solution of $HF:HNO_3:H_2O$ (1:40:1), which selectively etched the interface between the Si whiskers and the Si-Au "cap" (Thomas et al 1972, 1974) (Fig. 4c). After that the tips were additionally sharpened by oxidation with subsequent etching (Marcus et al 1990) (Fig. 4d).

Narrow tips are desirable for investigating trenches with perpendicular walls. The tips length should be at least 2 μm and the diameter as small as 100 nm. When a normal etching procedure is used the probes thus obtained are very sensitive to vibration. The two-stage VLS whisker growing process solves this problem to some extent. First, a relatively

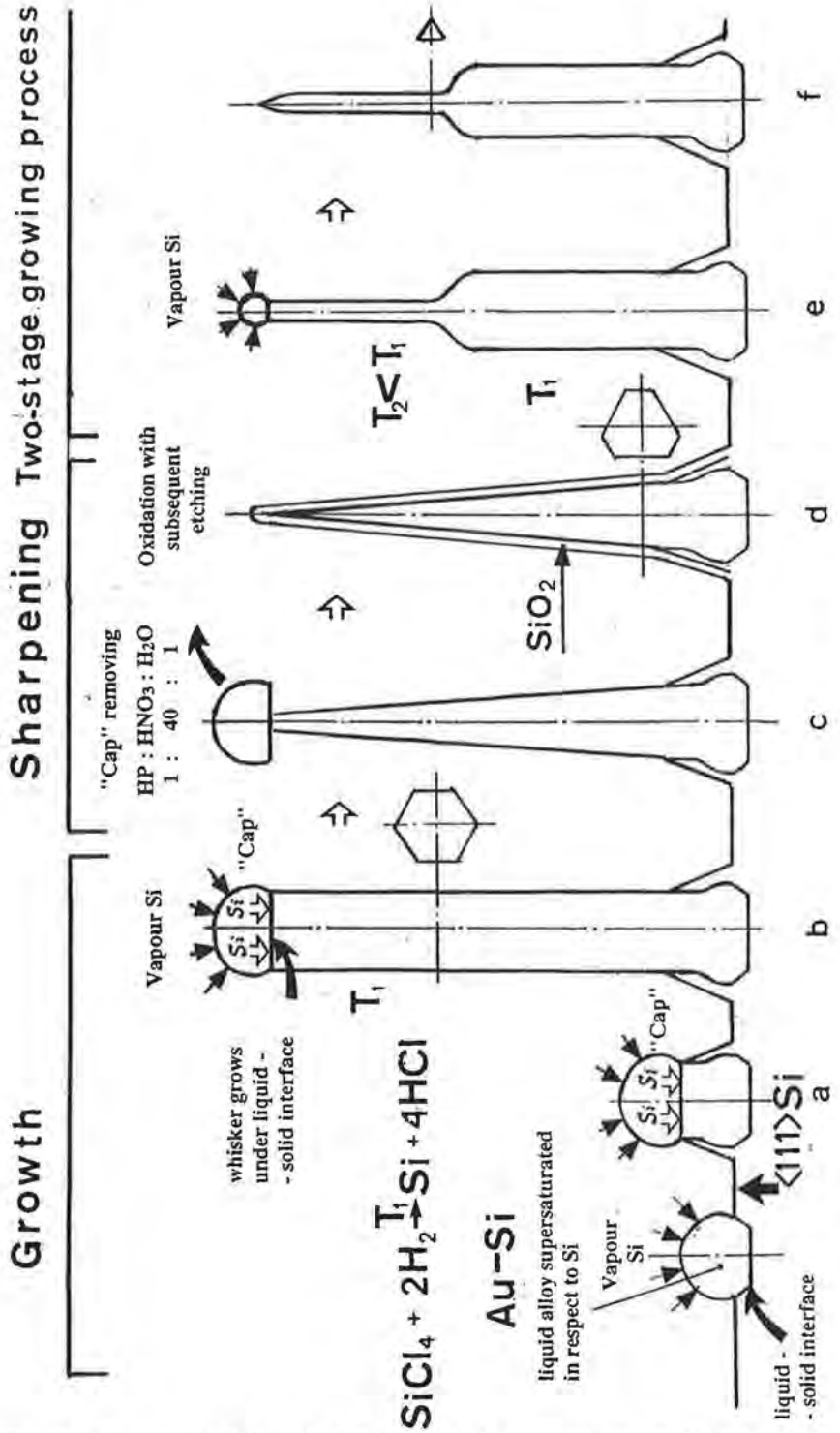

Fig. 4 Schematic representation of nanometric tip preparation from whiskers epitaxially grown on (111) using VLS techniques.

(a) Si absorption in the Si-Au alloy droplet. Excess of the Si is deposited on the solid-liquid interface. Droplet rises to the tip of the growing crystal (Wagner and Ellis 1964).
(b) Whisker grows under the liquid-solid interface.
(c) "Cap" removal (Thomas et al 1972, 1974).
(d) Oxidation with subsequent etching (Markus et al 1990).
(e) Two-stage growing process. The thin upper part is formed by lowering the growth temperature.
(f) "Cap" removal and sharpening (see Givargizov et al 1993).

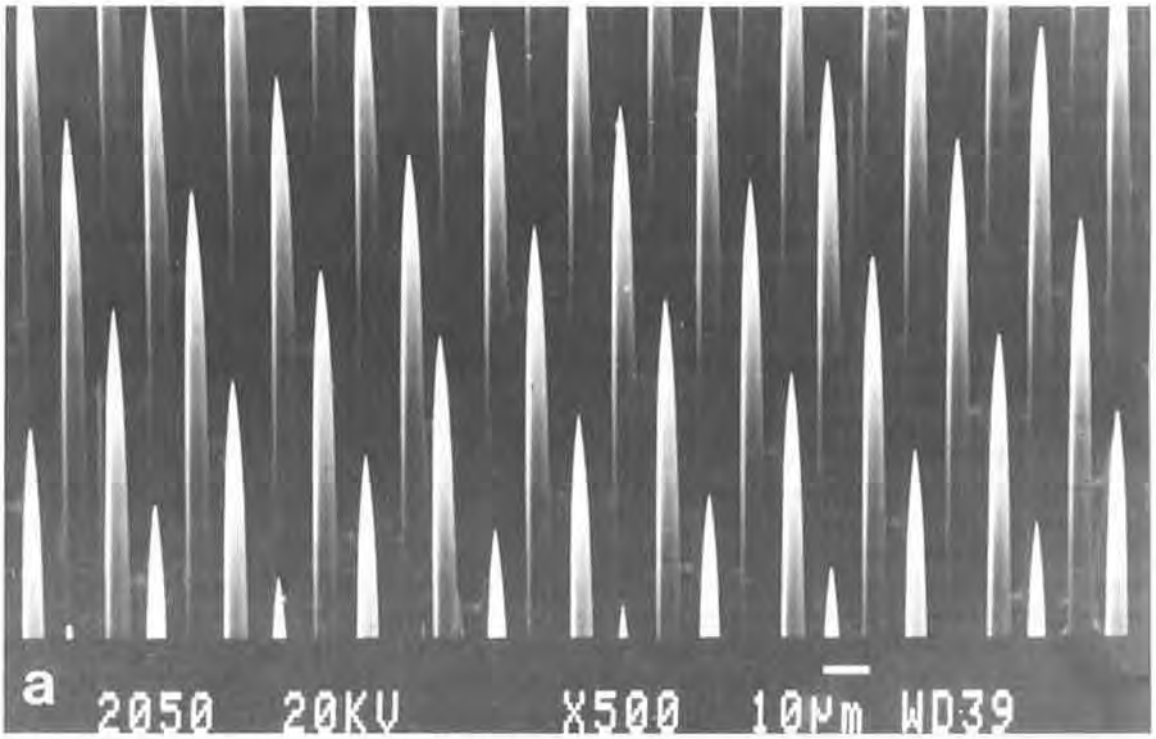

Fig. 5 SEM images of the Si tips obtained by one-stage (a) and by two-stage (b) growing processes.

Fig. 6 Schematic representation of the tips geometry: (a) One-stage process; (b) Two-stage process.

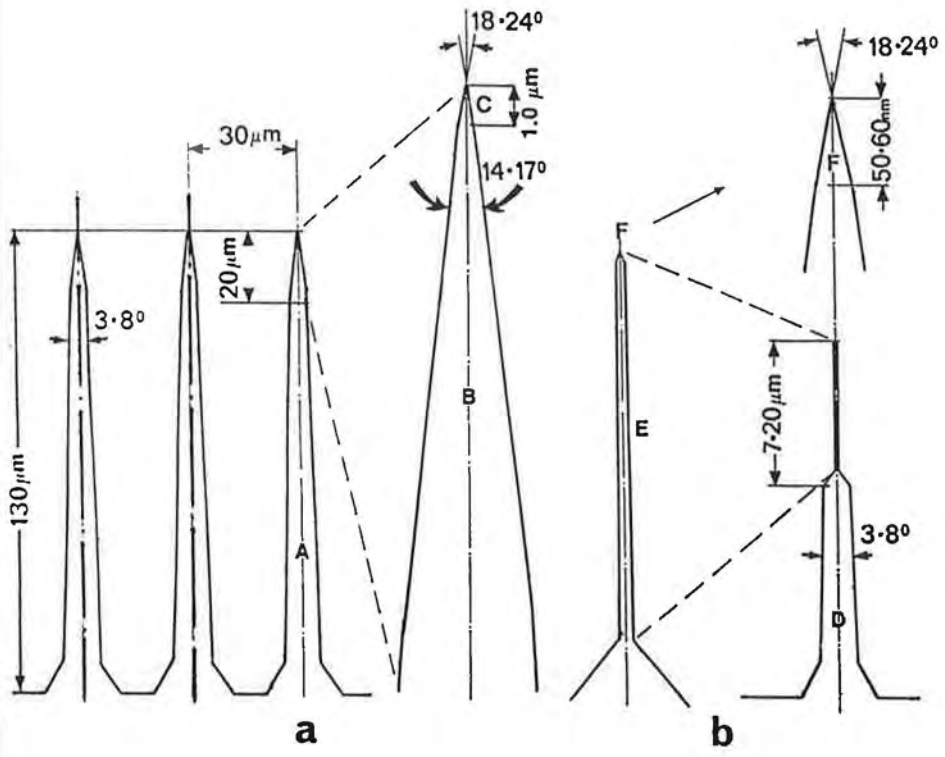

thick basis is grown and then, by lowering the growth temperature, the thin upper part is formed (Givargizov et al 1993) (Fig. 4e,f).

All stages of whiskers growth were studied in JEOL JSM-840 instrument in the secondary electron mode at 20 kV. Fig. 5a is an SEM image of the Si-tips forming a square lattice with a spacing between tips of 30 μm. Tips are very uniform in height (130 μm). Such a lattice of tips is covering an area 15 mm in diameter. This kind of specimen was prepared for field-emission studies (Kiselev, Vasiliev et al 1993).

Specially prepared plate-like substrates 0.23 x 2 x 10 mm in size were used to investigate the tips in orientation, optimal for HREM. The substrates were oriented using X-ray diffraction techniques. "Wide" substrate sides corresponded to (110)-Si, and the "butt-ends" to ($\bar{1}11$)Si. After the whisker growth and the necessary sharpening treatment, the specimens were glued onto supporting rings with the "butt-end" approximately in the center of the ring (Givargizov et al 1993).

Specimens were examined in a Philips EM-430 ST microscope at 200 kV, and a JEOL JEM 4000 EX at 390 kV. The lattice image in JEM 4000 EX was obtained, using the central beam, and all diffracted beams out to 0.15 nm^{-1}. Two-beam diffraction contrast images (g=111) were also obtained.

The geometry of the tips is schematically shown in Fig. 6. SEM can give information concerning region (A) and partially (B). TEM and HREM are most effective for investigations of the upper part of (B) and the end of the tips (C).

Two-beam diffraction contrast imaging of region C (Fig. 6a) usually revealed a striped structure, formed from alternation dark and bright bands, parallel to the tip sides. These bands represent equal thickness fringes, caused by dynamic diffraction effects (revealing electron extinction distances). The orientation of these bands indicate that the tips must be triangular in cross-section, with truncated corners. In the ideal case, when one side of the triangle is precisely parallel to the electron beam, no fringes must be seen at one of the sides. In reality, despite precise [110] orientation, one can see fringes on the left side of the tip as well. This phenomenon can be explained by step-like surfaces of the tip. The truncated triangle, enveloping the surface of the tip, is slightly rotated (Givargizov et al 1993).

HREM lattice image of the tip (C region) is shown in Fig. 8. In etched silicon six {111} planes are the most stable ones. Judging from HREM data in the case of tips there are two combinations of three {111} planes (two types of etching modes): (i) main stable grains are ($11\bar{1}$), ($\bar{1}\bar{1}\bar{1}$) and ($1\bar{1}1$) and (ii) ($\bar{1}1\bar{1}$), ($\bar{1}\bar{1}1$) and (111). The tips cone angles are 14-17° (B region) and 18-24° (C region). The extreme end of the tip (Fig. 7) is usually formed by a few atomic columns, viewed along <110>; the lattice image in this direction is an image of pairs of atomic columns. The very end of the tip can be thus considered as "atomically sharp".

The triangular cross-section of the tips is also confirmed by HREM data (Fig. 6b). The image character changes with growing distance from the tip's edge. Some areas demonstrate a "half-spacing contrast", appearing in regions, where the sample thickness is a multiple of the extinction distance of the (000) beam. Areas A', B', C', etc. are typical for wedge-shaped crystals, i.e. triangular in cross-section (Kiselev, Vasiliev et al 1993).

Typical SEM image of nanometric tip, obtained using the two-stage growing process with consequent sharpening, is shown in Fig. 5b. The diameter of the thin part (E, Fig. 5) of most tips is 10-25 times smaller than that of the base (D). The length of the tips' thin part (E) is 7-20 μm (Givargizov et al 1993, Kiselev, Vasiliev et al 1993).

On TEM micrographs it is possible to see that part E of the tips is becoming narrower towards the end of the tip. The angle which forms the edge profile of the tip with <111> growing direction is 2-3°. The diameter of the tips in this region is 50-100 nm. From HREM images a conclusion can be made that faceting of the tips is along (111) and slightly pronounced. Thus, at low magnification the tips look very smooth.

Sharp end (F, Fig. 6) cone angles are 18-24°, which means they are the same as for the tips grown by the one-stage process (B and C, Fig. 6). But the length of F region is only 50-60 nm, while the whole thin part (E) with small (2-3°) cone angle is usually one or two orders larger. The end of the tip is usually atomically sharp.

As it is observed on the HREM images (Fig. 8), the tip is covered by a thin (~ 2 nm thick) film of an amorphous material, most probably Si02. Many applications of the tips are

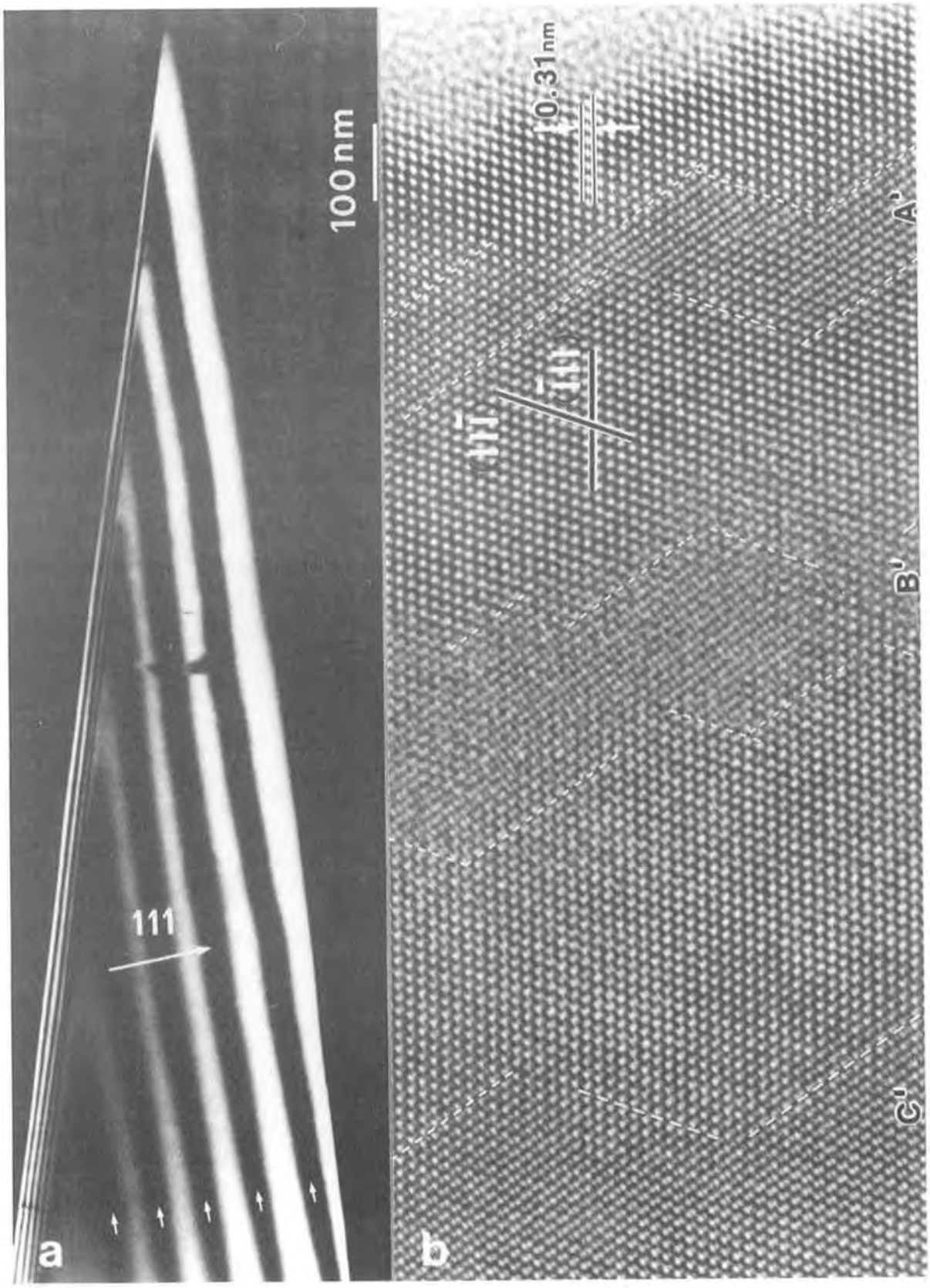

Fig. 7 Si tips (one stage process): (a) Two-beam diffraction contrast image. Equal thickness fringes are arrowed; (b) HREM image (390 kV) of tip's edge. Areas of half-spacing contrast are marked A', B', C'.

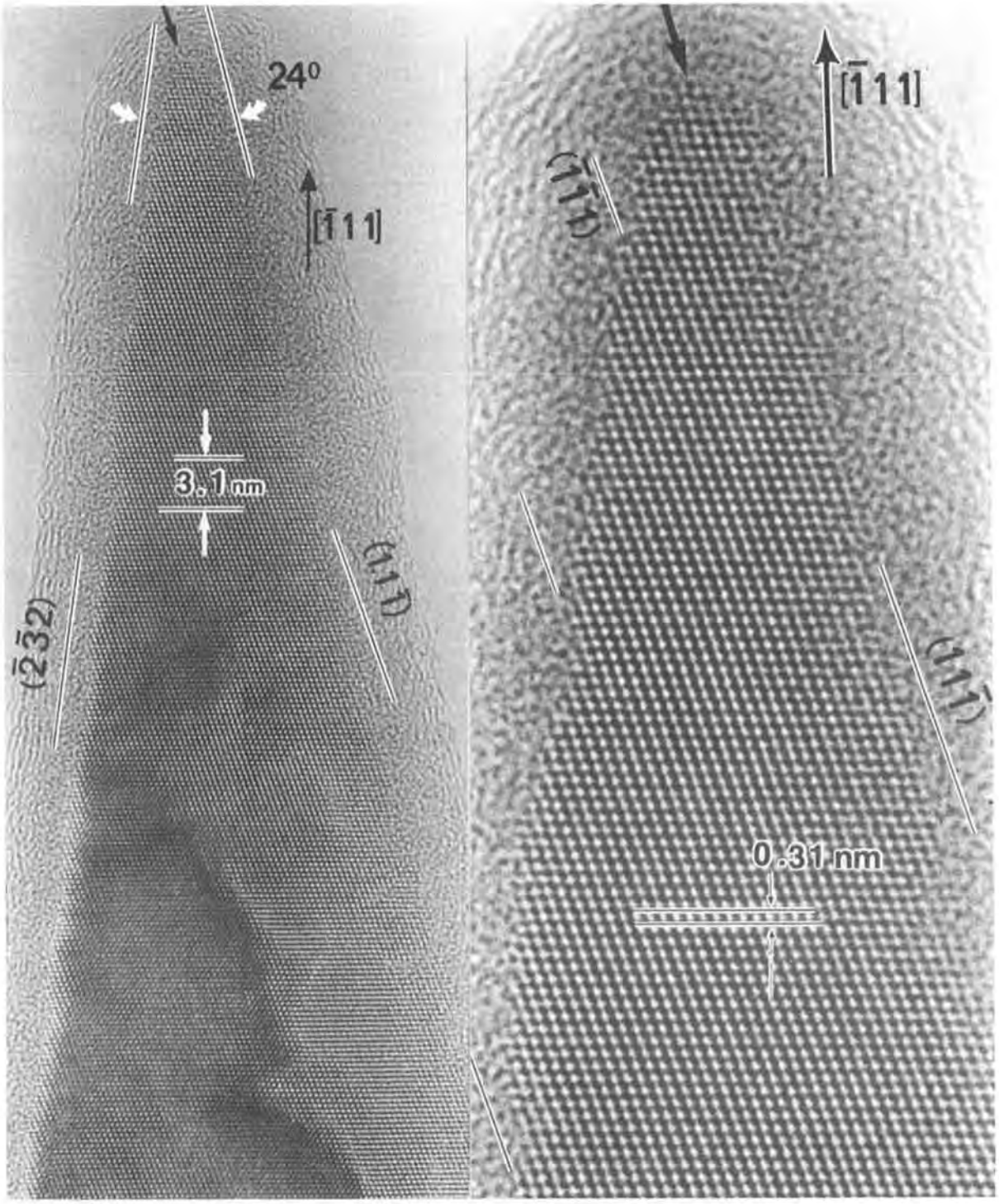

Fig. 8 HREM image (390 kV) of the Si tip (one stage process). Main stable grains are $(\bar{1}1\bar{1})$.$(\bar{1}\bar{1}1)$ and (111). Thin part of the tip is faceted by $(11\bar{1})$ planes (truncated vertex).

carried out in high vacuum, allowing one to remove this oxide layer. Another possibility would be carbidization of the tip directly in the growth chamber.

ACKNOWLEDGEMENTS

Discussions with Dr J L Hutchison (Department of Materials, University of Oxford), Professor E I Givargizov, A N Kiselev, O I Lebedev, Dr A N Stepanova, Dr E A Stepantsov and Dr A L Vasiliev are gratefully acknowledged. The author expresses his thanks to V Yu Karasev for micrographs of InAs islands and to L.N. Obolenskaya for tips preparation.

REFERENCES

Catana A, Schmid P E, Heintze M, Stadelman P and Bonnet R 1990 J. Appl. Phys. 67 1820-5
Dimos D, Chaudhari P, and Mannhart J 1990 Phys. Rev. B. 41 4038
Givargizov E I, Kiselev A N, Obolenskaya L N and Stepanova A N 1993 Appl. Surf. Sci. accepted for publication
Ivanov Z G, Nilsson P A, Winkler D, Alarco J A, Clarson T, Stepantsov E A and Tzalenchuk A Ya 1991 Supercond. Sci. Technol. 4 439
Karasev V Ju, Kiselev N A, Orlova E V, Gribelyuk M A, Gutakovsky A K, Kanter Yu O, Pintus S M, Rubanov S V, Stenin S I and Fedorov A A 1991 Ultramicroscopy 35 11
Kiselev A N, Velichko A A and Okomelchenko I A 1993 J. Cryst. Growth 129 163
Kiselev N A, Vasiliev A L, Lebedev O I, Givargizov E I, Stepanova A N, Kiselev A N and Hutchison J L 1993 Inst. Phys. Conf. (in press)
Lebedev O I, Vasiliev A L, Kiselev N A, Maso L A, Gaponov S V, Paveliev D G and Strikovsky M D 1992 Physica C. 198 278
Marcus R B, Ravsi T S, Gmittes T, Chin K, Liu D, Orvis W J, Ciasio D R, Hunt C E and Trujillo J 1990 Appl. Phys. Lett. 56 236
Stepantzov E A 1984 A.S.N. 1116100 Bulleten Izobreteniy Moscow N 3677
Thomas R N and Nathanson H C 1972 Appl. Phys. Lett. 21 384
Thomas R N, Wickstron R A, Shroder D K and Nathanson H C 1974 Appl. Phys. Lett. 17 155
Vasiliev A L, Kiselev N A, Dovidenco A M, Gaponov S V and Kalyagin M A 1990 Superconductivity 3 N4 557 (in Russian)
Vasiliev A L, Kiselev N A, Lebedev O I, Orlova E V and Orlikovsky A A 1991 Inst. Phys. Conf. Ser. No 117 297
Wagner R S and Ellis W C 1964 Appl. Phys. Lett. 4 89

Disorder in silver and copper halides

D A Keen,
ISIS Science Division, Rutherford Appleton Laboratory, Chilton, Didcot, OXON OX11 0QX, U.K.

The development of ionic disorder with increasing temperature has been investigated in AgI, AgBr, CuI and CuBr. Careful analysis of powder neutron diffraction data yields the disordering processes which give rise to ionic conduction in these materials. This paper summarises results and shows that, for disordered systems, modelling powder data can be as revealing as results from experimentally more difficult single crystal diffraction.

1. Introduction

Silver(I) and copper(I) halides have been widely studied because they form a group of compounds which show high ionic conductivity at elevated temperatures [Boyce and Huberman (1979)]. In some of these materials the ionic conductivity attains values below the melting point which are more typically found in molten salts (~$1\Omega^{-1}cm^{-1}$). This behaviour arises from the smaller cation migrating through the voids in the larger anion sublattice. Furthermore most of these compounds possess the diamond zinc-blende structure at ambient temperatures and pressures and form the end group of the class of tetrahedrally co-ordinated semi-conductors. The bonding is purely covalent in the case of group IV elements and is increasingly ionic as one goes through the III-V and II-VI to the I-VII compounds [Rapoport and Pistorius (1968)]. However copper and silver halides are still not purely ionic, for example CuI has an ionicity of f_i=0.692 on the Phillips scale [Phillips (1970)], close to the boundary between ionic and covalent crystals, and it is believed that the polarizability of the ions, as well as the small size of the cation, encourages fast-ion conduction.

Their borderline ionicity also induces complex phase diagrams, with many different structural phase transitions between room temperature and melting. These are summarised in Figure 1 (for the complete p-T phase diagrams the reader is referred to Merrill (1977)). γ-CuI has a zinc-blende structure (space group $F\bar{4}3m$) until 643K when it transforms to β-CuI, a disordered hexagonal structure ($P\bar{3}m$) based on

wurtzite, but different cation occupation of the tetrahedral viods in the anion sublattice gives the different symmetry assignment. Above 661K CuI exists as the α-phase, another face-centred cubic structure, only with cations disordered over all the available tetrahedral viods and $Fm\bar{3}m$ symmetry. AgI and CuBr have very similar structural phase transitions. Both possess the (γ) zinc-blende structure at room temperature and pressure. In AgI this phase coexists with β-AgI, a wurtzite structure and in CuBr a disordered wurtzite phase forms above T=658K. Both subsequently transform to an α-phase (at 420K for AgI and 742K for CuBr) which has a body-centred cubic arrangement of anions ($Im\bar{3}m$) and the cations distributed between the available tetrahedral 12(d) sites. The exception, AgBr, retains a rocksalt structure between room temperature and its melting point (T_M=701K) with octahedral co-ordination between distinct ions.

Figure 1. Schematic representation of the structural phase transitions in silver and copper halides at elevated temperatures.

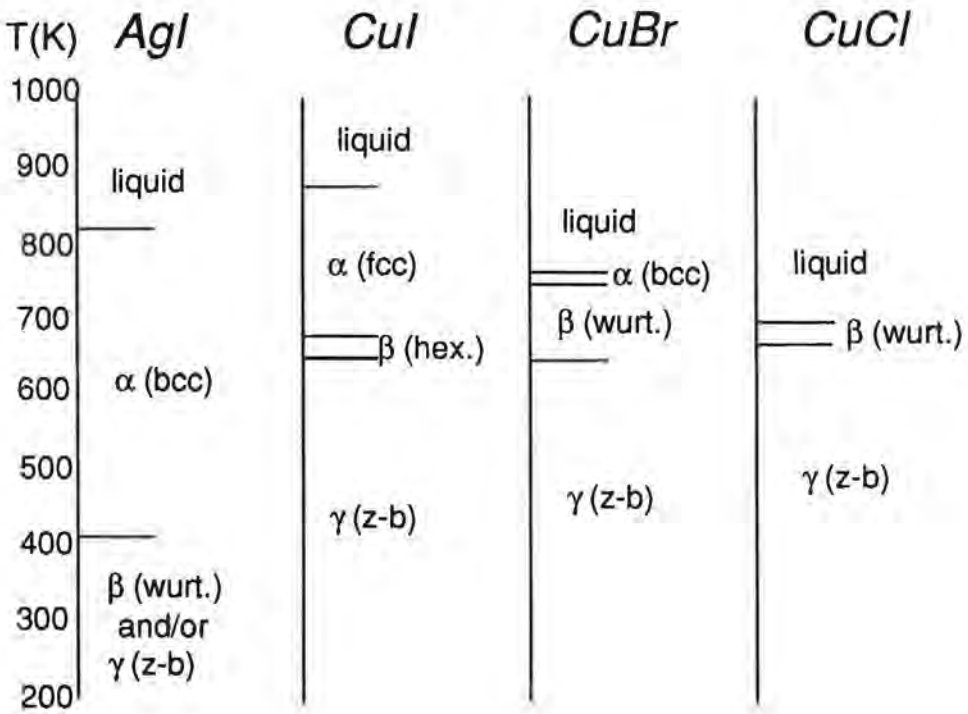

The ionic conductivity changes dramatically between different phases; at the first-order β/γ→α transition in AgI, σ changes by almost four orders of magnitude and large jumps are also observed in CuBr and CuI. However there are also more gradual temperature-induced changes in conductivity, in AgBr the conductivity rises anomolously 150K below T_M, and continues to rise until T_M when $\sigma \sim 1\Omega^{-1}cm^{-1}$. In CuI it is thought that the observed smooth rise in conductivity from well below the γ→β phase boundary actually continues into the α-phase, such that the γ→α transition

can be thought of as second-order, interrupted by the β-phase. This view is supported by specific heat measurements.

To understand the mechanism of ionic conduction in these materials one must have information on the deviations from the equilibrium structure. In standard crystallographic methods of analysis only the (elastic) Bragg scattering is used. This is determined by the time-average structure of the system. If the time-average structure deviates from the instantaneous structure then the intensities of the Bragg peaks decrease at high $\sin\theta/\lambda$ and scattering appears between Bragg peaks. This is (thermal) diffuse scattering. Diffuse scattering may also be produced by static disorder in the structure. As the level of disorder increases with temperature the number of resolvable Bragg peaks decreases and the number of parameters required to reproduce the effects of anharmonicity and anisotropy increases; the problem becomes poorly determined. In any case the elastic scattering, being related to a time average, does not provide information on the instantaneous local atomic correlations (though these may be imposed by the particular model used to fit the data). This information, which is of interest in the study of disorder, is provided by the total, i.e. energy integrated, scattering, that is both Bragg and diffuse scattering.

2. Experimental techniques

The majority of these investigations used neutron diffraction from powdered samples. In order to quantitatively measure the diffuse scattering, careful corrections to the data have been performed. These were similar to those typically performed in a structure factor measurement from a liquid or amorphous material [Mitchell *et al* (1976)], and great care has been taken to accurately subtract sample container and furnace scattering and correct for neutron absorption, multiple scattering and inelasticity. Measurements have been taken at a number of temperatures concentrating around phase boundaries. Diffuse scattering from single crystal samples of AgBr and α-AgI have also been measured in order to assess the reliability of the results obtained from modelling powder diffraction data. To produce a large single crystal of α-AgI the sample was grown from the melt *in-situ* on the diffractometer.

3. Data analysis methods

The technique of reverse Monte Carlo (RMC) modelling [McGreevy and Pusztai (1988)] has been applied to the interpretation of the total scattering. The technique has been described in great detail elsewhere [McGreevy *et al* (1990)]. In brief a Monte Carlo simulation is run, minimising the differences between measured and calculated structure factors. A large atomic configuration is produced (more than 4000 atoms in most cases) which satisfies periodic boundary conditions. The powder structure factor calculated from these configurations is consistent with the corrected experimental diffraction pattern. The RMC modelling technique therefore provides a method of reconstructing three-dimensional information, including short-range correlations, from a one-dimensional powder diffraction pattern. The principle incentive for the technique's development was the desire to understand the atomic arrangements of liquids and amorphous materials, where a three-dimensional measurement is clearly impossible. In order to model a crystalline material successfully using this method, care must be taken in the treatment of Bragg peaks. This is

because Bragg peaks represent long (essentially infinite) range order and therefore cannot be simulated in a finite-sized configuration, the maximum number of atoms being constrained by cpu time considerations. For materials where the structure factor is flat at the highest Q measured this problem can be circumvented by fitting to the radial distribution function (obtained by fourier transform of the structure factor) rather than to the structure factor itself. If the structure factor is not flat at high Q this approach is not applicable since serious truncation errors would be introduced. A more general approach [Nield et al (1992)] is to convolute the experimental data with the transform of a step function m(r) where m(r)=1 when r≤L/2 and m(r)=0 otherwise. L is the configuration box length. This more accurately represents the structure factor function calculated from the atomic configuration. The Bragg peaks become broader, because they now represent a finite range in real space (=L/2), but all the short-range order within the configuration size is retained. From the RMC produced configurations the ion density distribution in an average unit cell can be calculated. These can then be used to investigate the disorder in the material, conduction pathways and disorder across phase transitions.

4. Results and Discussion

This section summarises the temperature dependent behaviour in AgBr and AgI to give a flavour of the results possible using RMC. For a description of the behaviour in the corresponding copper compounds, the reader is referred to Nield *et al* (1993b), Hull & Keen (1993b) and Keen & Hull (1993b).

4.1. Silver Bromide

The diffraction patterns from AgBr have been analysed using RMC at many temperatures between room temperature and the melting point, approaching T_M to within 0.3±0.05K [Keen *et al* (1990a), (1990b) and Nield *et al* (1992)]. The aim of these studies was to investigate possible pre-melting effects, in other words whether the disorder introduced into the lattice could be a precursor of the eventual melting process at T_M. Pertinent results are summarised in Table 1, calculated directly from the RMC configurations. The displacements of Br^- ions are isotropic at all temperatures and increase rapidly as the melting point is approached, the root-mean squared displacement, $\langle u^2 \rangle^{1/2}$ reaching 13% of the lattice spacing at 699K. The Ag^+ ions have a larger $\langle u^2 \rangle$ than the Br^- ions at all temperatures, but the displacements are anisotropic, by far the greatest being in the <111> direction.

The interstitial occupancy is defined to be those Ag^+ ions within a certain radius (0.12a in this case) from the ideal tetrahedral (1/4,1/4,1/4) site. The slightly arbitrary defnition can be explained by inspection of Figure 2 which shows the Ag^+ ion density profile along the <111> direction from an octahedral site to a tetrahedral interstitial. The density is continuous between these two sites and hence some ions vibrating about their true lattice sites may be included in the summation. 0.12a corresponds to the minimum between the two sites. There is a rapid increase in the number of Ag^+ ion interstitials as the melting point is approached (Table 1).

Table 1. The mean square displacements of the ions about their lattice sites ($\langle u^2 \rangle$) in Å^2, and the increase in interstitial (tetrahedral) site occupancy by Ag^+ as a function of temperature up to 699K. For Ag^+ separate values are given for mean square displacements in the <100>, <110> and <111> directions, as well as an average over all directions (column 2). The mean square displacement of the Br^- is isotropic at all temperatures and so only the average is given.

T(K)	Ag^+ $\langle u^2 \rangle$	<100>	Ag^+ <110>	<111>	Br^- $\langle u^2 \rangle$	Ag^+ interstitials (%)
490(2)	0.50(1)	0.08(1)	0.08(1)	0.16(3)	0.28(1)	1.7(3)
669(2)	0.93(1)	0.15(2)	0.15(2)	0.29(5)	0.46(1)	2.5(2)
684(2)	1.00(2)	0.19(2)	0.18(2)	0.39(6)	0.50(1)	2.4(2)
689(2)	1.03(4)	0.18(2)	0.17(2)	0.35(9)	0.49(1)	2.5(3)
697(2)	1.10(4)	0.17(3)	0.17(2)	0.38(5)	0.52(1)	3.2(2)
698(2)	1.16(3)	0.19(3)	0.18(2)	0.45(6)	0.55(1)	3.6(2)
699(2)	1.20(4)	0.20(3)	0.19(3)	0.48(5)	0.56(1)	3.9(4)

Figure 2. The Ag^+ ion density profile in <111> directions across octahedral lattice sites in AgBr showing the development of Ag^+ ion occupation of tetrahedral sites. T=669(x), 689(+) and 699K(o).

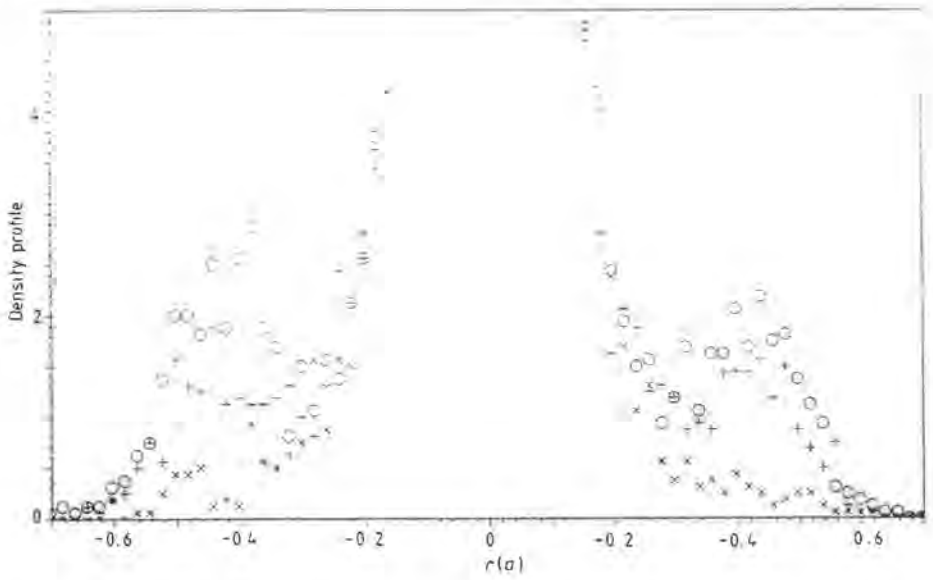

The disorder initiated in the solid phase can be seen to continue in the melt. For example, when investigating the bond angle distributions (Figure 3) there is no symmetry change in the Br-Br-Br distributions at 490, 699 and 703K (molten). However, a peak develops in the Ag-Br-Ag distribution below T_M which is the dominant feature in the molten distribution. It cannot conclusively be stated that these disorderings precipitate melting, and indeed measurements of the Bragg peak intensities very close to T_M (Figure 4) show first order behaviour. Indeed the occurrence of a change in symmetry in the local environment suggests that the disorder specifically does not precipitate melting, since, in molten salts, there is usually no such change [McGreevy and Pusztai (1990)]. The conclusion of this work therefore is that there is a second-order phase transition to a fast-ionic phase, similar to that observed in β-PbF_2, which is interrupted by a first-order melting transition. This work provides experimental evidence for the suggestion of Andreoni and Tosi (1983) who theoreti-

cally demonstrated that AgBr would become truly fast-ionic, only the lattice melts before such a transition is possible.

Figure 3. Ag-Br-Ag and Br-Br-Br bond angle distributions at 490, 699 and 703K (T_M=701K). Successive temperatures are displaced vertically by 1.0. Maximum bond lengths are 3.6 and 5.1Å for Ag-Br and Br-Br respectively. The cosines which would be obtained for various perfect fcc crystals are given, where T indicates four Ag^+ randomly occupying the eight tetrahedral sites, O indicates occupation of the four octahedral sites and B random occupation of the T and O sites; in all cases Br^- occupy a perfect fcc sub-lattice.

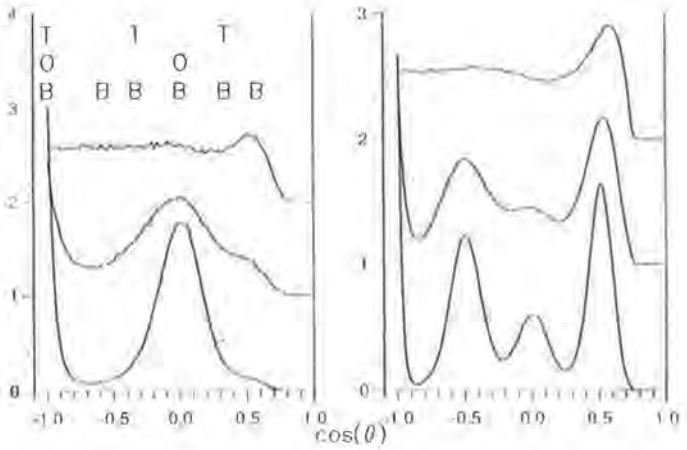

4.2. Silver Iodide

There have been many attempts to determine the distribution of Ag^+ ions in fast-ion conducting α-AgI, and the pathways which facilitate conduction. The results from RMC analysis of powder neutron diffraction at temperatures within this phase conclusively determine both the Ag^+ equilibrium positions and the routes for Ag^+ ion mobility [Nield *et al* (1993a)]. Previous work has concentrated on assigning the two silver ions per unit cell between available tetrahedral 12(d), octahedral 6(b) and trigonal 24(h) sites within the body-centred cubic iodine sublattice. Our analysis has shown that the Ag^+ ion density peaks at tetrahedral sites, although there is also significant density in trigonal 'bridging' positions which link neighbouring tetrahedral sites in <110> directions. This is therefore the most likely route for ionic conduction. The Ag^+ ion density in octahedral positions was six times less than that found in trigonal sites, suggesting a much reduced ionic conduction between tetrahedral sites in <100> directions. There is little temperature dependence of the Ag^+ ion density and the model is independant of which crystallographic sites the Ag^+ ions are initially placed on. Using the Ag^+ ion density along specific directions it is possible to determine an energy barrier to motion using simple diffusion theory. The results from RMC modelling of diffraction data are consistent with the activation energy determined from conductivity. It is however clear that the motion of the Ag^+ ions is not uncorrelated and that correlation with neighbouring I^- ions and Ag^+ ions must be considered. Implications of this will be described in the following section.

4.3. Comparison with single crystal diffuse scattering

Single crystal diffuse neutron diffraction has been carried out in the cases of AgBr [Keen at al (1990b)] and α-AgI [Keen et al (1993)]. These data have been used to validate the conclusions obtained by RMC analysis of powder diffraction data. This is possible since scattering in a reciprocal lattice plane can readily be calculated from the RMC configurations, and hence three dimensional correlations predicted by RMC can be further tested. Experimentally this was relatively straightforward in the case of AgBr although maintaining a large single crystal close to its melting point for the period of time required for a diffraction experiment is not trivial. For α-AgI the sample had to be grown *in-situ* on the diffractometer, since the large volume change at the β→α phase transition at 420K would shatter a crystal of a size suitable for diffuse neutron scattering. The results are shown in Figures 4 and 5, which also show the comparison with RMC calulation in the same reciprocal lattice planes. The first thing to note is that the RMC modelling predicts different forms of diffuse scattering in AgBr and α-AgI. In AgBr diffuse scattering peaks under certain Bragg peaks and the scattering joins these Bragg peaks together. In α-AgI, the main diffuse scattering features are rings at |**Q**|=1.9, 4.0 and 5.8 reciprocal lattice units. Secondly, the RMC calculations are entirely consistent with the experimental data. The configurations can also be used to identify which correlations contribute towards which observed features. In α-AgI, it is Ag-I correlations which principally produce the |**Q**| independent rings of diffuse scattering (Figure 6) and it is known that these features originate from short-range order as a result of Ag^+ ion motion. (Simulations which do not permit ions to move significantly away from equilibrium sites, although retaining the appropriate temperature factors, do not show these features.) Hence the Ag^+ ion motion is correlated to the surrounding I^- lattice, as suggested by a number of of workers [see references within Keen *et al* (1993)], but conclusively shown here using a relatively simple experimental technique.

Figure 4. Neutron scattering in the (hhl) plane of AgBr at T=669K. (a) Calculated from an RMC configuration generated from powder data and (b) experimental results from a single crystal sample. (Instrument geometry did not allow measurement above |**Q**|=4.1a*)

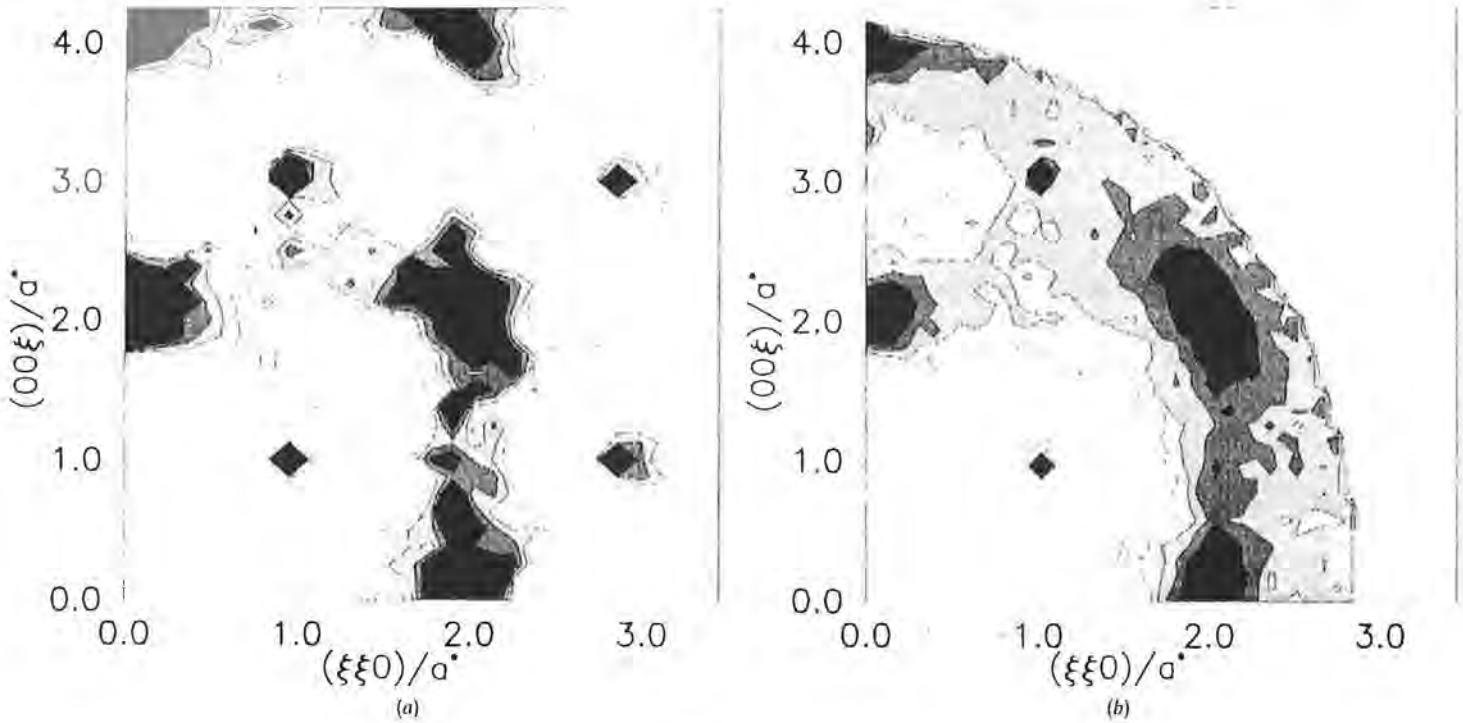

Figure 5. Neutron scattering in the (hk0) plane of AgI at T=515K. (a) Calculated from an RMC configuration generated from powder data and (b) experimental results from a single crystal sample.

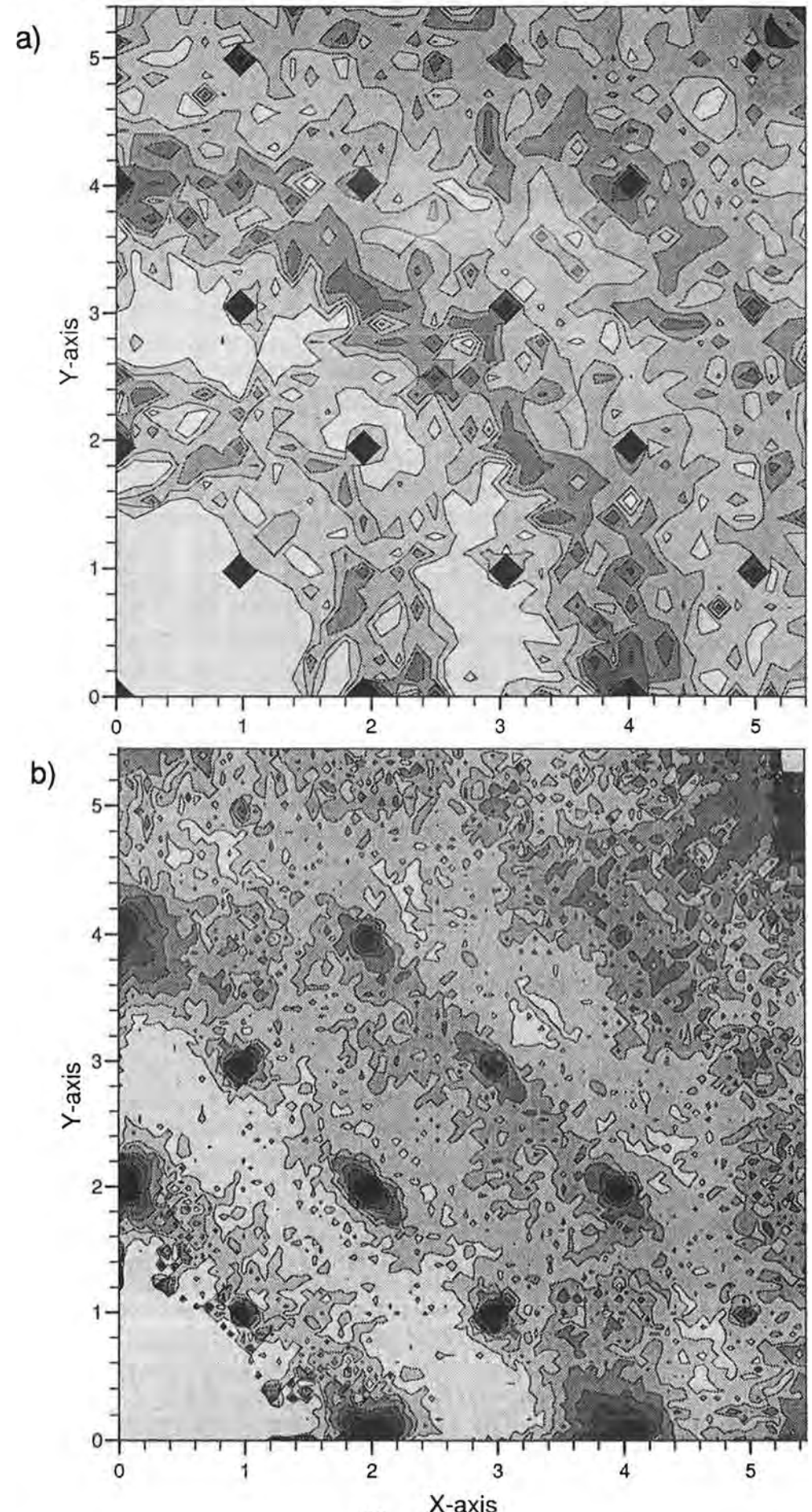

Figure 6. Partial scattering patterns in the (hk0) plane of AgI calculated from an RMC configuration generated from powder data (a) Ag-I correlations, (b) Ag-Ag correlations and (c) I-I correlations.

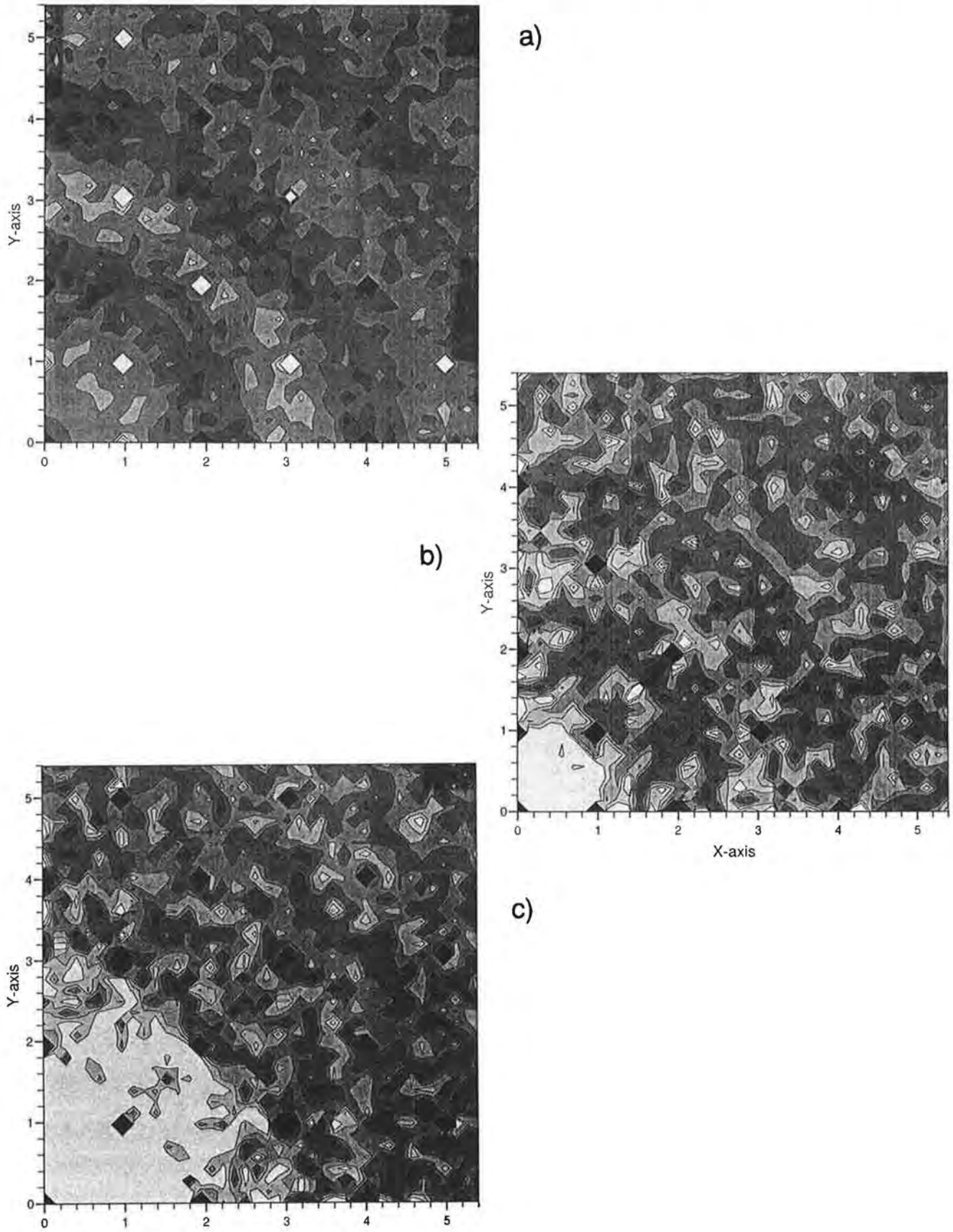

5. Conclusions

Powder neutron diffraction patterns, carefully analysed to include consideration of the diffuse scattering, yields important information about the temperature-induced disorder in fast-ion conductors. AgBr shows a gradual increase in interstitial site occupation as the temperature approaches T_M. This has been shown to be a precursor of a transition to a fast-ion phase which is interrupted by melting. The disorder is not indicative of pre-melting in the material. The tetrahedral equilibrium sites for Ag^+ in α-AgI have been successfully established experimentally. It has also been shown that ionic conduction predominantly occurs via trigonal 'bridging' sites in <110> directions. The Ag^+ ion density distributions are consistent with ion diffusion through an energy barrier whish is consistent with the activation energy determined from conductivity. The results from RMC modelling of powder diffraction data have been vindicated by comparison with diffuse scattering from single crystal samples. These also show that the diffuse rings in α-AgI are largely due to Ag-I correlations involving the mobile Ag^+ ions, and therefore the I^- ions assist the motion of the smaller Ag^+. Work is in progress to extend this study to other phases of these compounds which show fast-ion conduction but occur at high temperatures and pressures [Hull & Keen (1993a) and Keen & Hull (1993a)].

6. Acknowledgements

The work described has only been possible because of collaboration with V. M. Nield, R. L. McGreevy and W. Hayes at the Clarendon Laboratory and with S. Hull at the Rutherford Appleton Laboratory. Their considerable input is gratefully acknowledged.

7. References

Andreoni W. & Tosi M.P., *Sol. State Ionics* **11** 49 (1983)

Boyce J.B. & Huberman B.A., *Physics Reports*, **51** 189 (1979)

Hull S. & Keen D.A., *Europhys. Lett. in press* (1993a)

Hull S. & Keen D.A., *In preparation* (1993b)

Keen D.A. & Hull S., *J. Phys.: Condens. Matter* **5** 23 (1993a)

Keen D.A. & Hull S., *In preparation* (1993b)

Keen D.A., Hayes W. & McGreevy R.L., *J. Phys.: Condens. Matter* **2** 2773 (1990a)

Keen D.A., McGreevy R.L., Hayes W. & Clausen K.N., *Phil. Mag. Lett.* **61** 349 (1990b)

Keen D.A., Nield V.M. & McGreevy R.L., *In preparation* (1993)

McGreevy R.L. & Pusztai L., *Mol. Simulation* **1** 359 (1988)

McGreevy R.L. & Pusztai L., *Proc. R. Soc.* A **430** 241 (1990)

McGreevy R.L., Howe M.A., Keen D.A. & Clausen K.N., *IOP Conf. Ser.* Ed M W Johnson **107** 165 (1990)

Merrill L., *J. Phys. Chem. Ref. Data* **6** 1230 (1977)

Mitchell E.W.J., Poncet P.F.J. & Stewart R.J., *Phil. Mag.* **34** 721 (1976)

Nield V.M., Keen D.A., Hayes W., & McGreevy R.L., *J. Phys.: Condens. Matter* **4** 6703 (1992)

Nield V.M., Keen D.A., Hayes W., & McGreevy R.L., *submitted to Sol. State Ionics* (1993a)

Nield V.M., McGreevy R.L., Keen D.A. & Hayes W., *In preparation* (1993b)

Phillips J.C., *Rev. Mod. Phys.*, **42** 317 (1970)

Rapoport E. & Pistorius C.W.F.T., *Phys. Rev.*, **172** 838 (1968)

Non-Stoichiometric $M_{1-x}R_xF_{2+x}$ Crystals - New Multicomponent Inorganic Materials with Partially Disordered Structure and Specific Physical Properties

B P Sobolev and V B Alexandrov

Institute of Crystallography, Russian Academy of Sciences, Moscow

Introduction

In recent years crystals with complex chemical composition have been replacing traditional (single component) materials in various fields of modern technology. A more complex composition is, as a rule, a result of the application of more complicated sample preparation techniques. Single crystals of inorganic fluorides employed in industry comprise merely a dozen single-component compounds: LiF, CsF, MgF_2, CaF_2, BaF_2, LaF_3 and some others. Their constant chemical composition and fixed physical properties are the obstacles for choosing materials that could suit requirements in new fields of application.

At the beginning of the seventies a program of high-temperature chemistry studies of fluorides of 24 metals (Na, Ca, Sr, Ba, Cd, Pb, Sc, Y, La and 13 Lanthanides, Zr, Hf) in binary MF_2-RF_3 systems was undertaken at the Institute of Crystallography. The practical aim of the program was searching for and preparing new multicomponent fluoride materials for up-to-date technologies, notably applications in the field of lasers, which was most popular at that time. By the present time the chemical part of the program - studies of phase equilibrium and construction of phase diagrams of the condensed state for about 200 MF_2-RF_3 systems - has been mainly completed. The results of that stage of the program are briefly summarised in the reviews [1,2] etc.

These results are as follows:

- the most typical products of high-temperature chemical interactions of the metal fluorides are isovalent and heterovalent solid solutions;
- the larger number are heterovalent solid solutions with a variable number of atoms per unit cell (non-stoichiometric phases) which crystallise in two basic structural types: CaF_2 and LaF_3. About 50% of the total amount of non-stoichiometric materials known at present for MF_2-RF_3 systems crystallise in the CaF_2 type, while some 25% of them crystallise in the LaF_3 structural type;
- these phases exhibit the maximum stoichiometry perturbations among known ionic crystals. This possibility of varying the content of the second component over a wide range, while keeping the chosen structural type of the crystal, as well as a significant dependence of the physical properties on the composition, make the non-stoichiometric phases of materials most attractive for practical applications;
- CaF_2- and LaF_3-type non-stoichiometric phases have an unusually large capacity for keeping a disordered structure in the metastable state after cooling. This fact also promotes the application of such materials in various devices;
- passing over from single-component to two-component (in the basic composition, without account of the activators) materials yields a 50-60 fold increase in the number of promising phases that differ qualitatively (in M and R combinations);
- interaction of fluorides with water vapour at high temperatures (pyrohydrolysis) results in contamination of the materials by oxygen. This impurity, starting from minute contents, gravely affects many properties. Uncontrolled pyrohydrolysis is one of the major reasons for the existence of contradictory data on the chemistry, structure and properties of single- and multicomponent fluoride materials;
- the application of technological processes which ensure the minimum possible pyrohydrolysis during synthesis of fluoride materials is a prerequisite for extracting the correct data.

It is clear from the above that studies of the defect crystal structures of non-stoichiometric CaF_2- and LaF_3-type phases are of immediate and great interest in the search for and development of new

multicomponent fluoride materials with controlled characteristics. Taking into account the potential collaborative aspects of this seminar, I shall dwell on $M_{1-x}R_xF_{2+x}$ phases with the fluorite structure and ordered phases with structure derived from that type.

Main results and aims of structural studies of multicomponent crystals with fluorite type structure

The first study of a single crystal of the grossly non-stoichiometric $Ca_{0.69}Ce_{0.31}F_{2.31}$ was made by Dr V B Alexandrov in 1969 [3]. The study demonstrated that heterovalent replacement of M^{2+} by R^{3+} in the CaF_2 structure is the result of several mutually related processes of defect formation. Besides cation substitution, defects (vacancies) are formed in the basic anion motif and fluorine ions are incorporated into large cubic voids of the fluorite structure. Of principal value was the conclusion about the displacement of interstitial fluorine ions from the void centre (½,½,½) to the 32f site of the space group Fm3m. Further work [4] on the $Ca_{0.9}Y_{0.1}F_{2.1}$ system confirmed this conclusion and added one more possible site for interstitial fluorine ions, namely, a 48i position. According to [4], yttrium fluorite contained both types of interstitial fluorine ions.

These two almost simultaneous and separate publications represented the beginning of a long period of studies of specific structural features of strongly perturbed non-stoichiometric phases, which cannot indeed yet be regarded as complete. There are two approaches to the problem of which the first, experimental X-ray and neutron diffraction studies of the defect structure of $M_{1-x}R_xF_{2+x}$ phases, was the main approach developed at the Institute of Crystallography.

By the present time, crystal structures of $Ca_{1-x}R_xF_{2+x}$,where R = La, Ce, Er, Y; $0.05 < x < 0.39$; $Sr_{1-x}R_xF_{2+x}$, where R = La, Pr, Nd, Y; $0.10 < x < 0.31$ and $Ba_{1-x}R_xF_{2+x}$, where R = Ce, Pr, Nd, Ho; $0.1 < x < 0.5$ have been studied [5-7]. These investigations have confirmed the assumptions advanced in [8] that either i- or f-type of defects occur in such crystals. Recent data on neutron diffraction and diffuse scattering from a single crystal of $Ca_{0.94}Y_{0.06}F_{2.06}$ have also revealed only one interstitial fluorine site (32f) [9].

Figure 1 shows the main data on structural studies of $M_{1-x}R_xF_{2+x}$ crystals. The types of interstitial F-defects are denoted as f-and i- in accordance with the notation of crystallographic positions in space group Fm3m. They are shown on the left of each rectangle, corresponding to different combinations of M- and R-cations. In addition, the following details about the combinations studied are provided: RF_3 contents in $M_{1-x}R_xF_{2+x}$ in mole fractions (x); the technique used to study the structure (n=neutron diffraction); year of publication. On the lower right corner are given percolation thresholds (in mole fractions (x) obtained experimentally from data on ionic conductivity of the crystals. There is some correlation between these values and defect type, the defects, in their turn, being responsible for cluster sizes.

The first boundary between f- and i-type anionic defects is localised between $Sr_{1-x}Pr_xF_{2+x}$ (f-) and $Sr_{1-x}Nd_xF_{2+x}$ (i-). The second boundary lies in the family of $Ca_{1-x}R_xF_{2+x}$ phases with RF_3- trifluorides with yttrium as rare earth. The precise location of this boundary will be established in due course after further studies. The widely studied $Ca_{1-x}Y_xF_{2+x}$ system may turn out to be near this boundary or even exactly at it. The occupation of such a pivotal position in the range of structure instability makes the influence of some factors which are usually neglected vital for the crystalline form adopted by the material.

Another direction in the analysis of defect formation consists of calculations of possible configurations of defect clusters. The data reported in [10,11], as well as many other estimations, were used for the interpretation of experimentally observed behaviour of active ions in defect crystalline matrices. A review of theoretical models of suggested clusters has recently been published [12]. The number of suggested clusters is now about 30, with cluster formation beginning at very low concentrations of the impurity component RF_3 (see for example Ref [13]).

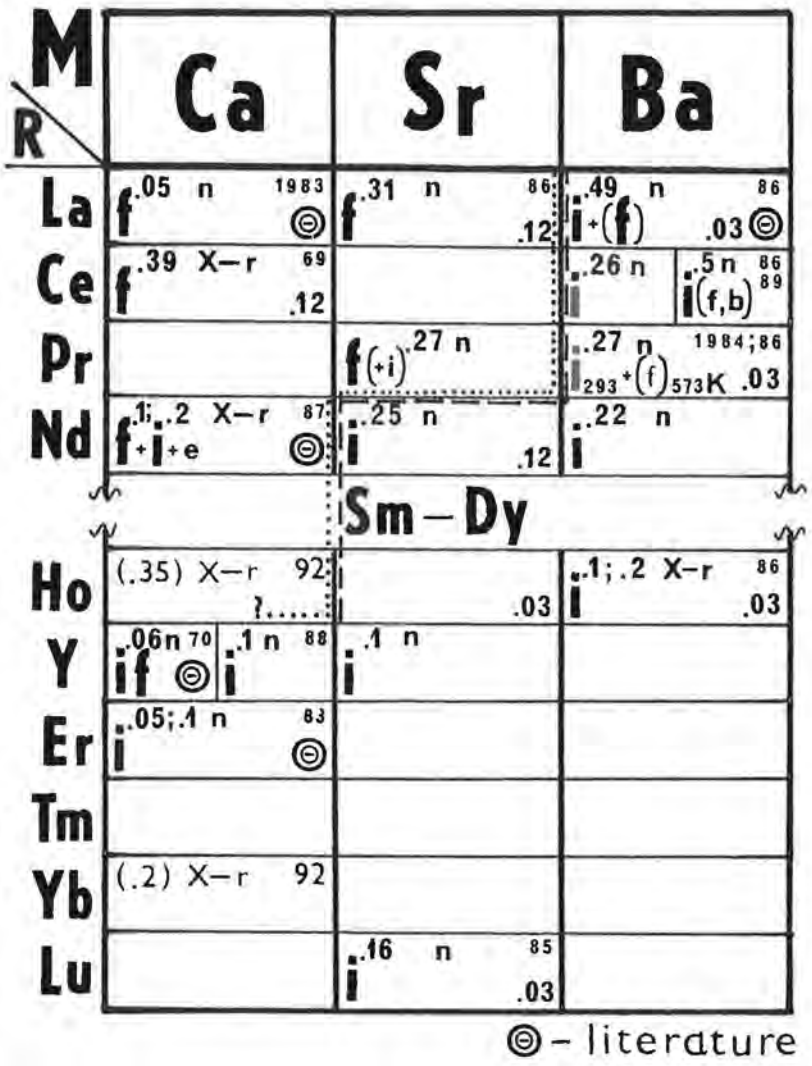

Figure 1 - Structural Studies of $M_{1-x}R_xF_{2+x}$ single crystals.

While the negligible formal difference between the two types of defects lies in fluorine ion displacements from the void centre along the two-fold (i-type) or threefold (f-type) axis, the forms and sizes of clusters show profound variation. These characteristics are responsible for many physical properties which makes studies of the cluster structure of non-stoichiometric fluorides indispensable for the prediction of properties of multicomponent materials. The most essential difference between the two types of crystals, as far as the character of defects is concerned, is the difference in interatomic distances. The phases with i-type defects exhibit a 12% or more reduction in (M,R)-F distances (where F is the interstitial 48i site) [5] as compared to the (M,R)-F basic motif (F in 8c site) distances. At the same time, the coordination number of fluorine ions at the 48i site is lowered, i.e. the anionic sublattice becomes more inhomogeneous and the ionic extent of chemical bounding is changed.

The inevitability of defect cluster formation in non-stoichiometric UO_{2+x} crystals was pointed out some time ago by Willis [14,15], this conclusion representing the only possibility of eliminating the shortened interatomic distances in the structure of non-stoichiometric phases which could result from the statistical distribution of anionic defects.

Structural studies of disordered crystals permit one to assess the configuration of anionic defects in the $M_{1-x}R_xF_{2+x}$ fluorite phases. More complicated is estimation of the extent of disorder in the cationic sublattice. This problem is connected with participation of different sorts of cations (M,R) in cluster formation and studies of ordered phases with structures derived from the fluorite-type can provide more reliable information on this. Such phases are formed either as a result of solid-phase decomposition of non-stoichiometric crystals as temperature is lowered (phases A, B, C in Figure 2a), or upon crystallisation from the melt (phase D in Figure 2b). These schemes of ordered phase formation are seldom encountered, which is why studies of their structures are restricted.

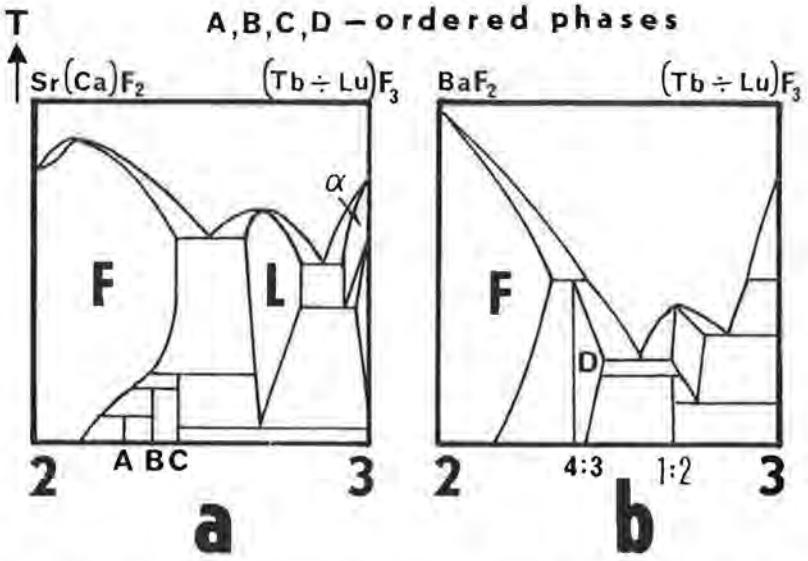

Figure 2 - The thermal behaviour of ordered phases in the MF_2-RF_3 systems.

The first data on the formation of ordered phases in MF_2-RF_3 systems were obtained [16,17] in the course of studies of their phase diagrams. Previously the only available work on ordered crystals was a study of Ca_2YbF_7 [19], apart from the natural mineral tveitite $Ca_{14}Y_5F_{43}$ [20]. The poor quality of the latter sample necessitates caution in evaluation of the results.

We have recently carried out a joint study of the ordered phases $Ba_4Yb_3F_{17}$ and $Ba_4Y_3F_{17}$ with collaborators at the University of Barcelona. Comparison of the new data with those obtained before [21] for the oxyfluoride phase $Pb_8Y_6F_{32}O$ showed that they are isostructural. The cause of the long range order in the above crystals is, in particular, the formation and ordered arrangement of octahedral associates of rare earth cations comprising a fluoride cuboctahedron with an additional fluorine inside. They can be regarded as a cationic framework of the type of clusters which exist in non-stoichiometric forms of materials of the same composition. The phases $Ba_4R_3F_{17}$ are the first example of ordered phases in the MF_2-RF_3 systems which have been characterised by the full differentiation of cations of different types over different sites. In this case partial disorder is retained in the anionic motif, by a statistical distribution of fluorine atoms inside the anionic cubooctahedron. Thus, up to now, there are still some unknown phases among such systems - which could be called strictly ordered.

The primary problems remaining to be solved in the course of structural studies of non-stoichiometric and ordered phases formed in the systems MF_2-RF_3 with the CaF_2-type or derived structure are as follows:

- **establishment of the boundary of the transition from i- to f- defects in the families of non-stoichiometric phases $M_{1-x}R_xF_{2+x}$ upon replacement of M- and R-cations by various alkali-earth and rare earth elements respectively;**

- finding possibilities for the development of non-stoichiometric materials with both types of interstitial fluorine ion defects. To do this, crystals with variable RF_3 content at the boundary of the (f-i)- transition, or three-compound $M_{1-x}(R, R')_xF_{2+x}$ materials, should be studied;
- refinement of the cationic composition of clusters (participation of M- and R-cations) in the non-stoichiometric state;
- preparation and structural studies of ordered phases derived from non-stoichiometric ones with i-type defects;
- further studies of ordered phases with the CaF_2 type structure. To date, single crystals with two types of ordering have been obtained, from up to ten types [18] in the MF_2-RF_3 systems;
- elucidation of the influence of thermal treatment, among others, on the structure of clusters.

This is far from covering all aspects of the problem of structural organisation of grossly non-stoichiometric fluorite crystals. Changes and additions will be made as new data are obtained on the above points. It is to be hoped that the combined efforts of InCr and ISIS will speed up and extend these studies.

Besides its obvious scientific importance, such structural data on non-stoichiometric fluorides are of great interest for practical applications, due to the large scale usage of multicomponent fluoride materials in modern technology.

Main directions of practical application of multicomponent fluoride materials for technological purposes

Although the dependence of the properties of non-stoichiometric crystals on their structure has not been completely studied, such materials are used on an industrial scale from year to year. Below we give the directions which represent the most essential needs and the effect of replacement of conventional single-component materials by those multicomponent, mainly non-stoichiometric, crystals with CaF_2 type defect structures.

1. The effect of inhomogeneous broadening of luminescence and absorption spectra of rare earth ions in crystalline $M_{1-x}R_xF_{2+x}$ matrices was first used for increasing the efficiency of using light energy for laser pumping. Our program of searching for new fluoride materials in the seventies was intended to find new laser active media with partially disordered structures. A review of the laser spectroscopic studies carried out for the most part using our crystals, is given in [22]. A similar direction of development was the study of converters of IR-quanta to visible light. Among the most effective IR-converters and low-threshold lasers were found to be compounds with the formula BaR_2F_8, found in the course of studies of phase diagrams [17,23-25].
2. The strong dependence of ionic transport parameters on the defect structure of $M_{1-x}R_xF_{2+x}$ led, simultaneously and independently, InCr with the Institute of Physics in Bratislava, along with some other Institutes, to develop a new family of fluorine-ion conductors based on multicomponent non-stoichiometric fluorides. Their conductivity exceeds, by 8-10 orders of magnitude, that of single-component MF_2 prototypes. We have carried out a systematic study of 220 fluorite type crystals [26,27], as well as some defect crystals $R_{1-y}M_yF_{3-y}$ of the LaF_3 type. These were used for the development of chemical sensors for fluorine in gaseous media and as fluorine generators for industrial applications [28].
3. The possibilities of varying the unit cell parameters of cubic $M_{1-x}R_xF_{2+x}$ from 5.39 to 6.20 Å, determined in the course of phase diagram studies [1,29], were used by us in 1983 for the preparation of substrates for semiconducting film elements with the minimum heterometry effect. Later, other authors used this technique for improving the quality of semiconductor devices.
4. The effect of the many-fold increase of mechanic hardness of crystals by incorporation of a high content of rare earth ions opens up wide prospects for the practical application of such hardened materials, for example as passive optical media (windows, lens, prisms etc) and active elements of devices subject to high loads. Of great importance is the fact that non-stoichiometric crystals exhibit significant weakening of the perfect fluorite cleavage that imposes restrictions on the

application of single crystals of MF_2. Some recent studies of mechanical characteristics of concentrated solid solutions of RF_3 in MF_2 are presented in [1,30].

5. Studies of ultrasound propagation in $M_{1-x}R_xF_{2+x}$ have highlighted the possibility of monitoring effectively propagation rates, for possible use as delay lines with various times, for fixed sizes of crystals. Crystals based on BaF_2 turned out to be close to elastic-isotropic media, which are better than molten quartz and glasses due to lower sound absorption and high transparency in the UV- and IR-ranges [31,32].
6. Studies of the radiation stability of grossly non-stoichiometric $M_{1-x}R_xF_{2+x}$ crystals began in 1979 [33]. This direction of research was continued in 1989 when we took part in the search for fast, radiation hard, dense scintillators for high energy physics, nuclear physics, nuclear medicine, astrophysics and related fields. Using the database for phase diagrams of MF_m-RF_n systems, we determined the range of two-component crystalline matrices formed in those systems, whose density exceeded 5.5 - 6.5 g/cm^3. Those optical media were transformed to scintillators with excited state lifetimes in the range of nanoseconds to dozens of nanoseconds. We found dopants which increased the radiation hardness of crystals up to several million Gy. The combination of low cost of starting materials and good technological prospects were the main criteria for the choice of new multicomponent scintillators. As result of the program, several dozen fluoride materials have been developed which matched the rather strict criteria of choice of scintillators for high energy physics and related fields of application [34-36].
7. An important possible application of high structural disorder of grossly non-stoichiometric fluorides are in materials for optical amplifiers fibre optics, with wavelength 1.3 μm. The required broadening of the luminescence spectrum of certain ions, as well as the displacement of the intensity maximum, can be controlled by the composition and defect structure of multicomponent fluoride materials.

All of the established and future directions of practical application of fluoride materials with complex chemical composition can be rapidly developed using the database on phase equilibria in binary and more complex fluoride systems, which we have obtained at InCr. Besides studies of chemical aspects of fluoride systems, we have also developed the technology and methods for obtaining new fluoride materials. The single-crystalline form is not of course the only one for fluorides, and indeed is not the best form for some practical applications. As for production costs, manufacture of single crystals is one of the most expensive tasks in modern materials science. Therefore, we have also developed techniques for the preparation of fluoride materials in polycrystalline (including optical ceramic) form, multiphase materials, including eutectic composites, amorphous materials and glasses. Each of these has its merits and shortcomings. The common feature of all fluoride materials obtained at the Institute of Crystallography, however, is maximum purity in terms of oxygen content. Oxygen is the most frequent and uncontrolled impurity in inorganic fluoride materials, the negative influence of which is well known for some of the physical properties of partially hydrolysed fluoride crystals.

This communication has been devoted to only one structural type of multicomponent fluoride materials - fluorite, which is of the most interest for scientific research and practical application. At the same time other new fluoride materials with complex chemical composition are diverse and present further interest for science and technology [37].

References

[1] B P Sobolev (1991) Non-stoichiometry in inorganic fluorides and phases with fluorite structure. Butll Soc Cat Cien 12 275-332.

[2] B P Sobolev (1992) The chemistry of single crystalline materials of variable composition formed in the systems MF_m-RF_n (m,n=4). *Zhurnal Vses Khim Obshestva* **36** 726-738 (in Russian, translated into English).

[3] V B Alexandrov, L S Garashina (1969) New data about structure of solid solutions CaF_2-TRF_3. *Dokl AN SSSR* **189** 307-309 [*Sov Phys Dokl* **14** 1040 (1970)].

[4] A K Cheetham, B E F.Fender, D Steel, R J Taylor, B T M Willis (1970) Defect structure of fluorite compounds containing excess anions. *Sol State Comm* **8** 171-176.

[5] V B Alexandrov (1991) X-ray and neutron diffraction studies of non-stoichiometric fluorite phases $M_{1-x}R_xF_{2+x}$ (M=Ca, Sr, Ba; R=Ln, Y). *Butll Soc Cat Cien* **12** 334-347.

[6] L P Otroshenko, V B Alexandrov, L A Muradyan, V A Sarin, B P Sobolev (1991) Neutron diffraction study of the features of fluorine ions incorporation into $Ba_{1-x}R_xF_{2+x}$ solid solutions. *Butll Soc Cat Cien* **12** 383-391.

[7] V B Alexandrov, L P Otroshenko, L E Fykin, V A Sarin, V I Simonov, B P Sobolev (1984) A new variety of defect structure in a nonstoichiometric phase of the fluorite type, $Ba_{0.73}Pr_{0.27}F_{2.27}$. *Sov Phys Crystallogr* **29** 229-230.

[8] B A Maximov, L A Muradyan, V I Simonov (1986) Non-stoichiometric phases of fluorite type. In *Kristallografia i kristallochimia*, pp 16-21, NAUKA Publ. Moscow 1986 (in Russian).

[9] S Hull, C C Wilson (1992) The defect structure of anion-excess $(Ca_{1-x}Y_x)F_{2+x}$ with x=0.06. *J Solid State Chem* **100** 101-114.

[10] C R A Catlow (1973) Defect clusters in doped fluorite crystals. *J Phys C* **6** L64-L70.

[11] Yu K Voron'ko, V V Osiko, I A Sherbakov (1969) Optical centers and interactions of Yb^{3+} ions in cubic fluorite crystals. *Zhurn Exp Teor Fisik* **56** 151-160 (in Russian).

[12] P P Fedorov (1991) Association of point defects in non-stoichiometric $M_{1-x}R_xF_{2+x}$ fluorite-type solid solutions. *Butll Soc Cat Cien* **12** 349-381.

[13] S A Kazanskii (1985) Optical EPR detected clusters of rare earth's and yttrium in the fluorite-type crystals. *Zhurn Exp Teor Fisik* **89** 1258-1268 (in Russian).

[14] B T M.Willis (1963) Neutron diffraction studies of the actinide oxides. *Proc Roy Soc* A**274** 122-144.

[15] B T M Willis (1963) Positions of oxygen atoms in $UO_{2.13}$. *Nature* **197** 755-756.

[16] B P Sobolev, L S Garashina, V B Alexandrov (1971) The study of the MF_2-$(Y,Ln)F_3$ systems (M=Ca, Sr, Ba). *International Congress of Crystal Growth, ICCG-3*, Abstracts p 168, Marcelle,
France, 5-9 July 1971.

[17] N L Tkachenko, L S Garashina, O E Izotova, V B Alexandrov, B P Sobolev (1973) Phase equilibria in BaF_2-$(Y,Ln)F_3$ systems. *J Solid State Chem* **8** 213-218.

[18] O Greis, M Haschke (1982). Rare earth fluorides. In *Handbook on the Physics and Chemistry of Rare Earths* **5** pp 387-460, eds K A Gschneidner, L Eyring, North-Holland.

[19] A Dib, S Aleonard (1986) Structure crystalline de $Pb_8Y_6F_{32}O$. *J Solid State Chem* **64** 148-161.

[20] D J M Bevan, J Strahle, O Greis (1982) The crystal structure of tveitite, an ordered yttrofluorite mineral. *J Solid State Chem* **44** 75-81.

[21] D J M Bevan, S E Ness, M R Taylor (1988) On the crystal structure of Ca_2YbF_7 and other closely-related structures with cubooctahedral anion clusters. *Eur J Solid State Chem* **25** 527-534.

[22] A A Kaminskii (1975) *Laser crystals* p 256, NAUKA Publ, Moscow 1975 (in Russian, with subsequent English editions).

[23] E G Ippolitov, L S Garashina, B M Zhigarnovski (1967) On the types of phase diagrams MF_2-LnF_3 systems. *Dokl AN SSSR* **173** 101-103.

[24] O E Izotova, V B Alexandrov (1970) Crystal structure of $BaTm_2F_8$. *Dokl AN SSSR* **192** 1037-1039

[25] A A Kaminskii, B P Sobolev, S E Sarkisov, G A Denisenko, V A Fedorov, T V Uvarova (1982) Physico-chemical aspects of synthesis, spectroscopy and stimulated emission of $BaLn_2F_8$-Ln^{3+} crystals. *Izv AN SSSR Neorganicheskie Materialy* **18** 482-497.

[26] P P Fedorov, T M Turkina, B P Sobolev, E Mariani, M Shvantner (1982) Ionic conductivity in the single crystals of non-stoichiometric fluorite phases $M_{1-x}R_xF_{2+x}$ (M=Ca, Sr, Ba; R=Y, La-Lu). *Solid State Ionics* **6** 331-335.

[27] A K Ivanov-Shitz, N I Sorokin, P P Fedorov, B P Sobolev (1989) Specific features of ion transport in non-stoichiometric fluorite-type $Ba_{1-x}R_xF_{2+x}$ (R=La-Lu) phases. *Solid State Ionics* **31** 253-280.

[28] E F Sudakova, E Ya Alksnis, R S Perlovskii, E A Krivandina, B P Sobolev (1992) Chemical sensor for F_2 and HF in gaseous atmospheres. *Symposium on Solid State Ionics*, section U-6.5, p 160, Nov 30 - Dec 4 1992, Boston, Massachusetts.

[29] P P Fedorov, B P Sobolev (1992) Concentration dependence of unit cell parameters of fluorite-type $M_{1-x}R_xF_{2+x}$. *Kristallografia* **37** 1210-1219.

[30] A M Aronova, G V Berezhkova, V B Alexandrov, P P Fedorov, B P Sobolev (1992) Mechanical properties of single crystals $M_{1-x}R_xF_{2+x}$ of the fluorite-type structure with gross perturbations of stoichiometry (crystals $Ba_{0.61}La_{0.31}F_{2.31}$). In *Fisicheskaya Kristallografiya*, pp 151-162, NAUKA Publ., Moscow 1992 (in Russian).

[31] P Hegedus, C Musil, S Kolnik, L Cap, B P Sobolev (1986) Velocity of ultrasonic waves in alkaline-earth and rare earth fluoride mixture crystals. *Acta Phys Slovaca* **36** 64-69.

[32] S Kolnik, B P Sobolev, V Trnovcova, Z I Zhmurova (1985) Crystalline materials with low anisotropy of elastic constants. CSSR Patent No 5298-85, PV 17-07-1985.

[33] Sh A Vachidov, G A Tavshunskii, Ya Rustamov, T S Bessonova, B P Sobolev (1979) The action of nuclear irradiations on mixed fluorite crystals. *Zhurn Techn Fisiki* **49** 1943-49.

[34] B P Sobolev, E A Krivandina, Yu D Prokoshkin, V G Vasilchenko (1993). New multicomponent heavy metal fluoride crystals for high energy physics. Proceedings of International Workshop *Crystal 2000*, Sept 22-26 1992, Chamonix, France (in press).

[35] M Kobayashi, M Ishii, E A Krivandina, M M Litvinov, A I Peresypkin, Yu D Prokoshkin, V I Rykalin, B P Sobolev, K Takamatsu, V G Vasilchenko (1991) Cerium fluoride, a highly radiation-resistive scintillator. *Nucl Inst Methods* A**302** 443-446.

[36] G I Britvich, A I Peresypkin, V G Vasilchenko, E A Krivandina, B P Sobolev, E G Devitsin, Yu I Hovsepyan, V A Kozlov, T V Uvarova (1991) A study on the characteristics of some materials for electromagnetic calorimeters. *Nucl Instr Methods* A**308** 509-513.

[37] B P Sobolev (1990) The multicomponent single crystalline fluoride materials (modern state of synthesis and perspectives). In *Growth of Crystals* **18**, pp 233-254, NAUKA Publ, Moscow 1990 (Translated into English by Consultants Bureau, New York and London).

Preparation Of Single Crystals Of Multicomponent Fluoride Materials From Melt Crystallization

E A Krivandina
Institute of Crystallography, Russian Academy of Sciences,Moscow

Introduction

Single crystals of fluorides hold a special place among technologically important crystalline materials. First, natural fluorite crystals served as a material for manufacturing optical parts of devices (lenses, prisms etc.) which had to be highly transparent. Further developments in technology required single-crystalline fluoride materials with new properties. In the mid sixties widescale production of about a dozen single component fluoride materials (CaF_2, BaF_2, SrF_2, MgF_2, LiF, NaF, LaF_3 etc.) was achieved all over the world. This limited number of materials has mainly been used up till now and it cannot practically be broadened. More strict requirements for fluoride crystalline materials can be met by considerable alterations in their chemical composition within a given structural type. Passing over to multicomponent fluoride crystals gives new impetus to the further development of modern materials with new properties. At present,the family of single crystals of multicomponent fluorides comprises over 130 laser materials [2], chemical sensors [3-5], scintillators [6-8], various optical materials - from vacuum ultraviolet (0.12 μm) to medium IR range (12 μm) [5,6] and so on. The worldwide interest in these crystals is still great judging by the growing number of published papers devoted to multicomponent fluoride - increasing from eight papers in 1960-1965 to 70 in 1981-1986.

Only 27 among the known 55 can be used, to some extent, as components of the MF_m - RF_n systems for production of such new two-component optical materials. This number can be increased to 34 provided that appropriate scintillators are developed [9]. They are evenly distributed over eight structural types (Figure1(left)). The situation changes greatly when we consider the distribution over the structural types which are formed in binary systems of heterovalent solid solutions (Figure 1(right)). It is evident that upon the transition

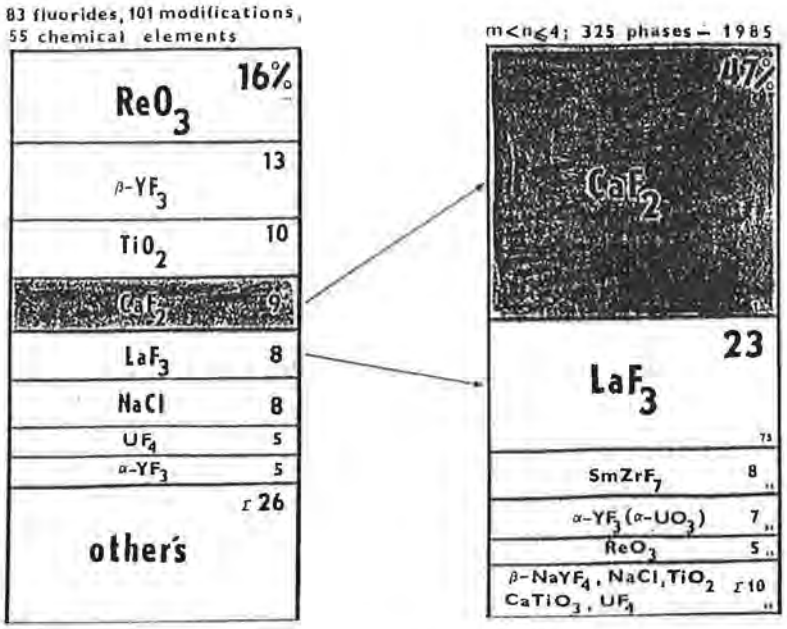

Figure 1 - Basic structural types for components MF_m, RF_n (left) and nonstoichiometric phases in MF_m- RF_n systems, for $m < n \leq 4$ (right).

to binary systems, solid solutions with the CaF_2 (47%) and LaF_3 (23%) type structure predominate. Dominant within the first structural type are the nonstoichiometric crystals with the general formula $M_{1-x}R_xF_{2+x}$, where M = Ca, Ba, Sr and R are the rare earth elements (REE), which are of special interest at this meeting.

We shall dwell on the following points:

The Growing of Multicomponent Crystals

a) The choice of composition for the preparation of a homogeneous single crystal.
b) The conditions for melt homogenisation.
c) The formation of dopant inhomogeneities (axial and radial) in samples and techniques to suppress the processes of cellular substructure formation.
d) Purity of the starting reagents, and conditions required for growing single crystals of high optical quality (without particles of phases having oxygen).

Crystallisation techniques and the equipment used at the InCr

The Growing of Multicomponent Crystals

(a) The choice of compositions of solid solutions is most important in the process of growing multicomponent crystals from the melt.

The content of the second component in the crystal is determined by the distribution coefficient $k=C_s/C_l$ (where C_s is the content of the impurity component in the crystals, C_l is its content in the melt). Figure 2a presents part of a diagram of the state of BaF_2-LaF_3. We see from this diagram that $k > 1$, if the LaF_3 content in the starting mixture is $0< C< 31$ mol%, and $k < 1$ if $31 < C < 50$ mol%. At C= 31 mol% k=l, which corresponds to the maximum on the melting curves and even impurity distribution within the sample length (Figure 3c). In the equivalent way, such composition of solid solutions as $Ca_{0.9}Y_{0.1}F_{2.1}$, $Ba_{0.78}Nd_{0.22}F_{2.22}$ and $Sr_{0.7}Pr_{0.3}F_{2.3}$ also correspond to k = 1.

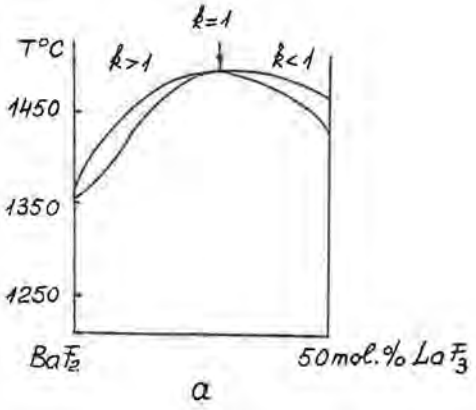

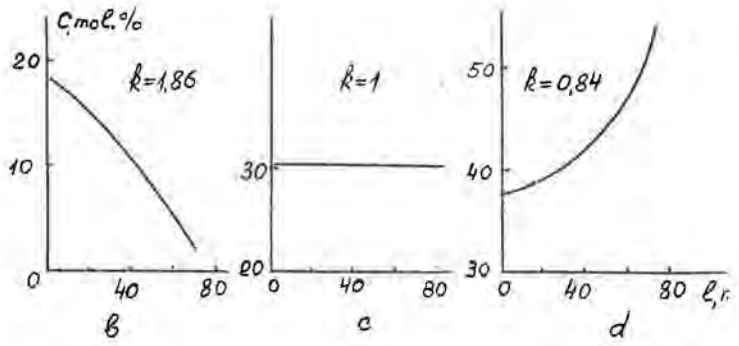

Figure 2 - Section of the phase diagram BaF_2-LaF_3 (a) and characteristics of LaF_3 distribution along the crystal for k = 1.86 (b), 1.0 (c), 0.84 (d) and starting composition C = 10 (b), 31 (c), 45mol.% (d).

In most cases, however, the studies of physical properties of new materials require multicomponent crystals with compositions characterised by distribution coefficients other than 1. Therefore, one should know how the coefficient k depends on the composition and determine the allowed limits of deviations from the ideal, although rare, case when k = 1.

The values can be calculated from the fusibility diagrams for the $M_{1-x}R_xF_{2+x}$ phase at contents 1 mol.% RF 50 mol.% [10]. However, even if $k \neq 1$, the impurity can be evenly distributed if the melt is effectively mixed in the course of crystallization and has the same composition over the entire bulk.

b) Homogenisation of melt

Studies of mixing of the melt components showed that the equilibrium distribution of the dopant is attained very quickly in the melt if the cell diameter exceeds 6 -8 mm [10]. Therefore during crystallization of fluoride melts whose features (viscosity, thermoconductivity, etc) are similar to fluorite melts, the decrease of the crucible diameter below these sizes results in a smaller degree of melt homogenization.

Now we shall consider the types of impurities which arise in crystals as a result of segregation processes during directed crystallization of multicomponent melts.

c) Formation of dopant inhomogeneities

Axial inhomogeneity of the distribution of the second component over the sample length arises, as shown in Figure 3, when $k < 1$ or $k > 1$. If $k < 1$ the impurity is drawn by the crystal into the melt and therefore the initial crystallized part contains the less of the impurity

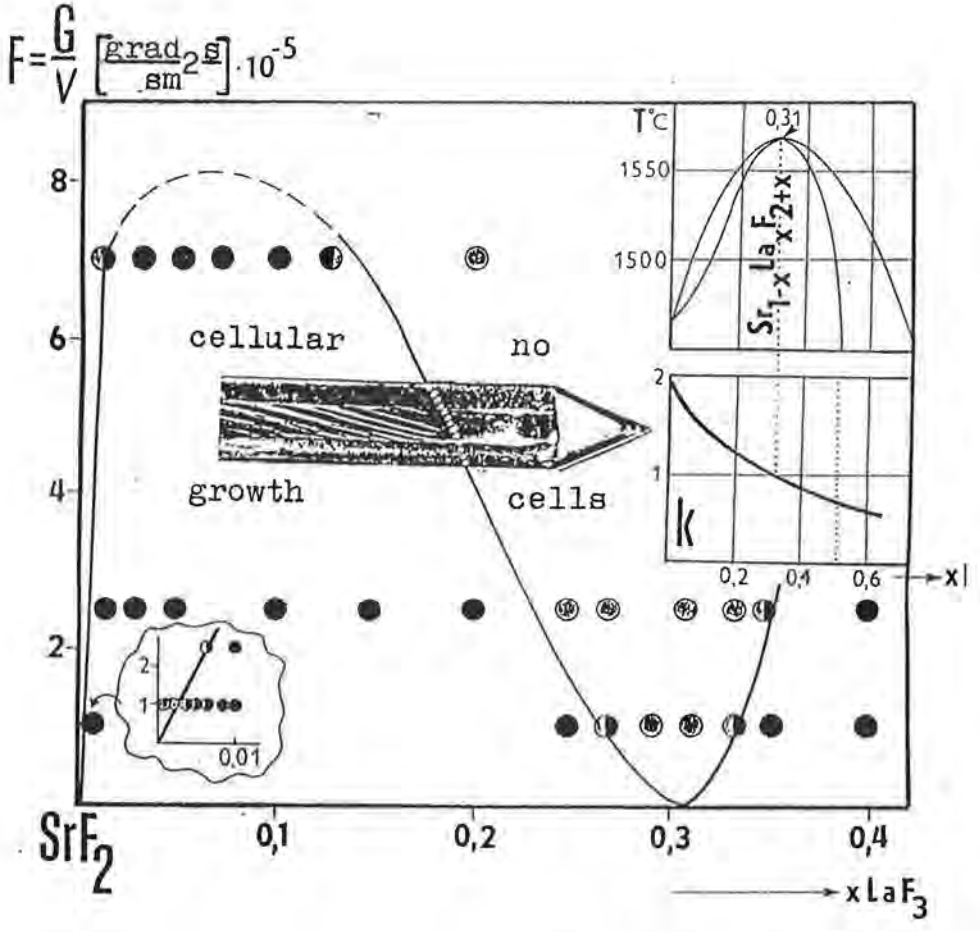

Figure 3 - Stability of planar crystallization front, phase diagrams and quality of crystals.

component. If k> 1, this is reversed. At k=1 the composition is the same over the entire length. The distribution of the impurity component over the sample length obeys the Pfann law if the melt is fully mixed [11]. Figures 3b and 3d show the distribution of LaF_3 over the crystal, calculated for the compositions $Ba_{0.9}La_{0.1}F_{2.1}$ and $Ba_{0.55}La_{0.45}F_{2.45}$.

Most frequently, along with axial inhomogeneity the so-called radial inhomogeneity is manifested. This feature is detected in crystals in the form of variations of the impurity composition in cuts perpendicular to the growth axis. This is due to the fact that during crystallization of solid solutions from melts, the melt is either enriched (at k < 1) or depleted (at k > 1) by the impurity component before the crystallization front. This results in lowering or raising of the temperature of the melt hardening equilibrium before the crystallization front, as well as constitutional undercooling, wich may lead to loss of stability of the planar crystallization front and the formation of cellular substructure [12].

Cellular substructure is manifest in optical inhomogeneity of single crystals due to variations of the chemical composition. Accordingly the refraction coefficient within the crystal bulk varies with typical sizes of the cells, some 0.1 mm. If this phenomenon can be avoided, crystals of high optical quality can be obtained. The stability of the planar crystallization front to constitutional undercooling is roughly determined using the Tiller criterion [13], which can be applied to melts with a high content of the second component, if the dependence of k on the content of the second component is introduced into the Tiller expression [14]. In this case the criterion can be written as

$$GD/V > m\Delta C = F(C),$$

where G is the temperature gradient, D is the diffusion coefficient of the second component in the melt, V is the growth rate, m is the slope of the liquidus curve and $\Delta C=C_s-C_l$ is the jump in the concentration of the impurity component at the crystallization front. The right-hand part of the inequality is called the function of planar front stability.

If the crystallization process takes place under conditions close to equilibrium, the function F(C) can be calculated from the phase diagram: $F(C)= \Delta T' \approx T$. Figure 3 presents the characteristics of the dependence F(C) on the concentration of LaF_3 for the SrF_2-LaF_3 system. It is evident that maximally homogeneous crystals of $M_{1-x}R_xF_{2+x}$ are obtained near the maximal compositions rather than for the region of low concentrations of the second component. Thus the possibility to influence directly the temperature gradient and the growth rate is highest in this region.

d) Purity of the starting reagents and crystallization atmosphere.
Preparation of single fluoride crystals of high optical quality is to a greate extent dependent on the purity of the starting material and the atmosphere in which the crystallization process is performed. The most common impurity which diminishes the optical quality of samples is oxygen.

An important specific feature of the behaviour of fluoride melts, single crystals and powders heated up to fairly high temperatures (usually, 500-700 °C), is not only their aggressiveness towards the materials used for crucibles, heaters, screens etc, but also a high tendency towards pyrohydrolysis, i.e. active interaction with moisture. For the starting mixtures, the main source of oxygen is the water adsorbed by powder surfaces, which is usually not removed during weak heating (drying). Pyrohydrolysis occurs more vigorously for melts of REE fluorides since REE are much more reactive relative to water vapor than alkali-alkali-earth fluorides [10].

There are several techniques for purification of high temperature melt fluorides from oxygen. We use the technique of creatng a fluoriding atmosphere by using products of tetrafluoroethylene hydrolysis performed immediately before the initiation of the growth experiment in the crystallization chamber. Crystallization in this way in a fluoriding

atmosphere ensures preparation of samples of high optical quality free from inclusions of oxygen-containing phases.

Crystallization technique and equipment used at the Institute of Crystallography, Russian Academy of Sciences, Moscow

Equipment for growing fluoride crystals has been developed at the Institute of Crystallography since 1960. Initially these were single-zone devices with induction, rather than ohmic, heating. Latterly, however, starting from 1985, we have been using the KRF-1 device, developed and manufactured at our own workshops, for growing crystals by the Bridgman-Stockbarger technique. The KRF-1 device consists of two controlled heat zones divided by a replaceable diaphragm, which allows control of the temperature gradient and thus makes it possible to widen the concentration ranges of preparation of homogeneous samples of multicomponent single crystals [16].

Conclusion

The utilization of multicomponent fluorides for growing single crystals creates more problems than the preparation of single crystals of monocomponent fluorides. One must know the phase diagram in order to be able to make the proper choice of the starting composition of crystallization materials. It is also necessary to ensure purity of the starting reagents and to ensure proper conditions for single crystal growth. One should also take into consideration the kinetics of growing, set the proper rate of crucible motion and the axial temperature gradient, and use crucibles of the correct size. When creating optimum conditions for growing crystals, it is necessary to take into consideration the character of the temperature fields during crystallization and cooling of crystals.

Mastering these techniques for growing single crystals of multicomponent fluorides and their preparation within a wide range of composition will provide new materials with novel properties for science and industry.

References

[1] D C Stockbarger (1949) *J Opt Soc Amer* **39**, 731-740.
[2] A A Kaminskii, L K Aminov, V L Ermolaev et al (1986) *Physics and Specroscopy of Laser Crystals* p 272. Moscow Sci.Publications (in Russian).
[3] J M Rean, J Grannec (1985) in *Inorganic solid fluorides*, ed P Hagenmuller, pp423-467. Academic Press. London-New York.
[4] I Riess (1989) in *Sci and Technol Fast Ion Conduct.* pp 23-50. Proceedings of NATO ASI,Erice, July 1-15, 1987.
[5] N I Sorokin, A K Ivanov-Shits, P P Fedorov et al (1991) *Mat Sci Forum* **76**, 9-12.
[6] J B Czirr, E Catalano (1977). *Nucl Inst. Meth* **143** 487-488.
[7] M Kobayashi, M Ishii, E A Krivandina et al (1991) *Nucl.Inst Meth* A**302**, 443-446.
[8] G I Britvich, A I Peresypkin, V G Vasilchenko et al (1991) *Nucl Inst Meth* A**308**, 509-513.
[9] B P Sobolev, E A Krivandina, V G Vasilchenko et al (1992) in *Proc. International workshop on heavy scintillators*, Chamonix, France, September 22-26,1992.
[10] B P Sobolev, Z I Zhmurova, V V Karelin et al (1991) in *Growth of Crystals* Vol **16,** pp 65-79. Consultants Bureau, New York.
[11] W G Pfann (1952) *Trans AIME* **194**, 747-753.
[12] J W Rutter, B Chalmers (1953) *Canad J Phys* **31** 15-39.
[13] W A Tiller, K A Jackson, J W Rutter et al (1953) *Acta Metallurgica* **1** 428-437.
[14] T M Turkina, P P Fedorov, B P Sobolev (1986) *Sov Phys Cryst* **31** 83-87.
[15] P P Fedorov, T M Turkina, V A Meleshina et al (1991) in *Growth of Crystals* Vol **17**, pp 165-176. Consultants Bureau. New York.
[16] E A Krivandina (1991) *Bull Soc Cat Cienn* **12** 393-412.

Neutron Scattering Studies of Fluorite Structured Fast-ion Conductors

S. Hull,
ISIS Science Division,
Rutherford Appleton Laboratory.

Abstract

Ionic compounds with the fluorite crystal structure form an important class of materials which find diverse technological applications as solid electrolytes, laser hosts and fuel cells. The results of investigations into the structure and dynamics of the fast-ion conduction process within fluorite structured compounds using neutron scattering techniques are presented.

Introduction

At high temperatures many compounds with the fluorite crystal structure exhibit phenomena associated with a diffuse transition to a so-called 'fast-ion' phase, characterised by extensive disorder of the anion sublattice. The fast-ion transition temperature T_c is typically ~$0.8T_m$, where T_m is the melting temperature. In the region of T_c the ionic conductivity rises rapidly, approaching that of the melt. Other measurements have indicated the presence of a λ-type peak in the specific heat C_p and anomalies in the thermal expansion coefficient α (for a recent review, see [1]).

In recent years the research interest in fluorite structured compounds has been extended to include a number of related systems, such as doped compounds and the antifluorites. This paper summarises the results of neutron scattering measurements conducted by the author, in collaboration with colleagues at ISIS and the Clarendon and Harwell Laboratories. A brief summary of the compounds to be discussed is given in table 1.

Class :	Fluorite		Antifluorite	
Compound :	β-PbF_2	UO_2	Li_2O	Mg_2Si
T_c(K) :	711	~2600	~1300	~1300 (?)
T_m(K) :	1128	3120	1705	1358
a_0(Å) :	5.94	5.47	4.61	6.35
Interest / application :	Model system with lowest T_c	Fission fuel in nuclear reactors	Tritium breeder in fusion reactors	Mixed covalent / ionic bonding
References :	[2,3]	[4]	[5-8]	[9]

Class :	Anion-excess Fluorite		Anion-deficient
Compound :	$(Ca_{1-x}Y_x)F_{2+x}$	$(Sr_{1-x}Y_x)Cl_{2+x}$	$(Zr_{1-x}Y_x)O_{2-x/2}$
T_c(K) :	~1200	~900	-
T_m(K) :	~1600	~1130	~2800
a_0(Å) :	5.47	6.02	5.14
Interest / application :	Model system for effect of doping. Laser host	Model system with anion which has incoherent scattering	Fuel cells, artificial gemstone, oxygen sensors
References :	[10,11]	[12-14]	[15,16]

Table 1. Summary of the fluorite structured compounds discussed in this paper. T_c and T_m are the fast-ion and melting temperatures, respectively. a_0 is the lattice parameter at ambient temperature.

Experimental

Neutron scattering has provided important insights into the nature of the thermally induced disorder within fluorite structured compounds. Table 2 summarises the specific techniques which provide information on the disorder processes in these systems.

Technique :	Diffraction	Coherent Diffuse Scattering (Elastic)	Coherent Diffuse Scattering (Quasielastic)	Incoherent Scattering (Quasielastic)	Inelastic (Phonons)
Description of measurement :	Determine large number of Bragg intensities.	Q distribution of coherent diffuse scattering.	Energy width of coherent diffuse scattering.	Energy width of incoherent scattering vs. Q.	Mapping phonon dispersion curves.
Information provided :	Time-averaged structure of unit cell, including interstitial sites. Thermal vibrations and expansivity.	Short-range correlations between disordered ions. Geometry of defect clusters.	Lifetimes of defects giving rise to coherent diffuse scattering.	Directions of hops and diffusion coefficient of mobile species.	Fit dispersion curves with inter-ionic potentials. Effect of disorder on elastic constants and properties.
Limitations :	Best with single crystals. T.D.S. corrections.	Concentration of defects must be large (>few%).	As left. Hard to model Q variation of widths.	Big single crystals. High instrumental resolution.	Needs good model for interionic potentials.

Table 2. Summary of the neutron scattering techniques relevant to the investigation of the fast-ion process in fluorite structured compounds.

Pure Fluorites

The fluorite structure (Fm3m) is illustrated in figure 1 with the cations in 4(a) sites at (0,0,0) and anions in 8(c) sites at ($^1/_4$,$^1/_4$,$^1/_4$). The structure can most conveniently be considered as a simple cubic array of anions, of spacing $a_0/2$, with cations occupying alternate cube centres. Single crystal neutron diffraction and coherent diffuse scattering studies of the high temperature disordered phase have been interpreted in terms of short-lived, fluctuating clusters of defective anions, comprising Frenkel pairs and surrounding relaxed anions [17]. Measurements of the quasielastic broadening of the coherent diffuse scattering within the fast-ion phase indicate that the clusters have a mean lifetime ~10^{-12} sec. The defect cluster, illustrated in figure 2, comprises anion interstitials in 48(i) sites at ($^1/_2$,u,u) with u~0.32, resulting in relaxations of the two nearest neighbour anions into 32(f) (w,w,w) sites with w~0.35.

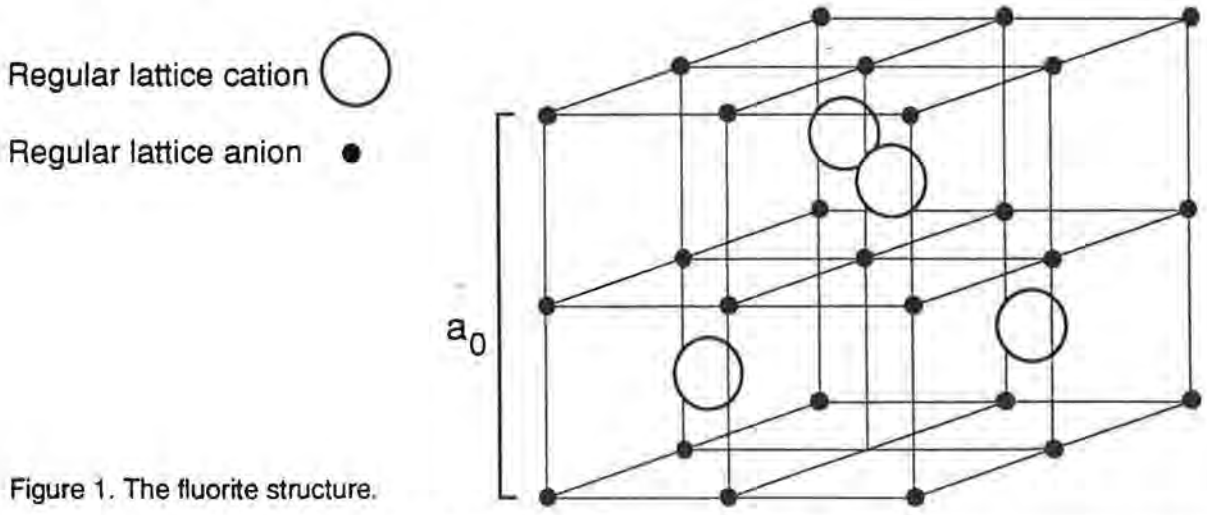

Figure 1. The fluorite structure.

A powder sample of β-PbF_2 has been studied using high resolution powder neutron diffraction, to provide detailed information on the temperature dependence of the lattice parameter, a_0, the fraction of anions leaving their regular sites (n_v) and the thermal vibration parameters [2,3]. Rietveld profile refinements have been performed on data collected at ~100 temperatures in the range 273<T(K)<1078K. The evolution of the diffraction pattern as a function of temperature is illustrated in figure 4. As shown in figure 3, anomalous behaviour of a_0 is observed in the vicinity of T_c (~700K).

The results of the neutron diffraction investigations have been used to determine the contributions to the specific heat anomaly in β-PbF_2 at T~T_c[18], arising from harmonic and

anharmonic lattice vibrations, thermally induced disorder and lattice dilation [3] (see figure 5). It is planned to apply this technique to the nuclear fission fuel UO_2, where the excess specific heat at elevated temperatures (~2500K) has important consequences for safety assessments of possible accident scenarios.

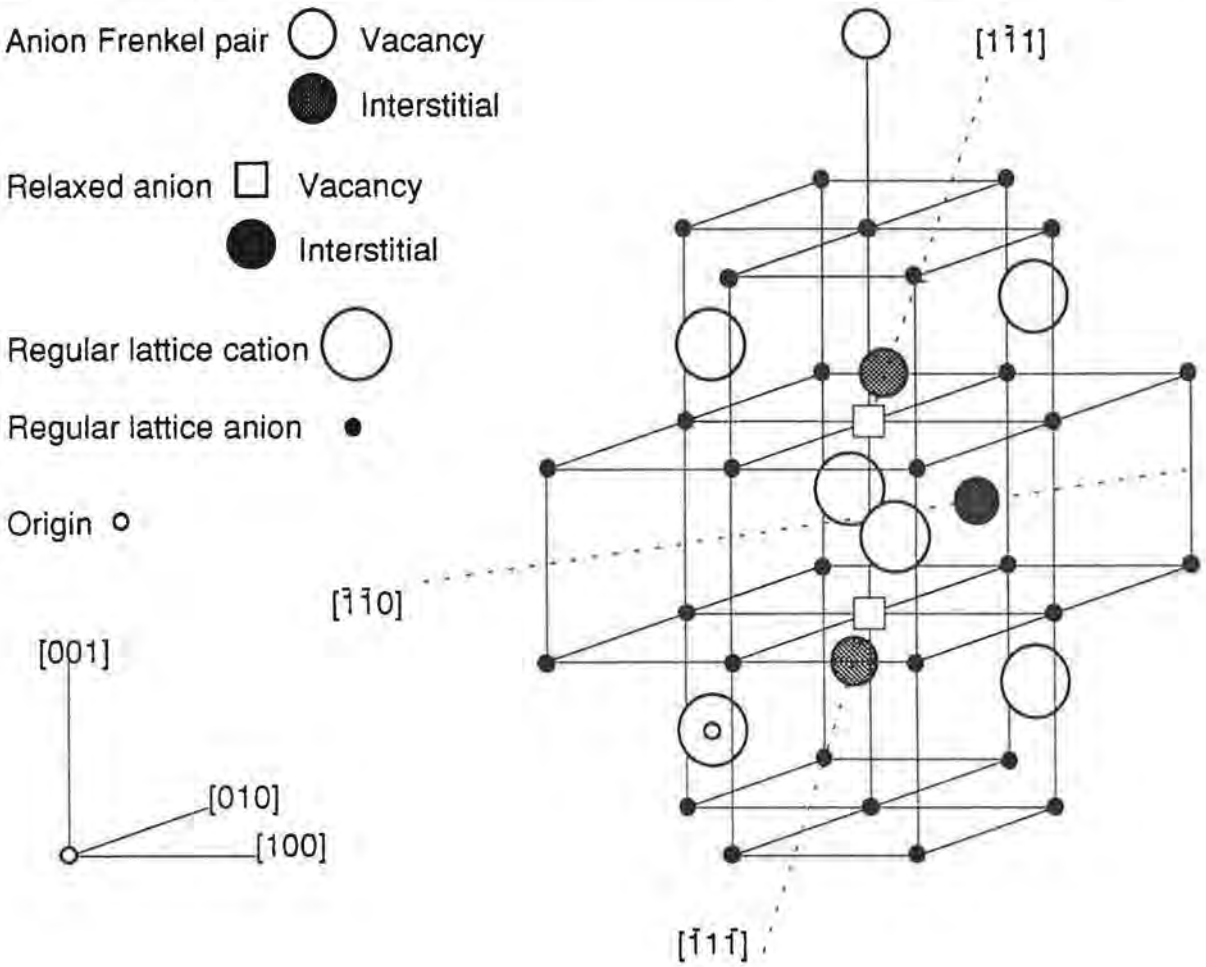

Figure 2. The high temperature defect in the fast-ion phase of fluorites [17]. The Frenkel pair comprises an interstitial anion at ($^1/_2$,u,u) and an associated anion vacancy. This causes relaxation of the two nearest neighbour anions towards empty cube centres a distance (w,w,w) from a cation site.

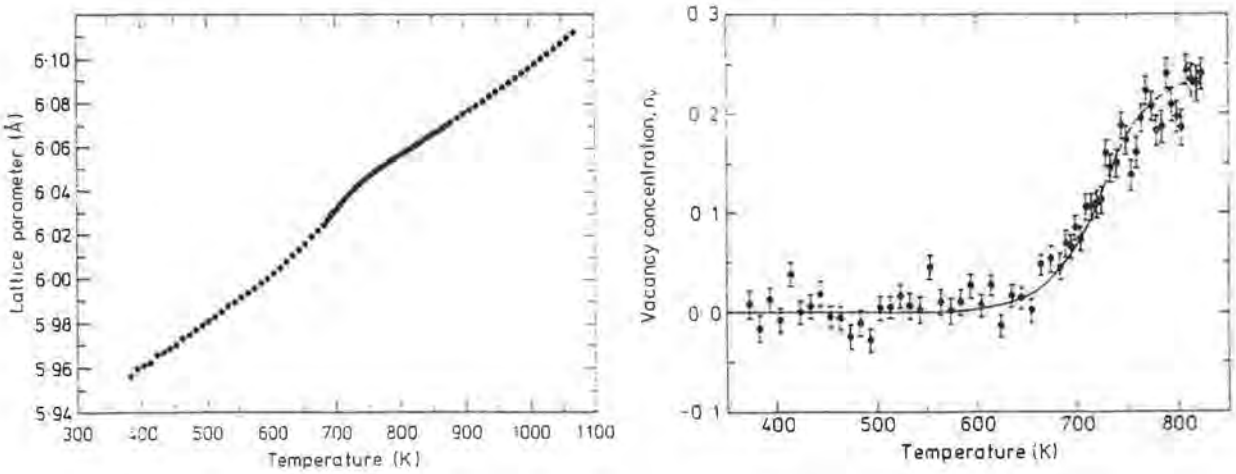

Figure 4. The temperature variation of the lattice parameter a_0 of β-PbF_2 and the concentration of vacancies on the anion sublattice, n_v.

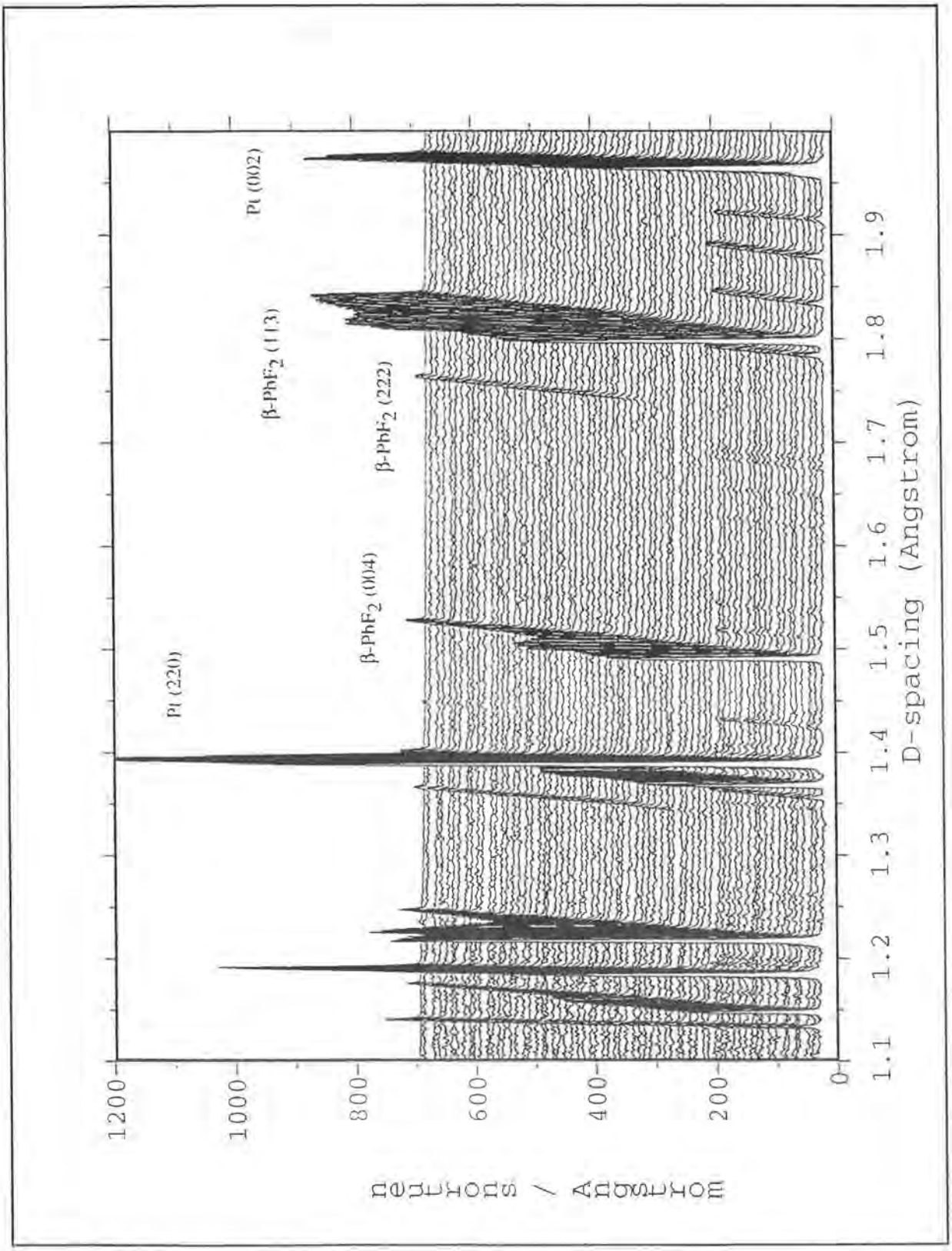

Figure 3. The evolution of the measured powder diffraction pattern from β-PbF_2 in the range from 413<T(K)<1073 in 10K steps. The weak reflections observed up to T~600K are due to a small quantity of orthorhombic α-PbF_2 present in the sample. The values of the coherent scattering lengths b_{Pb} and b_F are such that structure factor for the h+k+l=4n+2 reflections is very small. However, at the onset of fast-ion behaviour (T~700K) fluorine ions leave their lattice sites and the structure factor increases.

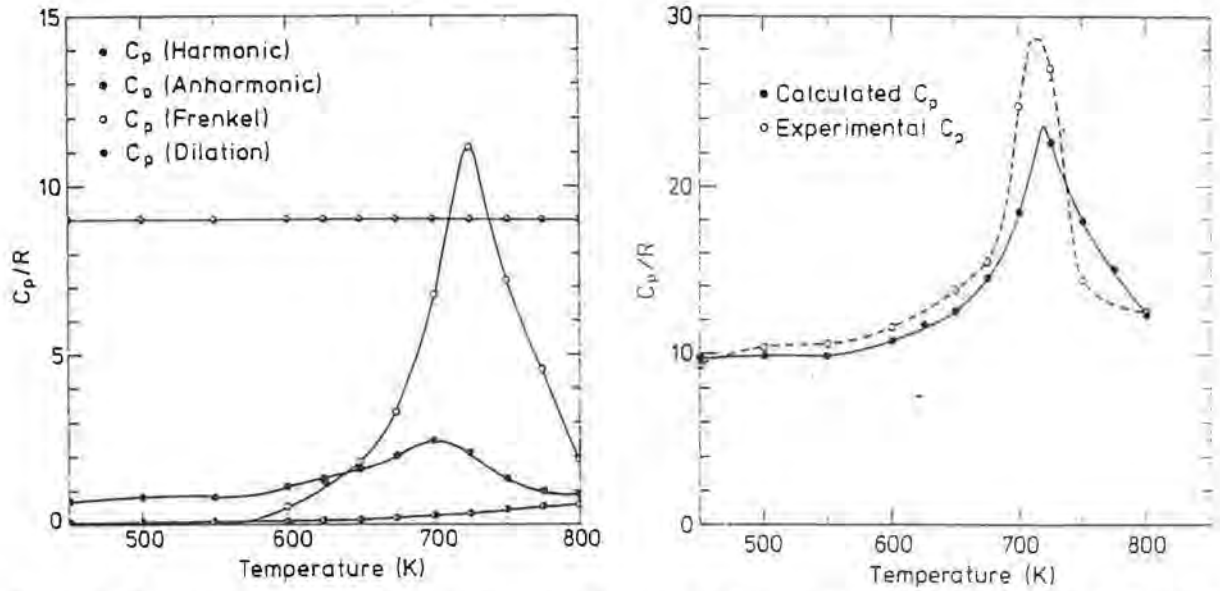

Figure 5. The contributions to the specific heat C_p of β-PbF_2 calculated using the results of neutron diffraction [2,3] and compared with that obtained by calorimeter measurements [18].

Anion Excess Fluorites

Halide compounds with the fluorite crystal structure have a remarkable ability to accommodate large concentrations of trivalent dopant ions substitutionally on the cation sites, overall charge neutrality being maintained by incorporating excess anions into the lattice. This doping dramatically reduces the fast-ion transition temperature T_c and technological interest in solid electrolytes has led to considerable research effort aimed at elucidating the structural changes which accompany doping.

The structure of the extrinsic defects in a sample of $(Ca_{1-x}Y_x)F_{2+x}$ with x=0.06 has been investigated [10,11]. A stringent test of the various defect models proposed in the literature is provided by the combined analysis of both Bragg scattering, which gives information on the average contents of the unit cell, and the coherent diffuse scattering arising from short-range correlations between disordered ions. Least-squares refinement of the Bragg intensities allowed the occupancy of the lattice anion site to vary, with the anions occupying disordered sites at (1/2,u,u), (w,w,w), (v,v,v) and (1/2,1/2,1/2), referred to as F1 to F4, respectively. The final fitted values for the structural and thermal vibration parameters are listed in table 3. The measured anion positions and site occupancies are found to agree well with those calculated on the basis of a cuboctahedral defect cluster, of the type illustrated in figure 6. The twelve anions which form the cuboctahedron lie in F1 (1/2,u,u) positions and the (v,v,v) F3 sites can be identified with small outward relaxations of the nearest neighbour lattice anions in <111> directions. The additional central anion is located at (1/2,1/2,1/2). The negligible occupancy of the disordered F2 site at (w,w,w) cannot be reconciled with the presence of 'Willis' type clusters [19] (the static equivalent of the dynamic Frenkel cluster in figure 2) or to square antiprism type clusters [20], since both incorporate additional anions at these positions.

However, Bragg diffraction does not directly determine the defect topology and the coherent diffuse scattering must be considered. Figure 7 illustrates the distribution of coherent diffuse intensity in the $(1\bar{1}0)$ plane of reciprocal space. Least-squares minimisation of the diffuse scattering data has been performed using the various defect models proposed in the literature (see [11] for a complete review) and the best fit is obtained using the cuboctahedral cluster. The final calculated diffuse scattering is shown in figure 7 and the fitted parameters are listed in table 3. The excellent agreement between the fitted parameters obtained by the independent analysis of Bragg and diffuse scattering data supports the presence of cuboctahedral type clusters in $(Ca_{1-x}Y_x)F_{2+x}$ solid solutions. Similar polyhedra are observed in several ordered anion excess fluorites [21] suggesting that they are a basic structural unit within these systems.

Atom	Site	Position	Bragg (measured)	Cuboctahedron (calculated)	Diffuse (measured)
Ca/Y	4(a)	(0,0,0)	B_{iso}=0.64(1)Å^2		
F	8(c)	($^1/_4$,$^1/_4$,$^1/_4$)	m=1.59(9) B_{11}=0.60(7)Å^2 B_{33}=0.81(9)Å^2	m=1.616	
F1	48(i)	($^1/_2$,u,u)	u=0.390(5) m=0.16(2) B_{iso}=1.4(4)Å^2	u=0.354 m=0.144	u=0.384(3) B_{iso}=1.86(8)Å^2
F2	32(f)	(w,w,w)	w=0.38(3) m=0.01(2) B_{iso}=2.2(43)Å^2	m=0.000	
F3	32(f)	(v,v,v)	v=0.270(8) m=0.31(5) B_{iso}=1.1(2)Å^2	v=0.250 m=0.288	v=0.265(5) B_{iso}=1.21(5)Å^2
F4	4(b)	($^1/_2$,$^1/_2$,$^1/_2$)	m=0.01(3) B_{iso}=3.2(55)Å^2	m=0.012	B_{iso}=4.6(33)Å^2

Table 3. The structural and thermal vibration parameters of $(Ca_{1-x}Y_x)F_{2+x}$ with x=0.06. The site occupancies, m, are given as the contribution to the overall fluorine content, 2.06.

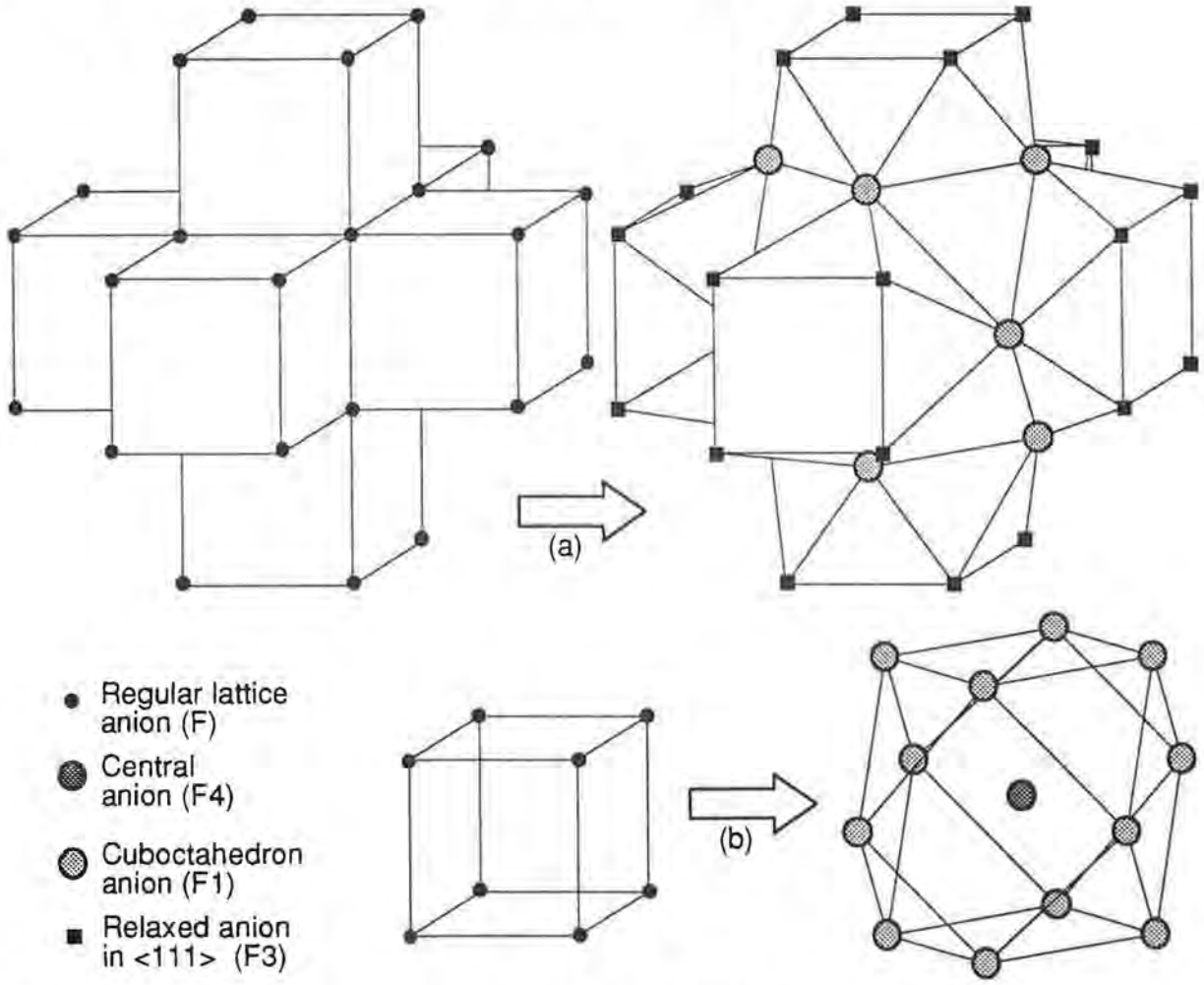

Figure 6. The formation of a cuboctahedral defect cluster by (a) the simultaneous conversion of six edge sharing $(Ca,Y)F_8$ fluorite cubes into corner sharing square antiprisms. With the additional central anion (on an F4 site) the conversion replaces a $(Ca,Y)_6F_{32}$ fragment by $(Ca,Y)_6F_{37}$, incorporating five additional anions into the lattice (b) without anomalously short F^--F^- distances.

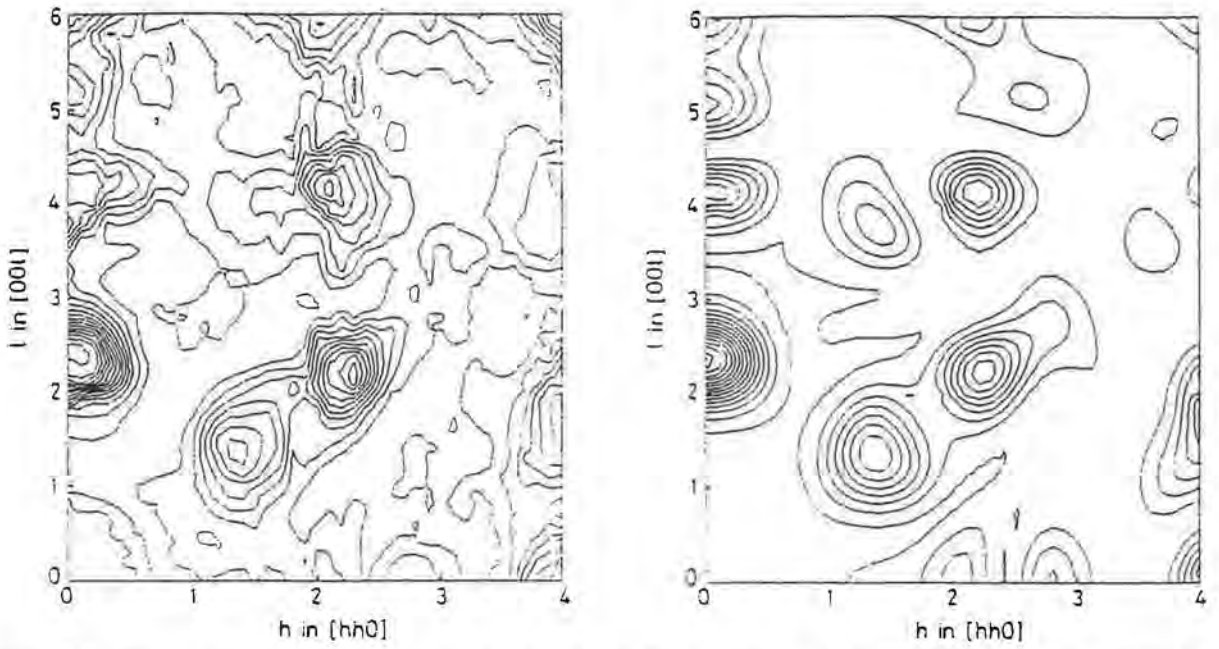

Figure 7. The measured and calculated coherent diffuse scattering in the $(1\bar{1}0)$ plane of reciprocal space from $(Ca_{1-x}Y_x)F_{2+x}$ with x=0.06, assuming a random distribution of cuboctahedral defects.

The work described above has been extended to investigate the changes in the distribution of the coherent diffuse scattering at elevated temperatures. A brief study of $(Sr_{1-x}Y_x)Cl_{2+x}$ with x=0.03 [14] (which also forms cuboctahedral defect clusters at ambient temperature) and preliminary analysis of recent, more detailed, measurements on $(Ca_{1-x}Y_x)F_{2+x}$ with x=0.06 suggest that the cuboctahedral clusters break up at temperatures below the fast-ion transition, T_c. The disorder within the fast-ion phase appears qualitatively similar to that in pure fluorites, illusrated in figure 2.

A detailed understanding of the diffusional processes in the fast-ion phase has been provided by high temperature studies of the anion excess chloride, $(Sr_{1-x}Y_x)Cl_{2+x}$ [12,13]. This compound is a particularly interesting case to study because the diffusing anion Cl^- has a significant incoherent neutron scattering cross-section. The incoherent scattering is uniformly distributed over reciprocal space but can be investigated in isolation in regions away from the coherent intensity. At ambient temperature, there is minimal anion diffusion and the incoherent scattering is elastic. However, in the fast-ion phase this becomes quasielastic, with a Lorentzian profile of width Γ which varies with $\underline{Q}$. Analysis of the measured $\Gamma(\underline{Q})$ using the Chudley-Elliott jump diffusion model has shown that the diffusion rate of Cl^- in $(Sr_{1-x}Y_x)Cl_{2+x}$ is significantly higher than in pure $SrCl_2$. However, the geometry of the diffusion process is essentially the same, as the anions hop predominantly between nearest neighbour sites in <001> directions with ~30% to next nearest neighbour sites in <110> directions.

Anion Deficient Fluorites

At room temperature pure zirconia, ZrO_2, has a monoclinic crystal structure. On heating it transforms firstly to a tetragonal phase at ~1273K and finally to a fluorite cubic structure which is stable between 2643K and the melting temperature T_m~2988K. The high temperature fluorite phase of ZrO_2 can be stabilised at ambient temperature the by addition of divalent (Ca^{2+}, Mg^{2+}, etc.) or trivalent (Y^{3+}, La^{3+}, etc.) cations. Electrical neutrality is maintained by vacancies on the anion sublattice and these defects give rise to its ionic conductivity. Yttria stabilised zirconia, $(Zr_{1-x}Y_x)O_{2-x/2}$, finds diverse technological applications within fuels cells, oxygen sensors and as artificial gemstones.

The defect structure of $(Zr_{1-x}Y_x)O_{2-x/2}$ has been investigated by measuring the coherent diffuse scattering as a function of concentration x in the range $0.09<x<0.24$ and temperature to 2700K [16]. In the anion deficient fluorite structure the O^{2-} vacancies order to form clusters (~10-20Å in size),

whilst in relatively vacancy free regions the oxygen sublattice undergoes a slight tetrahedral distortion (figure 8a), tending towards the tetragonal structure adopted at x<0.08. This gives rise to broad peaks observed at the forbidden fluorite positions in reciprocal space, such as (112) and (114). The clusters are based on vacancy pairs centred on a cation, with some relaxation of the surrounding anions and cations (figure 8c) in <001> and <111> directions, respectively. The pairs aggregate to form the clusters with a packing scheme resembling the structure of the ordered phase $Zr_3Y_4O_{12}$. The defects give rise to diffuse scattering observed at superlattice positions ±(0.4,0.4,±0.8) with respect to the fluorite reciprocal lattice points. A broad hump in the scattering occurs at $\underline{Q}$~(1.7,1.7,1.0), due to isolated single vacancies (figure 8b). As the x increases the (112) type features decrease in intensity, as the vacancy free regions become smaller, and the latter increases as more clusters are formed (figure 9).

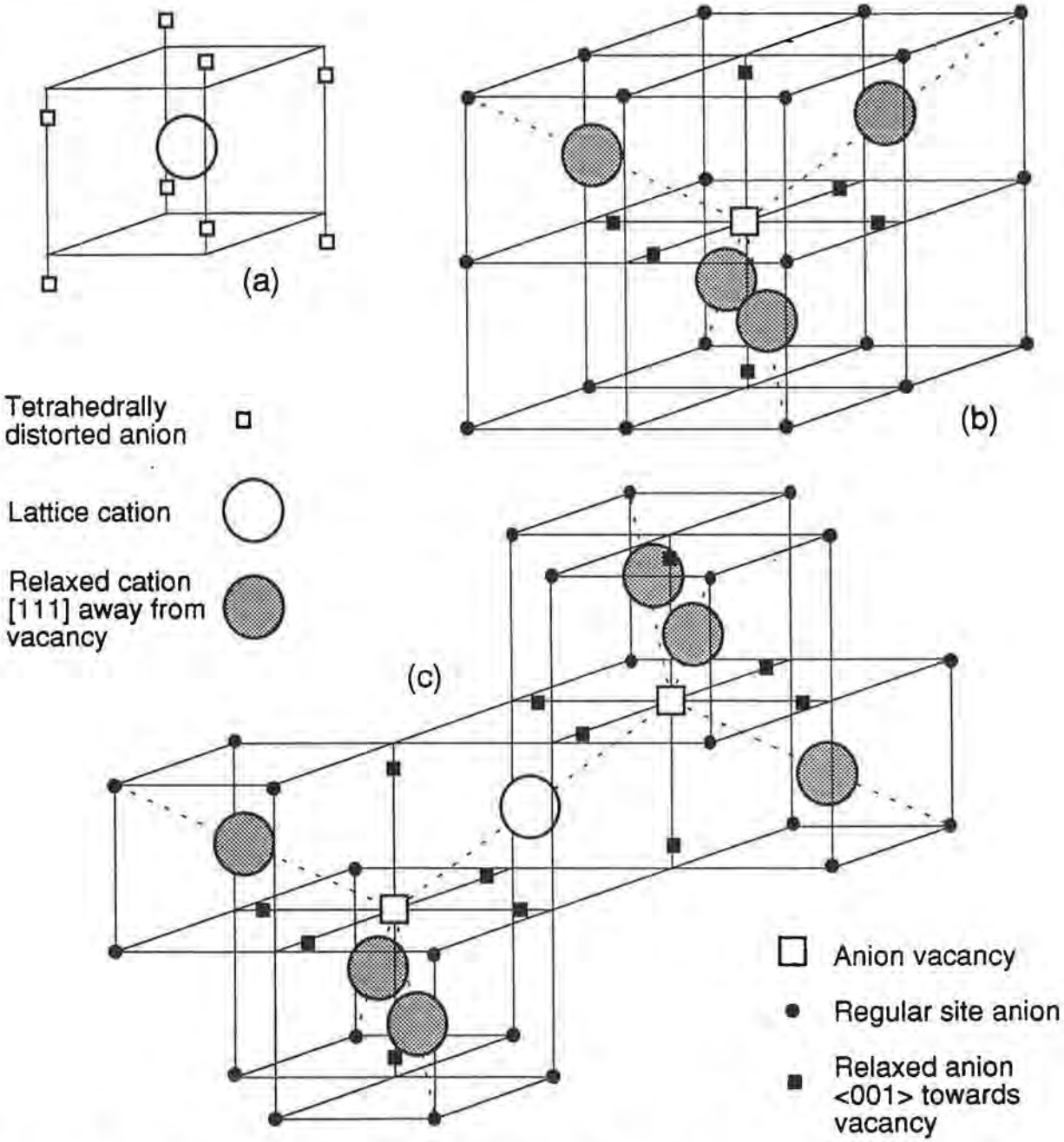

Figure 8. The defect clusters formed in $(Zr_{1-x}Y_x)O_{2-x/2}$ for 0.09<x<0.24. At x<~0.15 regions of the crystal undergo a tetrahedral distortion (a) whilst on increasing x there are increasing numbers of single vacancies (b) and clusters of vacancy pairs (c), both with a surrounding relaxation field.

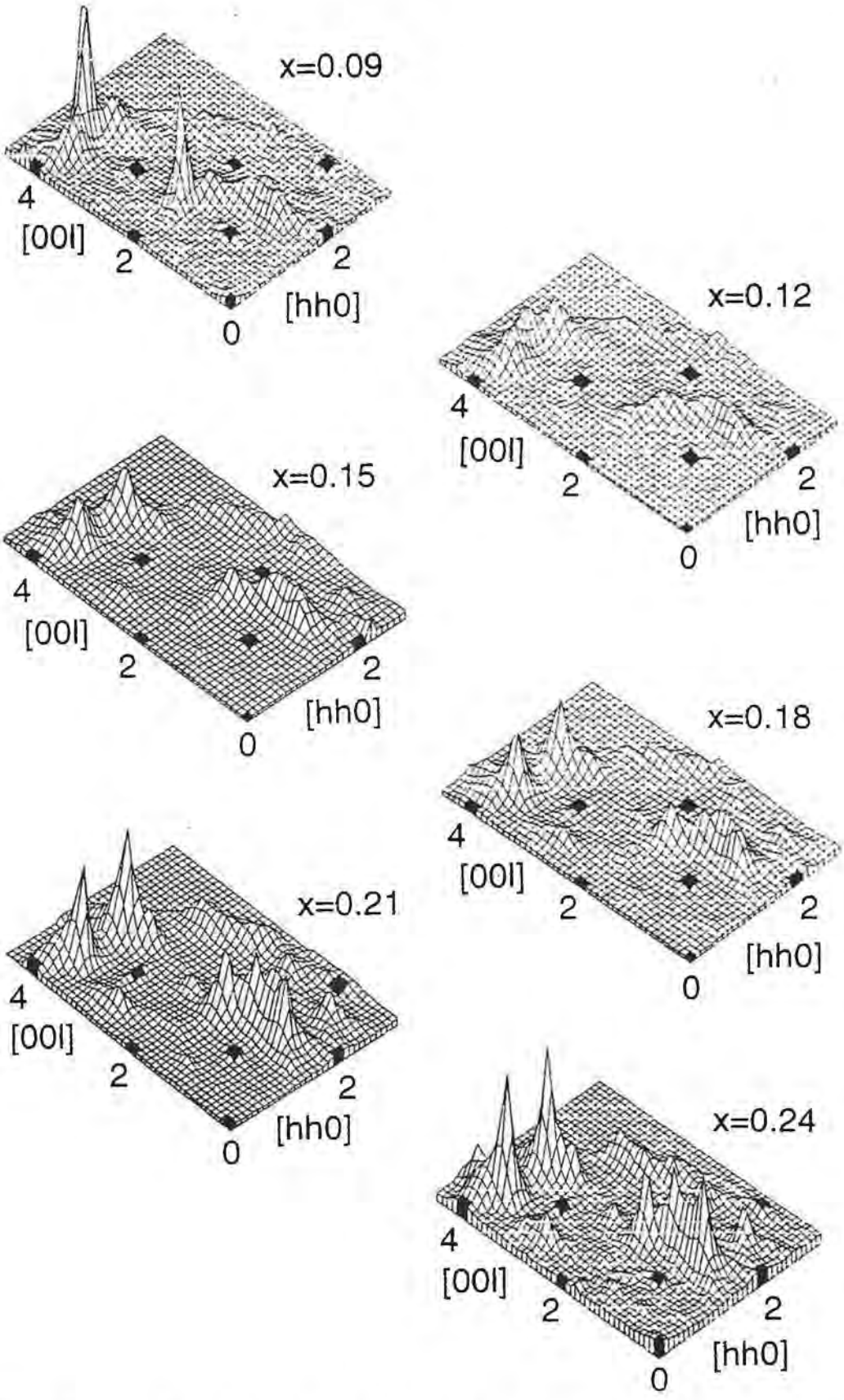

Figure 9. The evolution of the coherent diffuse scattering in the $(1\bar{1}0)$ plane of reciprocal space from $(Zr_{1-x}Y_x)O_{2-x/2}$ with concentration x. For reasons of clarity the Bragg peaks have been removed.

Having identified the regions of reciprocal space where coherent diffuse scattering arises predominantly from one defect species the defect dynamics can be studied by observing the quasielastic energy broadening of the diffuse scattering at high temperatures. As illustrated in figure 10a and 10b, the diffuse scattering arising from the vacancy pair clusters remains predominantly elastic up to very high temperatures, indicating that the defects remain static. However, there is significant broadening of that due to single vacancies (figure 10c & 10d) and the tetrahedral distortions (not shown). The former illustrates the diffusion of vacancies at high temperature and the latter shows that the tetrahedral distortion has an increasingly short lifetime, either due to fluctuations between tetragonal and cubic symmetry or to the diffusion of vacancies.

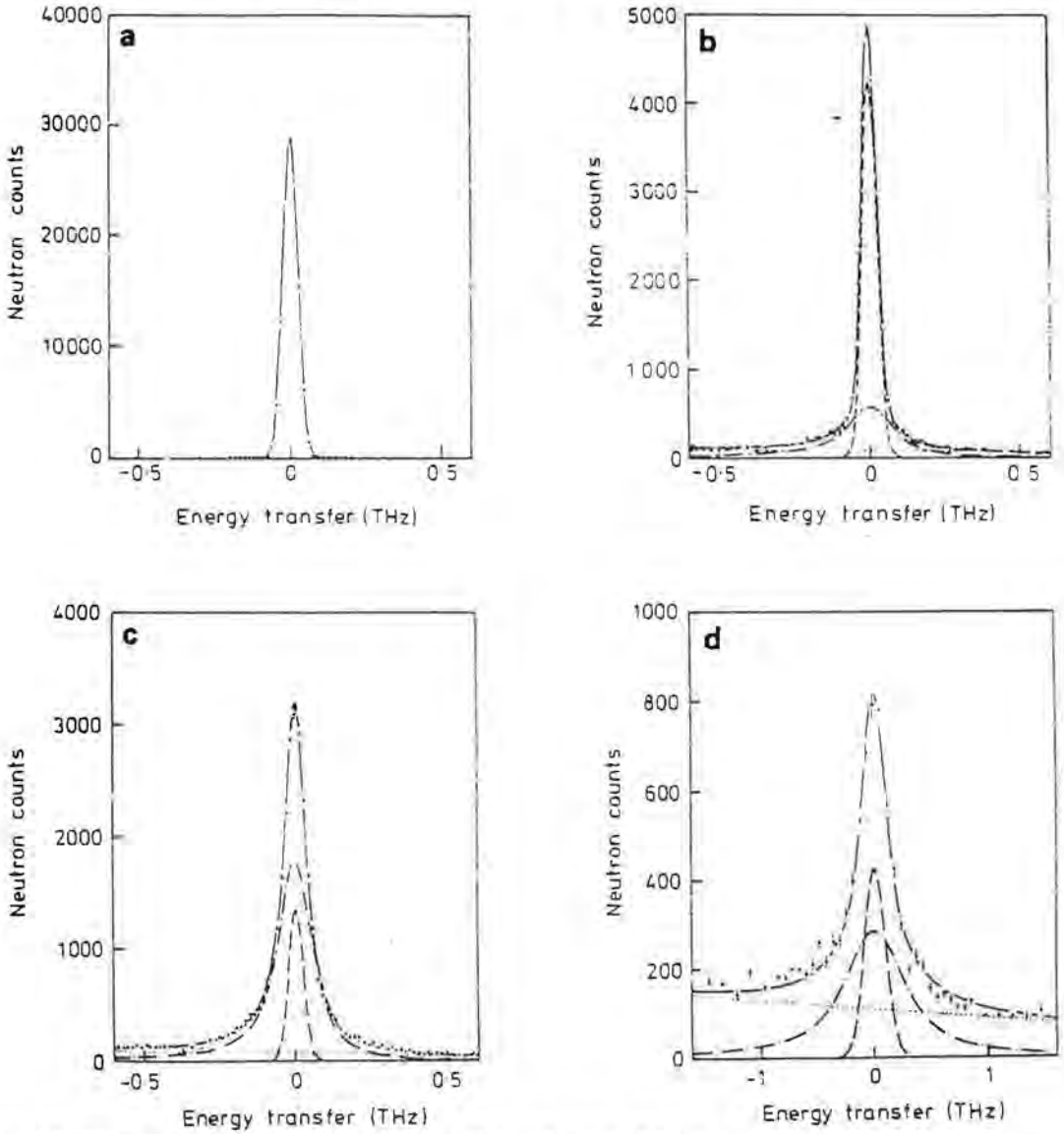

Figure 10. The quasielastic broadening of the coherent diffuse scattering in $(Zr_{1-x}Y_x)O_{2-x/2}$ due to vacancy pair clusters (a) x=0.12, $\underline{Q}$=(1.4,1.4,1.8), T=293K, (b) x=0.12, $\underline{Q}$=(1.4,1.4,1.8), T=1825K and from single vacancies (c) x=0.12, $\underline{Q}$=(1.7,1.7,1.0), T=1825K, (d) x=0.18, $\underline{Q}$=(1.7,1.7,1.0), T=2700K.

Antifluorites

Several alkali metal oxides and sulphides (eg. Li_2O, Li_2S, Na_2O) crystallise in the antifluorite structure in which the anions and cations are exchanged with respect to fluorite. Relatively little research effort has been devoted to these compounds or to the possibility of fast-ion behaviour analogous to that observed in the fluorites.

Diffraction measurements have been performed using single crystal $^7Li_2O$ in the range 293<T(K)<1603 [5]. The observed Bragg peak intensities have been successfully analysed using models of the time-averaged structure, with harmonic and anharmonic temperature factors to describe the effects of thermal vibration. The regular antifluorite arrangement accounts well for the structure up to 873K but the data at higher temperatures can only be well fitted if a fraction of cations leave their regular sites. This provides direct evidence for a disordered fast-ion phase within an antifluorite. In the fast-ion phase of Li_2O, mobile lithium ions occupy mean positions very close to the midpoint of the cube edge (see figure 2). The fraction of lithium ions occupying these cube-edge sites increases rapidly in the region of T~1200K (figure 11). There is evidence for slight <111> relaxations of the two nearest neighbour lithium ions towards the empty cube centres. However, the extent of the relaxation is less than in the fluorites, as might be expected with the smaller diffusing ion.

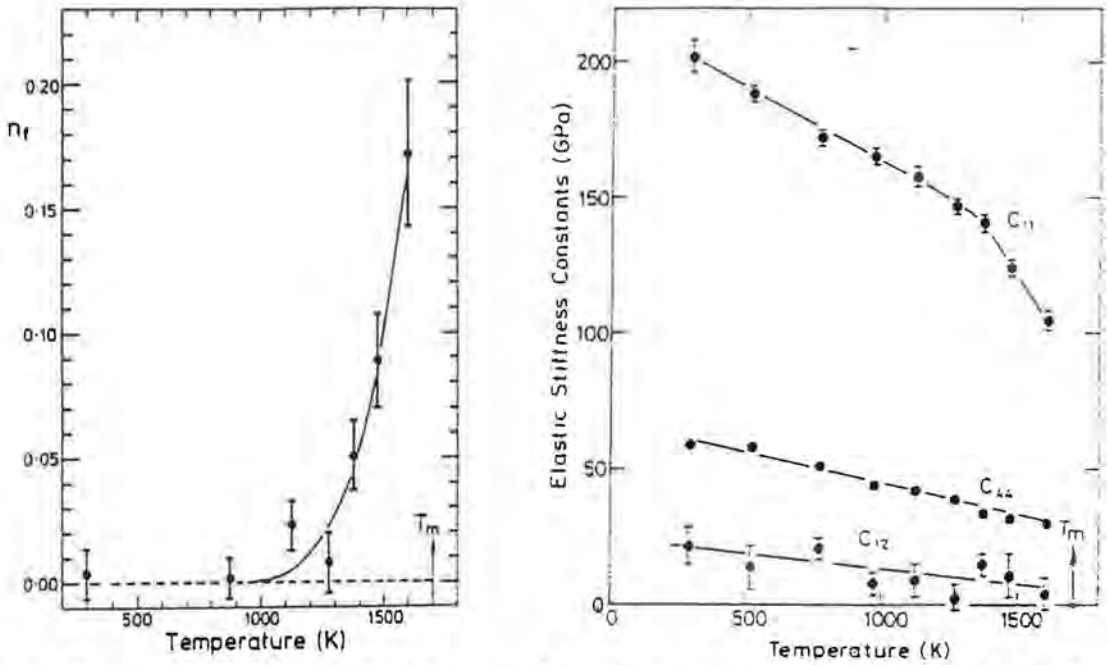

Figure 11. Temperature variation of the fraction of cations leaving their regular sites to form Frenkel interstitials, n_f, and the elastic stiffness constants, C_{ij}, of Li_2O.

The complete phonon energy dispersion curve of Li_2O has been measured at 293K using inelastic neutron scattering and fitted to rigid-ion and shell models for the interionic potentials [7]. The rigid-ion model assumes only a short-range core interaction between ions and an improved fit to the data, particularly the optic phonon branches, can be obtained using the shell model. The latter contains additional parameters describing the electrical polarisability and the short range mechanical polarisability and yields information on the dielecric properties of Li_2O. Attempts to vary the ionic charge gave a value close to +1.0 for Li^+, indicating essentially ionic bonding. The interionic potentials derived in this work have been used in computer simulations of the defect structures and confirm that intrinsic Frenkel disorder of the cation sublattice is energetically favourable to Schottky defect formation in Li_2O [22]. The temperature variation of the elastic constants of Li_2O has been determined by single crystal measurements of the acoustic phonon dispersion curves [8]. C_{11} is found to undergo a sharp decrease above ~1350K, giving further confirmation of a fast-ion transition at high temperature (figure 11). These results have been used to determine the Young's modulus, shear modulus, bulk modulus and Poisson's ration of Li_2O at elevated temperatures, important for its proposed technological applications as a tritium breeder material in future D-T fusion reactors [8].

An investigation of the antifluorite Mg_2Si is also in progress, motivated by conductivity evidence for a fast-ion phase in this predominantly covalent material [23]. Weak coherent diffuse scattering has been observed at T=1313K (~0.97T_m) [9] and described in terms of Frenkel defect clusters of the type illustrated in figure 2, but with a larger surrounding relaxation field. Diffraction data at high temperature is currently being analysed, to confirm the interstitial and relaxed anion sites.

Conclusions

Neutron scattering techniques can provide fundamental information on the fast-ion conduction process within fluorite structured compounds. Specifically, powder diffraction studies can give detailed information on the evolution of the structural disorder as a function of temperature. Diffraction and coherent diffuse scattering measurements using single crystals allow the structure of the intrinsic, thermally induced Frenkel clusters to be determined and compared with that of the extrinsic defects formed by doping with cations of a different valence. Quasielastic measurements of the coherent and incoherent scattering give a direct insight into the dynamics of the disorder, by probing the defect lifetimes and hopping rates, respectively. The interionic potentials can be modelled using the measured phonon energy dispersion relations and the elastic properties of these important materials can be investigated at elevated temperatures, via the elastic constants.

References

[1] W.Hayes and M.T.Hutchings, in: Ionic Solids at High Temperatures, ed. A.M.Stoneham (World Scientific, Singapore, 1989) Chapter 4, and references therein.
[2] S.Hull. M.T.Hutchings, J.P.Goff and W.Hayes, Physica B, 174, 91 (1991)
[3] J.P.Goff, W.Hayes, S.Hull and M.T.Hutchings, J. Phys.: Condens. Matter, 3, 3667 (1991)
[4] K.N.Clausen, M.A.Hackett, W.Hayes, S.Hull, M.T.Hutchings, J.E.MacDonald, K.A.McEwen, R.Osborn and U.Steigenberger, Physica B 156&157, 103 (1989)
[5] T.W.D.Farley, W.Hayes, S.Hull, M.T.Hutchings and M.Vrtis, J. Phys.: Condens. Matter, 3, 4761, (1991)
[6] T.W.D.Farley, W.Hayes, S.Hull, R.Ward, M.T.Hutchings and M.Alba, Solid State Ionics, 28-30, 189, (1988)
[7] T.W.D.Farley, W.Hayes, S.Hull, M.T.Hutchings, M.Alba and M.Vrtis, Physica B, 156&157, 99 (1989)
[8] S.Hull, T.W.D.Farley, W.Hayes and M.T.Hutchings, J. Nucl. Mater., 160, 125 (1988)
[9] M.T.Hutchings, T.W.D.Farley, M.A.Hackett, W.Hayes, S.Hull and U.Steigenberger, Solid State Ionics, 28-30, 1208 (1988)
[10] S.Hull and C.C.Wilson, Physica B, 180&181, 585 (1992)
[11] S.Hull and C.C.Wilson, J. Solid State Chem., 100, 101 (1992)
[12] J.P.Goff, K.Clausen, B.Fåk, H.Godfrin, R.Hadfield, W.Hayes, S.Hull and M.T.Hutchings, Physica B, 180&181, 819 (1992)
[13] J.P.Goff, W.Hayes, S.Hull, M.T.Hutchings and R.C.C.Ward, Physica B, 182, 307 (1992)
[14] J.P.Goff, M.T.Hutchings, S.Hull, B.Fåk and W.Hayes, J. Phys.: Condens. Matter, 4, 1433 (1992)
[15] N.H.Andersen, K.Clausen, M.A.Hackett, W.Hayes, M.T.Hutchings, J.E.MacDonald and R.Osborn, Physica 136, 315 (1986)
[16] S.Hull, T.W.D.Farley, M.A.Hackett, W.Hayes, R.Osborn, N.H.Andersen, K.Clausen, M.T. Hutchings and W.G.Stirling, Solid State Ionics, 28-30, 488 (1988)
[17] M.T.Hutchings, K.Clausen, M.H.Dickens, W.Hayes, J.K.Kjems, P.Schnabel and C.Smith, J. Phys. C: Solid State Phys. 17, 3903 (1984)
[18] N.H.Andersen, K.Clausen and K.J.Kjems, Solid State Ionics, 9&10, 543 (1983)
[19] B.T.M.Willis, Proc. Brit. Ceram. Soc., 1, 9 (1964)
[20] J.P.Laval and B.Frit, J. Solid State Chem., 49, 237 (1983)
[21] A.M.Golubev and V.I.Simonov, Sov. Phys. Crystallogr., 31, 281 (1986)
[22] A.V.Chadwick, K.Flack, J.H.Strange and J.H.Harding, Solid State Ionics, 28-30, 185 (1988)
[23] R.G.Morris, R.D.Redin and G.C.Danielson, Phys. Rev., 109, 1909 (1958)

Algorithm And Techniques For Refinement Of Twin Crystal Structures

M.I.Sirota
Institute of Crystallography, Russian Academy of Sciences, Moscow

Introduction

Precision investigations of crystal structures have revealed that microtwinning is a fairly widespread phenomenon. In particular, this effect accompanies phase transitions of crystals to ferroelectric and ferroelastic phases; it is often observed in solid electrolytes and most compounds possessing high-temperature superconductivity. In precision investigations of crystals of such materials one often needs to take account of twinning at the stage of least-squares refinement of structural parameters. For this purpose one adds to the list of refinable parameters coefficients to unify the scale of the structure factors of each twin partner. The values of these scale parameters allow one to estimate the relative volumes of the twin partners in the test specimen. The contribution of one partner, separated from the set of the observed structure factors, can be used for further refinement of positional and thermal parameters of the atoms and calculations of the electron density distribution corresponding to this twin partner alone.

Microtwinning and least-squares refinement

The INCRYS [1] program system is intended for the solution of a wide range of problems arising in the structure analysis of monodomain, microtwinned crystals and powdered specimens. The RFTWIN [2] procedure, which is included in this system, enables one to use the least-squares procedure to refine the structures of monodomain and microtwinned crystals, with both isotropic and anisotropic atomic thermal vibrations and allowance for anomalous scattering and isotropic extinction. Refinement of microtwins is possible both for merohedral and reticular-merohedral twinning [3]. We assume that all the twin partners have the same structure but differ by their positions relative to one another. The relative positions of the twin partners obey the symmetry elements (laws) of twinning.

To begin the operation of the RFTWIN procedure it is necessary to know the approximate atomic model of the structure and the twinning laws determining the relative positions of twin partners. The twinning laws can be written in the form of equations transforming the indices of reflections in reciprocal space

$$(H_i, K_i, L_i) = A_i \begin{bmatrix} h \\ k \\ l \end{bmatrix} \qquad (1)$$

where A_i are the transformation matrices.

To refine the structural parameters we use full-matrix least-squares, in which the refinement is performed by minimization of the function

$$S = \sum_{\underline{H}} \left[\frac{F_o^2 - F_c^2}{\sigma(F_o^2)} \right]^2 \qquad (2)$$

where $\sigma(F_o^2)$ is the standard deviation of F_o^2. The summation in (2) is made over the whole set of reflections. If one refines a microtwinned crystal, the structure factors at each step of the refinement are calculated by the expression

$$F_c^2 = \sum_{i=1}^{M} k_i^2 \left| F_c^{(i)} \right|^2 y^{(i)} \qquad (3)$$

where M is the number of twin partners in the test specimen and k_i is the coefficient describing the reduction of the calculated structure factor F_c^i of the i-th partner to a common scale. The h, k, l indices of the F_c^i factors are transformed by the matrices A_i (i=1,...,M) that determine the twinning laws as defined in equation (1). In the refinement of a monodomain specimen the value of M in (3) becomes equal to unity. The $y^{(i)}$ is the value of the correction factor that takes account of isotropic extinction of a particular reflection due to the i-th partner.

In precision investigations of atomic structures it is often necessary to take into account this extinction effect. The first approximate correction suitable for practical use was suggested for secondary extinction by Zachariasen [4]. In the Becker-Coppens formalism [5,6] used in the RFTWIN procedure, the Zachariasen theory is revised and extended. In particular, these authors treated both secondary and primary extinction. The analytical expression for the primary and secondary extinction corrections according to Becker and Coppens can be found in References [5] and [6].

The contributions of a twin partner to F_o and to the standard deviations $\sigma(F_o)$ are calculated using the expressions

$$F_o^{(i)} = kF_o/y^{(i)}\ ,\ \sigma(F_o^{(1)}) = k\sigma(F_o) \qquad (4)$$

where $k = k^{(1)}|F_c^{(1)}|/|F_c|$, $k^{(1)}$ is the coefficient of reduction of the calculated structure factors $F_c^{(1)}$ of one twin partner to a common scale and $y^{(1)}$ is the extinction correction for this partner. If the extinction is not refined, $y^{(1)} = 1$.

X-ray structural investigation of microtwinning of $Li_3Sc_2(PO_4)_3$ and $Li_3Fe_2(PO_4)_3$ crystals

Superionic lithium conductors of the composition $Li_3M_2(PO_4)_3$, where M = Sc or Fe. [7] were studied by X-rays at temperatures above and below the superionic phase transition. The main results of these structural investigations were as follows: (i) The single crystals $Li_3Sc_2(PO_4)_3$ and $Li_3Fe_2(PO_4)_3$ are isostructural; (ii) In the high ionic conductivity state the crystals are orthorhombic with space group Pcan. The high-temperature phase was refined to a final R factor of about 3%.

Below the superionic phase transition point, the $Li_3M_2(PO_4)_3$ crystals are monoclinic with marked pseudorhombicity, the degree of which depends on the specimen history. The lowering of symmetry to the monoclinic space group $P2_1/n$ with the conservation of the symmetry elements 2[100], 2_1[010], c(100), and a(010), as pseudosymmetry elements, was indicated by the presence of very weak h0l-type reflections with h = 2n+1 and the 0kl type reflections with l = 2n+1. This led to the hypothesis that the $Li_3M_2(PO_4)_3$ crystals exhibited microtwinning at temperatures below the phase transition to the superionic state. Such twinning can be effected either by any of two-fold axes parallel to the [100] or [010] directions, or by any of the symmetry planes m(100) or m(010).

In order to determine the atomic structure of $Li_3M_2(PO_4)_3$ and elucidate the effect of microtwinning on the structural parameters, we refined atomic models, with and without taking microtwinning into account, from experimental data collected from various specimens over a wide range of temperatures where the low-temperature phase exists. We refined the coordinates of all the basis atoms, their anisotropic temperature factors, extinction parameter, and the scale factors for the reduction of the intensities of the twin partners to a common scale, within the space group $P2_1/n$ with the m(100) twinning plane. The refinement of the atomic models without allowance for microtwinning was made in the same approximations. Table 1 gives some data for the atomic structures of the low-temperature phases of $Li_3M_2(PO_4)_3$ crystals refined by the experimental data from specimens with various v_1/v_2 ratio (where v_1 and v_2 are the volumes of the first and second twin partners) obtained at various temperatures. The R and R_w-factors obtained from the refinement with no allowance for microtwinning are given in parentheses in Table 1.

Table 1

Refinement parameters for $Li_3Sc_2(PO_4)_3$ and $Li_3Fe_2(PO_4)_3$

	$Li_3Sc_2(PO_4)_3$		$Li_3Fe_2(PO_4)_3$		
	293 K	**473 K**	**293 K (before annealing)**	**293K (after annealing)**	**513 K**
v_1/v_2	1.9	1.3	7.5	1.2	3.1
a (Å)	8.853	8.857	8.565	8.533	8.588
b (Å)	12.273	12.327	12.005	11.970	12.112
c (Å)	8.802	8.816	8.612	8.589	8.638
$R_{av}^{(mon)}$ (%)	4.4	4.5	3.1	2.9	3.2
$R_{av}^{(ort)}$ (%)	10.3	6.8	22.6	5.8	11.7
R_w (%)	3.0(9.5)	4.7(5.9)	3.0(6.7)	3.9(14.1)	4.5(5.3)
R (%)	4.4(12.3)	6.4(7.2)	2.7(5.6)	3.7(13.5)	3.8(4.6)

The reliability factors R and weighted R_w, the 'cleanness' of the difference electron density maps, the interpretation of the thermal vibrations of the atoms, and the agreement with the crystal-chemical standard interatomic distances suggested that the atomic models of the $Li_3M_2(PO_4)_3$ crystals obtained with allowance for microtwinning are more reliable.

The effect of microtwinning on the structure parameters thus established allows one to draw the following conclusions: (i) If $v_1/v_2 = 7.5$, the effect of microtwinning can be neglected; (ii) If $v_1/v_2 \approx 2$, the determination of the exact values of the thermal and positional parameters of the structure requires allowance to be made for microtwinning; (iii) If $v_1/v_2 \approx 1$, a reliable model for the atomic structure cannot be determined without allowance for microtwinning.

Neutron-diffraction investigation of microtwinning of NdF_3

Crystals of NdF_3 belong to the tysonite structural type, which occurs in highly nonstoichiometric fluoride phases formed in MF_m-RF_n (m < n <4) systems. The tysonite phases in MF_2-RF_3 systems (where *M* and *R* are alkaline-earth and rare-earth elements respectively) are of interest not only for their unusual atomic structure but also because of their optical (laser) and electrical (fluorine-anion conductivity) properties, both of which are controlled by the ratio *M*/*R*. We have determined the space group of NdF_3 [8] and detected the effect of twinning in this material.

A cylindrical specimen of diameter 7.5 mm and height 10 mm was used in the neutron diffraction study. The intensity data were measured with the NED ICAN full-circle diffractometer. The crystallographic characteristics of the NdF_3 crystal are as follows: a = 7.030(2), c = 7.200(2) Å, z = 6. Symmetrically equivalent reflections were averaged within the 6/mmm and $\bar{3}$m Laue symmetry groups and the corresponding R factors of averaging for the complete intensity set were 5.81 and 4.94%, respectively.

Analysis of the data refined in the hexagonal space group $P6_3cm$ (final R factors R = 7.14%, R_w = 7.78%) showed that the thermal parameters obtained are unrealistic. For example, the thermal parameters did not correspond to an ellipsoid for the F4 atom. There is also no structural basis for the observed scatter in the B_{eq} values for the fluorine atoms, from 0.48 to 2.5 Å^2, while the much heavier Nd atom has a B_{eq} value larger than that for the F1 atom (Table 2).

The refinement of the NdF_3 structure in the trigonal space group $P\bar{3}c1$ also resulted in unsatisfactory agreement (R_w = 23.0%, R = 19.5%). The next step was therefore to check merohedric twinning by the m(110) plane. In such a situation, the hkl and khl reflections from two independent twin partners superpose, which raises the diffraction symmetry from the group $\bar{3}$m to the group 6/mmm, if the v_1 and v_2 volumes of the twin partners are equal.

These hexagonal and trigonal models differ in the location of some fluorine atoms. The refinement of the structure with allowance for twinning, the isotropic extinction and the anisotropic thermal vibration

of the atoms led to the following final values of the R-factors: $R_w = 2.11\%$ and $R = 1.91\%$, at $v_1/v_2 = 0.831$. Table 2 gives the coordinates of the basic atoms and their isotropic equivalent thermal parameters.

Table 2

Refined parameters for NdF_3

		$P6_3cm$			
Atom	**Multiplicity**	**x/a**	**y/b**	**z/c**	**B_{eq}**
Nd	6	0.3252(4)	0	1/4[$]	0.53(5)
F1	2	0	0	0.321(2)	0.48(7)
F2	4	1/3	2/3	0.223(2)	2.5(2)
F3	6	0.2829(7)	0	0.581(1)	1.4(1)
F4	6	0.3767(5]	0	0.920(1]	2.2(1)
		$P\bar{3}c1$			
Atom	**Multiplicity**	**x/a**	**y/b**	**z/c**	**B_{eq}**
Nd	6	0.3414(1)	0	1/4	0.23(2)
F1	2	0	0	1/4	1.17(3)
F2	4	1/3	2/3	0.3145(2)	0.70(3)
F3	12	0.3104(1)	-0.0579(1)	0.5805(1)	0.93(3)

The correction for twinning for the trigonal space group shows that NdF_3 has the space group $P\bar{3}c1$, since the trigonal symmetry gives not only lower R_w and R values but also more physically realistic thermal vibration parameters. In this case, the thermal vibrations for all basic atoms are described by ellipsoids, while the B_{eq} values correspond to the atomic weights and to the atomic positions in the structure.

X-ray structural investigation of microtwinning of $Na_3Lu[Si_2O_7]$

$Na_3Lu[Si_2O_7]$ crystals were obtained by hydrothermal synthesis in the Na_2O-BaO-Lu_2O_3-SiO_2-H_2O system [12], under applied pressure of 1 Kbar and T = 450°C. The parameters of the hexagonal unit cell are a = 9.385(1), c = 13.716(2) Å. This compound is related to $A_3M[Si_2O_7]$-type phases and the idealized model of the structure has $P6_3/mmc$ symmetry. The models of real structures, however, become somewhat distorted, depending on the nature of the alkali cations *A* and the trivalent cations *M*, leading to a lowering of the actual symmetry of the real structures.

Table 3

Space groups of various $A_3M[Si_2O_7]$ phases

Compound	**Space group**	**r_M(Å)**	**References**
$Na_3Sc[Si_2O_7]$	*Pbnm*	0.81	[10]
$Na_3Lu[Si_2O_7]$	*$P6_3/m$*	0.85	Our data
$Na_3Tm[Si_2O_7]$	*$P6_3$*	0.87	[11]
$Na_3(Y,Sc)[Si_2O_7]$	*$P6_3$*	0.92 0.81	[12]
$Na_3Y[Si_2O_7]$	*$P6_3/m$*	0.92	[13]
$K_3Eu[Si_2O_7]$	*$P\bar{6}$ c2*	0.98	[14]

[$] The value defining the origin taken as z/c for the Nd atom in space group $P\bar{3}c1$.

Table 3 gives the data on the symmetry of a number of phases with the $A_3M[Si_2O_7]$ structural type.. It can be seen from this that as the radius r_M of the cation M increases, the symmetry tends to rise from the orthorhombic group Pbnm for $Na_3Sc[Si_2O_7]$ to the hexagonal group $P\bar{6}c2$ for $K_3Eu[Si_2O_7]$. It was therefore assumed that the symmetry of the phase under investigation must be either orthorhombic or hexagonal. The R factors after averaging of the equivalent reflections in the Laue groups 6/m, mmm and 2/m were equal to 0.08, 0.11 and 0.04, respectively.

The first attempt to refine the structure model was undertaken in the hexagonal space group $P6_3/m$. The results from this, however, were unsatisfactory: the R factor was equal to 0.092 with anomalously high B_{eq} values for the oxygen atoms. Moreover, the refinement with anisotropic thermal vibration parameters led to degeneracy of some thermal vibration ellipsoids. Attempts to refine the model in the monoclinic system (space group $P2_1/m$) were also unsatisfactory. The geometrical characteristics of the model were much worse; the scatter in the thermal parameters increased, and a strong correlation between the positional parameters of atoms related by the hexagonal symmetry appeared.

After absorption was taken into account by a semiempirical method, implemented within the DIFABS program [18], the scatter in the intensities of the equivalent reflections was reduced to $R_{av} = 0.036$ in the Laue group 6/m, but the reliability factor R_{iso} remained unchanged (0.086).

As mentioned above, an idealized model of the given structural type had symmetry $P6_3/mmc$ (Laue class 6/mmm). Owing to distortion of the crystal framework, the real symmetry of the compound either reduced to orthorhombic (the Laue class mmm) or remained hexagonal in the Laue class 6/m. The disappearance of symmetry elements relative to the idealized model was due only to slight distortions of the structural framework. This allowed us to regard the vanished elements as pseudosymmetry elements, and we know that twinning laws are determined by pseudosymmetry elements. Proceeding from the symmetry of the diffraction pattern, we can can choose between two possible variants of twinning in this material: (a) the element which accounts for the twinning law may be the three-fold axis directed along Z, if the twin partners have orthorhombic symmetry (Laue class mmm); (b) the twinning elements may be the mirror plane m(110), if the twin partners have hexagonal symmetry (Laue class 6/m).

Case (a)

The diffraction pattern can be obtained by twinning of the orthorhombic crystals, either with the parameters of the primitive unit cell a = 4.693, b = 8.127, c = 13.716 Å or with the parameters of the base-centered unit cell a = 9.385, b = 16.255, c = 13.716 Å. The first of these suggested unit cell is immediately rejected, because the structure does not contain any of the necessary translation vectors. The structure with the second suggested unit cell can exist only in the space group Cmcm and in all its subgroups. However, the allowance for twinning in this model gave unsatisfactory results. The lowest R factor attained for the model, in the space group C222, was R_{iso}= 0.11. We observed high scatter in the isotropic thermal parameters for the atoms of the same type and the geometrical characteristics of the model were much worse.

Case (b)

Twinning in hexagonal single crystals does not influence the symmetry of the diffraction pattern, but distorts the geometrical characteristics of the model, leading to a high value of the R factor. In this case the lowering of the symmetry of the diffraction pattern can be associated only with absorption in the crystal. The refinement of the structure with allowance for twinning and absorption by the DIFABS program led to R_{iso}= 0.036 and a twin volume ratio of 2.96(3).

After allowance for twinning in this model, the thermal parameters of the oxygen atoms were reduced by a factor of 1.6 and assumed reasonable values and thermal vibration ellipsoids were determined for all atoms. The allowance for twinning increased the accuracy of the atomic coordinate determination, with the standard deviations for the coordinates reduced by about five times. All these facts favour the existence of twinning in these crystals.

Conclusion

The analysis of structure parameters obtained without allowance for possible crystal microtwinning shows anomalous features indicating microtwinning in the specimens. Microtwinning, with the pseudosymmetry element being a twinning operation, is indicated by the following features: (i) a high R factor; (ii) 'dirty' zero electron-density maps; (iii) high values of B and degeneracy of the thermal vibration ellipsoids into unclosed surfaces; (iv) high extinction parameter; (v) pronounced pseudosymmetry in atomic coordinates; (vi) a high scatter in interatomic distances, especially for light atoms.

References

[1] M I Sirota (1990) *Kristallografiya* **35**, 832 [*Sov Phys Crystallogr* **35**, 488].
[2] M I Sirota (1990) *Kristallografiya* **35** 1076 [*Sov Phys Crystallogr* **35** 633].
[3] G Donnay and J D H Donnay (1974) *Canad Mineralogist* **12** 422.
[4] W H Zachariasen (1967) *Acta Cryst* **23** 558.
[5] P J Becker and P Coppens (1974) *Acta Cryst* A**30** 129.
[6] P J Becker and P Coppens (1974) *Acta Cryst* A**30** 148.
[7] I P Kondratyuk, M I Sirota, B A Maximov, L A Muradyan and V I Simonov (1986) *Kristallografiya* **31** 488 [*Sov Phys Crystallogr* **31** 287].
[8] I P Kondratyuk, A A Loshmanov, L A Muradyan, B A Maximov, M I Sirota, E A Krivandina and B P Sobolev (1988) *Kristallografiya* **33** 105 [*Sov Phys Crystallogr* **33** 57].
[9] R A Tamazyan, Yu A Malinovskii, M I Sirota and V I Simonov (1988) *Kristallografiya* **33** 1128 [*Sov Phys Crystallogr* **33** 668].
[10] S M Skshat, V I Simonov and N V Belov (1969) *Dokl Akad Nauk SSSR* **184** 337 [*Sov Phys Dokl* **14** 9].
[11] M Sebais, E A Pobedimskaya and O V Dimitrova (1985) *Kristallografiya* **30** 802 [*Sov Phys Crystallogr* **30** 466].
[12] B A Maximov, T A Zhdanova, A A Voronkov et al. (1979) *Dokl Akad Nauk SSSR* **247** 103 [*Sov Phys Dokl* **24** 511].
[13] B V Merinov, B A Maximov and N V Belov (1981) *Dokl Akad Nauk SSSR* **260** 1128 [*Sov Phys Dokl* 26 922].
[14] Yu I Smolin (1974) Author's Abstract of Doctorate Dissertation, Inst. Kristallografii, Moscow.
[15] N Walker and D Stuart (1983) *Acta Cryst* A**39** 158.

Organic Structures from High Resolution Neutron Powder Diffraction

R M Ibberson

ISIS Science Division, Rutherford Appleton Laboratory

Chilton, Didcot, Oxon., OX11 OQX, UK.

Abstract

High resolution neutron powder diffraction is a powerful technique that enables the precise and accurate determination of moderately complex molecular crystal structures to be performed. The inherently high resolution of powder diffractometers operating at pulsed neutron sources, such as HRPD at ISIS, permit the routine collection of high quality powder data that contain several hundred resolved reflections. High resolution powder diffraction data, particularly if recorded at low temperatures, contain a wealth of information from Bragg reflections collected well below *d*-spacings of 1Å. The technique provides a rapid alternative to single-crystal neutron diffraction for unit cell volumes up to 1500Å^3 and can be the only appropriate method for (i) crystals that undergo reconstructive first-order phase transitions and (ii) low melting point materials for which growing single crystals has practical difficulties.

In this paper recent results from HRPD are presented demonstrating high resolution neutron powder diffraction to be a versatile and powerful technique in the elucidation and description of organic structures.

1. Introduction

HRPD is one of the new generation of high resolution neutron powder diffractometers operating at pulsed sources, such as the spallation source ISIS, that permit the routine collection of data with a resolution, $\Delta d/d$, in excess of 10^{-3}. As a direct result of this inherently high resolution, high quality powder diffraction patterns that contain a large number of reflections and consequently high information content may be recorded. Moreover, the rich epithermal neutron flux available using HRPD permit these high resolution diffraction data to be collected for Bragg reflections at *d*-spacings of well below 1Å and so enabling powder diffraction using pulsed neutrons to provide an alternative to single crystal neutron diffraction for obtaining both accurate and precise structural parameters in moderately complex crystal structures. The study of phase transitions is also particularly appropriate on HRPD since the resolution remains approximately constant across the whole diffraction pattern. The observation of Bragg peak splitting associated with a transition is thus not limited to a small high resolution region of the pattern but all reflection orders are split equally. The powder technique is particularly appropriate in cases of crystals that undergo reconstructive first-order phase transitions and of low-melting point materials for which growing single crystals is technically difficult. It also has the advantage that data collection periods are typically hours not days.

The collapsing of 3-dimensional structural information on to a 1-dimensional powder diffraction pattern inevitably results in loss of information due to peak overlap. Increasing resolution minimises Bragg peak overlap therefore directly affects the complexity of structural study and refinement tenable using powder diffraction. Assuming a constant $\Delta d/d$ resolution, simple calculations show that the number of resolved peaks, N_R, in a time-of-flight powder diffraction pattern is of the order of $N_R = 1/[3(\Delta d/d)]$. Allowing a factor of ~7:1 for the number of resolved peaks to structural parameters refined to high precision implies that for $(\Delta d/d) \sim 4 \times 10^{-4}$ the number of potential structural parameters in a high precision study on HRPD is approximately 100. It is pertinent to consider the importance of this resolution in terms of a natural scale required for the study of organic structures. For example, in considering C-C bond lengths, values are typically 1.54Å for a single bond, 1.39Å for aromatic compounds and 1.33Å and 1.20Å for double and triple bonds respectively. This is a total range of some 0.34Å yet much smaller ranges separate very different bond characters. Assuming two bond distances cannot be satisfactorily compared at less than four esd this implies no useful chemical information is contained in a C-C bond length with an esd in excess of 0.01Å and thus in structural crystallographic data with esds on atomic co-ordinates greater than some 0.007Å. This is a somewhat arbitrary value but nevertheless defines clear limits on the experimental diffraction data. The accuracy of bond length determination is also reliant on the effectiveness of motional corrections which account for the apparent foreshortening of bond lengths due to librational movement. This type of correction is critically dependent on the determination of accurate atomic displacement parameters (ADPs) or 'anisotropic temperature factors' that again strongly affect the collection of diffraction data. For example, low-order X-ray diffraction data may well give errors in bond lengths in excess of 0.01Å (greatly in excess of the nominal experiment esd) due to breakdown of the spherical atom scattering density due to bonding electron density contamination. The requirement therefore for high order data puts an empirical limit on the $(\sin\theta)/\lambda$ of at least $0.7Å^{-1}$ (Seiler, Schweizer and Dunnitz, 1984) and, for example, in the X-ray case necessitates the use of Mo Kα radiation and ideally low-temperature measurements. The collection of such low-temperature high-order diffraction data is routine on a neutron diffractometer such as HRPD.

2. Nitromethane: a comparison with medium resolution powder diffraction data

Organic structures provide a number of challenging standards against which the quality of HRPD data may be tested. Moreover the application of HRPD in the study of small molecules provides an experimental basis for two major types of investigation. One is charge-density studies, where the nuclear co-ordinates obtained are used to construct the model for the electron density of the molecule consisting of isolated, unbonded, atoms. The other is for comparison with *ab initio* molecular orbital calculations of the structure of the isolated molecules, which also give the nuclear geometries. This yields information relating to the effect of intermolecular forces on molecular geometry. The development of these techniques relies on the availability of accurate and reliable structure determinations. The provision of this information is traditionally the sole domain of single crystal measurements, yet low melting point compounds present severe practical difficulties in growing single crystals of adequate size. By comparison, powder samples are easily prepared.

The motivation behind the study of the crystal structure of nitromethane, CH_3NO_2, was two-fold. Firstly, the crystal structure has a number of unusual features particularly in relation to the molecular conformation. These features have been subject to an exhaustive study using single crystal neutron diffraction (Jeffrey *et al.*, 1985) and so definitive data are available against which an HRPD study can be set. Secondly, previous attempts (Trevino *et al.*, 1980; Matias, 1989) from medium resolution neutron powder data to perform a detailed crystal structure analysis have been of limited overall success.

The crystal structure of nitromethane was solved by Trevino *et al.* (1980) from a single crystal CuKα X-ray study at 228K. Additionally reported were the results from refinements of the crystal structure at 78K and 4.2K from constant-wavelength neutron powder diffraction. The structure was found to be orthorhombic, space group $P2_12_12_1$, with four molecules in the unit cell. Of particular interest in the structure analysis was the unusual nature of the molecular conformation. *Ab initio* calculations (Binkley *et al.*, 1981) for the isolated molecule at rest reveal both lowest-energy conformers 1 and 2 have m point symmetry and insignificant differences in energy levels. However, despite having approximate m symmetry the two N-O bond lengths are different. Consideration of the crystal field environments of the two oxygen atoms provides a rational behind the N-O bonding asymmetry since the oxygen atom sites occupy different environments. O(1) has four nearest neighbour (intermolecular) deuterium atoms (E,F,G & H) over a range 2.69 to 2.58Å, whereas oxygen O(2) has five neighbouring deuterium atoms at longer distances of between 2.69 to 3.09Å (A,B,C,D & E) as shown in Figure 1. The X-ray single crystal structure analysis of Trevino showed the two N-O bonds to be slightly different in the expected direction; N-O(1) > N-O(2) by 0.018(5)Å. However, this difference was not confirmed by the powder diffraction measurements; indeed the opposite behaviour, N-O(1) < N-O(2), was observed in both cases! Further problems were encountered with the powder data with bond length and bond angle discrepancies attributed to the curvilinear nature of the deuterium thermal motion, i.e. the oscillatory nature of the methyl group. Since the structural differences are subtle, the rigorous re-investigation of deuterated nitromethane represents a stringent test of HRPD data.

Deuterated nitromethane has a melting point of 256K and so the preparation of a powder sample by hand grinding at liquid nitrogen temperature was routine. In fact this method may be used with much lower melting point materials, the lowest to date being tetrahydrofuran (C_4H_8O) m_p ~167K (David & Ibberson,1992). Data were recorded on HRPD using the higher resolution, 2m, sample position ($\Delta d/d \sim 4 \times 10^{-4}$) for a period of 10 hours (approximately 200μAhr). The HRPD deuteronitromethane data were refined within the range 0.56Å < d < 1.60Å, comprised

3491 points and included 1519 reflections. The single crystal data of Jeffrey *et al.* (1985) provided the starting model for a full and unconstrained profile analysis - unit-cell dimensions, atomic co-ordinates and anisotropic displacement parameters all converged successfully in a stable refinement.

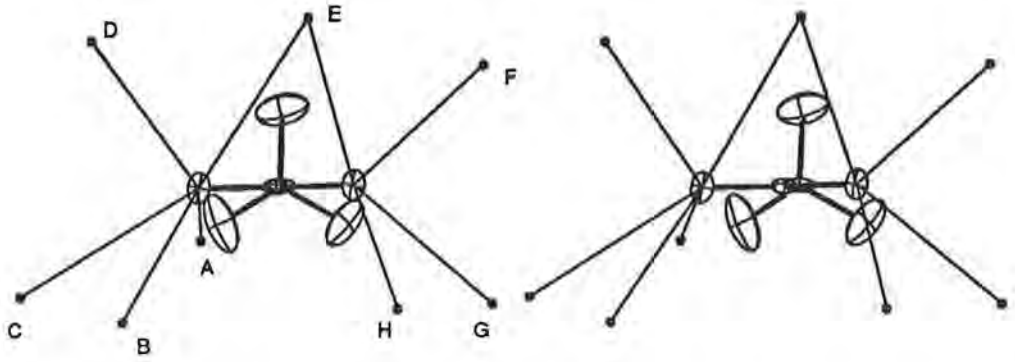

Figure 1 ORTEP (Johnson, 1976) stereo drawing showing the intermolecular environment of the two nitro oxygen atoms of deuteronitromethane. Structural parameters are taken from the present study using HRPD data.

The results from the structural analysis using HRPD are tabulated with medium resolution neutron time-of-flight data recorded using the General Purpose Powder Diffractometer (GPPD) at the Intense Pulsed Neutron Source of the Argonne National Laboratories and single crystal neutron data (Jeffrey *et al.*, 1985) (see Tables 1, 2 & 3). Interestingly the powder data of Matias (1989) were recorded with a similar aim to the HRPD study namely to address the problem: "can time-of-flight neutron powder diffraction data provide precision molecular structure analyses of small molecules?". The resolution of GPPD ($\Delta d/d = 2\text{-}2.5 \times 10^{-3}$) is some 5 times lower than HRPD, a fact that is clearly reflected in the structural parameters derived.

As can be seen in Table 1 the difference between the two N-O bond lengths determined from the HRPD data is maintained, if marginally significant. The overall agreement with the single crystal data however is excellent For example, valence and torsion angles, which are not affected by thermal motion, agree within 0.3° for both structures. The superior precision in determining unit-cell parameters from HRPD data (Table 2) is to be expected.

In contrast, the medium resolution powder diffraction data of Matias (1989) indicate a satisfactory analytical study however yield physically meaningless structural parameters. For example negative on-diagonal atomic displacement parameters and chemically unreasonable results - the difference in N-O bond lengths is reversed. More reasonable results are reported by imposing chemical constraints and also *a priori* knowledge of the thermal behaviour, however even by the utility of such an accurate model a stable and physically meaningful refinement was not forthcoming. Matias concludes that whilst the time-of-flight method shows promise in providing accurate molecular dimensions, even with more sophisticated peak shape functions to better model the sample contribution the high degree of peak overlap will permit only very approximate estimations of thermal motion parameters and ultimately compromise the quality of structural information obtained. The success of the HRPD study is testimony to the substantially increased instrumental resolution.

Table 1 - Bond lengths for deuteronitromethane
(top line HRPD 4.5K, middle line SCD[a], bottom line NPD 5.8K[b]

Bond (Å)	Uncorrected	Corrected†	Δ Uncorrected	Δ Corrected
N-O(1)	1.2315(29)	1.2402	+0.0045(30)	+0.0093
	1.2270(9)	1.2309		
	1.229(4)		+0.0020(41)	
N-O(2)	1.2249(31)	1.2318	+0.0025(32)	+0.0065
	1.2225(9)	1.2253		
	1.173(4)		-0.0495(41)	
C-N	1.4847(27)	1.4867	-0.0008(28)	-0.0020
	1.4855(4)	1.4887		
	1.496(3)		0.0113(30)	
C-D(1)	1.0649(38)	1.0911	-0.0102(40)	-0.0002
	1.0751(13)	1.0913		
	1.057(5)		-0.0181(52)	
C-D(2)	1.0690(41)	1.0838	-0.0046(39)	-0.0091
	1.0736(14)	1.0929		
	1.066(5)		-0.0076(52)	
C-D(3)	1.0737(37)	1.0858	+0.0002(43)	-0.0050
	1.0739(9)	1.091		
	1.055(5)		-0.0189(51)	
Mean C-D	1.0692	1.0874		
	1.0742	1.0916		
	1.059			

[a]- Jeffrey *et al.* (1985) extrapolated value.
[b]- Matias (1989) t-o-f data.
† - details of the thermal motion corrections may be found in Jeffrey *et al.* (1985).

Table 2 - Unit Cell Dimensions (Å) for deuteronitromethane

	HRPD (4.2K)	NPD	NPD	SCD
a	5.18579(3)	5.1832(1)	5.1861(1)	5.185(1)
b	6.23660(4)	6.2357(2)	6.2371(1)	6.237(1)
c	8.51273(4)	8.5181(2)	8.5175(1)	8.507(2)

Table 3 - Bond, valence and torsion angles for deuteronitromethane

Angle (°)	HRPD	SCD[c]	NPD[b]
N-C-D(1)	107.4(3)	107.2(1)	105.9(3)
N-C-D(2)	106.2(3)	106.4(1)	105.8(3)
N-C-D(3)	108.4(3)	108.5(1)	109.0(3)
D(1)-C-D(2)	111.0(4)		111.0(4)
D(1)-C-D(3)	112.1(3)		113.5(4)
D(2)-C-D(3)	111.4(4)		111.3(4)
C-N-O(1)	118.3(2)	118.2(1)	117.4(3)
C-N-O(2)	118.0(2)	118.0(1)	118.2(3)
O(1)-N-O(2)	123.6(3)	123.7(1)	124.5(3)
O(1)-N-C-D(1)	152.2(3)	151.7(1)	152.4(3)
O(2)-N-C-D(1)	-30.2(3)	-29.9(1)	-27.8(4)
O(1)-N-C-D(2)	-88.9(3)	-89.5(1)	-89.7(4)
O(2)-N-C-D(2)	88.7(3)	88.9(1)	90.0(4)
O(1)-N-C-D(3)	30.9(7)	29.9(1)	30.0(4)
O(2)-N-C-D(3)	-151.5(3)	-151.7(1)	-150.2(4)

[a]- Trevino *et al.* (1980) constant wavelength data.
[b]- Matias (1989) t-o-f data.
[c]- Jeffrey *et al.* (1985) extrapolated value.

3. Critical behaviour in methylammonium tin chloride

The benefit of the constant resolution of HRPD when measuring peak splitting associated with phase transitions is well known. However, high resolution also serves in the elucidation of more subtle phase transition phenomena involving only changes in peak intensities and may provide a very detailed description of the system under study.

Methylammonium tin chloride is one of a large family of compounds which have interesting structural, dynamic and phase properties. The general formula is $(MA)_2[MX_6]$ where MA denotes the methylammonium cation $CH_3NH_3^+$, M is a tetravalent metal or semi-metal and X a halogen. With M=Sn, Pb, Pt and Se they crystallise in the space group $R\bar{3}m$ (Wyckoff, 1966) in which all the halogens are equivalent, as are the MA ions which lie on the crystal 3-fold axis. For M=Te with X=Cl, Br or I the structural behaviour is slightly different and there are at least two additional phases however the lowest temperature phase is also $R\bar{3}m$ (Kitahama *et al.*, 1979).

A subtle phase transition occurs within the $R\bar{3}m$ phase of all of these compounds between 100 and 200K (Kume *et al.*, 1979), in which all of the structural and spectroscopic properties change only slightly, although there is a clear heat capacity anomaly (Matsuo *et al.*, 1981 & 1988). The most striking result is that a single crystal X-ray study (Kitahama & Kiriyama, 1978) finds the $R\bar{3}m$ structure at all temperatures, although the hydrogen atoms were not directly located. The X-ray data did not support suggestions that the phase transition is driven by displacements of the $SnCl_6^{2-}$ octahedra therefore it seemed most likely that the transition is associated with a disordering of the hydrogen positions, even though the deuterium isotope effect on the transition temperature is very small:

T_c $(CH_3NH_3)_2[SnCl_6]$ = 154.32K (Matsuo *et al.*, 1981)
T_c $(CD_3ND_3)_2[SnCl_6]$ = 154.96K (Matsuo *et al.*, 1988)

The aim of the present study was to determine the structures of the two phases from which a coherent picture would be developed of the phase transition undergone by a large group of the $R\bar{3}m$ compounds. The sample was fully deuterated and precipitated from solution in such a way as to give a fine powder - this avoids grinding which is known to broaden the transition (Matsuo *et al.*, 1988). Data were recorded on HRPD at 5 and 300K and also at smaller intervals passing through the transition at 155K.

The 300K data were initially refined using the X-ray parameters (Kitahama & Kiriyama, 1978) as a starting model and assuming the deuterium to be on the crystallographic mirror plane with the $CH_3NH_3^+$ ion in its staggered conformation. This model resulted in large elongated anisotropic ADPs for the deuterium (both of $-CD_3$ and $-ND_3$) suggestive of orientational disorder. A disordered structure retaining the $R\bar{3}m$ symmetry was subsequently tried, splitting the deuterium site and placing it off the mirror plane however with equal occupancies of the two sites. The refinement converged to well separated positions some 0.84Å apart.

Although no peak splitting was observed in the low temperature data analysis of the lattice parameter variation clearly indicated the presence of a transition (see Figure 3). The structure of the 5K data was determined following a similar procedure to the 300K data. With the deuterium on the mirror plane only a poor refinement was obtained however allowing the deuterium to move off the mirror plane, giving space group $R\bar{3}$, the refinement converged satisfactorily. In both cases the non-hydrogen parameters are in good agreement with the single crystal X-ray structure except that the Cl ions are displaced from their higher symmetry

positions by some 0.1Å. The low temperature structure is ordered with the ammonium groups adopting one of the two possible configurations of the disordered high temperature form. Fourier maps illustrating the two phases are shown in Figure 2.

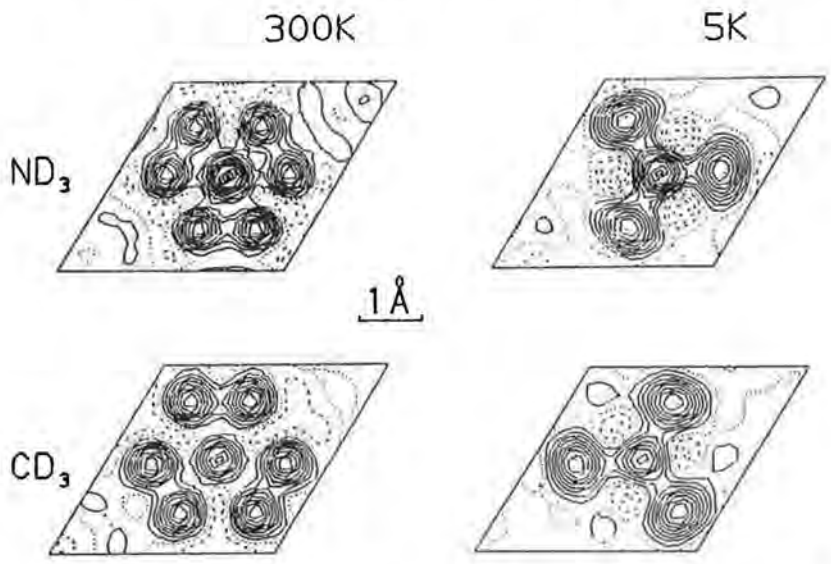

Figure 2 - Fourier maps of the $CD_3ND_3^+$ cation in the two phases showing the disordered high temperature and ordered low temperature structure.

The model for the phase transition is thus rotational ordering of the cation about the C-N axis with the two alternative proton positions separated by about 1.0Å - easily resolved using HRPD. The order parameter may be obtained by fitting the fractional site occupancies of the two deuterium sites (x and 1-x) in space group $R\bar{3}$. The results are shown in Figure 3c. The β exponent is consistent with a 3-D Ising model however more data are ideally required on approaching T_c.

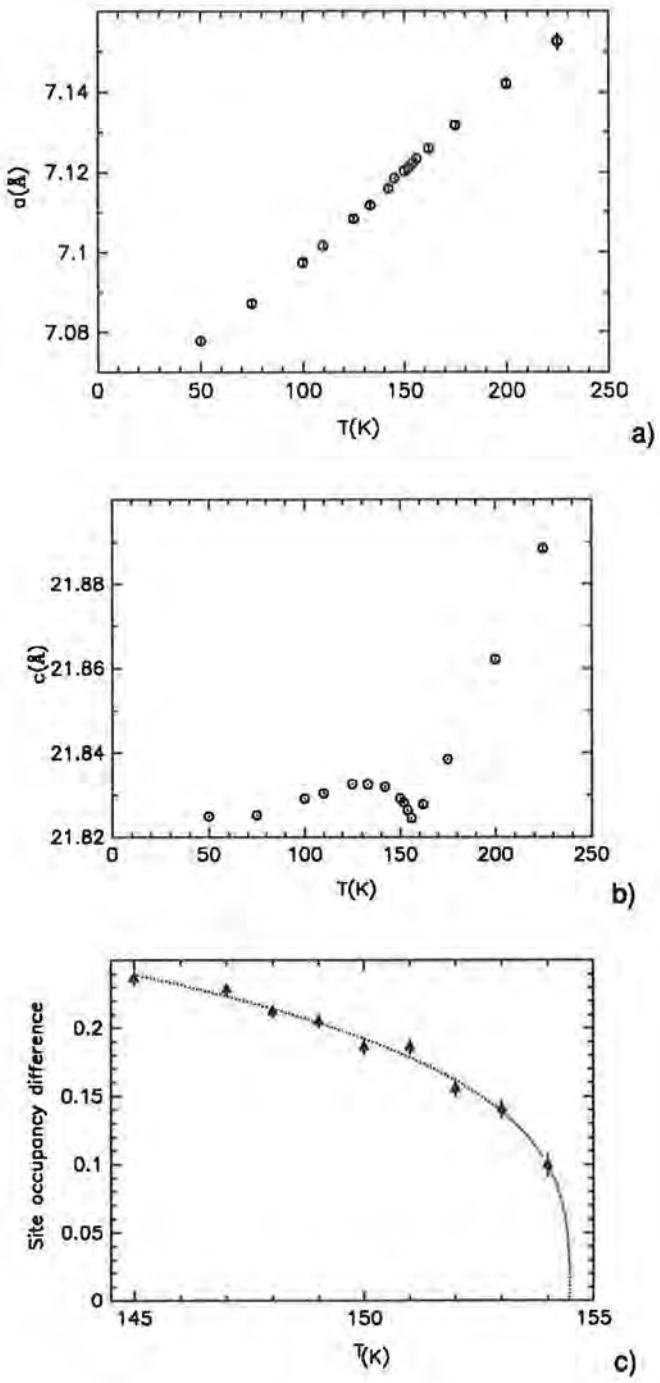

Figure 3 - a) Variation of the a lattice parameter of $(CD_3ND_3)_2[SnCl_6]$. b) Variation of the c lattice parameter of $(CD_3ND_3)_2[SnCl_6]$. c) Determination of the β exponent using a 3 parameter fit to the site occupancy difference. β = 0.294(34), T_c = 154.47(26)K.

4. Toluene - testing the present limits of precision and accuracy

In this section the potential of powder diffraction structure analysis is demonstrated by a full crystal structure refinement of toluene (V_c=1116.21Å^3). The refinement of high resolution neutron powder diffraction data that involves the accurate refinement of 274 parameters which include 48 hydrogen atom co-ordinates and 180 atomic displacement parameters illustrates what maybe regarded as the state-of-the-art in neutron powder diffraction. Whilst the accurate location of hydrogen positions using single crystal neutron diffraction is a standard technique, this comparable refinement using powder data, from a structure of the size and complexity of that of toluene, is notable. Indeed it represents the opening up of a new technique for the refinement of moderately complex crystal structure to high accuracy for structural problems that were previously considered to be the domain of single crystal crystallography.

Accurate structural data on toluene are required for studies comparing *ab-initio* calculation of methyl group rotation potentials from structural data with potentials derived from tunnelling and librational transitions (Prager *et al*, 1991). Though a simple molecule, toluene possesses comparatively complex crystal symmetry. The space group is monoclinic ($P2_1/c$) and there are two independent molecules in general positions in the asymmetric unit. Indeed this represents a severe test for the theory of model potentials.

The low melting point of toluene (177K) and its tendency to form an amorphous phase (Bruneaux-Poulle *et al*, 1979) provide severe problems in obtaining single crystals. In contrast a powder sample was readily prepared: 5 cm^3 of fully deuterated toluene was hand ground at liquid nitrogen temperatures under a cold dry nitrogen atmosphere; upon loading of the vanadium tailed cryostat the sample was first annealed at 162K for 30 minutes to form the crystalline α-phase before cooling to 5K.

Diffraction data were collected on HRPD for a period of 12 hours over a time-of-flight range 20 to 220ms corresponding to a *d*-spacing range of between 0.4 and 4.4Å. The success of the structural study of toluene was considerably helped by the recently acquired capability of the diffractometer to allow data over a 200ms (4Å d-spacing) wide window to be simultaneously recorded. With a structure of the size and complexity of toluene the peak overlap at sub-Å *d*-spacings is severe therefore the ability to measure over the longer *d*-spacing portion of the pattern is particularly important.

The crystal structure of α-toluene has been determined at 165K from single crystal X-ray data (Anderson *et al.*, 1977). A full profile refinement was performed taking the single crystal structure determination as a starting model. At 5K the refined lattice constants are: a = 7.47261(5); b = 5.78838(1); c = 27.08061(4)Å; β = 107.6512(2)°; V_c = 1116.21Å^3. The size of the cell in combination with the structural complexity (there are some 274 structural parameters in total) represent a stringent test for the powder diffraction technique. Surprisingly, extinction effects were observed but were minimised by performing the refinement on a limited data set extending to a maximum *d*-spacing of some 1.8Å. This necessitated the use of slack bond constraints throughout the analysis in order to assist convergence of the refinements, particularly in the initial stages when the hydrogen positions were poorly defined. Whilst permitting the bond lengths to vary, the effect of the constraints is to reduce the shifts in atomic co-ordinates that would produce bond lengths outside of a specified range. The use of bond length and bond angle constraints with structural studies of molecular crystals is a particular valuable and a relatively easy technique to apply since the molecular geometry of the majority of small molecules is a well know quantity. The use of such *a-priori* knowledge considerably enhances the stability of the refinement: values of the final constraints used were: C-D, 1.080(5)Å; ring C-C, 1.400(5)Å; methyl C-C, 1.50(1)Å. The quality of the profile fit as shown in Figure 4 is good as reflected by the agreement factors: R_p=1.54%, R_{wp}=1.88%, R_E=0.99%, χ

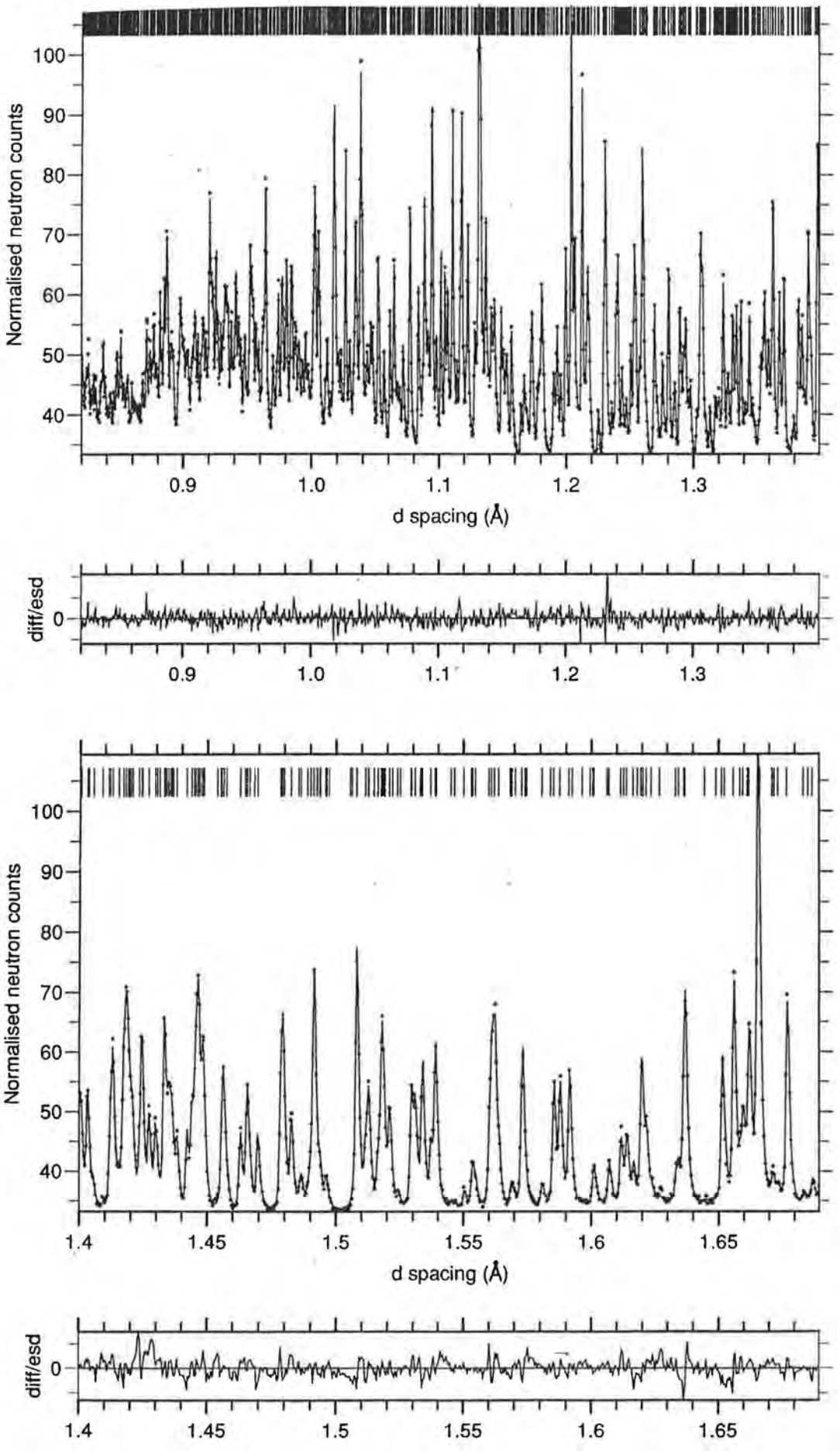

Figure 4 - Selected regions of observed (dots), calculated (line) and difference profiles for toluene-$_{d8}$ at 5K. Vertical tick marks represent calculated peak positions.

^{2}=3.63 for 3710 observations and 291 basic variables. Full details of the structural parameters obtained are presented elsewhere (Ibberson *et al.*, 1992).

The orientation of the methyl groups with respect to the benzene ring is of interest for theoretical studies. Because of intermolecular interactions, the methyl groups are rotated away from their symmetric equilibrium position as observed in the gas phase. In equilibrium two methyl protons are situated parallel to the ring plane having ideal torsion angles of 30° relative to the aromatic ring, while the third methyl proton has a torsion angle of 90°. In the current study these angles have been determined as: D(111)-C(11)-C(12)-C(13), -17.9(5)°; D(113)-C(11)-C(12)-C(17), 40.1(5)°;D(112)-C(11)-C(12)-C(13), 100.6(5)°; and D(211)-C(21)-C(22)-C(23), -20.6(5)°; D(213)-C(21)-C(22)-C(23), 96.8(5)°;D(212)-C(21)-C(22)-C(27), 34.3(5)°, reflecting the different environments of the two molecules in the structure. The use of constraints does not markedly diminish the sensitivity of the refinement and still allows the discrimination of subtle structural detail.

5. Summary

This paper discusses recent high resolution neutron powder diffraction research at ISIS applied to structural studies of organic or molecular crystals. The effectiveness and power of the technique of high resolution time-of-flight powder diffraction has considerably extended the scope of structural problems that may be solved using powder data. The powder diffraction data have been shown to be comparable to the best single crystal studies indeed *ab initio* structure determination from such data has been shown to be routine (see for example Delaplane *et al.*, 1993). Furthermore, with careful implementation of *a priori* chemical information in the form of bond length and bond angle constraints the technique has been successfully applied to structures of a size and complexity rarely attempted using more traditional powder methods.

References

Anderson M Bosio L, Bruneaux-Poulle J and Fourme R, J Chim Phys **74** (1977), 68.
Binkley, J.S., Whiteside, R.A., Krishnan, R., Seeger, R., DeFrees, D.J., Schlegel, H.B., Topiol, S., Kakn, L.R. & Pople, J.A., QPCE 13 (1981), 406.
Bruneaux-Poulle J, Bosio L and Dupont J M, J Chim Phys Chim Phys Biol **76** (1979), 333.
David, W.I.F, and Ibberson, R.M., Acta Cryst. C**48** (1992), 301-303.
Delaplane, R.G., David, W.I.F., Ibberson, R.M. & Wilson, C.C. Chem. Phys. Lett **201** (1993), 75-78.
Ibberson, R.M., David, W.I.F. & Prager, M. J. Chem Soc., Chem. Commun. 1992, 1438-1429.
Jeffrey, G.A., Ruble, J.R., Wingert, L.M., Yates, J.H. & McMullan, R.K., J. Am. Chem. Soc. 107 (1985), 6227-6230.
Johnson C K, Oak Ridge National Laboratory Report (1971), ORNL-3794.
Kitahama, K. & Kiriyama, H., Bull. Acta Cryst. (1978) **A34**, S302.
Kitahama, K., Kiriyama, H. & Baba, Y., Bull. Chem. Soc. Jpn. (1979) **52**, 324.
Matias, P.M., Ph. D. Thesis (1989), Department of Crystallography, University of Pittsburgh.
Matsuo, T., Ueda, M. & Suga, H., Chem. Phys. Lett. (1981) **82**, 577.
Matsuo, T., Yan, H.-K. & Suga, H., J. Phys. Chem. Solids (1988) **49**, 85.
Prager M, David W I F and Ibberson R M, J Chem Phys **92** (1991) 2490.
Seiler P, Schweizer W B and Dunnitz J D, Acta Cryst B**40** (1984), 319-327.
Trevino, S.F., Prince, E. & Hubbard, C.R., J. Chem. Phys. **73** (1980), 2996-3000.
Wyckoff, R.W.G., Crystal Structures, 2nd ed., vol. 5 (Interscience, New York, 1966), p.142.

SINGLE CRYSTAL STRUCTURE DETERMINATION USING TIME-OF-FLIGHT LAUE DIFFRACTION

C C Wilson

ISIS, Rutherford Appleton Laboratory, Chilton, Didcot, Oxon OX11 0QX

The potential of time-of-flight Laue diffraction in structural determination is discussed, Examples from the experimental programme on the ISIS single crystal diffractometer SXD are used to illustrate this potential.

Introduction

Neutrons can often play a crucial role in the elucidation of the fine details of crystal structures. The complementary nature of scattering from X-rays and neutrons means that even once a structure is 'known' and 'refined' from the former, there is often further information readily available from the latter.

Single crystal diffraction at a pulsed neutron source is most conveniently carried out using the Laue time-of-flight technique, in which the natural wavelength-sorted neutron beam is combined with a 2D position-sensitive detector to provide 3D volumes of diffraction information in a single measurement. While this technique has major advantages in the study of, for example, diffuse scattering, high quality structural information can also be obtained. Examples of the areas in which neutron time-of-flight Laue structural studies have particular applicability include:

- Location of unknown atoms, especially hydrogen, water and other light units, which are generally as visible to neutrons as heavier species;
- The detailed study of hydrogen bonding in organic materials, especially in very strong hydrogen bonds, including the study of schemes and mechanisms of polymorphism;
- Examination of structural disorder, for example in minerals, where the disordered species are close in atomic number;
- The study of phase transitions - the technique is of especial use when the phase transition can be monitored through a small subset of reflections, as these can often be obtained in a single measurement using time-of-flight Laue diffraction;
- High resolution effects, in which the very high $\sin\theta/\lambda$ values attainable at a spallation neutron source (greater than 3 $Å^{-1}$) can have extremely beneficial effects.

Examples of structural determinations in these areas using the time-of-flight Laue diffractometer SXD at the ISIS spallation neutron source are given below.

The time-of-flight Laue technique

Single crystal diffraction at a pulsed neutron source is an area rich in information. By the utilisation of both the time-of-flight technique to sort the white beam and large area position-sensitive detectors, it is possible to access large volumes of reciprocal space in a single measurement. The ISIS Single Crystal Diffractometer SXD[1] (Figure 1) is just such a time-of-flight Laue instrument. The scintillator-based position-sensitive detectors used are of fibre-optic encoded ZnS type[2].

The ability of such an instrument to probe reciprocal space volumes is a result of the combination of a time-sorted wavelength range (providing two Ewald sphere surfaces at $1/\lambda_{max}$ and $1/\lambda_{min}$) and the large scattering locus subtended by the detector, allows a full 3-dimensional reciprocal space volume to be accessed on SXD *in a single measurement.*

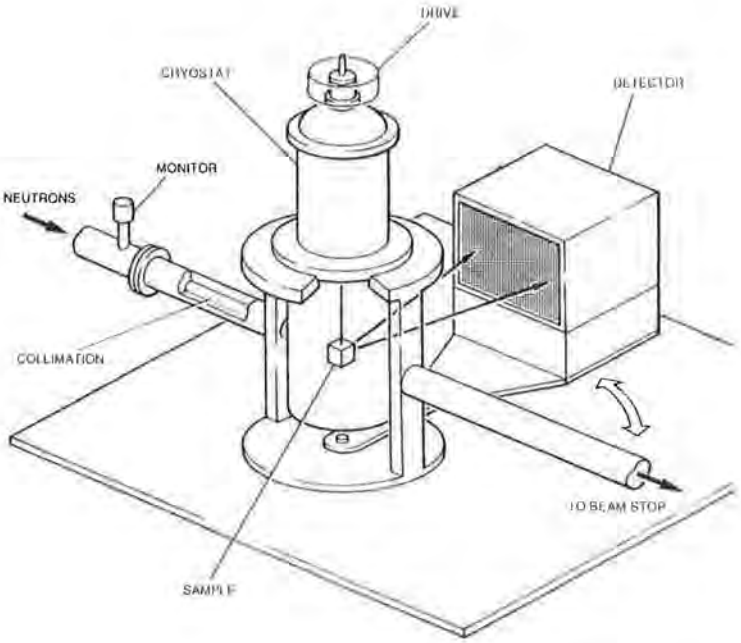

Figure 1 - The time-of-flight Laue diffractometer SXD at ISIS.

It is clear from the above that SXD is an ideal instrument for the surveying of reciprocal space. This capability has particular relevance in the study of incommensurate structures, phase transitions and diffuse scattering. In these fields the time-of-flight Laue technique is extremely powerful. However, the characteristics of the data collected on such an instrument can also have certain advantages in more routine structural work :

(i) The collection of many Bragg reflections simultaneously in the detector allows the accurate determination of crystal cell and orientation from a single data histogram (collected in one fixed crystal/detector geometry). It should also be noted that for some applications this single histogram may be the only data required;

(ii) The white nature of the incident beam enables the straightforward measurement of reflections at different wavelengths. This ability is invaluable in the precise study of wavelength dependent effects such as extinction and absorption;

(iii) The collection of data to the very high $\sin\theta/\lambda$ values accessible on SXD (exploiting the high flux of useful epithermal neutrons from the under moderated ISIS beams) allows more precise parameters to be obtained, enabling the examination of very subtle structural features.

For many problems in physics, the refinement parameters required are not the normal positional and vibrational parameters, but may be (or may be classed as) second, or higher, order effects. For example, disordered structures, higher order potential terms, incommensurate or satellite peaks, new minority phases etc. In order to be able to extract parameters such as these reliably and precisely, it is necessary both to extract accurate diffraction intensities to very high Q and to apply all necessary corrections to these data in the reduction to a set of structure factors for refinement.

Data analysis procedures

The extraction of structure factor information from an SXD data set proceeds in two stages. Given the provision of an accurate UB matrix from the earlier stages of the data processing procedure, integrated intensities are extracted from the raw data using Wilkinson's modification of the $\sigma(I)/I$ method[3,4]. This procedure involves fitting variable-shaped ellipsoidal integration volumes around the reflection position as predicted from the crystal UB matrix or as found from peak searching procedures. Local interpolation of the peak centroid improves the integration accuracy and can also

be used to improve the quality of the UB matrix. The 'learning' of the shapes of the stronger reflections is exploited by imposing these shapes upon the profiles of weaker reflections occurring in similar regions on the detector. The use of this peak shape library method allows significantly more reliable weak intensities to be extracted, along with the benefit of more accurate strong intensities from the application of the $\sigma(I)/I$ technique. Since reflections at high Q tend to be rather weak, the availability of data at very high $\sin\theta/\lambda$ values of > 2 $Å^{-1}$ on SXD depends strongly on the successful and reliable extraction of weak peak intensities.

Once a reliable set of integrated intensities has been extracted from the raw data, it is necessary to reduce these to structure factors. For this we use the formula of Buras and Gerward[5]

$$I_h = i_o(\lambda)\, V\, N^2\, |F_h|^2\, \lambda_h^4\, \varepsilon(\lambda,\alpha)\, A_h(\lambda)\, E_h(\lambda) / 2\sin^2\theta_h$$

where

I_h is the measured intensity of reflection *h*;
$i_o(\lambda)$ is the incident flux - wavelength dependent for a pulsed source of course;
V is the crystal volume;
N is the number density of unit cells;
$|F_h|$ is the structure factor magnitude of reflection *h*;
λ_h is the wavelength at which *h* is measured (λ^4 is reflectivity);
$\varepsilon(\lambda,\alpha)$ is the detector efficiency, a function of wavelength and detector coordinate [$\alpha = \alpha(x,z)$];
θ_h is the Bragg angle at which *h* is measured (the term $1/2\sin^2\theta_h$ is the Lorentz correction. It should be noted that in time-of-flight Laue diffraction, the 'moving' part to which this correction refers is the contraction of the Ewald sphere (radius $1/\lambda$) during the pulse time frame);
$A_h(\lambda)$ is the absorption correction;
$E_h(\lambda)$ is the extinction correction.

In practice on SXD at present this data reduction is accomplished in three stages :

(i) The detector spatial response correction $\varepsilon[\alpha(x,z)]$ is taken account of within the peak integration program PEAKINT;

(ii) In the main reduction program ITOF, the expression evaluated is

$$|F_h| = \{I_h\, 2\sin^2\theta_h / (i_o(\lambda)\, V\, N^2\, \lambda_h^4\, \varepsilon(\lambda))$$

(iii) In the Cambridge Crystallographic Subroutine Library (CCSL)[6] routine EXTTOF, the coefficients for the evaluation and subsequent refinement of wavelength-dependent absorption and extinction corrections are calculated.

Structure factor refinement is then carried out within the framework of CCSL using the least squares program SFLSQ. In addition, of course, the flexibility of the CCSL system allows special features to be conveniently built in to a refinement, such as bond constraints, relations between variables, magnetic structures etc.

The location of water

Water is a major component in many crystalline and non-crystalline materials, from geological materials, to physical and chemical structures to its role as a crucial solvent and reaction mediator in biological systems. It is thus vital in many structural studies to understand fully the behaviour of this component of the structure. However, with X-rays this is often difficult due to the relatively light nature of the water molecule - this situation is exacerbated when the hydrogen atom configuration is of importance as these still more difficult to see with X-rays. Problems can also arise when, as frequently happens, the water molecules are disordered in the structure. Neutrons, for which water is a relatively strong scatterer, are thus a more useful probe in these circumstances. In very complicated hydrated structures the option of contrast variation, in which some of the water

molecules can be substituted by heavy water with a still more enhanced scattering power, is a further extremely powerful use of neutrons, but this technique is beyond the scope of this paper.

Natural beryl

Beryl, a common constituent of granitic pegmatite rocks and an accessory mineral in many geological environments has ideal formula $Al_2Be_3Si_6O_{18}$, and a crystal structure consisting of an open tetrahedral framework enclosing hexagonal channels (Figure 2). These channels can host alkali atoms and water molecules in response to the isomorphic replacement of divalent Fe, Mg and Mn for octahedral Al^{3+} and of monovalent Li for tetrahedral Be. However, there is some controversy over the location of these host species where two positions (2a and 2b), of different size and environment, are available[7,8].

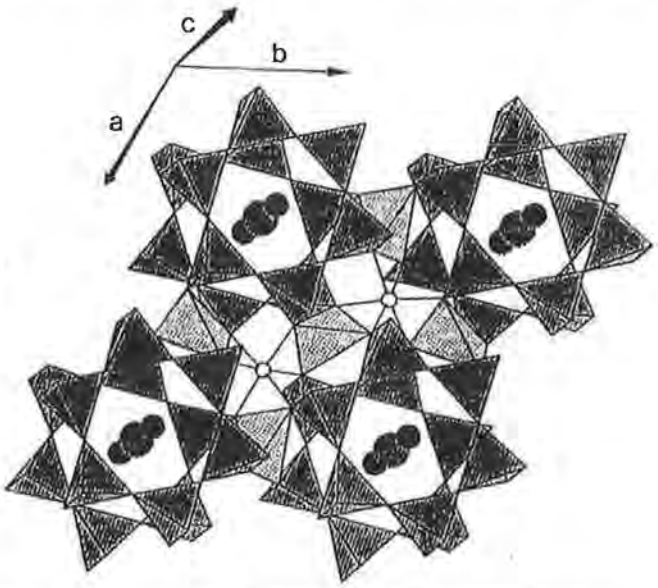

Figure 2 - The structure of beryl, showing the channels occupied by guest molecules.

Apart from the intrinsic interest of the crystal chemical problem, especially in view of the petrological relevance of alkali beryls, a thorough understanding of these substitution mechanisms is highly desirable in order to distinguish between crystal chemical and geochemical influence on bulk mineral composition. This can prove particularly useful in identifying petrogenetically related pegmatites and allowing a rapid estimation of the degree of fractionation of their host rock.

Assignment of the correct population of the two extra-framework sites is impossible to perform on the residual electron density from X-ray studies. However, single crystal neutron diffraction of a hydrous sodic beryl is an ideal technique for solving the problem of water and alkali location in the channels of the beryl structure. In addition, this residual density is smeared out by positional or vibrational disorder and so low temperature data collection can further assist in providing information on the degree of order (if any) between these two sites, the local configuration of the water molecules and the relevant hydrogen bonding scheme.

Data were collected on SXD at 100K from a single crystal of beryl (natural, from SE Ireland, analytical composition $Na_{0.45}(Al_{1.3}Fe_{0.31}Mg_{0.42})_{2.03}Be_{2.94}Si_{6.07}O_{18}.0.95H_2O$) of volume 2.3 mm^3, in some 12 data histograms[9]. The detector centre was positioned at 90°, and the wavelength range used was 0.48 - 4.8 Å. The unit cell was determined to have dimensions a = 9.23, c = 9.19 Å, space group $P6_3/mcc$, in good agreement with previous X-ray studies. Following normal data reduction procedures, a data set of some 774 reflections with $I>5\sigma(I)$ resulted, comprising 254 unique, merged reflections which were used in the refinement.

Refinement proceeded from previous coordinates determined from X-rays. Once the refinement with this model had converged, a series of Fourier maps were calculated (using F_{obs} as coefficients) to elucidate the positions of the Na^+ and H_2O groups. These maps (Figure 3) clearly revealed the presence of ordered Na^+ at the 2b site [at (0,0,0)] and the oxygen of the water molecule at the 2a site (0,0,¼). There were also indications of negative density at positions close to the latter indicating

disorder of the water molecule about the hexagonal axis. All atoms were refined anisotropically, apart from the hydrogens which were fixed at their located positions with isotropic thermal parameters. The site occupancies of all metal atoms were also refined, in refinement cycles with the temperature factors on these atoms fixed. The final parameters from the refinement are given in Table 1. These clearly show the location of the water (stoichiometry 0.95) and the Na^+ (stoichiometry slightly reduced at 0.39 from the expected value of 0.45) and an overall refined composition which agrees well with the analytical composition.

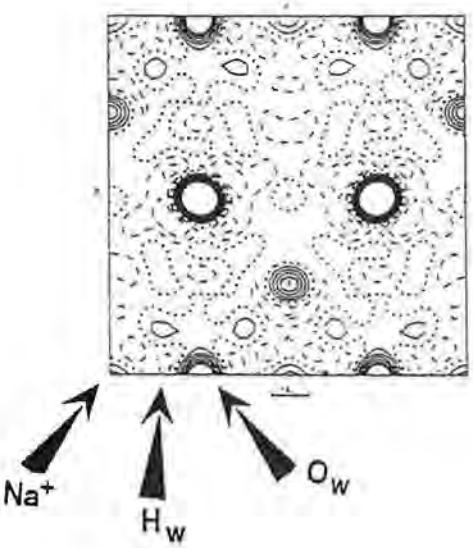

Figure 3 - Fourier map for beryl showing located positions of the oxygen at (0,0,¼) and Na^+ at (0,0,0). There is also evidence for the disordered hydrogen close to the water oxygen.

Table 1 - Atomic parameters in beryl at 100 K

254 unique, merged data, R=0.059, R_W=0.049 for 42 refined parameters

Atom	x	y	z
Si	0.3861(5)	0.1124(6)	0
Be	1/2	0	1/4
Al/Fe/Mg	2/3	1/3	1/4
O1	0.3045(4)	0.2298(5)	0
O2	0.4957(3)	0.1422(3)	0.1450(2)
O3	0	0	1/4
H1	0	0	0.1472(39)
Na	0	0	0

Atom	B_{11}	B_{22}	B_{33}	B_{23}	B_{13}	B_{12}	SITE
Si	0.82(13)	0.91(15)	0.34(10)			0.61(11)	
Be	1.00(8)	1.06(13)	0.34(8)			0.53(7)	
Al	0.96(18)	0.96(18)	0.83(23)			0.48(9)	0.62(3)
Fe							0.17(3)
Mg							0.21(3)
O1	1.81(13)	1.40(12)	1.04(9)			1.29(11)	
O2	1.06(6)	1.43(8)	0.46(5)	0.00(5)	-0.30(6)	0.88(7)	
O3	2.1(4)	2.1(4)	2.3(6)			1.04(19)	0.95(8)
H1	5.8(5)						0.49(4)
Na	2.2(9)	2.2(9)	1.9(12)			1.1(4)	0.39(5)

Further analysis of these data are in progress, especially with regard to the electrostatic implications of the positions located for the guest species and the further implications of these on the crystal chemistry.

Detailed studies of hydrogen bonded systems

Hydrogen bonding is frequently the dominant crystal packing and activity mediator in many biological, chemical and physical systems. These bonds, intermediate in strength between bonding and non-bonding interactions, thus play a crucial role in many areas. It follows that a full understanding of hydrogen bond geometry is of importance in understanding the behaviour in such materials, which may be drugs interacting with proteins, nucleic acid base pairs, ferroelectric substances in which the phase transition may be driven by hydrogen ordering, chemical interactions etc. A full appreciation of the subtleties of the hydrogen bond geometry obviously requires accurate location of all the atoms involved including the hydrogen atoms. Neutrons thus can play an important role in such studies, allowing the hydrogen parameters to be defined with equal precision to those of the other atoms involved even in the case of extremely strong (short) hydrogen bonding interactions.

Hydrogen location and tautomer assignment in 3-deazauracil

The crystal structure of the modified nucleic acid base 3-deazauracil (2-hydroxy-4-pyridone, $C_5H_5NO_2$) had previously been studied using several methods, including X-rays[10], neutron powder diffraction[11] and limited neutron single crystal diffraction[12]. The interest in this material, and the principal reason for its study by these different techniques, lies in the precise definition of the hydrogen atom positions and hence of the hydrogen bonding scheme. The latter is of particular interest as there is a very strong hydrogen bond present in the structure (O2...O4, separation some 2.55 Å in the original X-ray study), whose presence in the parent nucleoside, 3-deazauridine, is believed to play an important role in the powerful cytostatic properties of that molecule[13].

In previous structural work on this material, the heavy atom framework is well defined by X-rays, but there remains considerable ambiguity regarding the hydrogen atom parameters, especially with regard to the important hydrogen atom between O2 and O4. The obvious recourse under such circumstances is to neutron scattering, in which the hydrogen atom scattering power is on a par with that from the other atoms present in the structure, with the consequence that hydrogen parameters are more readily available.

The initial neutron work carried out on this sample was a neutron powder diffraction study[11] which allowed only a limited, severely constrained refinement of the atomic parameters. Nonetheless, there were strong indications in this work that the missing hydrogen atom was attached to O4 rather than O2.

Subsequently, large single crystals were obtained which were suitable for single crystal neutron diffraction (the sample volume for this is typically a few mm^3, some 100-1000 times larger than for X-rays). Initially, data were collected in only a very limited region of reciprocal space, yielding a small data set of only some 80 reflections[12]. Due to the limitations imposed by this, only a joint refinement of this limited neutron data set with the earlier X-ray data was deemed to be reliable. Once again, however, there were very strong indications regarding the location of H4 close to O4.

In order to finalise the hydrogen atom definition in the structure, it was obviously desirable to collect a full single crystal neutron diffraction data set and perform unconstrained refinement on these data alone. The installation of the larger area detector on SXD allowed an accordingly extended data set to be collected[14]. With the detector installed at a fairly short distance from the sample, some 115 mm, the angular range covered is a remarkable 80 x 80° in scattering angle. The detector centre was positioned at 90°, and the wavelength range used was 0.73 - 4.8 Å.

Some 15 data histograms were collected in this configuration. The unit cell was determined and refined from one of these histograms, using 40 of the strongest reflections. The unit cell found was a = 8.638(3), b = 5.315(3), c = 11.221(5) Å, V = 515.2 $Å^3$, space group $P2_12_12_1$, in good agreement with that obtained in the X-ray study. From these data, there are some 1514 reflections potentially accessible to a $\sin\theta/\lambda$ value of 0.85 $Å^{-1}$. Reflection intensities were extracted and reduced to structure factors using standard SXD data processing procedures. The resulting data set comprised 1390 reflections with $I > 5\ \sigma(I)$. This represents some 447 unique reflections after merging of equivalents and Friedel pairs.

Structural refinement was carried out, on F, in the CCSL least squares program SFLSQ. Anisotropic thermal parameters were refined for all atoms including hydrogen. Extinction was corrected for in a variable wavelength method using one angular mosaic parameter in a Becker-Coppens Gaussian model. In the final refinement, there were some 119 variable parameters, yielding agreement factors of R = 0.071, R_w = 0.065 ($w = 1/\sigma^2$).

The final structure is shown in Figure 4, which also contains a view of the hydrogen bonding scheme. There is found to be excellent agreement between the X-ray and neutron results and the hydrogen atom parameters determined from the latter data are now of the level of precision one would expect from a good quality neutron diffraction data set.

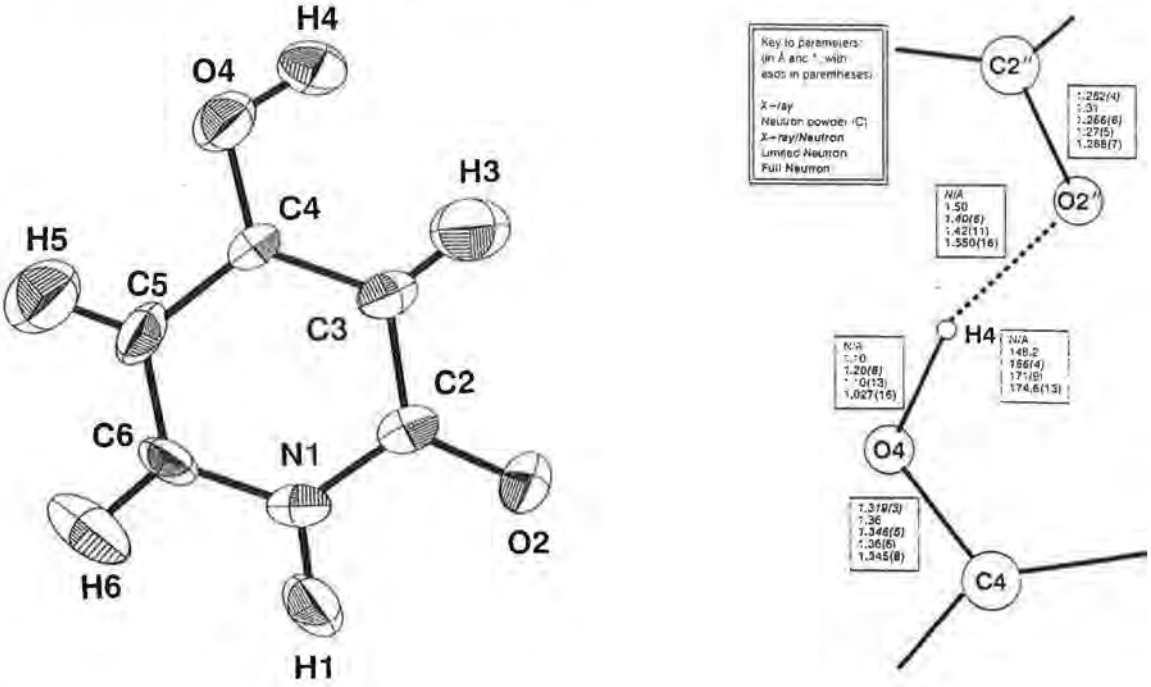

Figure 4 - Structure (drawn using ORTEP[15]) and hydrogen bonding scheme in 3-deazauracil.

As can be seen from Figure 4, the hydrogen bonding schemes determined from the various methods are in reasonable agreement with each other, with the additional precise hydrogen atom parameters in the present work. Crucially, the locations of all hydrogen atoms, including the important H4 atom, are unambiguous. The O4-H4 bond, at 1.027(16) Å, is a perfectly well defined O-H bond, confirming at much greater certainty than before the nature of both the tautomeric form and the hydrogen bonding in this material.

Charge density studies of urea phosphoric acid

Much work is currently performed on the accurate determination of charge densities by X-ray diffraction, and one of the questions remaining to be answered by these studies is whether it is possible to determine the effects of the environment (e.g. polarisation, charge transfer) on the crystalline electron density. Work on the archetypal material oxalic acid dihydrate suggests that the effect of strong hydrogen bonds on the electron density can be measured.

Another material in which these effects can possibly be measured is urea phosphoric acid[16,17], with a very strong non-symmetric hydrogen bond (O...O = 2.4 Å) indicated from the X-ray work. Accurate structure factors for these materials can be calculated, but adequate comparison of theory and experiment requires reliable positional and thermal parameters for the hydrogen atoms. Hydrogen positional parameters determined by X-ray diffraction are inaccurate due to the well known asphericity shift and the thermal parameters are inaccurate compared with those of the heavier atoms.

Positional parameters determined by neutron diffraction are an order of magnitude more precise than those determined from X-rays and therefore allow hydrogen atoms to be examined at the same accuracy as the other atoms in the structure. Thus neutrons can 'fill in' the gaps in an accurate charge density study of strongly hydrogen bonded materials that even a careful X-ray experiment can leave. Large single crystals of urea phosphoric acid can be obtained (volume > 20 mm^3) and thus single crystal neutron diffraction can be performed easily.

Data were collected from a large single crystal of urea phosphoric acid at 100 K[18], to match the temperature of the forthcoming X-ray experiment, with the detector installed at a short distance from the sample, some 120 mm, with its centre positioned at 70°. The wavelength range used was 0.48 - 4.8 Å. The large amount of information available in a single data histogram from this material is illustrated in Figure 5.

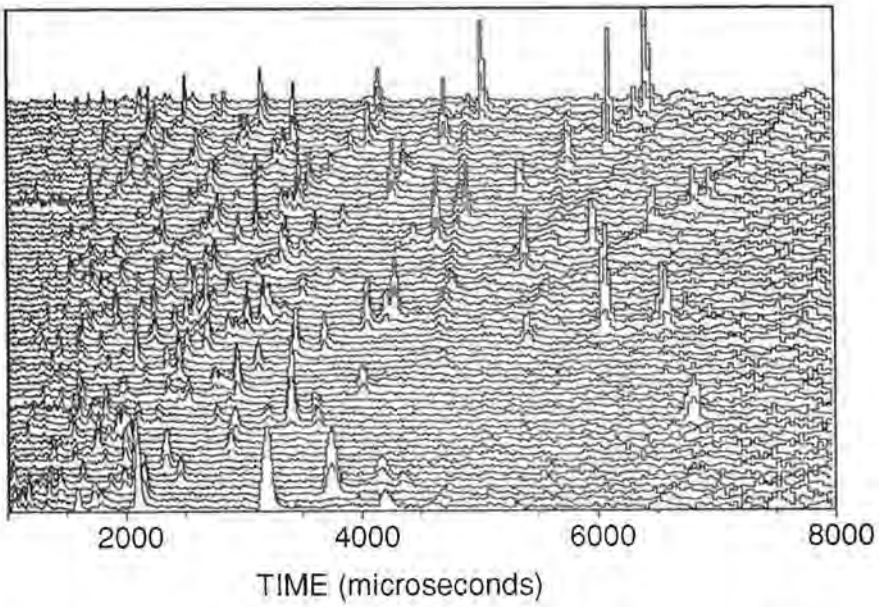

Figure 5 - Representation of the large number of reflections (around 400) measured in a single histogram on SXD from urea phosphoric acid.

Some 12 data histograms were collected in this configuration. The unit cell was determined to be a = 17.298(6), b = 7.438(4), c = 8.908(5)Å, V = 1146.1 $Å^3$, space group Pbca, in good agreement with that obtained in the X-ray study. Reflection intensities were extracted and reduced to structure factors using standard SXD data processing procedures. The resulting data set comprised some 2800 reflections with $I > 5\ \sigma(I)$. Structural refinement was carried out, on F, using SFLSQ. Anisotropic thermal parameters were refined for all atoms including hydrogen. In the final refinement, there were some 154 variable parameters, yielding agreement factors of R = 0.090, R_W = 0.089 ($w = 1/\sigma^2$).

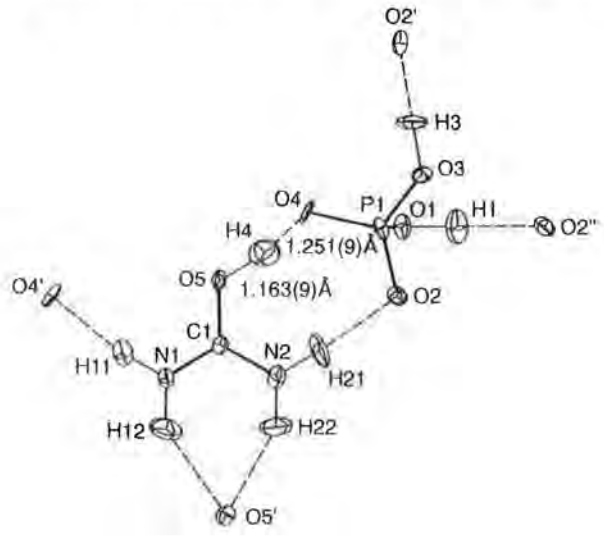

Figure 6 - ORTEP view of the structure of urea phosphoric acid, showing the strong, non-symmetric hydrogen bond.

Table 2

Bond Distances (Å) and Bond Angles (°) in urea phosphoric acid

Atom 1	Atom 2	Distance	Atom 1	Atom 2	Distance
P1	O1	1.546(5)	O5	H4	1.163(9)
P1	O2	1.522(5)	N1	C1	1.303(4)
P1	O3	1.540(5)	N1	H11	1.015(8)
P1	O4	1.496(5)	N1	H12	1.017(9)
O1	H1	1.013(8)	N2	C1	1.333(4)
O3	H3	1.042(8)	N2	H21	1.005(8)
O4	H4	1.251(9)	N2	H22	1.012(8)
O5	C1	1.290(5)			

Atom 1	Atom 2	Atom 3	Angle	Atom 1	Atom 2	Atom 3	Angle
O1	P1	O2	111.7(3)	C1	N1	H11	120.1(5)
O1	P1	O3	108.9(4)	C1	N1	H12	120.6(6)
O1	P1	O4	106.1(3)	H11	N1	H12	119.3(7)
O2	P1	O3	105.9(3)	C1	N2	H21	120.8(6)
O2	P1	O4	113.0(4)	C1	N2	H22	118.1(6)
O3	P1	O4	111.5(3)	H21	N2	H22	120.9(8)
P1	O1	H1	114.3(5)	O5	C1	N1	119.2(3)
P1	O3	H3	117.5(5)	O5	C1	N2	120.1(3)
P1	O4	H4	124.9(5)	N1	C1	N2	120.6(3)
C1	O5	H4	116.2(5)	O4	H4	O5	169.4(8)

The final interatomic separations are shown in Table 2, with a view of the molecular configuration in Figure 6. The excellent precision of the hydrogen atom parameters is clear from these parameters - note especially the accurate parameters obtained for atom H4, the hydrogen involved in the very strong, non-symmetric, hydrogen bond. Once an accurate low temperature X-ray data set is obtained from this material, it is hoped that the joint X-n data set will yield the desired information on the exact electron density distribution and the factors affecting this.

Long range structural order and disorder

In this case structural order and disorder can mean several things. First, 'average' disorder throughout a structure, involving for example random occupancy of two sites in a particular unit cell. In this case the structure determination based on Bragg intensities will lead to determination of the average relative proportions on each possible site. An example of this is given below in the study of the phase transition in schultenite. Secondly, more localised disorder can be studied, for example atomic clusters. Again Bragg refinement will yield positions, occupancies etc averaged throughout the whole structure. However, in this case of short range order, there is additional scattering in positions away from the Bragg peaks which yield crucial additional information. Finally, substitutional disorder can be studied. In this case two atoms occupy the same site in some proportion. The refinement can determine the relative proportions of these, again averaged through the whole crystal, especially if the scattering powers of the two relevant atomic species are significantly different.

The benefits of neutrons in the study of structural order and disorder are most evident under three types of circumstance:

(i) The disordered atoms are light in comparison to other species present in the material. In this case neutrons have their usual advantage over X-rays, that the scattering power is not a monotonic function of Z;

(ii) The disordered atoms are close in atomic number but have significantly differing neutron scattering lengths. In this case X-rays may be helpless to tell atoms apart where neutrons can succeed.

(iii) Under conditions of extreme sample environment, where the penetrating power of the neutron can be extremely beneficial in allowing experiments to be performed *in situ*.

Mg/Fe ordering in olivine

Olivine, $(Mg,Fe)_2SiO_4$, is the most common constituent of the upper terrestrial mantle and a common rock forming mineral. In the structure of olivine, Mg and Fe can be distributed over two structural sites, M1 and M2, which have slightly different octahedral configurations (Figure 7). There are, however, conflicting crystallochemical factors which influence the Mg-Fe ordering onto the two sites[19,20]. These are:

(i) The larger size of the M2 sire favours Fe^{2+} entry into the former;

(ii) The greater electrostatic potential of M2 relative to M1 means that Fe^{2+} will prefer site M1, due to its ability to make more covalent bonds than Mg^{2+};

(iii) The M1 octahedron, allowing as it does greater angular distortion, will be favoured for Fe^{2+} due to the crystal field stabilisation factor.

Superficially it therefore seems that there is more likelihood of Fe^{2+} occupying M1. There are also, however, other effects such as composition, oxygen fugacity, pressure and especially temperature, which can affect the relative distribution of the two cations.

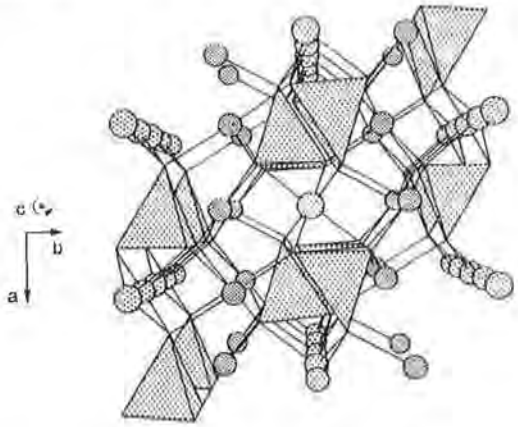

Figure 7 - Structure of olivine, showing the two possible metal sites M1 and M2.

The determination of the equilibrium in the exchange reaction

$$Fe_{M1} + Mg_{M2} \Leftrightarrow Fe_{M2} + Mg_{M1}$$

as a function of temperature can provide important information on the cooling history of the host rocks. Recent X-ray experiments on olivine samples quenched from various temperatures seem to indicate that iron tends to concentrate in site M1 as the temperature increases. However, olivines quenched from temperatures above 800°C show the same equilibrium constant as those of crystals quenched from 700°C, indicating that the maximum temperatures which can be determined by this technique is in the region of 700-800°C. This is because the rate of cooling, even for very rapid quenching techniques, is lower than the speed of the exchange reaction at temperatures above 800°C. The only way to truly monitor this equilibrium above 800°C is to carry out an *in situ* experiment at these temperatures. The convenience of high temperatures experiments using neutron diffraction allows a single crystal neutron scattering experiment to measure this equilibrium.

The sample used in the SXD experiment[21] was an olivine single crystal of volume some 5 mm^3 taken from a pallastic meteorite from Kansas, whose iron content (> 10%) is sufficient to allow a reliable determination of the site content. Data were collected at two temperatures (880°C and 1060°C) yielding data sets of some 319 and 238 unique, merged, reflections respectively. The unit cells determined at each temperature (880°C - a = 4.788(3), b = 10.349, c = 6.061(2) Å; 1060°C - a = 4.792(4), b = 10.361(3), c = 6.082(2) Å), and also a rapid cell dimension measurement after cooling to room temperature, show no anomalous features, and especially indicate no significant oxidation of the Fe^{2+} during the course of the experiment.

The results of the refinements at the two temperatures are shown in Table 3. All atoms were refined with anisotropic temperature factors, with the site occupancies refined both with Mg/Fe temperature factors fixed and with these parameters varying, with essentially identical results. The Fe temperature factors were fixed to be identical with those of the equivalent Mg atom and the overall site occupancies were constrained to add up to one on each site.

The most remarkable result is that, while the Fe occupies the site M1 preferentially at 880°C as expected from the previous experiments on quenched samples, there are clear indications that at the higher temperature Fe preferentially occupies site M2. This result, unexpected from all previous X-ray results, indicates that there is a significant alteration in the Fe/Mg equilibrium above 880°C. This shift in equilibrium occupancy is obviously masked in studies of quenched samples by the speed of the exchange reaction, and is therefore only accessible in an experiment performed at the higher temperature.. This shift in preferential occupancy will also have implications for the position of the equilibrium in those samples quenched from above 800°C. This reversal of the Fe/Mg ordering has major implications for models of rock-forming processes, especially in the derivation of formation temperature from structural parameters.

Table 3(a) - Atomic parameters in olivine at 880°C

588 reflections (I>5σ(I)), 319 unique, merged data, R=0.073, R_W=0.058 for 42 refined parameters

Atom	x	y	z
Mg1	0.000	0.000	0.000
Fe1	=Mg1	=Mg1	=Mg1
Mg2	0.9922(11)	0.2782(4)	0.250
Fe2	=Mg2	=Mg2	=Mg2
Si	0.4266(11)	0.0944(4)	0.250
O1	0.7671(9)	0.0913(3)	0.250
O2	0.2203(9)	0.4504(3)	0.250
O3	0.2813(7)	0.1631(2)	0.0356(3)

Atom	B_{11}	B_{22}	B_{33}	B_{23}	B_{13}	B_{12}	SITE
Mg1	2.4(3)	1.8(2)	1.5(1)	-0.2(1)	-0.3(1)	0.1(1)	0.860(26)
Fe1	=Mg1	=Mg1	=Mg1	=Mg1	=Mg1	=Mg1	0.140
Mg2	2.1(3)	1.1(2)	1.9(2)			-0.2(1)	0.900
Fe2	=Mg2	=Mg2	=Mg2	=Mg2	=Mg2	=Mg2	0.100
Si	0.5(3)	1.3(3)	1.6(2)			0.3(1)	
O1	1.0(3)	1.6(1)	1.6(1)			0.6(1)	
O2	1.0(2)	0.7(1)	2.3(2)			-0.2(1)	
O3	1.6(2)	1.4(1)	1.5(1)	0.7(1)	-0.2(1)	-0.1(1)	

Table 3(b) - Atomic parameters in olivine at 1060°C

507 reflections (I>5σ(I)), 238 unique, merged data, R=0.070, R_W=0.062 for 42 refined parameters

Atom	x	y	z
Mg1	0.000	0.000	0.000
Fe1	=Mg1	=Mg1	=Mg1
Mg2	0.9939(11)	0.2789(6)	0.250
Fe2	=Mg2	=Mg2	=Mg2
Si	0.4269(11)	0.0951(6)	0.250
O1	0.7640(10)	0.0926(5)	0.250
O2	0.2206(10)	0.4513(4)	0.250
O3	0.2806(7)	0.1624(3)	0.0361(5)

Atom	B_{11}	B_{22}	B_{33}	B_{23}	B_{13}	B_{12}	SITE
Mg1	2.1(3)	2.8(3)	2.4(3)	-0.2(2)	-0.2(2)	0.5(2)	0.919(40)
Fe1	=Mg1	=Mg1	=Mg1	=Mg1	=Mg1	=Mg1	0.081
Mg2	2.9(3)	1.7(2)	3.0(3)			-0.3(2)	0.841
Fe2	=Mg2	=Mg2	=Mg2	=Mg2	=Mg2	=Mg2	0.159
Si	0.8(3)	1.3(3)	1.2(2)			0.0(2)	
O1	1.6(3)	2.1(2)	2.4(2)			0.2(2)	
O2	2.3(3)	0.6(2)	2.6(2)			-0.2(2)	
O3	1.4(2)	2.4(2)	2.9(2)	0.7(1)	-0.1(1)	0.1(1)	

Anion-excess clustering in $(Ca,Y)F_{2+x}$

Anion excess fluorites are of technological interest since it became evident that incorporation of trivalent R^{3+} ions onto the M^{2+} cation sites leads to a drop in the transition temperature to the high ionic conductivity regime. In these systems, charge neutrality is maintained by the incorporation of excess X^- anions into the fluorite structure. The distribution of these excess anions within the doped fluorite structure remains, however, the subject of considerable debate.

In order to resolve this uncertainty, the doped material $(Ca_{1-x}Y_x)F_{2+x}$ was studied on SXD, with a view to examining both the average occupancies of the postulated sites for accommodation of the excess anions - by study of the Bragg intensities - and of the local clustering of these anions - by study of the diffuse scattering. The information obtained from the latter is discussed elsewhere in this volume (Hull, *vide infra*) and the discussion here is purely in terms of the information obtained on the average occupancies. Previous neutron diffraction experiments[22-25] had suggested the existence of disordered anions on sites at (½ u u) with u ~ 0.38 (48i sites), at (w w w) with w ~ 0.40 (32f sites) and at (v v v) with v ~ 0.29. The occupancies of these sites led to postulated local defect clusters consistent with these.

Intensity measurements were carried out on SXD[26] on a cylindrical single crystal of diameter 3 mm and length 9 mm, oriented with $[1\bar{1}0]$ vertical. Bragg reflections were measured to a $\sin\theta/\lambda$ value of some 1.47 $Å^{-1}$, resulting in a data set of some 75 independent intensities. The large number of independent reflections measured using SXD should provide a better determination of the mean occupancies of the disordered sites and allow a more critical assessment of the proposed defect models.

Least squares analysis of these data were carried out allowing the occupancies of the lattice anion sites to vary, with the anions occupying the three disordered sites at (½ u u), (w w w) and (v v v), with overall fluorine occupancy constrained to 2.06. The thermal vibrations of the lattice fluorine atoms were refined anisotropically while the disordered fluorines were constrained to have isotropic thermal parameters. A final weighted R-value of 5.54% was obtained, with structural parameters as shown in Table 4.

Table 4

$Ca_{0.94}Y_{0.06}F_{2.06}$: parameters from Bragg and diffuse data fitting

Atom	Site	Position	Bragg	Cuboctahedron	Diffuse
Ca/Y	4a	(000)	B_{iso}=0.64(1)Å^2		
F	8c	(¼¼¼)	m=1.59(9)	m=1.52	
			B_{11}=0.62(7)Å^2		
			B_{33}=0.83(9)Å^2		
F1	48i	(½uu)	u=0.390(5)	u=0.353	u=0.384(3)
			m=0.16(2)	m=0.18	
			B_{iso}=1.4(4)Å^2		B_{iso}=1.86(8)Å^2
F2	32f	(www)	w=0.38(3)		
			m=0.01(2)	m=0.00	
			B_{iso}=2.6(43)Å^2		
F3	32f	(vvv)	v=0.270(8)	v=0.25	
			m=0.30(5)	m=0.36	v=0.265(5)
			B_{iso}=1.2(2)Å^2		B_{iso}=1.21(5)Å^2

The measured positions and occupancies agree well with those calculated on the basis of simple cuboctahedral[27] defect clusters (Figure 8), the preferred model resulting from the combined Bragg and diffuse scattering measurements[28]. In this model the twelve anions which form the cuboctahedron lie in the (½ u u) positions, with the (v v v) sites being identified with small outward relaxations of the nearest neighbour lattice anions in <111> directions. The low measured occupancy of the disordered site at (w w w) was a significant factor in arguing against the previously postulated 'Willis' or square antiprism type defect clusters, which both incorporate additional anions at these positions. Final confirmation of the correctness of this model was obtained from the related diffuse scattering measurements[28].

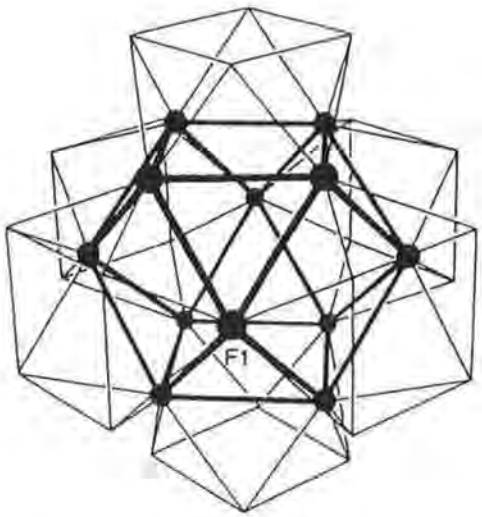

Figure 8 - The cuboctahedral defect cluster found in anion excess $(Ca,Y)F_{2+x}$. The Bragg intensities are consistent with this model, and the existence of isolated clusters of this type in the lattice is confirmed by the related diffuse scattering measurements.

Phase transition studies

The study of phase transitions can be carried out in two ways using time-of-flight Laue diffraction. The first is in the conventional manner in which full data sets are collected under each set of physical conditions, from which full refinements can yield the significant changes. This is most convenient for high symmetry systems if a single crystal sample is used, as then the amount of data comprising a more or less complete data set can be minimised. The alternative is to take advantage of the fact that frequently a phase transition can be characterised by the changes in a small subset of reflections - in this case the use of relevant $\Delta(F)/\Delta(\text{parameter})$ methods[29,30] on this subset can yield sufficient information. Ultimately, for the time-of-flight Laue method, the aim is to reduce the amount of data collected to a single histogram, with optimisation of the sample orientation to maximise the amount of unique information available in this single shot. In this way the experimental set-up is the most convenient for the alteration of sample environment parameters as the experimental set-up can remain completely stationary throughout the entire experiment.

Work on this concept is continuing, but the investigation of the use of reduced data sets in the examination of phase transitions was initiated in structural work on the ferroelectric material lead hydrogen arsenate[31].

Paraelectric-ferroelectric phase transition in schultenite

Lead hydrogen arsenate (LHA), which occurs naturally as the mineral schultenite, undergoes a paraelectric-ferroelectric phase transition at 313K[32]. The structure of the high temperature, paraelectric phase has space group P2/c and the hydrogen atom is disordered (necessarily 50:50) about the centre of symmetry (Figure 9). In the low temperature, ferroelectric phase, however, the space group is Pc, with the loss of the centre of symmetry. The structural phase transition is manifest as an ordering of the hydrogen atom onto one of the two, now non-equivalent, sites. In addition the loss of the two-fold axis allows the heavy atom lattice to distort significantly[33]. The hydrogen ordering in this type of phase transition is typically gradual, becoming complete some 100° below the transition temperature in the related material lead hydrogen phosphate, LHP[33].

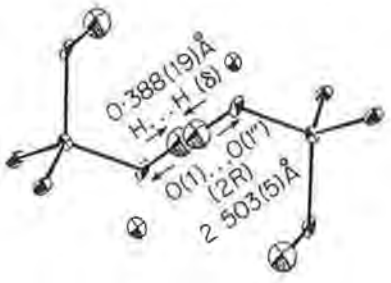

Figure 9 - Room temperature structure of schultenite, showing the disordered hydrogen atom.

The phase transition observed in materials such as the title compound is characterised by the ordering of hydrogen atoms involved in strong hydrogen bonds, and hence is intimately connected to the nature of hydrogen bonding. The relation of ordering characteristics to the separation of the disordered hydrogen atoms above the phase transition, and to the separation of the relevant oxygen atoms, should give significant information regarding the hydrogen atom potentials in such a material. In addition, determination of the structure in the high temperature phase serves two further aims - to verify the equal occupancies of the two hydrogen atoms (equivalent in the high symmetry structure) and to look for any deviations of the heavy atom structure, for which there is some evidence in the case of LHP.

A single crystal sample of schultenite was obtained from the British Museum collection [BM 1926,205]. The crystal was transparent, of dimension 4 x 3 x 1 mm^3, and contained a small amount of a green inclusion (ca. 0.75 x 0.75 x 0.25 mm^3), probably mimetite [$(PbCl)Pb_4(AsO_4)_3$]. For neutron diffraction, a bulk probe, the presence of this inclusion, of some 1% of the crystal volume, should not present a serious problem. Data were collected on SXD using neutrons in the wavelength range 0.48-4.8Å with the detector centred around $2\theta=90°$, at six temperatures below T_c, at 305, 290, 275, 250, 200 and 125K. Refinements in the low symmetry space group were carried out with isotropic thermal parameters at all temperatures.

The structure of LHA determined at room temperature[34] was found to be in good agreement with those of LHP. The separation 2R of the oxygen atoms involved in the O-H...O hydrogen bond in LHA is 2.503(5) Å, compared with 2.470 Å in LHP, and that the separation of the two disordered hydrogen atom positions is 0.388(19) Å (0.393 Å in LHP), but in general, the bonding parameters for LHA agree reasonably well with those in LHP, as expected.

The variation of hydrogen ordering with temperature is shown in Figure 10. The ordering characteristics closely follow the pattern found in LHP[35,33], with the ordering rising rapidly to some 30% of the fully ordered value within 10° below the phase transition. Full ordering is reached at some 100° below T_c as expected. Also plotted in Figure 10 are two parameters characterising the distortion of the heavy atom structure from the centrosymmetric P2/c arrangement. These are (after Ref [33]): Δ(As-Pb), the displacement of the As atom from the midpoint (in an *ac* projection) of the line joining two Pb atoms; Δ(As-O), the distortion of the AsO_4 group from two-fold symmetry, measured as the difference in bond lengths between As-O(1) and As-O(3). As can be seen from the Figure, these parameters follow approximately the same behaviour as the proton ordering.

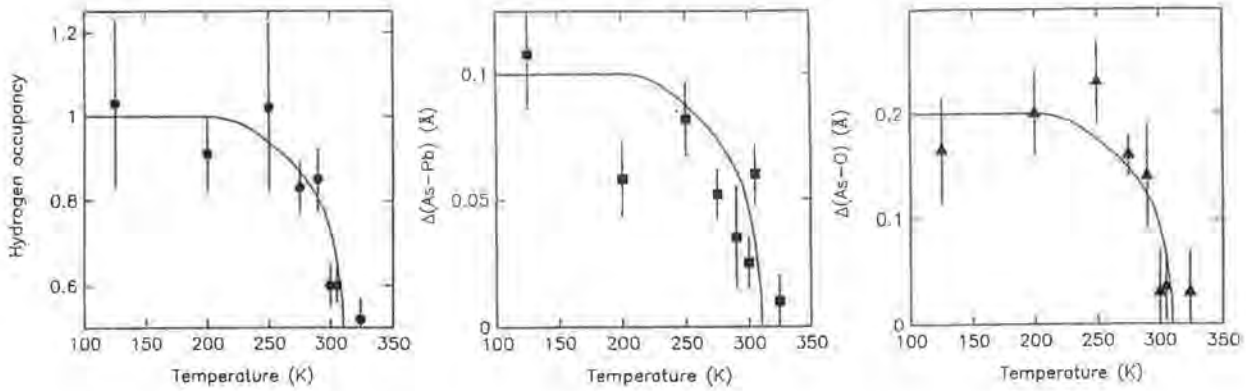

Figure 10 - Ordering patterns in schultenite: (o) Hydrogen occupancy; (□) Δ(As-Pb); (Δ) Δ(As-O).

While the precision of the parameters obtained is rather low from these limited data sets, the low temperature measurements have confirmed the gradual onset of full hydrogen ordering in the structure below the paraelectric-ferroelectric phase transition. This is paralleled by an increasing distortion of the heavy atom lattice in the same region. The measurements in the high symmetry phase are somewhat inconclusive, but do not, within experimental error, preclude the possibility of some distortion of the heavy atom lattice in this region.

The ability of these measurements of limited data sets to yield useful information on structural trends points the way towards future uses of single histogram data sets to yield rapid characterisation of phase transitions and structural differences.

High resolution refinements

High real space resolution, for example the study of fine details in temperature factors, the study of anharmonicity, and the decoupling of site occupancies from temperature factors, demands high reciprocal space resolution data, i.e. data to high $\sin\theta/\lambda$ (high Q). A single crystal instrument at a spallation neutron source such as ISIS offers unique opportunities to access the very highest resolution data:

(i) There is a very high flux of short wavelength epithermal neutrons - SXD typically can use neutrons with wavelengths as short as 0.25 Å;

(ii) There is no form factor fall off for nuclear scattering of neutrons, allowing high scattering angles to be accessed.

By combining these two factors, $\sin\theta/\lambda$ values of > 3 $Å^{-1}$ (Q > 40 $Å^{-1}$) should be achievable, allowing the very highest resolution studies to be carried out.

Debye-Waller factor in InP

Indium phosphide is a semiconductor of substantial technological importance, for which lattice dynamics have relevance to the electronic transport properties. Estimates of Debye-Waller factors in zincblende semiconductor materials show wide discrepancies both within experimentally determined values and often between these and the lattice dynamical calculations[36-39]. This is especially serious in X-ray determinations of the displacements, where there are large discrepancies in the values determined for In and P. Previous neutron diffraction measurements of InP covered only a very limited temperature range, and it is of importance to determine these temperature factors reliably over as wide a temperature range as possible in order to test the accuracy and validity of various proposed lattice dynamical models.

A neutron single crystal experiment on a material such as InP must access high Q reflections to yield good sensitivity in temperature factor determination. In addition, since In has a high absorption cross-section, use of short wavelength neutrons is important in allowing accurate data to be obtained. In such cases, the high flux of short wavelength, epithermal, neutrons on an instrument like SXD at a spallation source is a great advantage.

Data were collected on SXD form a quasi-cylindrical single crystal of InP, of diameter 1.5mm and height 5mm - the crystal shape was chosen to minimise path length dependent effects[40]. The sample was mounted with <110> vertical, allowing access to (hhl) reflections in the equatorial plane. data were accumulated with SXD in its quasi-equatorial geometry using the small position-sensitive detector. A complete quadrant of the (hhl) reciprocal lattice plane was collected at 293, 100 and 50K, reaching values of Q greater than 16 $Å^{-1}$ (involving measurement of reflections out to the (10 10 8) of this cubic material with lattice parameter 5.87 Å).

Structure factors were extracted from these data in the usual way, leading to data sets of 61 reflections at 293 K, 47 reflections at 100K and 86 reflections at 50 K and least squares refinement carried out on each of these. The wavelength dependence of the In scattering length was not taken into account. A total of four parameters were refined at each temperature, a scale factor, mosaic

spread (extinction correction applied using a Becker-Coppens Lorentzian model) and isotropic temperature factors on In and P. The results of the refinements are shown in Table 5.

Table 5

Refined parameters for InP

Temperature (K)	Scale	Mosaic (10^{-4} rad^{-1})	B_{In} (Å^2)	B_P (Å^2)
293	8.81(24)	3.1(2.2)	0.67(12)	0.52(10)
100	5.71(22)	5.1(2.1)	0.20(12)	0.24(10)
50	9.54(17)	5.4(1.9)	0.14(4)	0.17(3)

These results are found to be in reasonable agreement with a valence shell model calculation for P but the experimentally determined value for In is somewhat lower than that from the calculation. Further corrections of these data would be required to tie down the possible sources of these discrepancies and verify the accuracy of the parameters obtained. However, it is clear that accurate temperature factors can be obtained in reasonable counting times, even from strongly absorbing materials, by exploiting the high Q data available at a pulsed source such as ISIS.

Anharmonic temperature factors in SrF_2

In previous measurements on the fluorite material SrF_2 on SXD[41] it was found to be possible to refine the anharmonic thermal vibrations in this structure to high precision even at room temperature, where the effect is obviously smaller than at elevated temperatures. In this case the anharmonicity parameter β was determined from measurements of some 16 of those reflections most affected by anharmonicity. These measurements, encompassing (hhl) reflections to (11 11 9) ($\sin\theta/\lambda$=1.696 Å^{-1}), led to a value of β = -4.19(30) . 10^{-19} J A^{-3}, comparing favourably with the previous, high temperature measurement[42] of -3.95(46) . 10^{-19} J Å^{-3}.

However, even at room temperature there remains a significant contribution to the scattering at and around the Bragg peaks from thermal diffuse scattering (TDS). The simplest way to reduce TDS effects is to reduce the temperature but unfortunately this will also reduce the thermal vibrations of the atoms and hence make any anharmonic effects still more difficult to measure. However, the effect of anharmonicity on structure factors and hence on reflection intensities, increases with Q (and hence $\sin\theta/\lambda$) and given that higher Q data ought to be accessible at lower temperature as the Debye-Waller factors reduce, it may be possible to measure and refine anharmonic effects, uncorrupted by TDS, even at low temperatures.

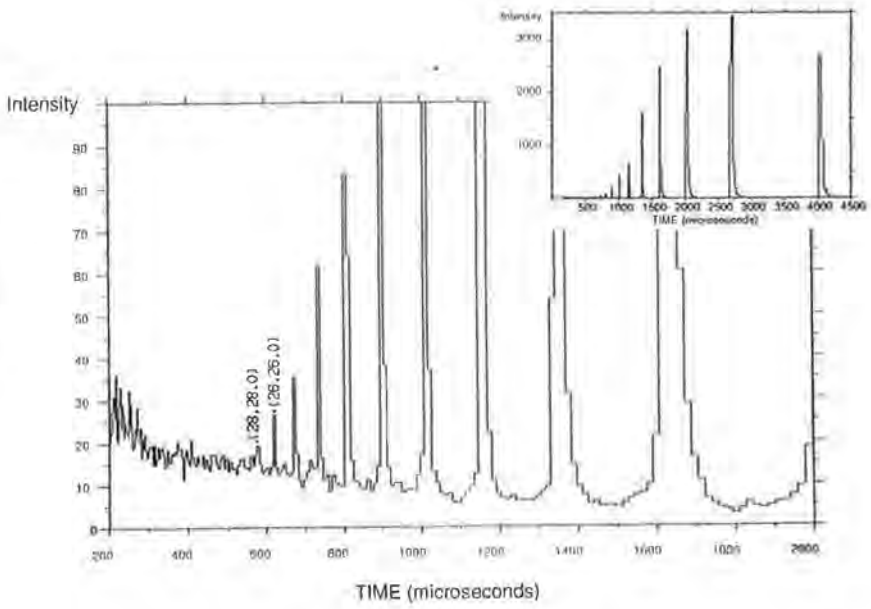

Figure 11 - The (hh0) row of reflections in SrF_2 measured at 25 K on SXD, showing the (28,28,0) reflection at $\sin\theta/\lambda$ of > 3.3 Å^{-1}.

SXD is an ideal instrument with which to attempt this, as the combination of the favourable properties of the neutron (no form-factor fall-off with Q) and of ISIS (high flux of epithermal neutrons, especially on the ambient water moderator on which SXD is sited) should allow very high resolution data to be accumulated. Accordingly, a data set has been measured from SrF_2 at 25 K on SXD. The data are in the process of being analysed, but the promise of this approach is indicated by the observation of the (28, 28, 0) reflection (from a cubic crystal, with a = 5.8 Å; Figure 11), representing a $\sin\theta/\lambda$ value of > 3.3 $Å^{-1}$ (Q > 40 $Å^{-1}$). Since the earlier work extended the $\sin\theta/\lambda$ range to < 1.7 $Å^{-1}$, the prospects for analysing detailed thermal effects at this low temperature seem realistic, and work is continuing on this[43].

Conclusions

It is clear that time-of-flight Laue single crystal diffraction, in addition to being an ideal reciprocal space surveying technique, also has major contributions to make in the conventional area of structural studies. Provided advantage is taken of the huge amount of information available in a single data histogram, a neutron single crystal diffractometer such as SXD can yield precise atomic parameters in a wide range of structural problems.

References

[1] C C Wilson (1990) in *Neutron Scattering Data Analysis 1990*, ed M W Johnson, pp 145-163, IoP Conference Series **107**, Adam Hilger, Bristol.

[2] P L Davidson, N J Rhodes and M W Johnson (1989) in *Advanced Neutron Sources 1988*, ed D K Hyer, pp 523-528, IOP Conference Series **97**, Adam Hilger, Bristol.

[3] C Wilkinson (1986) *J de Phys Colloque* C5-**47** 35.

[4] C Wilkinson, H W Khamis, R F D Stansfield and G J McIntyre (1988) *J Appl Cryst* **21** 471.

[5] B Buras and L Gerward (1975) *Acta Cryst* A**31** 372.

[6] P J Brown and J C Matthewman (1987) *Rutherford Appleton Laboratory Report* RAL-**87-010**.

[7] D J Ganguly (1977) *N Jb Min Abh* **130** 303-318.

[8] N R Kisina, L Belokenova, A V Ukhananov and S V Urusov (1985) *Geokhimiya* **2** 153-162.

[9] P-F Zanazzi, R Rinaldi, G Artioli and C C Wilson (1993) to be published.

[10] J N Low and C C Wilson (1983) *Acta Cryst* C**39** 1688-1690.

[11] J W Wadsworth, C C Wilson and W I F David (1989) *Nucleosides Nucleotides* **8** 537-549.

[12] C C Wilson, D A Keen and N S Stewart (1992) *JCS Chem Comm* **1992** 1160-1162.

[13] M J Robins, B L Currie, R K Robins and A Bloch (1969) *Proc Am Assoc Cancer Res* **10** 73.

[14] C C Wilson (1993) *J Cryst Spect Res*, submitted.

[15] C K Johnson (1970) ORTEP: a FORTRAN thermal ellipsoid plotting program for crystal structure illustrations. *Report ORNL-3794 (2nd edition)*. Oak Ridge National Laboratory, Tennessee, USA.

[16] D Mootz and K-R Albrand (1972) *Acta Cryst* B**28** 2459-2463.

[17] E C Kostansek and W R Busing (1972) *Acta Cryst* B**28** 2454-2459.

[18] S Harkema, D Feil and C C Wilson (1993) to be published.

[19] C Aurisicchio, C Fioravanti, O Grubessi and P F Zanazzi (1988) *Amer Mineral* **73** 826-837.

[20] G E Brown, Jr and B A Mills (1986) *Amer Mineral* **71** 547-556.

[21] G Artioli, R Rinaldi, P-F Zanazzi and C C Wilson (1993) *Nature*, submitted.

[22] A K Cheetham, B E F Fender, D Steele, R I Taylor and B T M Willis (1970) *Solid State Comm* **8** 171.

[23] A K Cheetham, B E F Fender and M J Cooper (1971) *J Phys* C **4** 3107.

[24] D Steele, P E Childs and B E Fender (1972) *J Phys* C **5** 2677.

[25] J P Laval and B Frit (1983) *J Solid State Chem* **49** 237.

[26] S Hull and C C Wilson (1992) *J Solid State Chem* **100** 101-114.

[27] D J M Bevan, J Strähle and O Greis (1982) *J Solid State Chem* **44** 75.

[28] S Hull (1993) This volume.

[29] C C Wilson (1993) in *Proceedings of ICANS-XII*, eds T A Broome, A K Soper, U Steigenberger, in press.

[30] C C Wilson (1993) *J Appl Cryst*, in preparation.

[31] C C Wilson (1993) *Min Mag*, submitted.
[32] B B Lavrencic and J Petzelt (1977) *J Chem Phys* **67** 3890-3896.
[33] D J Lockwood, N Ohno, R J Nelmes and H Arend (1985) *J Phys C* **18** L559-L565.
[34] C C Wilson, P J Cox and N S Stewart (1991) *J Cryst Spectr Res* **21** 589-593.
[35] R J Nelmes (1980) *Ferroelectrics* **24** 237-245.
[36] J S Reid (1983) *Acta Cryst* A**39** 1.
[37] J F Vetelino, S P Gaur and S S Mitra (1972) *Phys Rev* B **5** 2360.
[38] M G Shumskii, V T Bublik, S S Gorelik and M A Gorewich (1971) *Kristallografiya* **16** 779.
[39] U Pietsch (1985) *Phys Stat Sol* (a) **87** 151.
[40] C Ferrari, C Bocchi, O Moze, C C Wilson and R Fornari (1992) *Physica* B **180-181** 627-628.
[41] J B Forsyth, C C Wilson and T M Sabine (1989) *Acta Cryst* A**45**, 244-247.
[42] Cooper M J and Rouse K D (1971) *Acta Cryst* A**27** 622.
[43] D A Keen, L R Hannan and C C Wilson (1993), work in progress.